Doctoral Thesis

Non-linear Analysis and Optimisation Techniques for the Design of Multifunctional Oscillator Based Circuits Applied to Active Antennas

Carlos Vázquez Antuña

May 23, 2013

Universidad de Oviedo

Programa de Doctorado
Interuniversitario en Tecnologías de
la Información y Comunicaciones
en Redes Móviles

Doctoral Thesis

Non-linear Analysis and Optimisation Techniques for the Design of Multifunctional Oscillator Based Circuits Applied to Active Antennas

Carlos Vázquez Antuña

May 23, 2013

Universidad de Oviedo

Programa de Doctorado
Interuniversitario en Tecnologías de
la Información y Comunicaciones
en Redes Móviles

RESUMEN DEL CONTENIDO DE TESIS DOCTORAL

1.- Título de la Tesis	
Español/Otro Idioma: Técnicas de análisis y optimización no lineal para el diseño de circuitos multifuncionales basados en osciladores, con aplicación en antenas activas	Inglés: Non-linear Analysis and Optimisation Techniques for the Design of Multifunctional Oscillator Based Circuits Applied to Active Antennas

2.- Autor	
Nombre: Carlos Vázquez Antuña	
Programa de Doctorado: Programa de doctorado interuniversitario en tecnologías de la información y comunicaciones en redes móviles	
Órgano responsable: Departamento de Ingeniería Eléctrica	

RESUMEN (en español)

La presente Tesis Doctoral se ha orientado al desarrollo de nuevas herramientas de análisis y optimización no lineal para el diseño de circuitos multifuncionales basados en osciladores que, además de llevar a cabo la generación de las señales de oscilador local que habitualmente se requieren en los sistemas de comunicaciones, integran funcionalidades adicionales, necesarias en antenas activas de propósito general, tales como mezcla, multiplicación en frecuencia, desfase variable y amplificación.

Estas técnicas hacen posible el desarrollo de complejos circuitos activos de microondas que, con un número reducido de componentes activos, llevan a cabo multitud de funciones adicionales, que de otra manera deberían ser implementadas por otros subsistemas independientes. Mediante esta filosofía de diseño, el consumo de potencia, el tamaño y el número de fuentes de ruido presentes en el sistema pueden ser potencialmente reducidos de manera significativa.

Las contribuciones originales presentadas en este trabajo comienzan en el Capítulo 2, en el que se utilizan mezcladores autooscilantes armónicos sincronizados para el control de una agrupación de cuatro antenas receptoras. Estos circuitos integran, junto con la generación de la señal de oscilador local, funciones tales como la mezcla armónica y la introducción de un desfase controlable en un rango continuo que excede 360º, introduciendo una ganancia de conversión positiva. El sistema completo se ha validado mediante la construcción y medida de un prototipo, que ha constituido la primera realización práctica de una agrupación de antenas activas basada en mezcladores autooscilantes armónicos sincronizados. Se ha medido un rango continuo de barrido del haz entre -23.5 y 23.5º

La utilidad práctica de los mezcladores autooscilantes armónicos sincronizados se demuestra nuevamente en el Capítulo 3, mediante su integración en una antena receptora de polarización variable. La dinámica no lineal de estos circuitos es analizada y ajustada para su aplicación a la antena de polarización variable, en la que dos circuitos alimentan dos modos radiantes con polarización lineal y ortogonales entre sí, de una antena en tecnología impresa. Se ha desarrollado un novedoso prototipo del sistema completo que permite, mediante una única señal de control continua, la variación de la polarización en la antena receptora en un rango continuo que incluye polarización circular a derechas e izquierdas, junto con dos polarizaciones lineales perpendiculares entre sí.

Con el fin de extender el uso de circuitos multifuncionales basados en osciladores a sistemas de antenas activas en transmisión, en el Capítulo 4 se presenta una novedosa solución, basada en un oscilador controlado por tensión convencional, en el que se ha optimizado la generación de su cuarto armónico, que se utilizará como señal de salida. Se han desarrollado nuevas técnicas de optimización no lineal para la reducción del consumo de potencia de los circuitos, de modo que éstos se puedan utilizar en aplicaciones alimentadas mediante baterías.

The application of the fourth harmonic oscillators for the control of a transmitting active 4x4 antenna array is described in Chapter 5. The non-linear dynamics of the 4HOSC circuits in this application are analysed and potential practical sources of dysfunctional behaviour of the system, such as mutual coupling, are identified and restrained. In particular, a Defective Ground Structure design is developed for the reduction of the mutual coupling between elements of the 4x4 antenna array.

In Chapter 6, a novel multifunctional circuit topology is proposed for active antennas operating as both transmitter and receiver, for low power short range communications. The full duplex self oscillating mixer design has been conceived to manage both communication directions, including the corresponding frequency conversions.

SR. DIRECTOR DE DEPARTAMENTO DE INGENIERÍA ELÉCTRICA

Resumen

La presente Tesis Doctoral se ha dedicado al desarrollo de nuevas herramientas de análisis y optimización no lineal para el diseño de circuitos multifuncionales basados en osciladores que, además de llevar a cabo la generación de las señales de oscilador local que habitualmente se requieren en los sistemas de comunicaciones, integran funcionalidades adicionales, necesarias en antenas activas de propósito general, tales como mezcla, multiplicación en frecuencia, desfase variable y amplificación.

Estas técnicas hacen posible el desarrollo de complejos circuitos activos de microondas que, con un número reducido de componentes activos, llevan a cabo multitud de funciones adicionales, que de otra manera deberían ser implementadas por otros subsistemas independientes. Mediante esta filosofía de diseño, el consumo de potencia, el tamaño y el número de fuentes de ruido presentes en el sistema pueden ser potencialmente reducidos de manera significativa.

El presente documento se ha organizado en varios capítulos. El Capítulo 1 constituye una recopilación de los métodos teóricos de análisis y optimización, así como de múltiples estrategias de diseño no lineal de circuitos de microondas, que se han presentado en la literatura y que son de aplicación directa en los circuitos y sistemas que se abordarán en capítulos posteriores. Asimismo, las diferentes soluciones que se pueden encontrar en los circuitos que se estudian en este trabajo, junto con las bifurcaciones y fenómenos de dinámica no lineal más comunes, se ilustran mediante ejemplos desarrollados a tal efecto, introduciendo los métodos requeridos para su caracterización, análisis y optimización.

Las contribuciones originales presentadas en este trabajo comienzan en el Capítulo 2, en el que se utilizan mezcladores autooscilantes armónicos sincronizados para el control de una agrupación de cuatro antenas receptoras. Estos circuitos integran, junto con la generación de la señal de oscilador local, funciones tales como la mezcla armónica y la introducción de un desfase controlable en un rango continuo que excede 360°, introduciendo una ganancia de conversión positiva. La dinámica no lineal de esta topología circuital se analiza y describe en detalle, particularizándola para su aplicación en la agrupación de antenas activas que se ha propuesto. El sistema completo se ha validado mediante la construcción

y medida de un prototipo, que ha constituido la primera realización práctica de una agrupación de antenas activas basada en mezcladores autooscilantes armónicos sincronizados. Se ha medido un rango continuo de barrido del haz entre $-23{,}5$ y $23{,}5°$.

La utilidad práctica de los mezcladores autooscilantes armónicos sincronizados se demuestra nuevamente en el Capítulo 3, mediante su integración en una antena receptora de polarización variable. La dinámica no lineal de estos circuitos es analizada y ajustada para su aplicación a la antena de polarización variable, en la que dos circuitos alimentan dos modos radiantes con polarización lineal y ortogonales entre sí, de una antena en tecnología impresa. Se ha desarrollado un novedoso prototipo del sistema completo que permite, mediante una única señal de control continua, la variación de la polarización en la antena receptora en un rango que incluye polarización circular a derechas e izquierdas, junto con dos polarizaciones lineales perpendiculares entre sí. Una vez más, la utilización de esta topología circuital permite llevar a cabo la conversión a frecuencia intermedia de la señal recibida, introduciendo una ganancia de conversión positiva.

Los circuitos mezcladores autooscilantes armónicos sincronizados que se utilizan en los Capítulos 2 y 3, han demostrado de manera experimental sus ventajosas propiedades para aplicaciones de antenas activas en recepción, donde se puede asumir que la señales introducidas en el circuito tienen un nivel de potencia relativamente bajo. Sin embargo, este tipo de circuitos no es apropiado para soluciones transmisoras, en las que generalmente se requieren niveles de potencia de salida relativamente altos, dado que la presencia de señales de nivel elevado en el circuito puede perturbar su solución oscilatoria autónoma.

Con el fin de superar esta limitación, permitiendo extender el uso de circuitos multifuncionales basados en osciladores a sistemas de antenas activas en transmisión, en el Capítulo 4 se presenta una novedosa solución, basada en un oscilador controlado por tensión convencional, en el que se ha optimizado la generación de su cuarto armónico, que se utilizará como señal de salida. Puesto que la eficiencia en la generación de armónicos superiores que se consigue en osciladores es típicamente muy limitada, se han desarrollado nuevas técnicas de optimización no lineal para la reducción del consumo de potencia de los circuitos, de modo que éstos se puedan utilizar en aplicaciones alimentadas mediante baterías. Mediante la utilización de las técnicas de análisis de dinámica no lineal presentadas en el Capítulo 1, se ha evaluado el comportamiento del circuito en diversas condiciones de operación.

Para la validación experimental del diseño, se ha fabricado y medido un prototipo de oscilador armónico, analizando experimentalmente sus prestaciones. Se ha prestado especial atención a su comportamiento en cuanto a ruido de fase así como a su capacidad para transmitir señales moduladas en fase mediante dos

procedimientos: modulación directa de la señal de polarización del varactor o sincronización con una señal modulada.

Los osciladores armónicos desarrollados en el capítulo 4, se han empleado en el capítulo 5 para la realización práctica de una agrupación bidimensional de 4×4 antenas. La dinámica no lineal de los circuitos se ha analizado en profundidad, identificando y combatiendo posibles fuentes de problemas prácticos tales como el acoplo mutuo. En ese sentido, se ha desarrollado un diseño de ranuras en el plano de masa para la reducción del acoplo entre elementos de la agrupación de antenas.

Las especificaciones para las redes auxiliares necesarias, tales como divisores, acopladores direccionales, etc. se han establecido desde un punto de vista conservador, orientado a la prevención de posibles problemas prácticos que pudieran perturbar el normal funcionamiento del sistema. Los criterios de diseño aplicados dan prioridad a la obtención de prototipos operativos, por encima de otros objetivos, tales como maximizar la eficiencia, que se deberían que abordar en etapas posteriores de proceso de diseño.

La utilización práctica de esta novedosa topología circuital multifuncional se demuestra mediante la realización y caracterización de un prototipo de agrupación bidimensional de antenas controlada mediante osciladores armónicos.

En el Capítulo 6, se propone una original topología multifuncional basada en osciladores, capaz de operar de manera simultánea como transmisor y receptor, con aplicación en comunicaciones de baja potencia y alcance limitado. Esta nueva solución se ha concebido para formar, junto los osciladores armónicos presentados en el Capítulo 4, una topología en dos etapas. La combinación de ambos circuitos llevaría a cabo diversas funcionalidades en ambos sentidos de la comunicación, tales como las correspondientes conversiones de frecuencia, introduciendo una cierta ganancia de conversión, el desfase variable en rango continuo, así como la generación de la señal de oscilador local. En el Capítulo 6, las técnicas de diseño empleadas para la implementación de los diferentes elementos del circuito se describen en profundidad, con especial atención a las redes de polarización basadas en líneas de anchura modulada, además del multiplexor de entrada y el diplexor de salida.

Se han optimizado las soluciones estacionarias del circuito, así como los productos de intermodulación asociados a las operaciones de conversión de frecuencia deseadas, obteniendo ganancias de conversión positivas en ambos sentidos. Se ha fabricado un prototipo preliminar del circuito para la validación experimental del diseño. Sin embargo, se han detectado ciertas discrepancias entre el comportamiento práctico del circuito y los resultados de simulación, especialmente en lo que se refiere a la amplitud y frecuencia de la oscilación libre.

Conclusiones

En el presente trabajo se ha estudiado y evaluado experimentalmente la aplicación de diversos circuitos multifuncionales basados en osciladores a sistemas de comunicaciones de propósito general implementados mediante antenas activas.

En primer lugar, se han utilizado mezcladores autooscilantes armónicos sincronizados para el control de una agrupación de cuatro antenas en recepción. Dichos circuitos llevan a cabo diversas funciones, tales como la generación de la señal de oscilador local, conversión a frecuencia intermedia, generación armónica con ganancia, así como desfase variable en un rango de más de 360 grados. El sistema se ha validado experimentalmente mediante la fabricación de un prototipo, sobre el que se ha conseguido variar la orientación del haz en un rango continuo entre -23.5 y 23.5 grados.

La misma topología se ha empleado para la implementación de una antena activa de polarización variable, en la que dos circuitos alimentan dos modos con polarización lineal y ortogonales entre sí, de una antena en tecnología impresa. El prototipo fabricado permite la variación de la polarización de la antena en un rango que incluye polarización circular a derecha e izquierda, junto con dos polarizaciones lineales ortogonales.

Se ha presentado un novedoso diseño de oscilador armónico, en el que se ha reducido significativamente el consumo, para su utilización en transmisión. Se ha fabricado un prototipo del diseño optimizado, dando lugar a un consumo de 6 mW. Se ha caracterizado el comportamiento del circuito en cuanto a ruido de fase en diversas condiciones de operación y se ha estudiado la posibilidad de utilizar el circuito para la transmisión de señales moduladas.

El diseño de oscilador armónico se ha aplicado al control de una agrupación bidimensional de 4×4 antenas. La versatilidad del diseño se ha ilustrado experimentalmente mediante la caracterización de un prototipo de la agrupación de antenas en transmisión.

Finalmente, se ha propuesto un novedoso circuito capaz de operar de manera simultánea en transmisión y recepción, para comunicaciones de baja potencia y alcance limitado. El circuito se ha concebido para su utilización junto con el oscilador armónico, dando lugar a una topología en dos etapas, capaz de implementar

diversas funciones sobre ambos sentidos de la comunicación. Se han optimizado las soluciones estacionarias del circuito, así como las operaciones de mezcla deseadas, obteniendo valores positivos de ganancia de conversión en ambos sentidos. Sin embargo, se han encontrado ciertas discrepancias entre los resultados de las simulaciones y las medidas realizadas en un prototipo preliminar del circuito.

Contents

Introduction

The present doctoral work is devoted to the development of new analysis and optimisation techniques for the design of oscillator based circuits that, apart from generating a local oscillator signal required in general purpose communication systems, integrate additional functionalities that are generally required in active antenna topologies, such as phase-shifting in a continuous range, frequency multiplication, frequency mixing, and amplification.

The techniques enable the development of complex microwave active circuits and antennas that, with a reduced number of active elements, realise multiple functions that otherwise would be implemented with different sub-system blocks. With this design philosophy, the DC power consumption, the overall size as well as the number of inherent noise sources of the system are strongly reduced.

The document is organised in several chapters. Chapter 1 contains a custom compilation of the theory, analysis and optimisation methods, as well as of several design strategies that have been presented in the scientific literature, which have a direct application on the non-linear circuits and systems studied in later chapters. In the compilation the different solutions that can be found in the systems studied in this Thesis, the possible bifurcations and other dynamical phenomena, as well as the required methods for their calculation, analysis or optimisation, are described and explained through purpose developed examples.

The novel scientific contributions generated by the author start in Chapter 2, in which Injection Locked Third Harmonic Self Oscillating Mixers (IL3HSOM) circuits are used to control a four element receiving phased antenna array. The non-linear dynamics of these circuits, that perform several functions, such as the generation of the local oscillator signal, harmonic mixing with gain, and phase shifting in a continuous range that exceeds the generally required 360°, are analysed and described in detail, for their integration in the proposed receiving phased antenna array system. The operation of these circuits is demonstrated through the non-linear analysis of the overall system including the effect of the radiating elements of the antenna array, and validated by experimental results obtained through the fabrication and measurement of a prototype. The results presented in this chapter represent the first realisation of an IL3HSOM based

phased antenna array, in which a continuous beam scanning range between -23.5 and $23.5°$, has been achieved.

The demonstration of the practical usability of injection locked third harmonic self oscillating mixer circuits in active antennas is continued in Chapter 3, where these circuits are employed for the implementation of a receiving polarisation agile active antenna. The non-linear behaviour of the harmonic self oscillating mixer circuits is analysed and adjusted for their integration in the polarisation agile active antenna. The overall performance of the system, composed of two IL3HSOM circuits, feeding two orthogonal linearly polarised radiating modes of a microstrip antenna, is analysed through non-linear simulations and validated through the experimental characterisation of a prototype. The work presented in this chapter represents the first realisation of an IL3HSOM based polarisation agile antenna, enabling the selection—through a single DC control signal—of both right and left hand circular polarisations, along with two orthogonal linear polarisation states. The inherent operation of IL3HSOM circuits additionally performs the frequency downconversion operation and the local oscillator signal generation, obtaining an overall positive conversion gain.

The ILHSOM circuits presented in Chapters 2 and 3 have proved to be very useful for their application in receiving active antennas, where it can be assumed that the received signals present relatively low power levels. However, this type of circuits is not appropriate for transmitting solutions in which a relatively high power is required, as the presence of high level signals would generally perturb the autonomous oscillatory solution.

In order to overcome this limitation, enabling the use of oscillator based circuits in transmitting active antenna systems, a novel type of multifunctional circuit is proposed in Chapter 4, consisting in a voltage controlled oscillator in which the fourth harmonic component is optimised and used as the output signal. Since the efficiency in the harmonic generation in oscillators is typically very low, new non-linear optimisation techniques for the reduction of the DC power consumption of the circuit have been developed, enabling its use in general purpose battery powered applications. The design and optimisation techniques used during the realisation of the low power fourth harmonic oscillator are described step by step. The non-linear dynamics of the circuit are analysed by means of the techniques presented in Chapter 1, in both free running and injection locked operation regimes. In the latter, the phase shift tuning capability of the circuit is also analysed.

For the experimental validation of the design, a prototype of the circuit has been manufactured and measured. Its phase noise performance has been analysed under different operating conditions, as well as the dynamics of the circuit when employed for the transmission of phase modulated signals through two different

approaches: when modulating the varactor bias voltage and when introducing a phase modulated reference signal.

The application of the fourth Harmonic OSCillators (4HOSC), developed in Chapter 4, for the control of a transmitting active antenna array is described in Chapter 5. In the proposed system, four identical 4HOSC circuits are used to feed four different rows of a purpose designed 4×4 antenna array. The non-linear dynamics of the 4HOSC circuits in this application are analysed and potential practical sources of dysfunctional behaviour of the system, such as mutual coupling, are studied and restrained. In particular, a Defective Ground Structure (DGS) design is developed for the reduction of the mutual coupling between elements of the 4×4 antenna array.

The design requirements for all the auxiliary networks required, such as power dividers, synchronisation networks, sampling directional couplers, etc., have been established from a conservative standpoint, aimed at preventing the appearance undesired practical effects, that might hamper the normal operation of the circuit. The applied design criteria prioritises the obtention of operative proof of concept prototypes over other objectives, such as maximising the efficiency, which ought to be addressed in subsequent design stages.

The usability of this type of multifunctional oscillator based circuits is demonstrated through the realisation and experimental characterisation of a prototype of a 4HOSC based transmitting active antenna array.

In Chapter 6, a novel multifunctional circuit topology is proposed for active antennas operating as both transmitter and receiver, for low power short range communications. The Full Duplex Self Oscillating Mixer (FDSOM) proposed in Chapter 6, is meant to be used in a two stage topology, together with a 4HOSC circuit. The combination of both circuits is intended to provide several functionalities such as the frequency upconversion of the transmitted signals and the frequency downconversion of the received signals, both with positive conversion gain, the phase shifting in a continuous range that exceeds the 360°, generally required for most practical applications, as well as the generation of a local oscillator signal. In the chapter, the design techniques proposed for the realisation of the different FDSOM circuit elements are described in detail, paying special attention to the arbitrarily width modulated microstrip line based multiband DC feeding networks and harmonic loads, the input multiplexer and output diplexer networks and the required filters.

The steady state solutions of the circuit as well as the desired mixing operations have been optimised, obtaining positive conversion gain values. A preliminary prototype of the circuit has been manufactured for the experimental validation of the design. Several disagreements have been found between the simulated results and the measured performance of this first prototype, especially in the amplitude and frequency of the oscillatory solution. Future work

will be aimed at the identification of the causes of those deviations, as well as to their correction.

Chapter 1

Non-linear Circuit Analysis

Contents

1.1. Introduction

The mathematical description of non-linear systems relies on a series of specific theoretical concepts and definitions, whose understanding is necessary for the analysis and classification of the different types of dynamic behaviour. The purpose of this chapter is to give an introductory insight into these fundamental mathematical concepts, that will be extensively used throughout the present work, and to establish a homogeneous terminology and notation system. Although the scope of this preliminary theoretical summary has been restricted to the specific conceptual requirements of the particular non-linear phenomena addressed in the subsequent chapters, a comprehensive analysis of these concepts of non-linear dynamics can be found in the list of specialised bibliographic references provided.

The time domain formulation of non-linear systems is introduced in the first place, categorising the different types of steady state behaviour that can be observed in those systems, and describing the characteristic features of the associated solutions. Since, for a particular steady state regime to be practically

observable, it must be able to recover from perturbations, time domain stability analysis techniques will be presented, aimed at determining whether the calculated solutions are robust and thus potentially subject to physical observation. Furthermore, the resolution of the non-linear differential equations that rule the behaviour of these systems is usually very complex and requires the use of numerical integration techniques, whose fundamental principles will be briefly discussed at the end of the section.

In certain cases, it is advantageous to express the equations that describe the system dynamics in the frequency domain, as it significantly simplifies the representation of different components (such as the linear networks and distributed elements present in electronic circuits), and enables the use of efficient numerical resolution techniques. In Section 1.3, the frequency domain formulation of non-linear systems is presented, together with the corresponding frequency domain stability analysis techniques and different frequency domain numerical resolution methods.

The solution of a dynamical system is usually influenced by the value of the parameters that describe the system components and therefore, quantitative changes in the system solutions are normally observed when varying these parameters. However, under specific circumstances, a qualitative change in the solution known as *bifurcation* is observed. In Section 1.4 the fundamental concepts of bifurcation theory are introduced and the main different types of bifurcations are characterised.

Finally, the *synchronisation* or *injection locking* phenomena, which take place when an oscillator is perturbed by a periodic external signal under certain conditions, are addressed in Section 1.5. These non-linear effects are the basis for some functionalities of the circuit topologies dealt with in the present work and will thus be largely exploited in the remaining chapters.

1.2. Time Domain Formulation

The non-linear differential equations ruling circuit behaviour are generally expressed in terms of a vector of state variables $\bar{x} = [x_1, x_2, \ldots, x_N]$. This vector consists of the minimum number of variables such that its knowledge at time t_0, together with that of the system input for $t \geq t_0$, determine the circuit response for $t \geq t_0$. Let $\bar{x} \in \mathbb{R}^N$ be the vector containing the system state variables. A general non-linear circuit can be described with of a system of differential algebraic equations that, under certain conditions, can be expressed in explicit *state form* [1]. Depending on the presence or absence of time varying generators, two different explicit formulations are possible:

$$\frac{d\bar{x}}{dt} = \bar{f}(\bar{x}, t), \qquad \bar{x}(t_0) = \bar{x}_0 \qquad \text{Non-autonomous system} \tag{1.1a}$$

$$\frac{d\bar{x}}{dt} = \bar{f}(\bar{x}), \qquad \bar{x}(t_0) = \bar{x}_0 \qquad \text{Autonomous system} \tag{1.1b}$$

where $\bar{x}(t) \in \mathbb{R}^N$ is the system state vector at time t. The function $\bar{f}$, which is non-linear in $\bar{x}$, is called the *vector field*.

In the case of non-autonomous systems, the presence of at least one independent time varying generator brings about a differential equation of the form (1.1a), in which the vector field depends explicitly on time, $\bar{f} : \mathbb{R}^N \times \mathbb{R} \to \mathbb{R}^N$. For autonomous systems, on the other hand, a differential equation of the form (1.1b) is obtained, with a time independent vector field, $\bar{f} : \mathbb{R}^N \to \mathbb{R}^N$. In such a circuit, only external DC sources can be involved. The particular case in which the vector field $\bar{f}$ is only defined in a subset $U \subset \mathbb{R}^N \times \mathbb{R}$ (non-autonomous systems), or $U \subset \mathbb{R}^N$ (autonomous systems), could also be considered [1], although it is not interesting for the purpose of this work.

The vector field f generates, for a non-autonomous system, a *flow* $\bar{\phi}_t : \mathbb{R}^N \times \mathbb{R} \to \mathbb{R}^N$, which represents the state of the system at time t, given the initial condition $\bar{x}(t_0) = \bar{x}_0$. A solution of the system is a smooth function $\bar{\phi}_t(\bar{x_0}, t_0) = \bar{u}(t)$, defined in a given time interval $I_t = (a, b) \subseteq \mathbb{R}$, fulfilling (1.1a) for all t in I_t. Mathematically,

$$\frac{d\bar{u}(t)}{dt} = \bar{f}(\bar{u}(t), t), \qquad \bar{u}(t_0) = \bar{x}_0, \qquad \forall t \in I_t. \tag{1.2}$$

Therefore, $\bar{\phi}_t(\bar{x}_0, t_0)$ defines a *solution curve, trajectory* or *orbit* of the system, based at $(\bar{x}_0, t_0)$. An analogous definition could be formulated for autonomous systems, in terms of (1.1b). As a consequence of the lack of an independent time reference in this kind of systems, if $\bar{u}(t)$ is a solution of (1.1b), then $\bar{u}(t + \tau)$, with τ being an arbitrary time shift, is also a solution.

For compactness in the formulation, the same formal equation (1.1b) can be used both for autonomous and non-autonomous systems. The non-autonomous system can be expressed as an autonomous system if the time t is considered a state variable and included in the state vector $\bar{x}$. The variable t grows unboundedly as t tends to infinity so, for the particular case of periodic vector fields, the angular magnitude $\theta = \frac{2\pi}{T}t$ is usually introduced, where T is the period of variation ($\bar{f}(\bar{x}, t + T) = \bar{f}(\bar{x}, t)$). Under these conditions, the equations of the non-autonomous system are expressed as:

$$\begin{aligned} \frac{d\bar{x}}{dt} &= \bar{f}(\bar{x}, \frac{T}{2\pi}\theta) \\ \frac{d\theta}{dt} &= \frac{2\pi}{T} \end{aligned} \tag{1.3}$$

Because $\bar{f}$ is periodic in time with period T, the new system (1.3) is periodic in θ with period 2π, and its solution is defined in the cylindrical space $\mathbb{R}^N \times S$, with

$S = [0, 2\pi)$. The same transformation is possible for aperiodic non-autonomous systems although, in this case, the variation of θ might be unbounded.

The systems considered in this work are assumed to fulfil the theorem of Existence and Uniqueness [1], which states that, if the vector field $\bar{f}$ is continuously differentiable[1], then there exists a unique function $\bar{u}(t)$ satisfying the differential equation (1.1), for each given set of initial conditions $\bar{x}(t_0) = \bar{x}_0$.

The initial value of the state vector $\bar{x}_0$, and the initial time t_0, determine the circuit solution and, consequently, solution curves cannot intersect. If two solution curves intersected at the point $(\bar{x}_i, t_i)$, assuming the initial conditions $\bar{x}(t_i) = \bar{x}_i$, the solution would not be unique.

1.2.1. Steady State Solutions and Limit Sets

Dynamical systems can be classified in terms of their type of steady state solutions, which refer to the asymptotic behaviour of the system as time tends to infinity.

A trajectory of a dynamical system based at the initial state $\bar{x}(t_0) = \bar{x}_0$ settles, perhaps after a *transient* period, onto a *limit set*. The definition of *non-wandering state* is usually employed to determine when the system has reached the steady state. *Wandering* points correspond to transient behaviour, while steady state or asymptotic behaviour corresponds to orbits of *non-wandering states* [1].

A state $\bar{p}$ is called *non-wandering* for the flow $\bar{\phi}_t$ if, for any neighbourhood U of $\bar{p}$, there exists arbitrarily large t, such that $\bar{\phi}_t(U) \cap U \neq \varnothing$.

Qualitatively, a non-wandering state has arbitrarily close trajectories which, after a sufficient period of time, come back within any specified distance of this state.

The subset $S \subset \mathbb{R}^N$ is said to be *invariant* for a flow $\bar{\phi}_t$ on $\mathbb{R}^N$ if, for every $\bar{x} \in S$, $\bar{\phi}_t(\bar{x}) \in S \quad \forall t \in \mathbb{R}$.

A state $\bar{p}$ is an *ω-limit point* of $\bar{x}$ if there exists a succession of states in the orbit of $\bar{x}$, $\bar{\phi}_t(\bar{x})$, that tends to $\bar{p}$ as time tends to infinity.

$$\exists \{t_n\}_{n\in\mathbb{N}},\ \lim_{n\to\infty} t_n = \infty \mid \lim_{n\to\infty} \bar{\phi}_{t_n}(\bar{x}) = \bar{p} \tag{1.4}$$

Similarly, a state $\bar{q}$ is an *α-limit point* of $\bar{x}$ if there exists a succession of states in the orbit of $\bar{x}$, $\bar{\phi}_t(\bar{x})$, that tends to $\bar{q}$ as time tends to minus infinity.

$$\exists \{t_n\}_{n\in\mathbb{N}},\ \lim_{n\to\infty} t_n = -\infty \mid \lim_{n\to\infty} \bar{\phi}_{t_n}(\bar{x}) = \bar{q} \tag{1.5}$$

[1] In order to be a continuously differentiable function, the vector field must have continuous partial derivatives with respect to each state variable $x_i, \quad i \in [1, \ldots, N]$ and time t, (in the case of non-autonomous systems).

The α- and ω-limit sets $\alpha(\bar{x})$, $\omega(\bar{x})$, are the sets of α- and ω-limit points of $\bar{x}$. Limit sets are closed and *invariant* [2].

A closed invariant set $A \subset \mathbb{R}^N$ is called an *attracting set* if there is some neighbourhood U of A, such that $\bar{\phi}_t(\bar{x}) \in U$ for $t \geq 0$ and $\bar{\phi}_t(\bar{x}) \to A$ as $t \to \infty$, for all $\bar{x} \in U$. The set $\bigcup_{t \leq 0} \bar{\phi}_t(U)$ is the *domain* or *basin of attraction* of A. An attracting set ultimately captures all orbits starting in its domain of attraction. A *repelling* set can be defined analogously, replacing t by $-t$.

Domains of attraction of disjoint attracting sets are necessarily non-intersecting and separated by the stable manifolds of non-attracting sets [1].

1.2.2. Phase Space Representation of Solutions

The solutions of a non-linear system can be analysed by representing the variation of the different state variables versus time.

Alternatively, the value of the state vector at each time instant $\bar{x}(t)$ can be represented by a point in the phase space, which is defined by assigning a coordinate axis to each state variable $\bar{x}_i, \quad i \in [1, \ldots, N]$. The evolution of the system is indicated by a set of sequential points versus the implicit time variable, following a *trajectory* in the phase space. In the case of non-autonomous systems, a time related variable must be included in the phase space. Therefore, the phase space representation for a system with N state variables has N dimensions if the system is autonomous, whereas it has $N + 1$ if the system is non-autonomous.

In practice, the graphical phase space representation is limited to a maximum of three dimensions. However, the solution trajectories of higher order systems can be projected onto lower order phase spaces, with the subsequent loss of information.

The steady state solutions of non-linear systems can by classified into four principal types: equilibrium point or *dc* solutions, periodic solutions, quasiperiodic solutions, and chaotic solutions. The main characteristics of each type of solution are described in the following section.

1.2.2.1. Equilibrium Point or DC Solution

An equilibrium point $\bar{x}_{eq}$ of an autonomous system[2] is a constant solution of (1.1b), $\bar{\phi}_t(\bar{x}_{eq}) = \bar{x}_{eq}$ for all t. Except for some pathological cases [3], this kind of solutions can be obtained by equating $d\bar{x}/dt = \bar{0}$ and, therefore, they correspond to zeroes of the vector field $\bar{f}(\bar{x}) = \bar{0}$.

The phase space representation of the equilibrium point in the phase space is the point itself.

[2] A non-autonomous system does not have equilibrium points as the vector field varies with time.

1.2.2.2. Periodic Solution

The solution $\bar{x}_0(t)$ is periodic if $\bar{x}_0(t+T) = \bar{x}_0(t)$ for all t and for some minimal period $T \in \mathbb{R}$. A periodic solution can be expanded in a Fourier series with a fundamental frequency $\omega_0 = 2\pi/T$. In autonomous systems, the oscillation period is determined by the parameters of the circuit elements and bias sources whereas, for a forced circuit, it is determined by the input generator.

The periodic solution produces an isolated closed trajectory in the phase space, usually known as *limit cycle*. The trajectories surrounding the limit cycle are open, corresponding to transients which, depending on its stability, will converge to the cycle or depart from it.

In Figure 1.1(a), the solutions of a cubic non-linearity oscillator [4], have been represented in the phase space (constituted by two state variables: the inductor current i_L and the capacitor voltage v_C). The circuit presents an unstable equilibrium at $\bar{x}_{eq} = (v_C, i_L) = (0, 0)$ and a stable limit cycle.

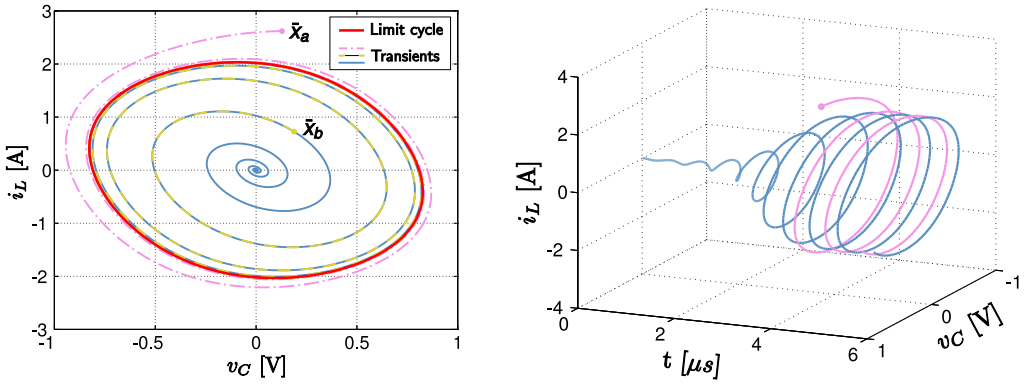

(a) (b)

Figure 1.1: Solutions of a cubic non-linearity oscillator for different initial conditions. [4]. (a) Phase space representation. (b) Time domain representation.

For the initial state $\bar{x}(t_0) = \bar{x}_{eq}$, under ideal noise free conditions, the circuit would remain at the equilibrium indefinitely. However, in practice, any instantaneous perturbation of the state of the system, will cause it to diverge from this solution exponentially, making it physically unobservable.

The stable limit cycle, on the other hand, shows robustness versus small perturbations, which means that the solution is continuously recovering from these deviations and returning to the limit cycle. The solution for some initial conditions in the surroundings of the equilibrium point $\bar{x}(t_0) = \bar{x}_{eq} + \bar{\delta}$, as shown in Figure 1.1(b), approaches the limit cycle exponentially and maintains this periodic behaviour steadily. In order to illustrate the fact that trajectories cannot intersect in the phase space, the evolution of the system from a point in the

transient of the previous orbit $\bar{x}_b$, has been superimposed in Figure 1.1(b). As expected, the solution follows the same trajectory to the limit cycle. Similarly, the system evolves from a state outside the cycle $\bar{x}_a$, with a transient leading to the same periodic solution.

In Figure 1.1(b), the solution curves based at $\bar{x}_{eq} + \bar{\delta}$ and $\bar{x}_a$ have been depicted versus time. For the sake of clarity, the initial condition $\bar{x}(t_a) = \bar{x}_a$ is applied at a time instant $t_a > 0$. After a transient, both solutions settle at the same periodic steady state, except for certain phase shift.

1.2.2.3. Quasiperiodic Solution

A solution of a dynamical system is quasiperiodic if it can be expressed as a sum of $p \geq 2$ periodic functions [2]:

$$\bar{x}(t) = \sum_{i=1}^{p} \bar{u}_i(t), \tag{1.6}$$

where each function $\bar{u}_i(t)$, has minimal period T_i and angular frequency $\omega_i = 2\pi/T_i$. These angular frequencies ω_i must be *rationally linearly independent* (or *incommensurable*), which means that if $m_1\omega_1 + \ldots + m_p\omega_p = 0$, for some set of integers $m_i \in \mathbb{Z}$, then $m_i = 0$, $\forall i \in \{1, \ldots, p\}$.

This kind of solution can thus be expanded in a Fourier series[3] with fundamental frequencies $\omega_1, \ldots, \omega_p$, as follows:

$$\bar{x}(t) = \sum_{k_1,\ldots,k_p} \bar{X}_{k_1,\ldots,k_p} e^{j(k_1\omega_1+\ldots+k_p\omega_p)t} \tag{1.7}$$

where $k_i \in \mathbb{Z}$, $i \in \{1, \ldots, p\}$ and $\bar{X}_{k_1,\ldots,k_p}$ is the vector containing the spectral components of all the state variables, at the frequency $k_1\omega_1 + \ldots + k_p\omega_p$. A key aspect of quasiperiodic solutions is that, although the number of required fundamental frequencies p, is uniquely defined, different sets of base frequencies $\omega_1, \ldots, \omega_p$ can be considered [2].

The simplest case of quasiperiodic solution, with two fundamental frequencies ($p = 2$), can be easily obtained by connecting a RF generator at frequency ω_1, to a free running oscillator with a frequency of operation ω_2. The *rotation number* [4] can be defined as:

$$r = \frac{\omega_1}{\omega_2} \tag{1.8}$$

and it must be irrational in order to obtain a quasiperiodic solution (the angular frequencies ω_1 and ω_2 must be incommensurate). If the rotation number is rational ($r = m/n$, $m, n \in \mathbb{N}$), then it is possible to write $n\omega_1 = m\omega_2$. Therefore, both

[3] In this work, the generalisation of the Fourier series expansion for quasiperiodic signals introduced in [5] is used.

frequencies are harmonic components of $\omega_0 = \omega_2/n$: $\omega_2 = n\omega_0$ and $\omega_1 = m\omega_0$ and the solution is periodic with period $T_0 = 2\pi/\omega_0$.

For an irrational rotation number, the solution is not periodic, and the trajectory in the phase space cannot be a cycle. The trajectory lies on a diffeomorphic copy of a two-torus [2]. Since the trajectory is a curve and the two-torus is a surface, not every point on the torus lies on the trajectory. However, it can be shown that the trajectory repeatedly passes arbitrarily closely to every point on the torus and, therefore, the torus is the limit set of the quasiperiodic behaviour.

The steady state solution of the cubic non-linearity oscillator used in the previous section, in which an external current signal at an incommensurate frequency has been introduced, is shown in Figure 1.2. The external current i_{ext}, has been included in the representation, obtaining a three dimensional phase space. As expected, the solution lies on the surface of a two-torus.

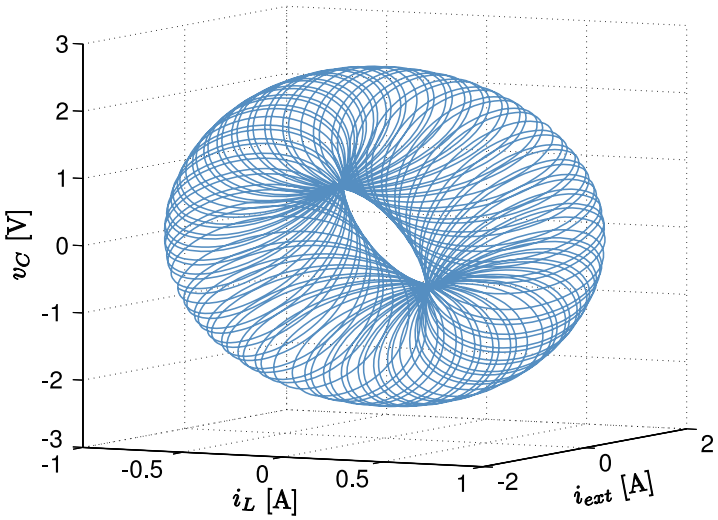

Figure 1.2: Phase space representation of the quasiperiodic solution of a cubic non-linearity oscillator with an external current generator. The solution lies on the surface of a two-torus.

Higher order quasiperiodic trajectories can occur in higher order dynamical systems. In general, a quasiperiodic solution with p incommensurate fundamental frequencies possesses a limit set that is p-dimensional figure, diffeomorphic to a *p-torus*.

1.2.2.4. Chaotic Solutions

There is no generally accepted definition of chaos. However, from a practical viewpoint, chaos can be defined as a steady state behaviour that is not an equilibrium point, not periodic and not quasiperiodic. This type of solutions presents

a sensitive dependence on the initial conditions. This means that two solutions with an arbitrarily close initial state $\bar{x}(t_0) = \bar{x}_0$, diverge at a rate characteristic of the system until, for all practical purposes, they are uncorrelated. Since, in practice, initial conditions cannot be known with infinite accuracy, the time evolution of the circuit variables $\bar{x}(t)$ is unpredictable. Nonetheless, this unpredictable behaviour, as opposed to noise and random signals, is deterministic.

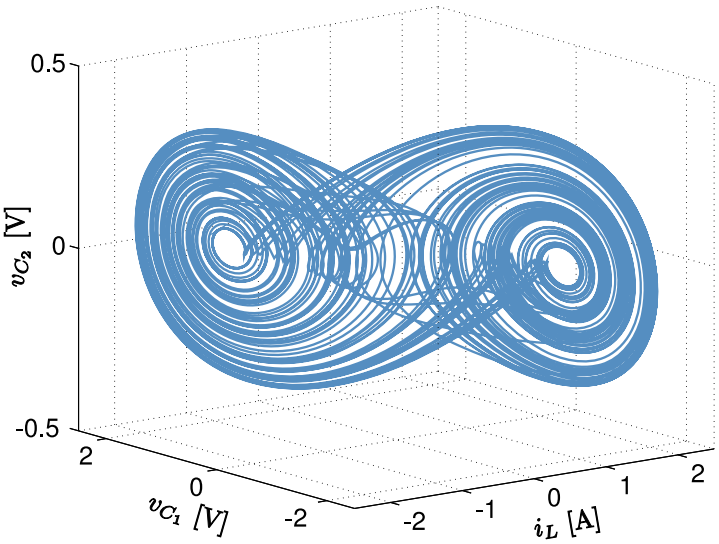

Figure 1.3: Phase space representation of the chaotic solution of Chua's oscillator.

Because the chaotic solution is neither periodic, nor quasiperiodic, it presents a continuous spectrum, at least in certain frequency intervals. When represented in the phase space, the limit set of a chaotic solution is a bounded figure which, unlike cycles and tori, is not entirely covered. Some sections of the figure are not filled by any trajectory and thus, the dimension of the figure is fractal. As an example, the chaotic solution of Chua's oscillator [6], has been represented in phase space in Figure 1.3.

1.2.3. Stability Analysis

As shown in previous sections, not all the steady state solutions of a given circuit are physically observable. To be observable, a solution must be robust versus the small perturbations that are always present in practical systems (noise, small fluctuations in the generators, etc.). This robustness is usually defined in terms of *asymptotic stability*.

Qualitatively, a limit set is *asymptotically stable* if all the neighbouring trajectories in the phase space lead to it as $t \to \infty$. Note that these neighbouring trajectories are, in fact, all the transient trajectories that might be initiated by

the small perturbations. The more general term *stable* refers to a limit set whose neighbouring trajectories always remain close, without necessarily tending to it as $t \to \infty$. Since this latter concept has limited interest for the purpose of this work, the term stable will henceforth refer to asymptotically stability.

If a small perturbation is applied to a stable solution, the system will return to it exponentially in time. In contrast, if a small perturbation is applied to an unstable solution, the system will evolve to a different steady state solution after an initially exponential transient. The solution obtained after the transient will be a stable solution and thus, physically observable.

A stable limit set is an attracting set or an *attractor*, as defined in Section 1.2.1, for all the trajectories in a neighbourhood called its basin of attraction. Similarly, a repelling set—or *repellor*—is an unstable limit set. However, there is a third essential type of limit set called *saddle type*, whose basin of attraction does not contain all its neighbouring points. This type of limit set is, therefore, unstable and unobservable.

Note that, for the stability analysis, no assumption is made as to the value of the instantaneous perturbation applied. The only condition is that it has to be small. This is because two or more stable steady state solutions may coexist and a large perturbation may lead the system to a different stable solution. Thus, the stability definition is local in nature; it refers only to the system behaviour near the steady state solution. The stability or instability of a given steady state solution depends on the system and on the particular solution, without regard to the value of the applied small perturbation. This necessary restriction to small perturbations is advantageous, as it allows linearisation of the circuit equations about the particular steady state solution. Since an arbitrary perturbation may have components in any direction of an N-dimensional phase space, the stable steady state solution must be attracting for all the neighbouring trajectories.

For the stability analysis of a given steady state solution $\bar{x}_s(t)$, either constant or time varying, a small perturbation is applied at a given time instant t_0 and, from this state, the system is allowed to evolve according to its own dynamics. Beginning at this time instant, the system analysed is a perturbed system in which the stimulus that was applied is no longer present. Due to the effect of the instantaneous perturbation, the solution becomes $\bar{x}_s(t) + \Delta\bar{x}(t)$. Since the perturbation is small, it is possible to expand the non-linear equation system in a Taylor series around $\bar{x}_s(t)$. The expansion is carried out only up to first order (higher order is rarely necessary), which provides the following linear time varying system:

$$\frac{d\bar{x}_s(t)}{dt} + \frac{d\Delta\bar{x}(t)}{dt} = \bar{f}(\bar{x}_s(t)) + J\bar{f}(\bar{x}_s(t))\Delta\bar{x}(t) \tag{1.9a}$$

$$\frac{d\Delta\bar{x}(t)}{dt} = J\bar{f}(\bar{x}_s(t))\Delta\bar{x}(t) \tag{1.9b}$$

where $J\bar{f}(\bar{x}_s(t))$ is the Jacobian matrix of the non-linear function $\bar{f}$, evaluated at the steady state solution $\bar{x}_s(t)$, as defined in (1.10). Since $\bar{x}_s(t)$ fulfils (1.1), equation (1.9a) can be simplified to (1.9b). For the steady state solution $\bar{x}_s(t)$ to be stable, the perturbation $\Delta\bar{x}(t)$ must vanish exponentially in time, which will be determined by the properties of the Jacobian matrix $J\bar{f}(\bar{x}_s(t))$. Because the Jacobian matrix is evaluated at the steady state solution, it will have the same type of behaviour as the particular solution (constant, periodic, quasiperiodic or chaotic). The method to address the stability analysis in the different cases is described in the following sections.

$$J\bar{f}(\bar{x}_s(t)) = \left(\frac{\partial f_i}{\partial x_j}\right)\Bigg|_{\bar{x}_s(t)} = \left(\begin{array}{cccc} \frac{\partial f_1}{\partial x_1} & \frac{\partial f_1}{\partial x_2} & \cdots & \frac{\partial f_1}{\partial x_N} \\ \frac{\partial f_2}{\partial x_1} & \frac{\partial f_2}{\partial x_2} & \cdots & \frac{\partial f_2}{\partial x_N} \\ \vdots & \vdots & \ddots & \vdots \\ \frac{\partial f_N}{\partial x_1} & \frac{\partial f_N}{\partial x_2} & \cdots & \frac{\partial f_N}{\partial x_N} \end{array}\right)\Bigg|_{\bar{x}_s(t)} \tag{1.10}$$

1.2.3.1. Equilibrium Point or DC Solution

For the stability analysis of an equilibrium point $\bar{x}_{eq}$, the Jacobian matrix is constant and thus, (1.9b) becomes a time invariant linear system. The general solution of this kind of system is given by [7]:

$$\Delta\bar{x}(t) = \sum_{n=1}^{N} c_k e^{\lambda_k t}\bar{u}_k \tag{1.11}$$

where the exponents $\lambda_k \in \mathbb{C}$, $k \in \{1, \ldots, N\}$, are the eigenvalues of the Jacobian matrix $J\bar{f}(\bar{x}_{eq})$, the vectors $\bar{u}_k$ are the eigenvectors of this matrix, and c_k are constants that depend on the initial conditions, namely the instantaneous perturbation applied. In order for expression (1.11) to be valid, all the eigenvalues λ_k, of the Jacobian matrix $J\bar{f}(\bar{x}_s(t))$, must be different. In case an eigenvalue λ_j is repeated p times and there are not N independent eigenvectors, the coefficient of the associated exponential term $e^{\lambda_j t}$, becomes time dependent as $(c_{0j} + c_{1j}t + \ldots + c_{(p-1)j}t^{\,p-1})e^{\lambda_j t}$, and the calculation of generalised eigenvectors is required [1].

The stability of the solution is determined by the real part of the eigenvalues $\Re\{\lambda_k\}$. According to (1.11), if all the eigenvalues have negative real parts, the perturbation $\Delta\bar{x}(t)$ vanishes exponentially in time, and the equilibrium point $\bar{x}_{eq}$ is stable. Conversely, if any of the eigenvalues had positive real part, the perturbation would grow exponentially and tend to infinity over time. However, the linearised equation (1.9b) assumes a small perturbation $\Delta\bar{x}(t)$ and therefore, it becomes invalid as the perturbation value grows. In reality, the solution does

not tend to infinity; it tends to a different steady state that cannot be predicted with this linearisation.

In case a zero eigenvalue—or eigenvalues with zero real parts—are obtained, the equilibrium is called *non-hyperbolic* and higher order terms must be considered in the Taylor series development of the vector field for the determination of its stability [4].

Note that, not all the eigenvalues have the same weight on the transient response to the perturbation, given by (1.11). This transient will be dominated by the eigenvalues with maximum real part. For a dominant pair of stable complex conjugate eigenvalues $\sigma_c \pm j\omega_c$, an oscillation at the pole frequency ω_c, with amplitude decaying to zero at a rate controlled by σ_c is observed. An unstable solution in which all the eigenvalues are real, and at least one of them is positive and at least one is negative, is generally called a *saddle*.

1.2.3.2. Periodic Solution

Periodic solutions are possible both in autonomous and non-autonomous systems. For compactness in the notation, the two types of systems will be described in terms of the characteristic equation of a non-autonomous system (1.1b). For non-autonomous systems, the angular magnitude θ will be included in the state vector and the equations will be expressed in the form (1.3). The same dimension N of the state vector will be considered in both cases.

For the stability analysis of a periodic steady state solution $\bar{x}_0(t)$, with period T, the linearisation of the perturbed system must be particularised at the periodic solution $\bar{x}_0(t)$. Thus, a periodic Jacobian matrix $J\bar{f}(\bar{x}_0(t))$, with the same period T is obtained, and equation (1.9b) becomes a periodic time varying linear system:

$$\frac{d\Delta\bar{x}(t)}{dt} = J\bar{f}(\bar{x}_0(t))\Delta\bar{x}(t) \tag{1.12}$$

Using Floquet theory, the behaviour of a linear time varying system with periodic coefficients can theoretically be studied in terms of a reduced case with constant coefficients.

In general, all the possible solutions of a N-dimensional linear system (1.9b), by the *principle of superposition*, form a vector space and they can thus be represented as a linear combination of N independent solutions $\Delta\bar{x}_1(t), \ldots, \Delta\bar{x}_N(t)$. If these independent solutions are arranged as columns of a matrix $Y(t)$, it is obvious that $Y(t)$ fulfils the system equation (1.9b):

$$\frac{dY(t)}{dt} = J\bar{f}(\bar{x}_s(t))Y(t) \tag{1.13}$$

The matrix $Y(t)$ is usually referred to as *fundamental matrix solution* of the system (1.9b) and, any solution $\Delta\bar{x}(t)$ can be written as $\Delta\bar{x}(t) = Y(t)\bar{v}_0$, where

the constant vector $\bar{v}_0$ depends on the initial conditions. Furthermore, since this matrix is not unique, it is advantageous to choose the fundamental matrix that satisfies $Y(t_0) = I$, where I is the $N \times N$ identity matrix and t_0 is the time instant when the initial condition is established. This matrix is called *canonical fundamental matrix* and it is denoted as $Y(t, t_0)$. The solution of the system (1.9b) for the initial conditions $\Delta\bar{x}(t_0) = \Delta\bar{x}_0$ is therefore given by $\Delta\bar{x}(t) = Y(t, t_0)\Delta\bar{x}_0$. Any fundamental matrix solution $U(t)$ can be expressed as $U(t) = Y(t, t_0)U(t_0)$, where $U(t_0)$ is the initial condition matrix.

In the particular case of a linear system with periodic coefficients, like (1.12), the canonical fundamental matrix $Y(t, t_0)$, satisfies:

$$Y(t + T, t_0 + T) = Y(t, t_0) \tag{1.14}$$

since it fulfils (1.12): $\frac{d}{dt}Y(t + T, t_0 + T) = J\bar{f}(\bar{x}_0(t + T))Y(t + T, t_0 + T) = J\bar{f}(\bar{x}_0(t))Y(t + T, t_0 + T)$, and $Y(t_0 + T, t_0 + T) = I$ so, by the uniqueness theorem, it must be equal to $Y(t, t_0)$. Consequently, the *monodromy matrix*, which accounts for the evolution of the system over one period:

$$M(t_0) = Y(t_0 + T, t_0) \tag{1.15}$$

is periodic with period T, $M(t_0 + T) = M(t_0)$. Looking into the evolution of the system in steps of one period [8], an exponential behaviour is observed:

$$\begin{aligned} Y(t_0 + nT, t_0) &= Y(t_0 + nT, t_0 + (n-1)T)Y(t_0 + (n-1)T, t_0) \\ &= M(t_0 + (n-1)T)Y(t_0 + (n-1)T, t_0) \\ &= M(t_0)Y(t_0 + (n-1)T, t_0) \\ &= M(t_0)^n Y(t_0, t_0) = M(t_0)^n. \end{aligned} \tag{1.16}$$

A general solution $\Delta\bar{x}(t)$ of (1.12), such that $\Delta\bar{x}(t_0) = \Delta\bar{x}_0$, must then satisfy the following expression:

$$\begin{aligned} \Delta\bar{x}(t + nT) &= Y(t + nT, t_0)\Delta\bar{x}_0 = Y(t, t_0)Y(t_0 + nT, t_0)\Delta\bar{x}_0 \\ &= Y(t, t_0)M(t_0)^n\Delta\bar{x}_0. \end{aligned} \tag{1.17}$$

It can be proved [9] that, if A is an $N \times N$ matrix and $\lambda_1, \ldots, \lambda_N$ are its eigenvalues, repeated according to their algebraic multiplicity, then $\lambda_1^k, \ldots, \lambda_N^k$ are the eigenvalues of A^k and $e^{\lambda_1}, \ldots, e^{\lambda_N}$ are the eigenvalues of e^A.

Floquet's theorem states that any fundamental matrix $Y(t)$ of a periodic linear system (1.12) can be expressed in the *Floquet normal form* [10]:

$$Y(t) = Z(t)e^{Rt}, \qquad \text{where } Z(t + T) = Z(t) \tag{1.18}$$

and R is a constant matrix ($Z(t)$ and R are $N \times N$ matrices). In particular, for the canonical fundamental matrix, $Y(t, t_0) = e^{R(t_0)(t-t_0)}$, since $Y(t_0, t_0) =$

I. Similarly, the monodromy matrix can be represented in the same form as $M(t_0) = e^{R(t_0)T}$.

Hence, if $\Delta\bar{x}_\lambda$, is an eigenvector of $R(t_0)$ corresponding to the eigenvalue λ, so that $M(t_0)\Delta\bar{x}_\lambda = e^{\lambda T}\Delta\bar{x}_\lambda$, then the solution $\Delta\bar{x}(t)$ of (1.12) for the initial condition $\Delta\bar{x}(t_0) = \Delta\bar{x}_\lambda$, satisfies:

$$\begin{aligned}\Delta\bar{x}(t+nT) &= Y(t,t_0)M(t_0)^n\Delta\bar{x}_\lambda = Y(t,t_0)\left[e^{\lambda T}\right]^n\Delta\bar{x}_\lambda \\ &= m_\lambda^n Y(t,t_0)\Delta\bar{x}_\lambda = m_\lambda^n\Delta\bar{x}(t)\end{aligned} \tag{1.19}$$

where $m_\lambda = e^{\lambda T}$ has been introduced. Additionally, the solution $\Delta\bar{x}(t) = Y(t)\Delta\bar{x}_\lambda$ is of the form $\bar{z}(t)e^{\lambda t}$ and, by (1.18), the vector $\bar{z}(t) = Z(t)\Delta\bar{x}_\lambda$ has the period T. More generally, if $\Delta\bar{x}(t)$ is the solution of (1.12), it is expressible as a linear combination of the form [10]:

$$\Delta\bar{x}(t) = \sum_{k=1}^{N} c_k t^{\delta_k} e^{\lambda_k t}\bar{u}_k(t) \tag{1.20}$$

where $\bar{u}(t+T) = \bar{u}(t)$, $\delta_k \in \mathbb{Z}$, $0 \leq \delta_k \leq N-1$ and λ_k, $k \in 1,\ldots,N$ are the eigenvalues of R. Even though neither the matrix R nor its eigenvalues $\lambda_1,\ldots,\lambda_N$ are uniquely determined, the eigenvalues of e^{RT}, which are called the *Floquet multipliers* of the system:

$$m_k = e^{\lambda_k T} \qquad k \in \{1,\ldots,N\} \tag{1.21}$$

are unique for all the fundamental matrices $Y(t)$ of (1.12).

From (1.20) follows that, whether the increment $\Delta\bar{x}(t)$ will decay to zero or grow unboundedly over time will depend solely on the limit value of m_k^n for $n \to \infty$, as the vectors $\bar{u}_k(t)$ are periodic with period T. Note that, the stability of the solution of the periodic system (1.12), can thus be analysed in terms of the eigenvalues of the constant matrix R.

Clearly, if any of the multipliers has a modulus greater than one, $|m_k| > 1$, the perturbation will tend to infinity and the solution will be unstable.

For the periodic solution $\bar{x}_0(t)$ to be stable, all the multipliers must have moduli smaller than 1, except for one corresponding to the perturbations tangent to the periodic cycle, with value $m_j = 1$. In non-autonomous circuits, it can be shown that this multiplier is associated with the time related variable θ [7].

As already pointed out, an arbitrarily time shifted solution of an autonomous system is also a solution, so perturbations tangent to the limit cycle will not vanish, as the solution is invariant under displacements along the cycle. Therefore, one of the multipliers of the periodic solution must be $m_j = 1$, which means that the perturbation neither grows nor decays over time. The associated vector $\bar{u}_j(t)$ must be tangent to the cycle at each time value or, in other words, parallel to the

time derivative of the periodic solution $\bar{x}_0(t)$: $\bar{u}_j(t) = c\frac{d}{dt}\bar{x}_0(t) = c\dot{\bar{x}}_0(t)$. Consequently, $\Delta\bar{x}_j(t) = m_j\bar{u}_j(t) = c\dot{\bar{x}}_0(t)$, (note that $m_j = 1$), must be a solution of (1.12). This can be shown as follows:

$$J\bar{f}(\bar{x}_0(t))c\dot{\bar{x}}_0(t) = c\frac{d}{dt}\bar{f}(\bar{x}_0(t)) = c\frac{d\dot{\bar{x}}_0(t)}{dt}, \tag{1.22}$$

where the fact that $\bar{x}_0(t)$ is a solution of (1.1): $\dot{\bar{x}}_0(t) = \bar{f}(\bar{x}_0(t))$, has been taken into account.

Different considerations can be made as to how the specific type of instability of the periodic solution can determine the kind of stable steady state the system will evolve to after the transient [7]. Nonetheless, for the purpose of this work, it is enough to bear in mind that, for the solution $\bar{x}_0(t)$ to be stable, all the Floquet multipliers of (1.12) must have moduli smaller than one, except for the one associated with perturbations tangent to the limit cycle:

$$m_j = 1 \quad \text{and} \quad |m_k| < 1, \quad \forall\, k \in \{1, \ldots, N\},\ k \neq j \tag{1.23}$$

The computation of the Floquet multipliers requires a representation of the monodromy matrix in the form $M(t_0) = e^{RT}$, which can only be obtained by actually generating a set of N linearly independent solutions of (1.12) to constitute a fundamental matrix solution $Y(t)$. Except in special theoretical cases, this calculation is generally a greatly challenging task.

1.2.3.3. Lyapunov Exponents

Lyapunov exponents are a generalisation of the eigenvalues at an equilibrium point and of the Floquet multipliers for periodic orbits. They are used to determine the stability of any type of steady state behaviour, including quasiperiodic and chaotic solutions.

Consider the general non-linear differential equation for autonomous systems[4]:

$$\frac{d\bar{x}}{dt} = f(\bar{x}), \qquad \bar{x} \in \mathbb{R}^N \tag{1.24}$$

with flow $\bar{\phi}_t$. If $\varepsilon \in \mathbb{R}$, $\bar{u}, \bar{v} \in \mathbb{R}^N$, the two solutions $\bar{\phi}_t(\bar{u})$, $\bar{\phi}_t(\bar{u} + \varepsilon\bar{v})$, start at two points in $\mathbb{R}^N$ whose separation is bounded by $\varepsilon\,||\bar{v}||$, where $||\cdot||$ is the usual norm in $\mathbb{R}^N$.

The Taylor expansion of the difference between the two solutions at $\varepsilon = 0$ is given by:

$$\bar{\phi}_t(\bar{u} + \varepsilon\bar{v}) - \bar{\phi}_t(\bar{u}) = \varepsilon J\bar{\phi}_t(\bar{u})\bar{v} + O(\varepsilon^2) \tag{1.25}$$

where $J\bar{\phi}_t(\bar{u})$ denotes the Jacobian matrix of the flow $\bar{\phi}_t(\bar{x})$, with respect to the initial condition $\bar{x}$, evaluated at $\bar{x} = \bar{u}$. The first order approximation of the

[4]For non-autonomous systems, the equivalent formulation (1.3) is used.

difference between the two solutions at time t is $\varepsilon J\bar{\phi}_t(\bar{u})\bar{v}$, and $J\bar{\phi}_t(\bar{u})$ is the canonical fundamental matrix solution at $t = 0$ of the linearised equation:

$$\frac{dW}{dt} = J\bar{f}(\bar{\phi}_t(\bar{u}))W \tag{1.26}$$

along the solution of the original system (1.24), starting at $\bar{u}$. To prove this, substitute $\bar{\phi}_t(\bar{z})$ for $\bar{x}$ in the general system equation (1.24): $\frac{d}{dt}\bar{\phi}_t(\bar{z}) = \bar{f}(\bar{\phi}_t(\bar{z}))$, $\bar{\phi}_t(0) = \bar{z}$ and differentiate versus the initial condition $\bar{z}$ at $\bar{z} = \bar{u}$:

$$\frac{dJ\bar{\phi}_t(\bar{u})}{dt} = J\bar{f}(\bar{\phi}_t(\bar{u}))J\bar{\phi}_t(\bar{u}), \qquad \bar{\phi}_t(0) = I. \tag{1.27}$$

Suppose that $\bar{u}, \bar{v} \in \mathbb{R}^N$, $\bar{v} \neq \bar{0}$ and $\bar{\phi}_t(\bar{u})$ is a solution of (1.24) based at $\bar{u}$, defined for all $t \geq 0$. The *Lyapunov exponent* at $\bar{u}$ in the direction $\bar{v}$ for the flow $\bar{\phi}_t$ is defined as:

$$\chi(\bar{u}, \bar{v}) = \lim_{t\to\infty} \frac{1}{t} \ln\left(\frac{\left|\left|J\bar{\phi}_t(\bar{u})v\right|\right|}{||v||}\right) \tag{1.28}$$

if the limit exists[5]. Let $\nu_1, \ldots, \nu_N$ be the eigenvalues of $J\bar{\phi}_t(\bar{u})$ and $\bar{\eta}_1, \ldots, \bar{\eta}_N$, the corresponding eigenvectors, the definition (1.28) can be expressed as [2]:

$$\chi(\bar{u}, \bar{\eta}_i) = \lim_{t\to\infty} \frac{1}{t} \ln|\nu_i(t)|. \tag{1.29}$$

For the particular case of an equilibrium point, the Lyapunov exponents are equal to the real parts of the eigenvalues of the perturbed system at the equilibrium point, and they indicate the contraction ($\chi_i < 0$) or expansion ($\chi_i > 0$) of the trajectories originated close to the equilibrium point. Since the Lyapunov exponents are defined in terms of the limit as $t \to \infty$, any finite transient of the orbit may be neglected and therefore, in general, every point in the basin of attraction of an attractor has the same Lyapunov exponents as the attractor[6].

Similarly, the Lyapunov exponents χ_i of a limit cycle have a simple relationship with the Floquet multipliers m_i:

$$\chi_i = \frac{1}{T} \ln|m_i|, \qquad i = 1, \ldots, N \tag{1.30}$$

One Lyapunov exponent χ_j is always 0, corresponding to the multiplier that is always one. The proof of this fact can be generalised to show that, for any

[5]The existence of the Lyapunov exponents can be guaranteed by considering the *superior limit*. Nevertheless, the interpretation of the exponents presented below is only valid if the limit in (1.28) exists [2].

[6]For some definitions of *strange attractors*, this statement may need to be changed to *almost every point*, although it is always valid for *non-strange* attractors [2].

Steady State	Limit Set	Lyapunov Exponents	Dimension
Equilibrium Point	Point	$0 > \chi_1 \geq \cdots \geq \chi_N$	0
Periodic	Closed Curve	$\chi_1 = 0$ $0 > \chi_2 \geq \cdots \geq \chi_N$	1
Quasiperiodic (2 fundamentals)	Torus	$\chi_1 = \chi_2 = 0$ $0 > \chi_3 \geq \cdots \geq \chi_N$	2
Quasiperiodic (K fundamentals)	K-torus	$\chi_1 = \cdots = \chi_K = 0$ $0 > \chi_{K+1} \geq \cdots \geq \chi_N$	K
Chaotic	Cantor-like	$\chi_1 > 0$ $\sum_{i=0}^{N} \chi_i < 0$	Noninteger

Table 1.1: Classification of the different types of hyperbolic steady states depending on the Lyapunov exponents [2].

bounded attractor of an autonomous system, except an equilibrium point, one Lyapunov exponent is always 0 [2].

The Lyapunov exponents represent the average rate of contraction or expansion in a particular direction close to a particular trajectory. Ordering the χ_i such that $\chi_1 \geq \cdots \geq \chi_N$, there are N nested subspaces, $W_1 \supset \cdots \supset W_N$, such that almost all perturbations in W_j evolve, on average, as $e^{\chi_j t}$. Obviously, these conclusions are only valid for small perturbations, in order for the first order approximation of (1.25) to be accurate.

Lyapunov exponents are convenient for categorising steady state behaviour. For an attractor, contraction must outweigh expansion so:

$$\sum_{i=1}^{N} \chi_i < 0. \tag{1.31}$$

Attractors can be classified using their Lyapunov exponents as shown in Table 1.1. As already commented, chaotic behaviour is highly dependent on the initial conditions; orbits originated at arbitrarily close points diverge in time until they are uncorrelated. Hence, a feature that distinguishes strange attractors from other types of attractor is the existence of at least one positive Lyapunov exponent, which produces this divergence of trajectories, maintaining relation (1.31) for stability.

1.2.4. Poincaré Map

The Poincaré map allows the representation of the system solution with a reduction of its dimension; it transforms the N dimensional continuous solution $\bar{x}(t) = \bar{\phi}_t(\bar{x}_0, t_0)$ into a discrete solution of dimension $N-1$. This reduction of the dimension simplifies the analysis of the system solution (qualitative variations as a function of a parameter, evolution from a perturbed state, and so forth).

Let $\gamma = \bar{x}_0(t)$ be a periodic orbit of some flow $\bar{\phi}_t$ in $\mathbb{R}^N$, arising from a non-linear vector field $\bar{f}(\bar{x})$. Consider a *local cross section* $\Sigma \subset \mathbb{R}^N$, of dimension $N-1$. Although the *hypersurface* Σ need not be planar, it must be chosen so that the flow is everywhere *transverse* to it. This is achieved by assuring that, if $\bar{n}(\bar{x})$ is the unit normal to Σ at a point $\bar{x} \in \Sigma$, then $\bar{f}(\bar{x}) \cdot \bar{n}(\bar{x}) \neq 0$ must be fulfilled for all $\bar{x} \in \Sigma$. The size of Σ must be adjusted to provide a single point of intersection with γ, denoted as $\bar{p} = \gamma \cap \Sigma$. Let $U \subset \Sigma$ be some neighbourhood of $\bar{p}$. The Poincaré map $\bar{P} : U \to \Sigma$ is defined for a point $\bar{q} \in U$ by:

$$\bar{P}(\bar{q}) = \bar{\phi}_\tau(\bar{q}), \tag{1.32}$$

where $\tau = \tau(\bar{q})$ is the time taken for the orbit $\bar{\phi}_t(\bar{q})$ based at $\bar{q}$ to first return to Σ. Note that τ generally depends upon $\bar{q}$ and need not be equal to T, the period of γ. However, τ tends to T as $\bar{q}$ approaches $\bar{p}$. In the periodic regime, the time τ agrees with the period T, $\bar{P}(\bar{p}) = \bar{p}$, and $\bar{p}$ is a *fixed point* of the Poincaré map.

It can be shown that the stability properties of the point $\bar{p}$ for the discrete flow defined by the Poincaré map are the same as those of the continuous solution $\bar{x}_0(t)$. The stability of the fixed point $\bar{p}$ can be checked by applying a small perturbation and analysing the evolution of the successive points of the map which, in the case of a stable solution, must progressively approach $\bar{p}$. In Figure 1.4(a), the Poincaré map of the periodic solution of an autonomous system has been represented. Since the steady state solution is stable, the two perturbations introduced in the system converge in the Poincaré map to the fixed point $\bar{p}$.

For non-autonomous systems with a periodic forcing, with period T, an angular magnitude $\theta = \frac{2\pi t}{T} \pmod{2\pi}$, can be included in the state vector $\bar{x}$. A global cross section Σ can then be defined as:

$$\Sigma = \left\{ (\bar{x}, \theta) \in \mathbb{R}^N \times S \,|\, \theta = \theta_0 \right\} \tag{1.33}$$

since all the solutions cross Σ transversely with period T. The intersection of Σ with the solution orbit produces a Poincaré map $\bar{P} : \Sigma \to \Sigma$ of the form:

$$\bar{P}(\bar{p}) = \bar{\phi}_T(\bar{p}, t_{\theta_0}) \tag{1.34}$$

Note that, in a non-autonomous system with a periodic forcing term of period T, the period of the solution $\bar{x}(t)$ does not necessarily agree with T; it might not even be periodic.

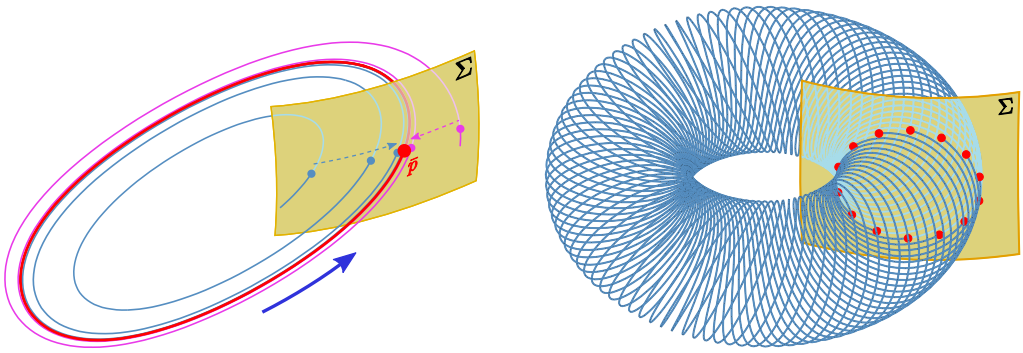

(a) (b)

Figure 1.4: Schematic diagram of the obtention of Poincaré maps. (a) For the periodic solution of an autonomous system. Two perturbations have been introduced to verify the robustness of the solution. (b) For the quasiperiodic solution of a non-autonomous system. For the sake of clarity, the solution has been truncated, obtaining a finite set of intersection points between the solution and the Poincaré surface Σ.

In Figure 1.4(b), the Poincaré map of the quasiperiodic solution of a non-autonomous system has been represented. Since the solution is not periodic, the Poincaré map of the limit torus is an infinite set of discrete points distributed along a closed cycle. However, for the sake of clarity, only a truncated version of the continuous solution has been represented, yielding a finite number of points in the Poincaré map. Both examples show how the Poincaré map enables the two dimensional representation of solutions belonging to three dimensional phase spaces.

1.2.4.1. Stability of Periodic Solutions using the Poincaré Map

The stability analysis of periodic steady state solutions can be performed using the linearised Poincaré map, by applying analogous techniques to those already explained for continuous flows. As previously pointed out, a periodic orbit γ, with period T, produces a fixed point $\bar{p}$ in the Poincaré map, such that

$$\bar{P}(\bar{p}) = \bar{\phi}_T(\bar{p}) = \bar{p}. \tag{1.35}$$

The stability properties of the fixed point $\bar{p}$ can be determined by studying the evolution of the Poincaré map of a perturbed point $\bar{p}_p \in U$, $\bar{p}_p = \bar{p} + \Delta\bar{p}$. Providing the magnitude of the applied perturbation $||\Delta\bar{p}||$ is small, the first order Taylor expansion of the flow about the fixed point $\bar{p}$, can be considered,

yielding the following $N-1$ dimensional linear perturbed map, $U \rightarrow \Sigma$:

$$\bar{P}_l(\Delta\bar{p}) = J\bar{P}(\bar{p})\Delta\bar{p}, \tag{1.36}$$

where $J\bar{P}(\bar{p})$ represents the Jacobian matrix of the map $\bar{P}$, evaluated at the fixed point $\bar{p}$.

The eigenvalues of this Jacobian matrix λ_i, $i \in \{1, \ldots, N-1\}$, determine the stability of the fixed point $\bar{p}$. If $|\lambda_i| < 1$, $\forall i \in \{1, \ldots, N-1\}$, the magnitude of the perturbation $||\Delta\bar{p}||$ will progressively decay and the fixed point $\bar{p}$ will be asymptotically stable. Conversely, the solution will be unstable if any of the eigenvalues has modulus greater than one. In case one of the eigenvalues has modulus one $|\lambda_i| = 1$, the fixed point is non-hyperbolic and its stability cannot be determined with the first order Taylor expansion; higher order terms must be considered.

It can be shown [1] that the $N-1$ eigenvalues of $J\bar{P}(\bar{p})$ agree with $N-1$ Floquet multipliers of the periodic orbit γ. As has been commented in Section 1.2.3.2, the remaining multiplier—equal to unity—is associated with perturbations tangent to the periodic orbit. Furthermore, the stability properties of the map can be proved to be independent of the considered cross section Σ.

1.2.5. Time Domain Circuit Simulation

The time domain mathematical formulation of non-linear circuits presented in previous sections, provides a natural description of the circuit dynamics in terms of a system of non-linear differential equations, which simplifies the theoretical identification and classification of the different possible types of solutions, from a qualitative viewpoint. Nevertheless, the solution of a particular circuit, that accurately predicts its behaviour, is generally difficult to obtain and requires the use powerful numerical simulation techniques.

The purpose of this section is to introduce the principles of the time domain integration techniques applied to the numerical simulation of non-linear circuits, highlighting their main practical advantages and drawbacks, that must be contemplated by the circuit designer, without addressing a detailed analysis of the underlying numerical algorithms, which lie beyond the scope of this work.

An important aspect for the simulation of non-linear circuits is the accurate modelling of the non-linear devices involved. Since these non-linear elements are usually described in terms of their constitutive functions, which relate the instantaneous value of the non-linear magnitude (current, charge, etc.), to those of the control variables, these equations can be directly introduced in the time domain circuit formulation.

On the other hand, distributed elements (such as transmission lines, coupled lines, and so on), widely used in high frequency circuits—in the microwave band

and above—are difficult to simulate in the time domain, as they are originally described in terms of partial differential equations. The most general approaches are based on the numerical calculation of the impulse response of the element from the inverse Fourier transform of its transfer function. This transfer function can be straightforwardly computed from the frequency dependent Z, Y or S parameters of the distributed element. It is also possible to use the Laplace transform of the partial differential equation that rules the distributed element, and adopt its truncated Taylor series expansion as a reduced order model. This expansion can be subsequently matched to a complex rational function in terms of pole–residue pairs, whose inverse Laplace transform can be analytically calculated, yielding the impulse response. The impulse response of the distributed element, obtained through either procedure, can be incorporated in the differential equation as a convolution operation—that must be computed at each time step—to determine the time domain response of the element. Alternatively, from the initial description in the Laplace domain, it is possible to model the distributed element with a set of linear differential equations, related to the rest of the circuit equations through Kirchhoff's laws. Detailed information about these techniques can be found in [7].

To determine the circuit solution, the non-linear differential equation that rules its behaviour (including non-linear devices, distributed elements, and so on) must be integrated from the initial conditions established at a time point t_0. To do this, the continuous time variable t is discretised, with a constant or variable time step, and replaced with the time points $\{t_0, \ldots, t_n, \ldots, t_N\}$. This transforms the continuous system of non-linear differential equations into an algebraic system of non-linear equations, in terms of the time samples of the circuit variables at the time instants t_n. The derivatives $d\bar{x}/dt$ at a time instant t_{n+1} can be approximated, in multiple manners, as a function of the values $\{\ldots, \bar{x}_{n-1}, \bar{x}_n, \bar{x}_{n+1}\}$, and each particular approximation constitutes a different integration algorithm (such as forward or backward Euler, Runge–Kutta, Gear, etc.). Each algorithm leads to a different discrete system with its characteristic accuracy, efficiency and stability properties [7]. The system resulting from the application of the selected integration algorithm is usually resolved using the Newton–Raphson method, which converts the non-linear problem into a sequence of linear equations, that can be solved iteratively.

Direct integration methods can, in principle, be used for the simulation of any kind of regime, periodic, quasiperiodic or chaotic and with periodic or aperiodic input signals. The complete solution curve is computed; the steady state solution is reached after the calculation of the whole transient so, if convergence is achieved and the integration method and time step are adequately chosen, the steady state solution is stable.

The time step must be selected to provide an accurate representation of the waveforms present in the circuit. In case the spectrum of the solution contains both high and low frequency components, the time step must be short enough to represent the high frequency components accurately, and the integration time interval must be long enough to account for the evolution of the low frequency components, giving rise to an enormous number of calculation points. Usually, most of the simulation time is devoted to the transient regime, while the interest of the designer lies in the steady state. To overcome this limitation, fast time domain algorithms [7] have been proposed. Nevertheless, for the simulation of periodic or quasiperiodic regimes of circuits with distributed elements, the harmonic balance method presented in the following section may be more appropriate.

1.3. Frequency Domain Formulation

As already mentioned, the description of linear networks is generally straightforward in the frequency domain. In particular, for distributed elements, the convolution integrals used in the time domain formulation can be substituted by simple transfer function products in the frequency domain. Taking advantage of this property, the frequency domain formulation transforms the set of non-linear differential equations that rule the circuit behaviour into a set of non-linear algebraic equations in the frequency domain. It uses the simplified frequency domain descriptions of linear networks, retaining the natural time domain constitutive equations of the non-linear elements.

The frequency domain formulation of non-linear circuits is closely related to the harmonic balance simulation method. In fact, in some bibliographic references, the formulation is introduced as a part of the simulation method. However, in this work, the frequency domain formulation of non-linear circuits is presented separately, in analogy to the time domain formulation described in Section 1.2, while the peculiarities of the harmonic balance resolution method are commented in a dedicated subsection.

In the frequency domain formulation, it is assumed that the circuit variables can be expanded in a Fourier series with a finite set of irrationally related fundamentals $\{\Omega_1, \ldots, \Omega_K\}$, such that $\Omega_i = 2\pi F_i$. Moreover, in practice, the series must be truncated to a finite number N_H of positive frequency components, in the general form:

$$u(t) = \sum_{m=-N_H}^{N_H} U_m e^{j\omega_m t} \qquad \omega_m \equiv \bar{\lambda}_m \bar{\Omega} \qquad \bar{\Omega}^t = [\Omega_1 \ldots \Omega_K] \tag{1.37}$$

where $u(t)$ is a generic circuit variable. The vector $\bar{\lambda}_m^t \in \mathbb{Z}^K$ contains the integer coefficients of the intermodulation product m, given by $\omega_m \equiv \bar{\lambda}_m \bar{\Omega} = \lambda_m^1 \Omega_1 + \ldots + \lambda_m^K \Omega_K$, with $\lambda_m^j \in \mathbb{Z}$. The superscript j in λ_m^j indicates the fundamental frequency Ω_j that is affected by that particular integer. The subscript m places the resulting frequencies in increasing order $\omega_1 < \cdots < \omega_{N_H}$. Note that only positive frequencies are included in the set $\{\omega_1, \ldots, \omega_{N_H}\}$. Their negative counterparts (and the dc component) are also considered in the Fourier series, as shown in (1.37), although—for real variables—the coefficients U_m are known to fulfil the hermitian symmetry $U_m = U_{-m}^*$.

For series with more than one fundamental, different systematic truncation criteria [7], can be used to establish the maximum order of the harmonic components and intermodulation products taken into account. Nonetheless, when there are significant differences in the amplitude of the signals at the different fundamental components, it may be interesting to assign a specific maximum harmonic order M_j for each fundamental $j \in [1, K]$, such that $|\lambda_m^j| \leq M_j$, $\forall m \in [1, \ldots, K]$, as well as a maximum order for the intermodulation products M_{im}, so that $|\lambda_m^1| + \ldots + |\lambda_m^K| \leq M_{im}$. Thus, the frequency basis can be efficiently adapted to take into account the higher harmonic content generated for the fundamentals with higher signal amplitude, while disregarding the terms of the same order of fundamentals with lower signal level, which would have a negligible value.

The representation of the variables in a Fourier series restricts the variety of regimes that can be studied in the frequency domain to periodic or quasiperiodic steady state solutions. Due to the truncation of the series, this formulation is only appropriate for mild non-linear regimes and might not be convenient for periodic signals with short rise and fall times. Furthermore, unlike in the time domain simulation, the obtained solution may be either stable or unstable, so a complementary stability analysis is necessary.

Two different frequency domain formulations have been presented in the literature [7]. The first formulation, known as *nodal harmonic balance*, results from directly introducing the Fourier series expansions in the time domain circuit equations. The state variables are all the node voltages and inductance currents, usually leading to a system with a large number of unknowns. On the other hand, the second formulation, known as *piecewise harmonic balance*, is based on a strict separation of the circuit elements into linear and non-linear. The non-linear elements are modelled as dependent sources and their control variables constitute the set of state variables. Compared to the nodal formulation, the number of unknowns is considerably reduced at the expense of an increase in the complexity of the relationships representing the linear embedding network, which will have higher order in the frequency ω. The frequency domain description of non-linear circuits illustrated in the following is based on the piecewise formulation.

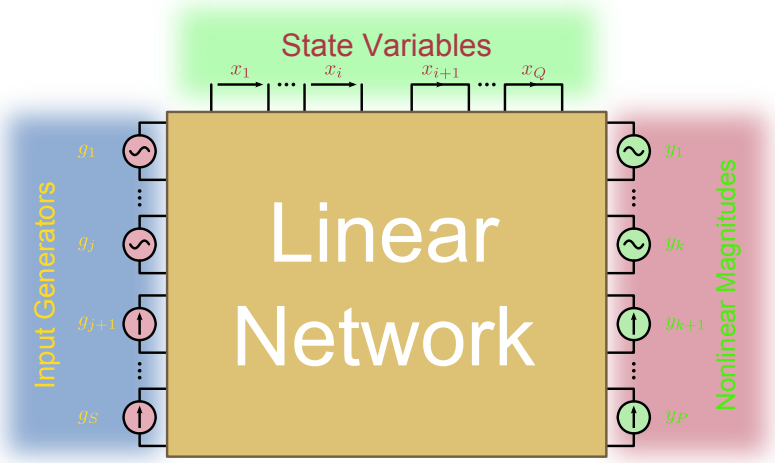

Figure 1.5: Representation of a generic circuit in the frequency domain formulation.

For the definition of the frequency domain formulation, the general circuit shown in Figure 1.5 is considered. The P non-linear magnitudes produced by the non-linear devices involved in the circuit are firstly identified and represented by dependent sources. Their Q control variables constitute the set of state variables. The S external input generators are also considered separately. Since the rest of the circuit is a linear network, the application of Kirchhoff's laws yields a linear relationship that interlinks the evolution of the non-linear magnitudes $\bar{y}(t) = [y_1(t), \ldots, y_P(t)]^t$, the state variables $\bar{x}(t) = [x_1(t), \ldots, x_Q(t)]^t$ and the input signals $\bar{g}(t) = [g_1(t), \ldots, g_S(t)]^t$, where the superscript t represents the transpose operation. Obviously, the non-linear magnitudes grouped in $\bar{y}(t)$ are still related to the state variables $\bar{x}(t)$ through the non-linear function:

$$\bar{y}(t) = \bar{f}_{nl}(\bar{x}(t)) \tag{1.38}$$

The three vectors $\bar{x}$, $\bar{y}$ and $\bar{g}$ are represented in the frequency domain by the coefficients of the Fourier series expansion, grouped respectively in the vectors $\bar{X}$, $\bar{Y}$ and $\bar{G}$, defined as follows:

$$\begin{aligned} \bar{X}^t &= [\bar{X}_{-N_H}, \ldots, \bar{X}_i, \ldots, \bar{X}_{N_H}] & \bar{X}_i &= [X_i^1, \ldots, X_i^q, \ldots, X_i^Q] \\ \bar{Y}^t &= [\bar{Y}_{-N_H}, \ldots, \bar{Y}_i, \ldots, \bar{Y}_{N_H}] & \bar{Y}_i &= [Y_i^1, \ldots, Y_i^p, \ldots, Y_i^P] \\ \bar{G}^t &= [\bar{G}_{-N_H}, \ldots, \bar{G}_i, \ldots, \bar{G}_{N_H}] & \bar{G}_i &= [G_i^1, \ldots, G_i^s, \ldots, G_i^S] \end{aligned} \tag{1.39}$$

The column vectors are structured in $2N_H+1$ subvectors, one for each analysis frequency. Each subvector—dedicated to the frequency component indicated by

the subscript i—contains the coefficients of the Fourier series corresponding to the Q state variables for $\bar{X}_i$, the P non-linear magnitudes for $\bar{Y}_i$ and the S input generators for $\bar{G}_i$.

The application of Kirchhoff's laws to the circuit of Figure 1.5 provides the linear relationships existing between the componets of the vectors $\bar{X}$, $\bar{Y}$ and $\bar{G}$, that can be expressed in the general form:

$$\bar{E}(\bar{X}) = A_x\bar{X} + A_y\bar{Y} + A_g\bar{G} = \bar{0} \tag{1.40}$$

where A_x, A_y and A_g are constant matrices, obtained from the evaluation of the frequency dependent linear relationships given by Kirchhoff's laws, at the frequency basis considered.

The basis functions of the Fourier series expansion are known to be eigenfunctions of the linear invariant systems [11]. Assuming time invariance of the linear network and taking into account the superposition principle, the linear network can only interrelate the coefficients of the different circuit variables corresponding to the same frequency component. Therefore, considering the structure of the vectors shown in (1.39), the matrices must have a block diagonal structure composed of submatrices dedicated to each of the $2N_H + 1$ frequency components, in the general form:

$$A = \begin{pmatrix} [A_{-N_H}] & [0] & \cdots & [0] \\ [0] & [A_{-N_H+1}] & \cdots & [0] \\ \vdots & \vdots & \ddots & \vdots \\ [0] & \cdots & [0] & [A_{N_H}] \end{pmatrix} \tag{1.41}$$

where A stands for any of the matrices A_x, A_y or A_g. The blocks $[A_i]$, $i \in [-N_H, \ldots, N_H]$ have dimensions $Q \times Q$ for A_x, $Q \times P$ for A_y and $Q \times S$ for A_g. Hence, (1.40) represents a system of $(2N_H + 1)Q$ equations in $(2N_H + 1)Q$ unknowns, grouped in the set of state variables $\bar{X}$. Note that the external input generators are known and the non-linear magnitudes $\bar{Y}$, are related to the state variables through (1.38).

1.3.1. Frequency Domain Circuit Simulation: Harmonic Balance

The frequency domain formulation that has been introduced can be used to efficiently represent non-linear circuits working in periodic or quasiperiodic operating regimes. The harmonic balance simulation method relies on the resolution of the non-linear algebraic system (1.40), that represents a particular circuit, to determine the specific solution that rules its behaviour. This resolution is normally carried out using numerical iterative techniques.

The vector of state variables $\bar{X}$, that cancells out the error vector $\bar{E}(\bar{X})$, is determined through a minimisation method (usually based on the Newton–Raphson algorithm), applied to the norm of the error vector $||\bar{E}(\bar{X})||$.

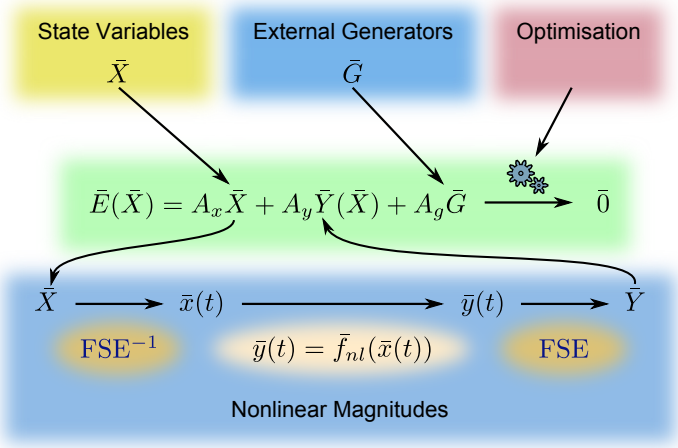

Figure 1.6: Evaluation of equation (1.40).

The evaluation of equation (1.40) for a given state vector $\bar{X}$, is performed as shown schematically in Figure 1.6. The state vector $\bar{X}$ and the external input signals $\bar{G}$ are directly introduced in the equation. The non-linear magnitudes $\bar{Y}$ are dependent on the state variables through the time domain equation (1.38), which relates $\bar{y}(t)$ with $\bar{x}(t)$. Therefore, in order to use this equation, the time domain representation of the state vector $\bar{x}(t)$, is required. From the coefficients of the Fourier series expansion $\bar{X}$, the time domain signal $\bar{x}(t)$ can be obtained through the summation of the series (1.37). Equation (1.38) can then be applied to calculate the non-linear magnitudes in the time domain, $\bar{y}(t)$. Finally, the non-linear magnitudes in the frequency domain $\bar{Y}$, are simply the coefficients of the Fourier series expansion of $\bar{y}(t)$. In Figure 1.6, the process of calculation of the coefficients for the Fourier Series Expansion is indicated as FSE, while the summation of the series to obtain the time domain signal is labelled as FSE^{-1}. These operations are usually referred to in the literature as, respectively, analysis and synthesis of the Fourier series [11].

The optimisation process starts with an initial value $\bar{X}^0$, which can be determined with a DC analysis of the circuit. The system is subsequently resolved through an iterative process, usually based on the Newton–Raphson algorithm, whereby the state vector for the iteration $j+1$, $\bar{X}^{j+1}$, is estimated from a linearisation of the system about the point $\bar{X}^j$, corresponding to the iteration j. Mathematically:

$$\bar{X}^{j+1} = \bar{X}^j - [JE]^{-1}\big|_{\bar{X}^j} \bar{E}^j(\bar{X}^j) \tag{1.42}$$

where $JE|_{\bar{X}^j}$ is the Jacobian matrix of the error function of (1.40), with respect to the state vector $\bar{X}$, evaluated in the iteration j, $\bar{X}^j$. The process finishes when the variation of the state vector $\bar{X}^{j+1}$, with regard to the previous iteration $\bar{X}^j$, lies within the desired tolerance.

The convergence of the Newton–Raphson algorithm is highly influenced by the initial value $\bar{X}^0$. As has been stated, the DC solution can be an appropriate starting point, especially for small signal operation. However, when the level of the input generators is high, the large signal solution may be considerably different from the DC starting point, seriously compromising the convergence of the optimisation process.

Different methods, known as continuation techniques, have been proposed in the literature to tackle this problem [7]. They basically consist in introducing a parameter η, that can either belong to the original system or be artificially defined, in such a way that the system can be easily solvable for some value of the parameter η_i, while completely agreeing with the original system for another value η_f. The harmonic balance system is successively solved, varying the parameter from η_i to η_f in a certain number of steps. The resolution in the first step is, by the definition of the parameter, straightforward and, for the each of the following steps, the solution of the previous one is taken as the initial value. For instance, in the case of high amplitude generators, the parameter can be introduced as a factor multiplying the external sources $\bar{G}_c(\eta) = \eta\bar{G}$, which is varied from a small value, corresponding to small signal operation, to $\eta = 1$, corresponding to the original situation.

The practical application of the methods that have been described is, in general, highly demanding in terms of computational resources. A great variety of works can be found in the bibliography, focusing on the efficient numerical implementation of the different challenging parts of the simulation algorithm, such as the Fourier series expansion calculation or the inversion of the Jacobian matrix required in (1.42). However, since the details of these improved numerical techniques are not interesting for the purpose of this work, they are not addressed here.

1.3.2. Simulation of Autonomous Regimes

In the introduction of the frequency domain formulation, it was assumed that all the circuit variables can be represented in a conveniently truncated Fourier series, with a finite number of analysis frequencies $\{\omega_{-N_H}, \ldots, \omega_{N_H}\}$. This requires an a priori knowledge of the type of signals present in the circuit, since the range of solutions that can be obtained is restricted to those expressible in terms of the pre-established frequency basis. In pure non-autonomous regimes, the frequency basis can be straightforwardly determined, taking into account the signals delivered by the external generators and their significant harmonic com-

ponents and intermodulation products. When the circuit exhibits autonomous behaviour, on the other hand, additional frequency components—not necessarily present in or related to the frequency content of the input signals—can be generated, which, if not included in the frequency basis, would be overlooked in the simulation process, leading to incorrect or unphysical solutions.

Furthermore, even if the additional frequency components are correctly included in the basis, the simulation might still not converge to the autonomous behaviour, producing a non-oscillatory coexisting mathematical solution. As has been pointed out, the Newton–Raphson algorithm used in the resolution of the harmonic balance system is very dependent on the initial value. Unless an appropriate starting point with accurate values of the coefficients at the self generated frequency components is provided, the method tends to converge to a coexisting non-autonomous steady state regime, in which the coefficients at the additional frequency components vanish.

In circuits with an autonomous oscillation, the exact frequency of this oscillation ω_0, can be considered as an unknown, and added to the set of state variables of the frequency domain formulation. The associated simulation technique, known as *mixed harmonic balance*, yields an unbalanced system of $(2N_H+1)Q$ equations in $(2N_H+1)Q+1$ unknowns. However, as discussed in Section 1.2, an arbitrarily time shifted solution of an autonomous system is also a solution which, in the frequency domain, means that the solution is independent of the phase origin. Consequently, the real or imaginary part of one of the state variables in $\bar{X}$ can be arbitrarily set to 0, for instance $\Im\{X_j^k\} = 0$, equating the number of unknowns to the number of equations.

Nevertheless, this method still requires a suitable initial value to avoid convergence to trivial, non-oscillatory solutions. Different complementary techniques have been proposed in the literature for the efficient initialisation of the mixed harmonic balance system [7]. A different approach is presented in what follows.

The main problem with autonomous regimes derives from the fact that the oscillation frequency is internally generated, without being excited by any generator. The *auxiliary generator technique* overcomes this issue by introducing an artificial generator at the frequency of oscillation $\omega_{AG} = \omega_0$. Thus, the auxiliary generator imposes the oscillation and prevents the default convergence towards non-oscillatory regimes; the autonomous behaviour can therefore be analysed as a conventional forced regime.

Two different types of auxiliary generators can be considered: voltage generators connected in parallel to a circuit node, and current generators connected in series at a circuit branch, as shown in Figure 1.7. It is important to note that voltage and current sources behave as, respectively, short and open circuits at the frequencies different from those that they deliver. Therefore, an ideal filter is necessary in either case, to prevent the auxiliary generator from perturbing

the circuit at different frequencies $\omega \neq \omega_{AG}$. The response of these filters in terms of impedance $Z_s(\omega)$, for the voltage generator and admittance $Y_p(\omega)$, for the current generator, is given by:

$$Z_s(\omega) = Y_p(\omega) = \begin{cases} 0 & \omega = \omega_{AG} \\ \infty & \omega \neq \omega_{AG} \end{cases} \tag{1.43}$$

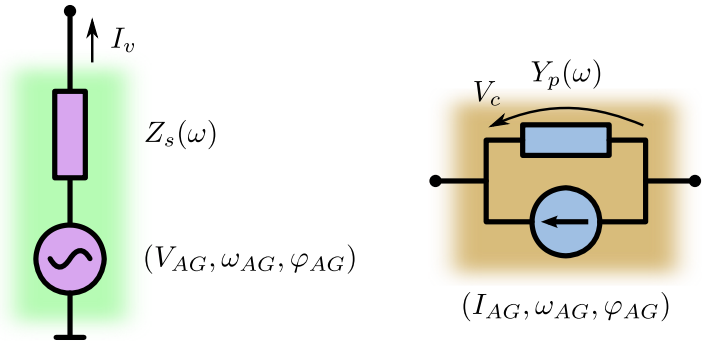

Figure 1.7: Auxiliary generators: (a) voltage generator and, (b) current generator.

Finally, it is important to guarantee that the auxiliary generator has no influence over the solution or, equivalently, that the solution of the circuit with the auxiliary generator is actually a solution of the original circuit. To fulfil this condition, the auxiliary generator must neither deliver energy to the circuit, nor dissipate it, which is assured if the current delivered by the voltage generator I_v, is zero, or if the voltage drop across the current generator V_c, is zero. Nonetheless, these conditions can still be fulfilled for trivial solutions in which the oscillation vanishes ($V_{AG} = 0$, for the voltage generator or $I_{AG} = 0$, for the current generator). In order to avoid convergence to this type of solutions, the *non-perturbation conditions* are formulated in terms of the admittance Y_{AG}, for the voltage generator or in terms of the impedance Z_{AG}, for the current generator, as follows:

$$Y_{AG} = \left.\frac{I_v}{V_{AG}}\right|_{\omega=\omega_{AG}} = 0 \qquad \text{Voltage auxiliary generator} \tag{1.44}$$

$$Z_{AG} = \left.\frac{V_c}{I_{AG}}\right|_{\omega=\omega_{AG}} = 0 \qquad \text{Current auxiliary generator} \tag{1.45}$$

These complex equations can be directly translated into two additional real equations for the harmonic balance system. In vector notation, the non-perturbation

condition can be expressed as:

$$\bar{E}_{np} = \left[\begin{array}{c} \Re\{U_{AG}\} \\ \Im\{U_{AG}\} \end{array} \right] = \bar{0} \tag{1.46}$$

where U_{AG} represents the admittance Y_{AG}, for the case of a voltage source or the impedance Z_{AG}, for the case of a current source.

The inclusion of the auxiliary generator adds two additional equations to the harmonic balance system, due to the non-perturbation condition, along with three additional parameters: the amplitude V_{AG} or I_{AG}, the frequency ω_{AG} and the phase ϕ_{AG}. However, taking into consideration the particular operation regime studied, one of the parameters can be usually fixed, leading to a balanced system that can be solved through the normal procedure.

For instance, for a free running oscillator, as has been commented, the solution is independent of the phase origin, and therefore, the phase of the auxiliary generator can be arbitrarily set to zero, $\phi_{AG} = 0$, producing the following balanced system:

$$\left. \begin{array}{l} \bar{E}(\bar{X}, A_{AG}, \omega_{AG}) = \bar{0} \\ \bar{E}_{np}(\bar{X}, A_{AG}, \omega_{AG}) = \bar{0} \end{array} \right\} \tag{1.47}$$

where $\bar{E}$ represents the error function of the standard harmonic balance system, taking into account the inclusion of the auxiliary generator, $\bar{E}_{np}$ are the non-perturbation conditions as defined in (1.44), $\bar{X}$ is the standard state vector and A_{AG} stands for the amplitude of the auxiliary generator (V_{AG} or I_{AG}, depending on the type of source chosen).

Although, as has been commented, either a voltage or a current auxiliary generator may be used, voltage generators are usually considered in this work. Current generators can be more efficient for the analysis of series resonances, though they are rarely necessary [7].

The auxiliary generator technique has proved to be a highly efficient and versatile complementary tool for the harmonic balance simulation method, enabling the analysis of non-linear circuits with autonomous behaviour as normal forced systems. This provides remarkable flexibility for the control and optimisation of the different parameters of interest in this kind of circuits, that will be largely exploited throughout this work, addressing the simulation procedures for other operation regimes, as well as for the optimisation of certain properties.

1.3.3. Stability Analysis

It has already been pointed out that, unlike in time domain simulation, when using frequency domain analysis techniques, no information is obtained about

the evolution of the circuit during the transient regime, and so the robustness of the determined steady state solution versus perturbations is uncertain.

Furthermore, in the frequency domain techniques, it is assumed that the signals present in the circuit are expressible in terms of a pre-established frequency basis, restricting the analysis to this set of signals. However, the obtention of a solution does not ensure that the chosen basis is complete; there might still exist additional frequency components in the circuit that have been ignored, leading to an incorrect solution.

Thus, in order to verify the physical existence of the solutions obtained, the use of a complementary stability analysis method is needed. The method must evaluate the behaviour of the system under small perturbations of the steady state solution obtained through the frequency domain techniques. This approach, usually referred to in the literature as *local stability analysis*, provides information about the *local* robustness of a specific steady state solution to small perturbations, without regard to the response of the system to large perturbations.

In this section, three different stability analysis techniques in the frequency domain are presented. The first one, conceptually analogous to the time domain stability analysis described in Section 1.2.3, is based on the study of the linearised perturbed system in the frequency domain. This approach is appropriate if an in-house harmonic balance implementation is available, since it requires the operation with certain internal data, not usually accessible to the user in commercial simulators. The other two approaches, on the other hand, are based on the closed loop transfer function of the circuit, which can be easily determined through conventional harmonic balance simulations.

1.3.3.1. Characteristic Determinant of the Harmonic Balance System

The result of the harmonic balance simulation of a given circuit is a steady state solution in the general form:

$$\bar{x}_s(t) = \sum_{m=-N_H}^{N_H} \bar{X}_{s_m} e^{j\omega_m t} \tag{1.48}$$

which may represent a constant, periodic or quasiperiodic operating regime.

Let $\bar{u}(t)$ be a small amplitude vector perturbation of the form:

$$\bar{u}(t) = \bar{a} e^{(\sigma + j\omega)t} \tag{1.49}$$

where ω is not an integer multiple of ω_m, $m \in \{-N_H, \ldots, N_H\}$. If the steady state solution $\bar{x}_s(t)$ is perturbed through the injection of $\bar{u}(t)$, due to the non-linearity of the system, all the intermodulation products between ω and $\{\omega_1, \ldots, \omega_{N_H}\}$ will be generated. Taking into account the small amplitude of the perturbing signal,

the higher order terms in ω may be neglected, and the resulting perturbation takes the form [12]:

$$\Delta\bar{x}(t) = \bar{a}e^{\sigma t} \sum_{m=-N_H}^{N_H} \Delta\bar{X}_m e^{j(\omega+\omega_m)t} \tag{1.50}$$

where $\Delta\bar{X}_m$ are a priori undetermined complex amplitudes. The following perturbed regime will be considered:

$$\bar{x}(t) = \bar{x}_s(t) + \Delta\bar{x}(t) \tag{1.51}$$

which, according to (1.48) and (1.50), represents a linear combination of exponential terms of the form $e^{\xi t}$, $\xi \in \mathbb{C}$. Since these signals are known to be eigenfunctions of the linear invariant systems [11], the response they produce in this type of systems is simply a version of the same signal, conveniently weighted by a complex constant $H(\xi)$, that depends on the complex frequency $\xi = \alpha + j\beta$, of the exponential term.

Thus, considering the time invariance of the linear networks involved in the circuit, a linear frequency dependent relationship between the different frequency components of the state variables $\bar{X}(s)$, the non-linear magnitudes $\bar{Y}(s)$, and the external generators $\bar{G}(s)$, can be defined. These vectors have been introduced in order to take into account the new frequency components produced in the perturbed regime considered, given by the intermodulation products $s + j\omega_m$, where $\omega_m \in \{\omega_{-N_H}, \ldots, \omega_{N_H}\}$ and $s = \sigma + j\omega$. Since their structure is analogous to that of $\bar{X}$, $\bar{Y}$ and $\bar{G}$, as defined in (1.39), they reduce to these vectors for $s = 0$ ($\bar{X}(0) = \bar{X}$, $\bar{Y}(0) = \bar{Y}$ and $\bar{G}(0) = \bar{G}$). Assuming that the linear relationship between the vectors exists for the values of s considered, it can be written as follows:

$$B_x(s)\bar{X}(s) + B_y(s)\bar{Y}(s) + B_g(s)\bar{G}(s) = \bar{0} \tag{1.52}$$

where $B_x(s)$, $B_y(s)$ and $B_g(s)$ are frequency dependent matrices. Note that, as the evaluation of these matrices at $s = 0$ leads to the respective matrices A_x, A_y and A_g, as they appeared in (1.40), the expression (1.52) is equivalent to (1.40) for $s = 0$.

The non-linear magnitudes $\bar{Y}(s)$ are non-linearly related to the state variables $\bar{X}(s)$ through the time domain equation (1.38). However, taking into account the fact that a small amplitude perturbation is considered in (1.51), the non-linear relationship can be approximated by a Taylor series expansion around the steady state solution $\bar{x}_s(t)$:

$$\bar{Y}(s) \approx \bar{Y}_s + J\bar{Y}(\bar{X}_s)\,(\bar{X}(s) - \bar{X}_s) \tag{1.53}$$

where $\bar{X}_s$ and $\bar{Y}_s$ are the frequency domain representation of the state variables and the non-linear magnitudes respectively, at the steady state solution $\bar{x}_s(t)$.

The operator $J\bar{Y}(\bar{X}_s)$ represents the Jacobian matrix of the non-linear function (1.38) in the frequency domain, evaluated at the steady state conditions $\bar{X}_s$, defined as:

$$J\bar{Y}(\bar{X}_s) = \left(\frac{\partial Y_i^j}{\partial X_k^l}\right)\Bigg|_{\bar{X}_s} = \left(\begin{array}{cccc} \frac{\partial Y_{-N_H}^1}{\partial X_{-N_H}^1} & \frac{\partial Y_{-N_H}^1}{\partial X_{-N_H}^2} & \cdots & \frac{\partial Y_{-N_H}^1}{\partial X_{N_H}^Q} \\ \frac{\partial Y_{-N_H}^2}{\partial X_{-N_H}^1} & \frac{\partial Y_{-N_H}^2}{\partial X_{-N_H}^2} & \cdots & \frac{\partial Y_{-N_H}^2}{\partial X_{N_H}^Q} \\ \vdots & \vdots & \ddots & \vdots \\ \frac{\partial Y_{N_H}^P}{\partial X_{-N_H}^1} & \frac{\partial Y_{N_H}^P}{\partial X_{-N_H}^2} & \cdots & \frac{\partial Y_{N_H}^P}{\partial X_{N_H}^Q} \end{array}\right)\Bigg|_{\bar{X}_s} \tag{1.54}$$

The calculation of the individual partial derivatives $\partial Y_i^j/\partial X_k^l$, can be carried out as follows:

$$\begin{aligned} \frac{\partial Y_i^j}{\partial X_k^l} &= \frac{\partial}{\partial X_k^l} \lim_{T\to\infty} \int_0^T y_j(t) e^{-j\omega_i t} dt = \\ &= \lim_{T\to\infty} \int_0^T \frac{\partial y_j(t)}{\partial x_l(t)} \frac{\partial x_l(t)}{\partial X_k^l} e^{-j\omega_i t} dt = \lim_{T\to\infty} \int_0^T h(t) e^{j\omega_k t} e^{-j\omega_i t} dt = \\ &= H_{\omega_i - \omega_k} \end{aligned} \tag{1.55}$$

First, the coefficient Y_i^j can be expressed as a function of the non-linear magnitude $y_j(t)$ through the analysis equation of the Fourier series expansion[7]. Since the non-linear relationship $\bar{y}(t) = \bar{f}_{nl}(\bar{x}(t))$ is analytically known, the partial derivative of the non-linear magnitude $y_j(t)$ with respect to the state variable $x_l(t)$: $\partial y_j(t)/\partial x_l(t)$, can be straightforwardly calculated. Similarly, from (1.48), the partial derivative of the state variable $x_l(t)$ with respect to its harmonic component X_k^l, is directly the exponential term $e^{j\omega_k t}$. Therefore, the frequency domain partial derivative $\partial Y_i^j/\partial X_k^l$ is simply given by the spectral component of the corresponding time domain derivative of the non-linear function (1.38), $h(t) = \partial y_j(t)/\partial x_l(t)$, at the intermodulation product $\omega_i - \omega_k$, $H_{\omega_i-\omega_k}$.

Introducing the linear approximation (1.53) into (1.52) and considering the perturbed regime given by (1.51), the following simplified frequency domain system is obtained:

$$\left[B_x(s) + B_y(s) J\bar{Y}(\bar{X}_s)\right] \Delta\bar{X}(s) = \bar{0} \tag{1.56}$$

taking into account the fact that the steady state solution $\bar{X}_s$, fulfils (1.52). Since the external generators are not influenced by the presence of the perturbation,

[7] For the general case of a quasiperiodic signal $y_j(t)$, the coefficient Y_i^j of its Fourier series expansion can be calculated through the expression: $Y_i^j = \lim_{T\to\infty} \int_0^T y_j(t) e^{-j\omega_i t} dt$ [5]. For periodic signals, this procedure is equivalent to the traditional calculation of the coefficients of the Fourier series.

they produce no signals at the intermodulation products $s + j\omega_m$ and thus, $\bar{G}(s)$ vanishes for $s \neq 0$, cancelling out the corresponding term in (1.52).

Because (1.56) is an homogeneous linear system, in order for the perturbation $\Delta\bar{X}(s)$ to be different from zero, its characteristic matrix must be singular, fulfilling:

$$\Delta(s) = \det\left[B_x(s) + B_y(s)J\bar{Y}(\bar{X}_s)\right] = 0 \tag{1.57}$$

Note that the perturbation $\Delta\bar{X}(s)$ necessarily differs from zero, as an instantaneous perturbation was in fact introduced in the system. The roots of the characteristic determinant (1.57) will determine the evolution of the perturbation (1.50). For the steady state solution (1.48) to be stable, the roots must not have positive real parts. This means that the perturbation $\Delta\bar{x}(t)$ vanishes exponentially in time (due to the negative sign of σ) and the system evolves towards the steady state solution $\bar{x}_s(t)$.

Direct calculation of the roots of the characteristic equation is usually extremely complicated, owing to the normally high order in s of the matrices $B_x(s)$ and $B_y(s)$. Since, in most cases, the interest lies in determining the stability of the steady state regime, rather than the exact solutions of (1.57), this information can be graphically obtained through the application of Nyquist's analysis to the determinant $\Delta(s)$ [12].

1.3.3.2. Closed Loop Transfer Function: Admittance or Impedance Diagrams

The obtention of the characteristic determinant of the harmonic balance system used in the previous section is basically restricted to in-house harmonic balance formulations, as it requires access to internal parts of the process, not usually available to the user in commercial simulators. The approach illustrated in this section, on the other hand, is based on the closed loop transfer function of the circuit, that can be readily determined through conventional harmonic balance simulations.

Let $\bar{x}_s(t)$ be a steady state solution of a given non-linear circuit, obtained through harmonic balance simulation. A closed loop transfer function of the system, associated with a linearisation about the steady state solution $\bar{x}_s(t)$, can be determined by conveniently perturbing the system operation regime [13]. If a small amplitude current $I_n(\omega)$ at the frequency ω is introduced into the circuit by connecting an ideal generator in parallel at a circuit node, a single input single output transfer function can be defined in terms of the input impedance at the node $Z_n(\omega)$, given by the relationship between the node voltage V_n, and the current delivered I_n, at the frequency ω:

$$Z_n(\omega) = \left.\frac{V_n}{I_n}\right|_{\omega} \tag{1.58}$$

Analogously, the transfer function could be defined in terms of the input admittance by the introduction of a small amplitude voltage in series at a circuit branch. In either case, it must be ensured that the system, operating at the steady state regime $\bar{x}_s(t)$, presents a linear behaviour with respect to the perturbation. The perturbation amplitude must be small enough to avoid disturbance of the steady state regime, yet sufficiently high to prevent numerical inaccuracy problems.

Unless exact pole zero cancellations occur, all the possible transfer functions $Z_n(\omega)$, associated with each of the circuit nodes share the same characteristic equation [13], providing the required stability information of the circuit. Hence, the transfer function can theoretically be obtained by simply connecting a current generator at any node of the circuit and sweeping the frequency ω. Nonetheless, in practice, as some nodes are less numerically sensitive and pole zero cancellations may take place, it is advisable to perform the analysis at different nodes; the terminals of the active devices are generally an appropriate choice.

The frequency of the perturbation ω must be included in the frequency basis and swept throughout the desired interval, to obtain the transfer function $Z_n(\omega)$. Due to the linear behaviour of the system with respect to the perturbation, no harmonic components of the perturbation frequency are required. In order for this transfer function to represent a linearisation of the system about the steady state solution $\bar{x}_s(t)$, the external generators, as well as—when necessary—the non-perturbing auxiliary generators that sustain the autonomous behaviour, must maintain the same operating conditions as for the simulation of the steady state, so that the circuit remains at this operating regime throughout all the process.

The presence of the perturbation at ω (and, because it is a real signal, at $-\omega$) will generate intermodulation products with the frequency components present in the system at $\pm\omega + \omega_m$, $m \in \{-N_H, \ldots, N_H\}$. Providing enough harmonic components have been included in the basis (and they are actually present in the system), it can be proved that the onset of a spurious oscillation at ω will produce a component in the interval $[0, \Omega_{min}/2]$, where Ω_{min} is the minimum non-zero positive fundamental frequency of the considered basis. Thus, for the stability analysis, it would be theoretically sufficient to determine the transfer function in this frequency interval, although, with this single node approach, taking into account the behaviour in a wider frequency range usually brings about more reliable results.

The instability of a particular solution is generally associated with the existence of a pair of complex conjugate poles $s = \sigma \pm j\omega_0$, with positive real part ($\sigma > 0$) in the linearised transfer function $Z_n(\omega)$. Under these conditions, any perturbation around the frequency ω_0 will progressively increase its amplitude, leading the system towards a different stable solution that cannot be predicted

using this linearisation. An intuitive method to detect the presence of unstable complex conjugate poles in the closed loop transfer function is presented next.

A pair of complex conjugate poles $s = \sigma \pm j\omega_0$ produces a factor in the transfer function $Z_p(s)$ of the form:

$$Z_p(s) = \frac{\sigma^2 + \omega_0^2}{s^2 - 2\sigma s + \sigma^2 + \omega_0^2} \tag{1.59}$$

It will be assumed that this factor is the dominant contribution in the pole residue expansion of the closed loop transfer function $Z_n(s)$ [13]. Since the transfer function is obtained in the pure sinusoidal regime excited through the perturbing generator, replacing s with $j\omega$, the factor associated with the dominant pair of poles in this regime becomes:

$$Z_p(\omega) = \frac{\sigma^2 + \omega_0^2}{\sigma^2 + \omega_0^2 - \omega^2 - j2\sigma\omega} \tag{1.60}$$

Applying the mathematical property: $\text{sign}(d\phi/dx) = \text{sign}(d\tan(\phi)/dx)$, which holds for any real angle ϕ and independent variable x, from:

$$\tan(\text{angle}(Z_p(\omega))) = \frac{\Im\{Z_p(\omega)\}}{\Re\{Z_p(\omega)\}} = \frac{2\sigma\omega}{\sigma^2 + \omega_0^2 - \omega^2} \tag{1.61}$$

it can be stated that, for positive σ, the phase of $Z_p(\omega)$ has a positive slope at the resonant frequency ω_0. The function $Z_n(\omega)$ agrees with the inverse of the input admittance at the observation port $Y_n(\omega) = Y_n^r(\omega) + jY_n^i(\omega)$. Therefore, it is possible to write:

$$\tan(\text{angle}(Z_p(\omega))) = -\frac{Y_n^i(\omega)}{Y_n^r(\omega)} \tag{1.62}$$

Assuming a slow frequency variation of $Y_n^r(\omega)$, a resonance ($Y_n^i(\omega_0) = 0$) in which the real part of the admittance is negative and the imaginary part presents a positive slope, entails a positive slope in the phase of the closed loop transfer function $Z_n(\omega)$, corresponding to a pair of unstable ($\sigma > 0$) complex conjugate poles [7]. In summary, these rules, usually referred to in the literature as *oscillation start-up conditions*, can be written as:

$$\begin{aligned} Y_n^r(\omega_0) &< 0 \\ Y_n^i(\omega_0) &= 0 \\ \frac{\partial Y_n^i(\omega_0)}{\partial \omega} &> 0 \end{aligned} \tag{1.63}$$

In Figure 1.8, the fulfilment of these conditions in a practical circuit is illustrated. Depending upon the type of steady state solution $\bar{x}_s(t)$, about which

the linearisation has been performed, the interpretations might be slightly different. In case $\bar{x}_s(t)$ represents a non-autonomous regime, the input admittance response shown in Figure 1.8 generally means that an autonomous oscillatory transient of growing amplitude will start (initially) at 2.5 GHz, taking the circuit to a stable solution that cannot be predicted using this analysis. Although the precise stable solution must be determined through the simulation methods that have been described for autonomous regimes, such as the auxiliary generator technique, the frequency at which conditions (1.63) are fulfilled is usually a good starting point for the optimisation. Depending on the intended application of the circuit, this situation may be interesting (oscillators, frequency dividers, etc.) or utterly detrimental (amplifiers, etc.), in which case the design must be appropriately modified.

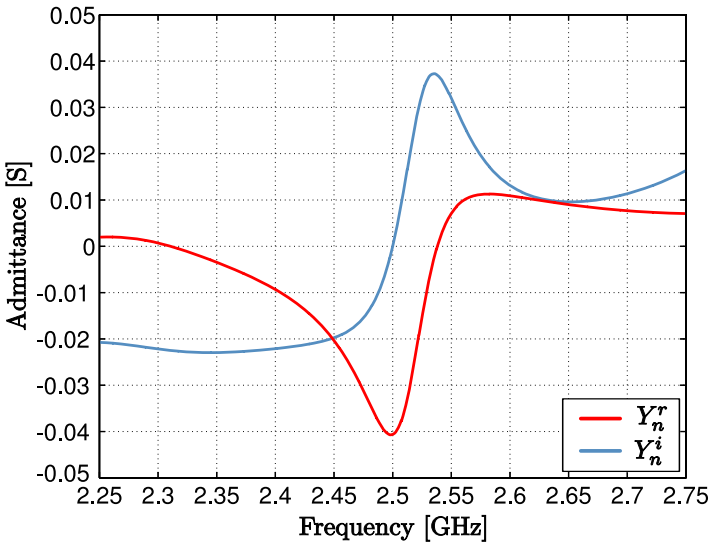

Figure 1.8: Fulfilment of conditions (1.63) at 2.5 GHz in a practical circuit.

On the other hand, if $\bar{x}_s(t)$ represents an autonomous regime, duly sustained in the simulation by non-perturbing auxiliary generators, fulfilment of (1.63) only means that the solution is unstable. No further assumption can be made as to the type of solution the circuit will present in practice, since the linearisation has been performed about an artificially sustained regime that cannot be experimentally observed, due to its lack of robustness versus perturbations.

Nonetheless, as has been commented, even if the system is unstable, an inappropriate choice of the observation node or branch may lead to incorrect results in terms of stability. Hence, it is convenient to repeat the analysis with different closed loop transfer functions obtained from different observation nodes or

branches; maximum sensitivity is usually found on the terminals of the non-linear devices.

This analysis, based on the input admittance (or impedance) diagram, constitutes a simple and efficient method for the qualitative detection of unstable poles in the linearised transfer function $Z_n(\omega)$, that can be straightforwardly implemented in any harmonic balance simulator.

1.3.3.3. Closed Loop Transfer Function: Pole Zero Identification

Alternatively, instead of verifying the fulfilment of conditions (1.63) in the input admittance diagrams, pole zero identification techniques can be applied to a closed loop transfer function associated with the linearisation of the system about the steady state solution $\bar{x}_s(t)$ [14]. Despite the fact that, in a linear system, all the possible closed loop transfer functions can be defined with the same denominator [13], a convenient choice is normally the input impedance $Z_n(\omega)$, as has been defined in (1.58), due to the proximity between input and output.

Using pole zero identification techniques, the complex function $Z_n(\omega)$ is fitted, through a least squares method, to a quotient of polynomials of the form [14]:

$$Z_n(\omega) \quad \rightarrow \quad Z_f(s) = A\frac{\prod_{i=1}^{M}(s - z_i)}{\prod_{i=1}^{N}(s - p_i)} \tag{1.64}$$

The identification must be performed from $\omega = 0$ to the maximum frequency at which any of the active devices shows gain. As already mentioned, even though the considered interval may be reduced under certain conditions, taking into account a wider frequency range generally leads to more reliable results. Note that the identification in a wide frequency range may require a high order N in the denominator polynomial, degrading the identification accuracy that can be attained. However, as the transfer function $Z_n(\omega)$ is linear, the total frequency interval can be divided into subintervals, allowing a piecewise accurate identification process with a low order of the denominator polynomials in (1.64).

The set of poles $\{p_1, \ldots, p_N\}$ of (1.64) determines the stability of the steady state solution $\bar{x}_s(t)$. In order for this solution to be robust versus small perturbations, all the poles must have negative real parts. In these conditions, any small perturbation will vanish exponentially in time and the system will recover the steady state solution $\bar{x}_s(t)$, making it stable.

The stability analysis using pole zero recognition techniques generally provides accurate quantitative information about the roots of the characteristic determinant of the system, linearised about the considered steady state solution

$\bar{x}_s(t)$. Nevertheless, since the procedure relies on the same closed loop transfer function used in the foregoing approach, based on the admittance or impedance diagrams, the limitations commented in terms of the possible lack of sensitivity of the chosen node and the convenience to repeat the analysis from different observation ports, as well as the interpretation criteria for the results, can be directly applied here.

1.3.4. Envelope Transient Simulation

The harmonic balance simulation technique, as presented in Section 1.3.1, is a powerful and efficient method for the analysis of non-linear circuits. However, the frequency domain representation of the signals, in terms of Fourier series, restricts the range of solutions that can be studied using this technique to constant, periodic and quasiperiodic steady state regimes. No information about the transient response of the circuit or about its behaviour when dealing with modulated signals can be obtained using this method.

On the other hand, although the time domain integration techniques can theoretically be applied to any kind of operating regime or input signals, as has been commented in Section 1.2.5, practical limitations arise when signals with both low and high frequency components are present in the system. The time step must be short enough to accurately represent the high frequency components, while the integration time must be long enough to take into account the variation of the low frequency components, leading to an enormous number of calculation points.

In the analysis of communication systems, where high frequency carriers modulated by relatively low frequency signals are usually present, the problem of the different frequency scales has traditionally been addressed using the low-pass equivalents of bandpass signals and functions. The generic bandpass signal $s(t)$ is expressed as $s(t) = \Re\{\tilde{s}(t)e^{j\omega_0 t}\}$, where $\tilde{s}(t)$ is the slowly varying *complex envelope* of $s(t)$.

A similar approach is used in the *envelope transient* simulation technique for the analysis of non-linear circuits. It is assumed that the signals present in the circuit can be expanded in a series of the general form [7; 15]:

$$\bar{x}(t) = \sum_{m=-N_H}^{N_H} \bar{X}_m(t) e^{j\omega_m t} \tag{1.65}$$

where $\bar{x}(t)$ is the state vector of the circuit. The frequency components ω_m, $m \in \{-N_H, \ldots, N_H\}$ constitute a user defined frequency basis, analogous to the one used in the frequency domain formulation, as described in (1.37). The slowly time varying coefficients $\bar{X}_m(t)$, represent the complex envelope of the bandpass

signal associated with each frequency component ω_m. These baseband equivalents $\bar{X}_m(t)$ can be related to their frequency domain representations through the Fourier transform:

$$\bar{X}_m(t) = \frac{1}{2\pi} \int_{-B_m/2}^{B_m/2} \bar{X}_m(\xi) e^{j\xi t} d\xi \tag{1.66}$$

where each vector $\bar{X}_m(\xi)$ contains the spectra of the different state variables $x_1(t), \ldots, x_Q(t)$, about the carrier frequency ω_m, and therefore, the continuous frequency ξ, represents an offset with respect to this central frequency. The envelopes $\bar{X}_m(t)$ must present slow variation rates with regard to the carrier frequencies ω_m and thus, their bandwidth B_m must be relatively narrow. In particular, in order for the series expansion to be unique, the spectra of the different envelopes $\bar{X}_m(\xi)$, centred at their corresponding carrier frequency ω_m, must not overlap one another. However, this condition is not particularly restrictive, as this method is optimised for passband signals and it is only efficient in comparison with the full time domain integration for relatively narrowband envelopes.

The representation based on the time varying coefficients $\bar{X}_m(t)$, that has been illustrated for the state vector $\bar{x}(t)$, is extended to the rest of the circuit variables, namely the non-linear magnitudes $\bar{Y}_m(t)$ and the external generator signals $\bar{G}_m(t)$. Moreover, in agreement with the notation that has been used in the frequency domain formulation, these time varying coefficients for the different components $\{\omega_{-N_H}, \ldots, \omega_{N_H}\}$, are grouped in the vectors $\bar{X}(t)$, $\bar{Y}(t)$ and $\bar{G}(t)$, with the structure shown in (1.39). Similarly, the frequency domain representation of these vectors, given by the Fourier transform, are denoted by $\bar{X}(\xi)$, $\bar{Y}(\xi)$ and $\bar{G}(\xi)$, respectively.

As has been shown in the stability analysis described in Section 1.3.3.1, a linear frequency dependent relationship can be defined between the state variables $\bar{X}(\xi)$, the non-linear magnitudes $\bar{Y}(\xi)$ and the external generator signals $\bar{G}(\xi)$, in terms of the matrices $B_x(s)$, $B_y(s)$ and $B_g(s)$, introduced in (1.52). Particularising the matrices for the purely imaginary frequency $s = j\xi$, the following system of $(2N_H + 1)Q$ equations can be obtained:

$$\bar{E}(\bar{X}(\xi)) = B_x(j\xi)\bar{X}(\xi) + B_y(j\xi)\bar{Y}(\xi) + B_g(j\xi)\bar{G}(\xi) = \bar{0} \tag{1.67}$$

Under the assumption of slowly varying envelopes, the spectra $\bar{X}(\xi)$, $\bar{Y}(\xi)$ and $\bar{G}(\xi)$ must be narrowband, allowing a Taylor series expansion of the frequency dependent matrices $B_x(j\xi)$, $B_y(j\xi)$ and $B_g(j\xi)$, about $\xi = 0$. If the frequency variation of these matrices is smooth, a first order approximation is usually sufficient [16]:

$$B(j\xi) \approx B(0) + \left.\frac{\partial B(j\xi)}{\partial j\xi}\right|_{\xi=0} j\xi \tag{1.68}$$

where $B(j\xi)$ stands for any of the matrices $B_x(j\xi)$, $B_y(j\xi)$ or $B_g(j\xi)$. Replacing the matrices in (1.67) with their Taylor expansion yields:

$$\begin{aligned}&\left[B_x(0) + \left.\frac{\partial B_x(j\xi)}{\partial j\xi}\right|_{\xi=0} j\xi\right] \bar{X}(\xi) + \left[B_y(0) + \left.\frac{\partial B_y(j\xi)}{\partial j\xi}\right|_{\xi=0} j\xi\right] \bar{Y}(\xi) + \\ &+ \left[B_g(0) + \left.\frac{\partial B_g(j\xi)}{\partial j\xi}\right|_{\xi=0} j\xi\right] \bar{G}(\xi) = \bar{0}\end{aligned} \tag{1.69}$$

Note that the only frequency dependent terms in this equation are the $j\xi$ factors and the vectors $\bar{X}(j\xi)$, $\bar{Y}(j\xi)$ and $\bar{G}(j\xi)$; the matrices are constant versus frequency. Differentiating both sides of (1.66), the following property is obtained:

$$\dot{\bar{X}}(t) = \frac{d\bar{X}(t)}{dt} = \frac{1}{2\pi} \int_{-B_m/2}^{B_m/2} j\xi \bar{X}_m(\xi) e^{j\xi t} d\xi \tag{1.70}$$

The application of this property, together with the Fourier transform synthesis equation (1.66) to (1.69), leads to the time domain system:

$$\begin{aligned}\bar{E}(\bar{X}(t)) = B_x(0)\bar{X}(t) + \left.\frac{\partial B_x(j\xi)}{\partial j\xi}\right|_{\xi=0} \dot{\bar{X}}(t) + B_y(0)\bar{Y}(t) + \\ + \left.\frac{\partial B_y(j\xi)}{\partial j\xi}\right|_{\xi=0} \dot{\bar{Y}}(t) + B_g(0)\bar{G}(t) + \left.\frac{\partial B_g(j\xi)}{\partial j\xi}\right|_{\xi=0} \dot{\bar{G}}(t) = \bar{0}\end{aligned} \tag{1.71}$$

Since a first order Taylor expansion of the matrices that describe the linear networks of the circuit has been considered, this equation is only valid for slowly varying envelopes $\bar{X}(t)$, $\bar{Y}(t)$ and $\bar{G}(t)$, associated with narrowband spectra. A more accurate representation of these matrices can be achieved by considering higher order terms of the Taylor series expansion (1.68) [15], leading to higher order time domain derivatives of the envelopes in (1.71). Alternatively, a different envelope transient formulation without these bandwidth constraints can be defined, based on the nodal harmonic balance technique [17]. Nonetheless, a major drawback of this approach lies in the fact that it requires the calculation of the impulse responses of the distributed elements and the computation of convolution products. Furthermore, as previously commented, the envelope transient technique is only advantageous versus a full time domain integration when dealing with strictly narrow passband signals.

The resolution of the time domain non-linear system (1.71) is performed using the general time domain integration techniques described in Section 1.2.5. The continuous variable t is discretised and replaced by a set of sampling points, and the continuous system of non-linear differential equations is thereby transformed into an algebraic system of non-linear equations. Because the complex envelopes

$\bar{X}(t)$, $\bar{Y}(t)$ and $\bar{G}(t)$ present a considerable slower variation rate than the real circuit signals $\bar{x}(t)$, $\bar{y}(t)$ and $\bar{g}(t)$, this formulation admits an accordingly larger time step in comparison with a complete time domain integration, leading to a substantial reduction in the number of computation points.

Depending on the particular integration algorithm chosen, the time domain derivatives are approximated by a different function of the discrete values of the variables at the considered sampling points. For instance, using the backward Euler approach, the derivative of the state variables and non-linear magnitudes at the sampling point t_n are expressed as:

$$\dot{\bar{X}}(t_n) \approx \frac{\bar{X}(t_n) - \bar{X}(t_{n-1})}{\Delta t}, \qquad \dot{\bar{Y}}(t_n) \approx \frac{\bar{Y}(t_n) - \bar{Y}(t_{n-1})}{\Delta t} \tag{1.72}$$

where $\Delta t = t_n - t_{n-1}$ is the time step selected. Substituting these approximations for the corresponding time domain derivatives in (1.71), the following non-linear algebraic system is obtained:

$$\begin{aligned} \bar{E}(\bar{X}(t_n)) = & \left[B_x(0) + \frac{1}{\Delta t} \left. \frac{\partial B_x(j\xi)}{\partial j\xi} \right|_{\xi=0} \right] \bar{X}(t_n) + \\ & + \left[B_y(0) + \frac{1}{\Delta t} \left. \frac{\partial B_y(j\xi)}{\partial j\xi} \right|_{\xi=0} \right] \bar{Y}(t_n) + \\ & + B_g(0)\bar{G}(t_n) + \left. \frac{\partial B_g(j\xi)}{\partial j\xi} \right|_{\xi=0} \dot{\bar{G}}(t_n) \\ & - \left. \frac{\partial B_x(j\xi)}{\partial j\xi} \right|_{\xi=0} \frac{\bar{X}(t_{n-1})}{\Delta t} - \left. \frac{\partial B_y(j\xi)}{\partial j\xi} \right|_{\xi=0} \frac{\bar{Y}(t_{n-1})}{\Delta t} = \bar{0} \end{aligned} \tag{1.73}$$

Note that, as the signals introduced by the external generators $\bar{g}(t)$ are analytically known, the derivative of their complex envelopes $\dot{\bar{G}}(t)$ can be directly calculated.

The solution of the circuit at the initial time t_0 is obtained through a preliminary harmonic balance analysis, considering constant envelopes of the the external signals $\bar{G}_0$, which may correspond to either the initial or average value of the time varying envelopes $\bar{G}(t)$. For the general time point t_n, once the solution values of the circuit at the instant t_{n-1} have been conveniently substituted for the corresponding variables $\bar{X}(t_{n-1})$ and $\bar{Y}(t_{n-1})$, the equation (1.73) reduces to a conventional harmonic balance system, that can be normally solved through an error minimisation process based on the Newton–Raphson algorithm, as explained in Section 1.3.1.

A simplified example of the envelope transient simulation procedure is schematically illustrated in Figure 1.9. The considered input signal $g_1(t) = \Re\{\tilde{g}_1(t)e^{j\omega_m t}\}$, shown in blue, is defined as a tone of frequency ω_m

modulated by a slowly varying real envelope $\tilde{g}_1(t)$, displayed in red. For the simulation, the input signals must be expanded in a series of the form (1.65), with time varying coefficients $\bar{G}(t)$, that are subsequently discretised and replaced by their values at a set of sampling points $\{t_1, t_2, \ldots\}$. The magnitude of the sampled coefficients associated with $g_1(t)$, $|\bar{G}^1(t_i)|$ are represented with yellow spectral lines. Note that, for the particular case of $g_1(t)$, only the coefficient corresponding to the frequency component at ω_m is non-zero, and its amplitude varies according to the same envelope $|G^1_m(t)|$, displayed in dotted red line.

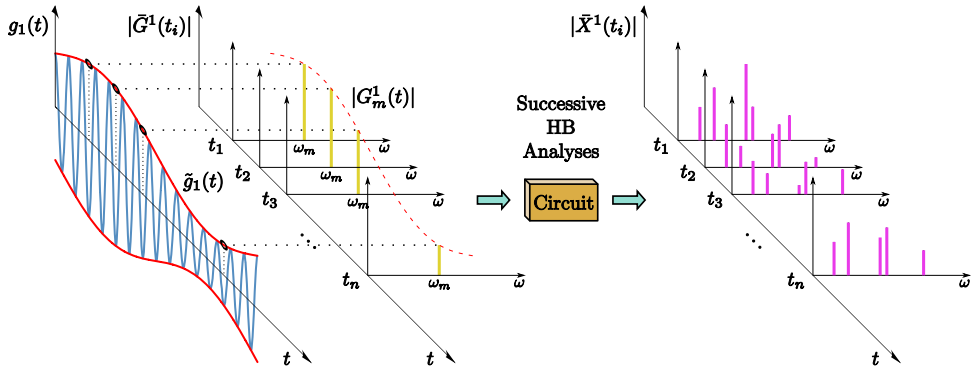

Figure 1.9: Schematic envelope transient simulation procedure.

With the coefficients of all the signals at each time step t_i, a system of the form (1.73) is obtained, whose resolution is analogous to a harmonic balance simulation. The results of this simulation are the coefficients of all the state variables corresponding to all the frequency component in the basis, for this particular time step t_i. For simplicity, the pink spectral lines only represent the amplitudes of the coefficients $|\bar{X}^1(t_i)|$, associated with the state variable $x_1(t)$. The coefficients at the different sampling points are thus determined through successive harmonic balance analyses.

1.3.4.1. Simulation of Autonomous Regimes

The envelope transient method, described in the previous section, can be straightforwardly applied to the simulation of purely forced circuits, enabling the analysis of their performance in presence of modulated bandpass signals. Nonetheless, as was the case with harmonic balance, the application of this method to circuits with autonomous behaviour generally requires complementary techniques, in order to avoid convergence towards coexisting non-autonomous solutions. The user defined frequency basis, as well as the chosen sampling rate of

the time varying complex envelopes, are sensitive factors that may compromise the convergence of the simulation to the desired solution.

Taking advantage of the fact that stable solutions behave as attractors for the neighbouring trajectories, a systematic technique for the selection of the particular operating regime to analyse in the simulation, can be developed. The solution of the circuit at the initial time t_0 is determined through a traditional harmonic balance simulation with constant coefficients. Providing the intended autonomous operating regime can be expressed in terms of the pre-established frequency basis (the solution must be either periodic or quasiperiodic and its fundamentals must be included in the basis), it can be conveniently initialised in this preliminary harmonic balance analysis, using non-perturbing auxiliary generators, as explained in Section 1.3.2. The results of this analysis are provided as initial values to the envelope transient simulation, in which the circuit is allowed to evolve in accordance with its own dynamics. Therefore, as long as the intended autonomous regime is stable, once initialised, the circuit will spontaneously maintain this solution, without requiring auxiliary generators or any other complementary techniques.

Even though the envelope transient method is available in some commercial circuit simulation packages, these implementations usually lack built-in tools for the analysis of autonomous operating regimes. However, the initialisation technique that has been described can be externally applied by the user, as explained below.

First of all, a harmonic balance simulation of the circuit must be carried out, disregarding the possible modulation of the input signals and conveniently sustaining the autonomous behaviour through auxiliary generators, that must fulfil the corresponding non-perturbation conditions. The envelope transient simulation is set up with the same frequency basis, auxiliary generators and circuit parameters. Note that, since the non-perturbation conditions were fulfilled in the preliminary harmonic balance simulation of the circuit, they need not be imposed again in this analysis. The auxiliary generator must be disconnected from the circuit for $t > t_0$, once the circuit variables have been initialised, in order to allow the circuit to evolve in accordance with its own dynamics. When using commercial software, this disconnection can be carried out with the aid of a time varying resistor $R_{AG}(t)$, in series with the voltage auxiliary generator, defined as follows:

$$R_{AG}(t) = \begin{cases} 0 & t = t_0 \\ \infty & t > t_0 \end{cases} \tag{1.74}$$

For the case of a current auxiliary generator, a component with conductance $G_{AG}(t) = R_{AG}(t)$, must be connected in parallel with the generator.

The introduction of modulated signals into the system, its evolution in a transient regime or, in general, the appearance of any type of signal not expressible in

a conventional Fourier series, with constant coefficients, will be represented with time varying envelopes $\bar{X}(t)$. For instance, let us consider a simple free running oscillator with a design operating frequency ω_{AG}, which will be the only fundamental in the frequency basis established for the simulation. The fulfilment of the non-perturbation condition in the preliminary harmonic balance set-up indicates that a steady state solution of the circuit has been found. However, no assumption can be made as to the stability of the solution without further analysis. Suppose the steady state solution at ω_{AG}, although unstable, is located within the basin of attraction of a stable solution $\bar{x}_s(t)$, with slightly different frequency ω_0. Under these conditions, when the circuit is allowed to evolve freely in the envelope transient simulation, the perturbation associated with the disconnection of the auxiliary generator or even the numerical inaccuracies of the method might trigger a transient regime, leading to the stable solution $\bar{x}_s(t)$, which will be expressed as follows:

$$\begin{aligned} \bar{x}_s(t) &= \sum_{m=-N_H}^{N_H} \bar{X}_m^0 e^{jm\omega_0 t} = \\ &= \sum_{m=-N_H}^{N_H} \bar{X}_m^0 e^{jm(\omega_0-\omega_{AG})t} e^{jm\omega_{AG}t} = \sum_{m=-N_H}^{N_H} \bar{X}_m(t) e^{jm\omega_{AG}t} \end{aligned} \tag{1.75}$$

The solution $\bar{x}_s(t)$ can be expanded in a Fourier series with the fundamental frequency ω_0. However, since only the fundamental ω_{AG} has been included in the established frequency basis, time dependent coefficients $\bar{X}_m(t)$, with a periodic variation at the offset frequency $\omega_0 - \omega_{AG}$, need to be used. Note that, as the envelopes are discretised, the chosen sampling rate might be insufficient to represent their variations, leading to incorrect results. Thus, the integration step is a critical factor in this simulation method, that must be carefully selected to avoid convergence to incorrect solutions. Under these particular circumstances, however, it would be advisable to try and determine the stable solution precisely and modify the frequency basis accordingly, instead of reducing the integration step, which would considerably increase the simulation time. In general, in order to improve the efficiency, the frequency basis must be adjusted to minimise the bandwidth of the complex envelopes $\bar{X}(t)$.

1.4. Bifurcation Analysis

In the set of equations that describes a dynamical system, parameters are magnitudes that characterise the specific elements present in the system, without affecting its general nature. In circuit analysis, examples of parameters can be, among others, the values of the linear components, the amplitudes of the bias sources or the levels or frequencies of the input signal generators.

The continuous variation of a parameter η generates a set of steady state solutions $\bar{x}(\eta)$, known as *solution path* [7]. While the variation of this parameter ordinarily brings about quantitative changes in the circuit solutions, in some cases, a qualitative change may also take place at a particular value η_b. A *bifurcation* is defined as a qualitative change in the stability of a solution—or in the number of solutions—of a dynamical system when a parameter is varied continuously.

Bifurcations can be classified as *local* or *global*. Local bifurcations involve variations in the stability properties of a single solution and thus, they can be studied through the pole analysis of this specific solution. Global bifurcations, on the other hand, are qualitative variations in the phase space that cannot be analysed at local level, as they generally involve intersections between the stable and unstable manifolds of one or more solutions [1].

The present section is devoted to the analysis of the main different types of bifurcations, focusing on the characterisation of those influential in the dynamic behaviour of the circuit topologies addressed in this work.

1.4.1. Local Bifurcations

As already stated, local bifurcations are associated with qualitative changes in the stability properties of a single steady state solution $\bar{x}_s(t)$. These properties are determined through applying a small instantaneous perturbation and analysing the subsequent evolution of the circuit variables. Due to the small amplitude of the applied perturbation, the circuit equations:

$$\dot{\bar{x}} = \bar{f}(\bar{x}, \eta), \tag{1.76}$$

can be linearised about the particular steady state solution, that is generally dependent on the value of the parameter η, $\bar{x}_s(t, \eta)$, giving rise to the system:

$$\Delta\dot{\bar{x}}(t) = J\bar{f}(\bar{x}_s(t), \eta)\Delta\bar{x}(t). \tag{1.77}$$

The bifurcation analysis will thus be based on the magnitudes that determine the stability of the particular steady state solution considered; the eigenvalues of the linearisation for constant solutions, the Floquet multipliers for periodic solutions or the Lyapunov exponents for quasiperiodic and chaotic solutions. Alternatively, as has been described in Section 1.3.3, it is possible to study the stability properties of a constant, periodic or quasiperiodic steady state solution $\bar{x}_s(t)$, in terms of the poles of any of the possible linearised closed loop transfer functions that can be defined in the frequency domain, by introducing a small signal perturbation into the system, while it operates at this particular solution.

At a specific point in the solution path $\bar{x}(\eta_b)$, indicated by parameter value η_b, a real pole γ (or a pair of complex conjugate poles $\sigma \pm j\omega$) may cross the imaginary

axis, producing a bifurcation of the steady state solution $\bar{x}_s(t,\eta)$, versus the parameter η. If the solution was stable, it will obviously become unstable after the bifurcation. The bifurcation is called *direct* if the real pole, or the pair of complex conjugate poles, crosses the imaginary axis to the right hand side of the complex plane, and *inverse* if it crosses the imaginary axis in the opposite direction. Furthermore, when approaching a bifurcation from a stable regime, the circuit transient response, described by exponential terms of the form $e^{\sigma t}$ or $e^{\gamma t}$, becomes progressively slower, as the magnitude of the real pole γ (or of the real part of the complex conjugate poles σ) decreases.

Since the bifurcation analysis in the time domain depends on the type of solution considered, some bifurcations of equilibrium points and periodic solutions are considered next.

1.4.1.1. Bifurcations of Equilibrium Points

For the stability analysis of a constant steady state solution or equilibrium point $\bar{x}_{eq}$, as presented in Section 1.2.3.1, the perturbed system (1.77) becomes a time invariant linear system that can be generally[8] solved as:

$$\Delta\bar{x}(t) = \sum_{k=1}^{N} c_k e^{\lambda_k t}\bar{u}_k, \tag{1.78}$$

where the exponents $\lambda_k(\eta) \in \mathbb{C}$, $k \in \{1,\ldots,N\}$ are the eigenvalues of the matrix $J\bar{f}(\bar{x}_{eq},\eta)$, and $\bar{u}_k(\eta)$ are the corresponding eigenvectors. A bifurcation will be obtained if, for certain parameter value η_b, the corresponding equilibrium $\bar{x}_{eq}(\eta_b)$ is non-hyperbolic (it has a zero real eigenvalue $\lambda_k = 0$, or a pair of complex conjugate eigenvalues $\sigma \pm j\omega$, with zero real part $\sigma = 0$), and it brings about a qualitative change in the stability properties of the solution. The two possible *codimension*[9] one bifurcations of constant solutions are described below. Other bifurcation types, which require symmetry or additional constraints, are not considered due to their *structural instability*, in the sense that they are not robust versus slight perturbations of the vector field.

Saddle–node. Suppose the system (1.76) has an equilibrium point $\bar{x}_{eq}$, for the parameter value η_b, $\bar{f}(\bar{x}_{eq},\eta_b) = \bar{0}$. Providing this equilibrium point presents a single zero eigenvalue—with the remaining eigenvalues having non-zero real parts—the *centre manifold theorem* enables the analysis of the orbit structure of

[8] The case with repeated eigenvalues and less than N independent eigenvectors is not considered in the expression (1.78).

[9] The codimension of a bifurcation indicates the number of parameters that must be varied for the bifurcation to occur.

the system, in the vicinity of $(\bar{x}_{eq}, \eta_b)$, in terms of the one dimensional equation [18]:

$$\dot{y} = g(y, \mu), \tag{1.79}$$

where $\mu = \eta - \eta_b$. Furthermore, this centre manifold equation must satisfy:

$$g(0,0) = 0, \tag{1.80a}$$

$$\frac{\partial g}{\partial y}(0,0) = 0. \tag{1.80b}$$

Equation (1.80a) reflects the existence of the equilibrium point $\bar{x}_{eq}$, which has been translated to the origin of the centre manifold by (1.79), taking place for $y = 0$ and $\mu = 0$. The existence of the zero eigenvalue is indicated by the non-hyperbolicity condition (1.80b).

The system (1.79) will undergo a saddle–node bifurcation at the non-hyperbolic equilibrium $(y, \mu) = (0, 0)$ (or, equivalently, the system (1.76) will be subjected to a saddle–node bifurcation at the non-hyperbolic equilibrium $\bar{x}_{eq}$, for the parameter value η_b), if the following conditions are satisfied:

$$\frac{\partial g}{\partial \mu}(0,0) \neq 0, \tag{1.81a}$$

$$\frac{\partial^2 g}{\partial y^2}(0,0) \neq 0. \tag{1.81b}$$

It can be shown [18] that equation (1.81a) implies that a unique solution path passes through $(y, \mu) = (0, 0)$, and (1.81b) implies that this curve lies locally on one side of $\mu = 0$. This kind of behaviour is shown schematically in Figure 1.10(a).

Note that, the presence of a non-hyperbolic equilibrium point, as defined by conditions (1.80), is a necessary but not sufficient condition for the existence of a saddle–node bifurcation. In fact, the presence of the non-hyperbolic equilibrium does not even guarantee the existence of a bifurcation; the stability properties throughout the solution path may not change at the non-hyperbolic equilibrium. Fulfilment of conditions (1.81), together with (1.80b), indicates the presence of a saddle–node bifurcation.

Although similar conditions can be derived for the *pitchfork* and *transcritical* bifurcations, as previously mentioned, they are not interesting for the purpose of this work, due to their structural instability.

At the saddle–node bifurcation, also known as *turning point* or *fold* bifurcation, the solution path folds over itself and is tangent to $\mu = 0$, giving rise to a multivalued solution either for $\mu < 0$, as shown in Figure 1.10(a), or for $\mu > 0$. However, only one of the branches is formed by stable nodes (the upper branch

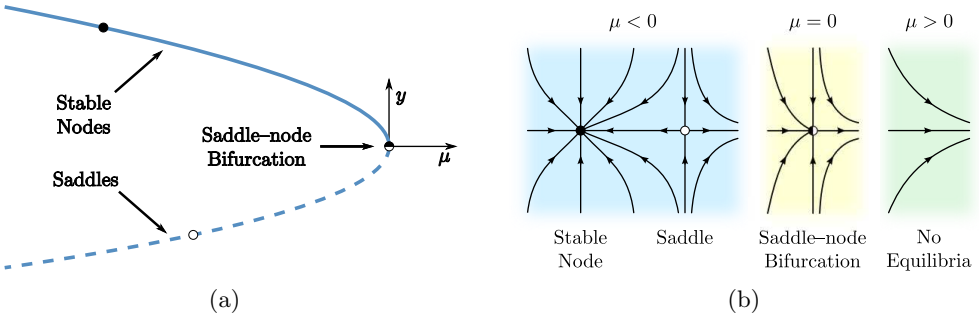

(a) (b)

Figure 1.10: Saddle–node bifurcation: (a) Bifurcation diagram: solution path versus the parameter μ. The stable part is indicated in solid line. (b) Schematic representation of the vector field; The saddle and stable node type solutions, coexistent for $\mu < 0$, coalesce for $\mu = 0$ and annihilate one another, leaving (locally) no equilibria for $\mu > 0$. The stable and unstable equilibria are represented with filled and open circles, ● and ○ respectively, and the bifurcations are represented with half filled circles, ◐.

in the figure, represented in solid line), and thus it represents stable equilibria, whereas the other is formed by unstable saddle type solutions.

The phase portrait of the system restricted to the centre manifold before, during and after the bifurcation is presented in Figure 1.10(b). Two equilibrium points coexist for $\mu < 0$; a stable node and an unstable saddle type solution, that approach one another as μ tends to zero. These two solutions coalesce at the bifurcation point $\mu = 0$, giving rise to a local annihilation of both equilibrium points. No equilibrium points can be found in this area of the phase space for $\mu > 0$.

It is important to highlight the fact that the stability properties of the equilibrium points that have been discussed, refer exclusively to the system restricted to the centre manifold (1.79), and they can only be extrapolated to the complete N-dimensional system (1.76), if the remaining eigenvalues—overlooked in the centre manifold—have negative real parts. Otherwise, the presence of an eigenvalue with positive real part would make the whole solution path unstable, although the equilibria in one of the branches would still have an additional unstable eigenvalue in comparison with the other.

Although, in the graphical example presented in Figure 1.10, the complete solution path is defined for $\mu < 0$, this is not a necessary condition for the existence of a saddle–node bifurcation, which may still take place as long as—in the vicinity of the bifurcation point—the solution path lies on one side of $\mu = 0$.

In practice, saddle–node bifurcations can lead to hysteresis cycles when a circuit parameter in varied, as shown in Figure 1.11, where a state variable x_i is

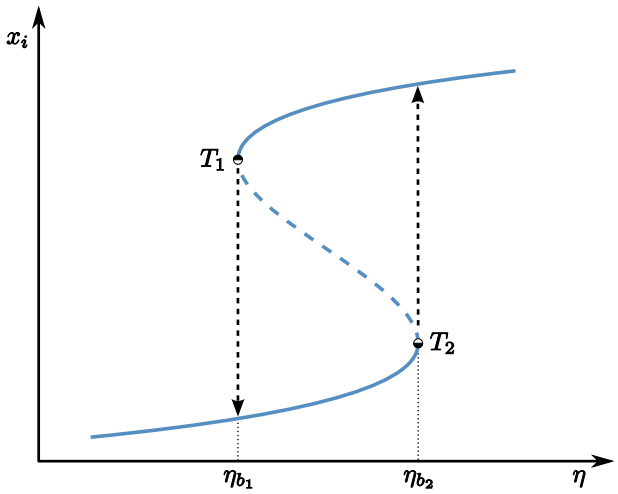

Figure 1.11: Hysteresis cycle originated by the existence of two saddle–node bifurcations. The solution in the interval (η_{b_1}, η_{b_2}) is determinded by the direction in which the parameter η is varied.

represented versus the varied parameter η. Two turning points, T_1 and T_2 take place for the values η_{b_1} and η_{b_2} of the bifurcation parameter. The segment of solution path between the bifurcations, represented in dotted line, is unstable, while the parts represented in solid line are stable. When the parameter η is progressively increased starting from a value $\eta < \eta_{b_1}$, the observed equilibrium point follows the lower stable segment of the solution path until $\eta = \eta_{b_2}$, where the solution undergoes an abrupt change. Beyond this point the value indicated by the upper stable segment is observed. Nonetheless, if the parameter is decreased from a value $\eta > \eta_{b_2}$, then the observed solution follows the upper segment until $\eta = \eta_{b_1}$, and the lower segment beyond this point. Therefore, in the interval (η_{b_1}, η_{b_2}), the direction in which the parameter is varied determines the solution of the system, giving rise to a hysteresis cycle.

Hopf Bifurcation. Consider an equilibrium point $\bar{x}_{eq}$ of the system (1.76), with a pair of complex conjugate eigenvalues $\lambda_{k,k+1} = \sigma \pm j\omega$, , that crosses the imaginary axis for the parameter value η_b. Providing the remaining eigenvalues of the equilibrium point have non-zero real parts, the existence of a Hopf bifurcation at the point η_b is subjected to the fulfilment of the following conditions:

$$\lambda_{k,k+1}(\eta_b) = \pm j\omega, \tag{1.82a}$$

$$\left.\frac{d\sigma}{d\eta}\right|_{\eta=\eta_b} \neq 0, \tag{1.82b}$$

The transversality condition (1.82b) implies that the pair of complex conjugate eigenvalues actually crosses the imaginary axis.

As previously commented, the centre manifold theorem provides a systematic procedure for the analysis of the orbit structure in a neighbourhood of the non-hyperbolic equilibrium $(\bar{x}_{eq}, \eta_b)$. In this case, a family of vector fields on the two dimensional centre manifold, indexed by the parameter $\mu = \eta - \eta_b$, is obtained, in which the equilibrium at $(\bar{x}_{eq}, \eta_b)$, has been translated to the origin, $(\bar{y}, \eta) = (\bar{0}, 0)$.

The eigenvalues of the vector field, restricted to the centre manifold, about the equilibrium point at the origin, are denoted by $\lambda(\mu)$ and $\lambda^*(\mu)$, where

$$\lambda(\mu) = \sigma(\mu) + j\omega(\mu). \tag{1.83}$$

Note that, according to the previous assumptions, the eigenvalues must become purely imaginary for $\mu = 0$: $\sigma(0) = 0$ and $\omega(0) \neq 0$.

The behaviour of the system in the vicinity of the equilibrium point can be locally studied in terms of the corresponding normal form, which is a simplified—although topologically equivalent—version of the vector field (1.76). By calculating the third order Taylor expansion of the normal form about $\mu = 0$, in the polar coordinates r and θ, the following general expression is obtained:

$$\begin{aligned} \dot{r} &= d\mu r + ar^3, \\ \dot{\theta} &= \omega + c\mu + br^2, \end{aligned} \tag{1.84}$$

where the parameters a and b are coefficients of the Taylor expansion of the normal form [18], $\omega = \omega(0)$ and

$$d = \left.\frac{d\sigma}{d\mu}\right|_{\mu=0}, \qquad c = \left.\frac{d\omega}{d\mu}\right|_{\mu=0}. \tag{1.85}$$

Providing $d \neq 0$ and $a \neq 0$, it can be proved [18], that the normal form (1.84) possesses a surface of periodic orbits that lies locally on one side of the plane $\mu = 0$, being tangent to it at the origin $(\bar{y}, \mu) = (0, 0)$. Furthermore, these periodic solutions will be asymptotically stable for $a < 0$ and unstable for $a > 0$.

Since the equilibrium point at $\bar{y} = \bar{0}$ and a degenerated periodic orbit of zero amplitude coalesce at the Hopf bifurcation $\mu = 0$ (note that the surface of periodic orbits is tangent to the plane $\mu = 0$ at that point), both solutions cannot be simultaneously stable. Thus, at the side of the plane $\mu = 0$ where they coexist, $\mu < 0$ or $\mu > 0$, either the equilibrium point at $\bar{y} = \bar{0}$ or the periodic orbits will be asymptotically stable.

The direction in which the pair of complex conjugate eigenvalues crosses the imaginary axis, indicated by the parameter d, determines the stability properties of the equilibrium point at $\bar{y} = \bar{0}$. For $d > 0$, because the eigenvalues cross from

the left half plane to the right half plane as μ is increased, the equilibrium point will be asymptotically stable for $\mu < 0$. Conversely, if they cross the axis in the opposite direction, the equilibrium will be asymptotically stable for $\mu > 0$.

Hence, the stability properties of the solutions that coexist in a Hopf bifurcation are determined by the parameters d and a. The case in which the periodic orbits are unstable ($a > 0$) is usually referred to as *subcritical* and the case in which the periodic orbits are stable ($a < 0$) is usually referred to as *supercritical*. Both types of bifurcations are schematically shown if Figure 1.12 for $d > 0$ (the case with $d < 0$ is directly symmetrical with respect to the plane $\mu = 0$).

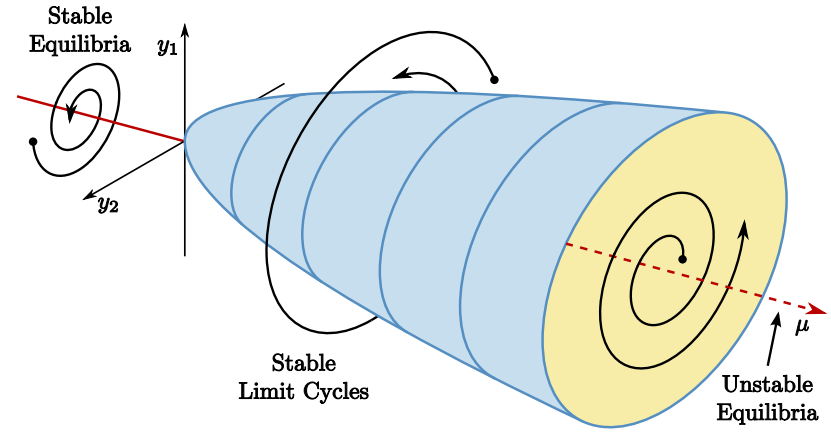

(a)

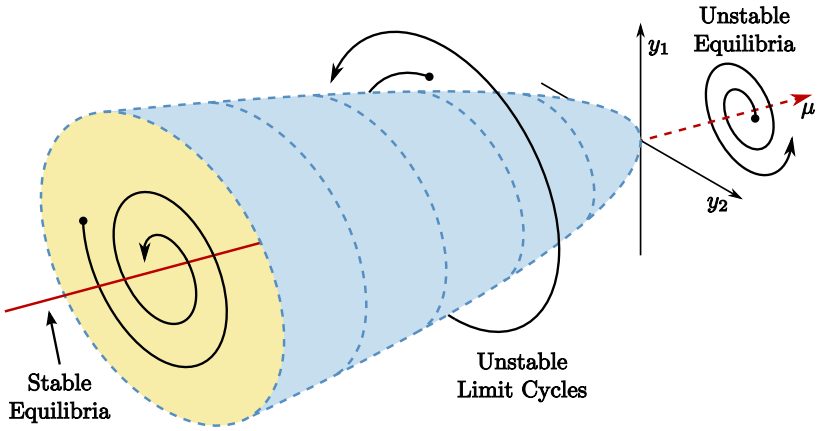

(b)

Figure 1.12: Hopf bifurcations when the pair of complex conjugate eigenvalues crosses the imaginary axis in the positive direction ($d > 0$): (a) Supercritical ($a < 0$), the surface of limit cycles is stable. (b) Subcritical ($a > 0$), the periodic solutions are unstable.

The supercritical case ($a < 0$), is presented in Figure 1.12(a). For μ negative and sufficiently close to the bifurcation point, the equilibrium at $\bar{y} = \bar{0}$ has a dominant pair of complex conjugate eigenvalues with negative real parts $\sigma < 0$. The equilibrium behaves as a *stable focus* that attracts the neighbouring trajectories in a rotating transient. This pair of eigenvalues crosses the imaginary axis for $\mu = 0$, and the equilibrium becomes an unstable focus that repells the adjacent orbits in the same rotating fashion. The surface of limit cycles will be stable, locally attracting both the interior an exterior trajectories. Note that, because they are associated with the same pair of eigenvalues, the direction of rotation is the same for all the orbits.

In the subcritical case ($a > 0$), shown in Figure 1.12(b), the equilibrium point exhibits the same stability properties, behaving as a stable focus for $\mu < 0$ and as an unstable focus for $\mu > 0$. The surface of limit cycles, on the other hand, is unstable and appears for $\mu < 0$, repelling all the neighbouring trajectories. Therefore, the basin of attraction of the stable equilibria for $\mu < 0$ is limited by the surface of repelling limit cycles, as the orbits originated outside this surface depart from it in an initially exponential rotating transient.

The foregoing discussion about the stability properties of the coexisting solutions in a Hopf bifurcation, refers solely to the system restricted to the centre manifold, and it only applies to the complete N-dimensional system if the remaining eigenvalues—not considered in the centre manifold—have negative real parts. If any of them had a positive real part, the solutions coexisting in the bifurcation would be unstable, albeit a qualitative change in their properties would still take place at the bifurcation point, consisting in a variation of the number of unstable eigenvalues.

1.4.1.2. Bifurcations of Periodic Solutions

In this section, the evolution of a periodic solution $\bar{x}_0(t)$ of the non-linear system (1.76), with respect to the continuous variation of the parameter η is studied. Since the periodic solution gives rise to a limit cycle in the phase space, its representation as a function of the parameter η is not as simple as in the case of equilibrium points. The Poincaré map, as introduced in Section 1.2.4, enables the representation of each steady state periodic solution as a fixed point or—at most—as a limited number M of fixed points, which makes it a convenient approach for the analysis of this type of solutions. A representative state variable can generally be chosen to evaluate the qualitative behaviour of the steady state solution, versus the variation of the parameter.

The stability analysis of a periodic steady state solution $\bar{x}_0(t)$, requires the linearisation of the perturbed system about this periodic solution, leading to a time varying linear system with periodic coefficients, whose behaviour can be addressed using the Floquet theory, that has been described in Section 1.2.3.2.

The stability properties of the solution can ultimately be studied in terms of the Floquet multipliers m_k, $k \in \{1, \ldots, N\}$, associated with the linearisation of the system (1.76) about the periodic solution $\bar{x}_0(t, \eta)$, for each value of the parameter η.

The periodic solution will possess a Floquet multiplier $m_j = 1$, corresponding to perturbations tangent to the periodic orbit. The limit cycle will be asymptotically stable if the remaining multipliers have moduli smaller than one, or unstable if any of them has modulus greater than one.

Equivalently, as has been commented in Section 1.2.4.1, the stability analysis of periodic solutions can be performed through the linearisation of the corresponding Poincaré map about the fixed point that represents the solution, leading to a linear time invariant system. The $N-1$ eigenvalues of this system agree with the Floquet multipliers associated with the periodic solution $\bar{x}_0(t)$, except for that corresponding to perturbations tangent to the orbit, which is equal to unity. Therefore, the Floquet multipliers or the eigenvalues of the Poincaré map linearisation can be used indistinctively, to determine the stability properties of periodic steady state solutions.

When, for some value of the parameter η, the solution becomes non-hyperbolic (at least one Floquet multiplier has modulus one), its stability analysis analysis cannot be performed using the linearisation, and the variation of the parameter may result in a qualitative change in the properties of the solution (bifurcation).

If the stability of the periodic solution is studied using the associated Poincaré map, the analysis of the orbit structure in the vicinity of the fixed point that represents the solution, can be carried out by restricting the map to the centre manifold, in an analogous process to that followed for the bifurcations of equilibrium points. The main different types of bifurcations of periodic solutions are described next.

Saddle–node. If, for a parameter value η_b, the periodic solution $\bar{x}_0(t, \eta)$ has a single real multiplier equal to one, and the remaining multipliers have moduli not equal to one, the corresponding Poincaré map restricted to the one-dimensional centre manifold can be written as:

$$Q(y, \mu) = g(y, \mu), \tag{1.86}$$

where the non-hyperbolic fixed point associated with the periodic solution $\bar{x}_0(t, \eta_b)$, has been translated to the origin $(y, \mu) = (0, 0)$. The Poincaré map restricted to the centre manifold must thus fulfil the following conditions:

$$g(0, 0) = 0, \tag{1.87a}$$

$$\frac{\partial g}{\partial y}(0, 0) = 1, \tag{1.87b}$$

that reflect the existence of a non-hyperbolic fixed point at the origin of the centre manifold, which may originate different types of bifurcations, namely pitchfork, transcritical or saddle–node. Nonetheless, due to the structural instability of the others, only the saddle–node bifurcation is considered in this work.

Hence, assuming the Poincaré map (1.86) has a non-hyperbolic fixed point at the origin $(0,0)$, fulfilling equations (1.87), a saddle–node bifurcation will take place at that point if the following conditions are satisfied:

$$\frac{\partial g}{\partial \mu}(0,0) \neq 0, \tag{1.88a}$$

$$\frac{\partial^2 g}{\partial y^2}(0,0) \neq 0. \tag{1.88b}$$

Conditions (1.88) indicate that a single curve of fixed points of the map (1.86), passes through $(y,\mu) = (0,0)$, and that this curve lies locally on side of $\mu = 0$. This behaviour is completely analogous to the saddle–node bifurcation of equilibrium points and therefore, the bifurcation diagram of the corresponding Poincaré map has the same appearance shown in Figure 1.10(a), although, in this case, the fixed points of the map represent periodic solutions. The curve of periodic orbits $\bar{x}_0(t,\eta)$, folds over itself versus the parameter η, at the value η_b. Two different periodic steady state solutions coexist on one side of $\eta = \eta_b$, either $\eta > \eta_b$ or $\eta < \eta_b$, coalesce and annihilate each other at η_b, and leave (locally) no steady state solution on the other side. The bifurcation point divides the solution path into two branches with different stability properties; the solutions on one of the branches have an additional multiplier with modulus greater than one in comparison with those on the other.

In case the non-hyperbolicity of the periodic solution were caused by a real multiplier equal to minus one, a different type of bifurcation, known as *flip* or *period-doubling*, might be originated. This kind of bifurcation results in the appearance of a periodic steady state solution of double period, coexisting with the original solution. Nevertheless, this bifurcation is not interesting for the purpose of this work and will not be addressed.

Secondary Hopf or Neimark–Sacker Bifurcation. Consider a periodic solution $\bar{x}_0(t,\eta)$ of the system (1.76), with a pair of complex conjugate multipliers $m_{k,k+1}$, that crosses the unit circle for certain parameter value η_b. Assuming the remaining multipliers have moduli not equal to one, the system (1.76) will undergo a secondary Hopf or Neimark–Sacker bifurcation for the parameter value η_b, under the following conditions:

$$m_{k,k+1} = e^{\pm j\theta}, \tag{1.89a}$$

$$\left.\frac{d|m_{k,k+1}|}{d\eta}\right|_{\eta=\eta_b} \neq 0, \tag{1.89b}$$

where $m_k = m_{k+1}^*$ and $\theta \neq m\pi/2$, $m \in \mathbb{Z}$. The transversality condition (1.89b) implies that the multipliers actually cross the unit circle. The orbit structure in the vicinity of the non-hyperbolic steady state solution $\bar{x}_0(t, \eta_b)$, can be analysed by restricting the associated Poincaré map to the two-dimensional centre manifold, in a process (initially) similar to the approach outlined for the Hopf bifurcation of equilibrium points.

It can be shown [18] that, the fulfilment of conditions (1.89) implies the appearance of an invariant cycle in the Poincaré map, which has zero area for the parameter value η_b. The stability properties of the solutions coexisting in a Secondary Hopf bifurcation, namely the fixed point that represents the periodic solution $\bar{x}_0(t, \eta)$, and the invariant cycle, can be discussed versus the parameters of the associated normal form, as was done for the Hopf bifurcation of equilibrium points, leading to similar bifurcation diagrams.

Despite the similarities, a fundamental aspect differentiates the secondary Hopf bifurcation from the remaining bifurcations described thus far. In all the previous bifurcations, either of equilibrium points or of periodic solutions, the invariant sets created consisted of single orbits, whereas, in this case, an invariant surface that contains innumerable orbits is obtained, for each parameter value η. As shown schematically in Figure 1.4(b), in the original N-dimensional phase space, this invariant cycle in the Poincaré map results in an homeomorphic two-torus, that contains all the possible solutions. Furthermore, depending on the parameter value η, the steady state orbits may be periodic, closing over themselves at some point, or quasiperiodic, and densely filling the two-torus. Note that, although the orbits in the former case are periodic, the invariant set is not a limit cycle, due to the fact that, depending on the initial conditions, different periodic solutions lying on the surface of the two-torus invariant set may be obtained.

1.4.2. Global Bifurcations

As has been previously stated, global bifurcations are dynamical properties that cannot be studied in terms of the local stability analysis of single solutions, as opposed to local bifurcations, since these situations usually involve global aspects of the flows.

The saddle type solutions are characterised by being attractive for a subset of the phase space $\mathbb{R}^N$, which is referred to as the stable manifold of the solution. Since the solution must have at least a real eigenvalue with positive real part, for the case of an equilibrium point (a real multiplier with modulus greater than one, for a periodic orbit), the solution will still be unstable and physically

unobservable. However, the capability of saddle type solutions to attract certain trajectories of the phase space can give rise to global bifurcations involving more than one solution. The two main kinds of global bifurcations originated by saddle type solutions are considered in the following sections.

1.4.2.1. Saddle Connection

Let a saddle type solution of an equilibrium point be considered. The variation of a parameter η of the system may bring about an intersection of the stable and unstable manifolds of the saddle type solution, for the parameter value η_b, giving rise to the appearance of a *homoclinic orbit* (a trajectory that starts and ends at the equilibrium point). The intersection of the stable and unstable manifolds is necessarily tangential, due to the fact that, at any point $\bar{x}$ of the orbit, the vector $\dot{\bar{x}}$ that determines the time evolution of the system, is tangent to both manifolds. As a result of this tangential intersection, the homoclinic orbit obtained is structurally unstable and will be destroyed by the slightest perturbation with components in the full phase space $\mathbb{R}^N$. Nonetheless, under certain circumstances, the destruction of the homoclinic orbit may lead to the appearance of a limit cycle, or even chaotic behaviour [1]. This phenomenon is illustrated schematically in Figure 1.13.

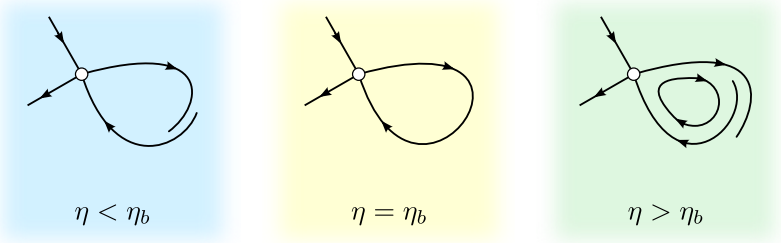

Figure 1.13: Saddle connection bifurcation. A tangential intersection between the stable and unstable manifolds of a saddle type solution takes place at $\eta = \eta_b$, giving rise to a homoclinic orbit. The destruction of the homoclinic orbit for $\eta > \eta_b$, results in the creation of a limit cycle.

Assuming a limit cycle has been generated from the homoclinic orbit, it will have non-zero amplitude and infinite period at the bifurcation point η_b, and will continue to exist (with a decreasing period), when further varying the parameter η in the same direction.

Saddle connections can also take place in fixed points of Poincaré maps, that represent periodic solutions. Under certain conditions, the saddle connection may produce either an invariant cycle, equivalent to a two-torus invariant set in the N-dimensional phase space, or chaotic behaviour. As was the case in the

Neimark–Sacker bifurcation, the invariant cycle may be composed of periodic or quasiperiodic orbits.

1.4.2.2. Saddle–node Homoclinic Bifurcation

In the saddle–node bifurcation, as has been previously described, the solution path folds over itself at the bifurcation point η_b, leaving two coexisting solutions on one side of $\eta = \eta_b$, that annihilate one another at the bifurcation. On the other side of $\eta = \eta_b$, the two previous steady state solutions no longer exist, and the system evolves towards a different solution that cannot be locally determined. However, a completely different phenomenon may take place at the turning point, corresponding to a global bifurcation known as saddle–node homoclinic or saddle–node local–global bifurcation.

Let the case of a saddle–node bifurcation of an equilibrium point be considered. The turning point divides the solution path into two branches, which differ in the sign of a real eigenvalue. Assuming the remaining eigenvalues have negative real parts, one of the branches is composed of asymptotically stable equilibrium points (stable nodes), and the other is composed of unstable saddle type solutions. These equilibria approach each other as the parameter η tends to the bifurcation point η_b, where they coalesce and disappear. Under specific circumstances, before the bifurcation point is reached, the unstable manifold of the saddle solution forms a closed connection passing through the stable node, as illustrated in Figure 1.14. Note that this closed connection is not a periodic orbit, as both angular directions are simultaneously present. Thus, the only stable and physically observable solution continues to be the node. Nonetheless, when the turning point is reached at η_b and both equilibrium points merge, the loop becomes a homoclinic orbit with infinite period.

If the parameter is varied further beyond the bifurcation point in the same direction ($\eta > \eta_b$ in the figure), a limit cycle is created from the homoclinic orbit, and its period progressively decreases as the parameter η is varied away from the bifurcation point. A fundamental difference between this limit cycle and those generated in Hopf bifurcations of equilibrium points, lies in the fact that this cycle is generated with an amplitude different from zero, which is determined by the homoclinic orbit generated at the bifurcation point.

Saddle–node homoclinic bifurcations may also take place in a Poincaré map. When this is the case, the fixed points represent periodic solutions of node and saddle type in the N-dimensional phase space. Prior to the bifurcation, the unstable manifold of the saddle type solution forms a closed loop including the stable node which, at the bifurcation point, results in a homoclinic orbit. Beyond the bifurcation, an invariant cycle corresponding to a two-torus invariant set in the N-dimensional phase space is generated which, depending on the parameter value η, may be composed of either periodic or quasiperiodic orbits,

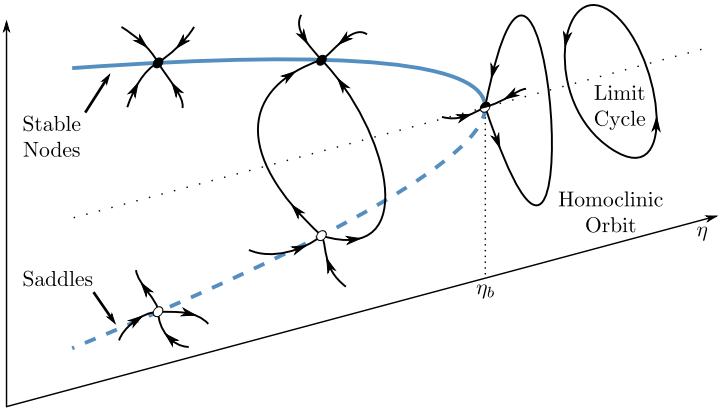

Figure 1.14: Saddle–node homoclinic bifurcation. At some point before the bifurcation, the unstable manifold of the saddle type solution forms a closed loop that includes the stable node. When both equilibrium points coalesce at $\eta = \eta_b$, a homoclinic orbit is generated which, for $\eta > \eta_b$, results in the creation of a limit cycle.

The saddle–node homoclinic bifurcation in the Poincaré map is found in injection locked oscillators, for relatively low levels of the input generator. This bifurcation, also referred to as *mode-locking bifurcation*, is responsible for the synchronisation and desynchronisation phenomena that will be studied in detail in a dedicated section.

1.4.3. Frequency Domain Bifurcation Analysis

The frequency domain circuit simulation techniques that have been described in Section 1.3.1, enable the obtention of constant, periodic or quasiperiodic steady state solutions, regardless of their stability properties. Thus, the complete solution path, as a function of a parameter η can be determined—including both the stable and unstable parts—which can be subsequently discriminated, using the complementary stability analysis methods that have been introduced in Section 1.3.3. Note that, since the range of operating regimes that can be simulated in the frequency domain is limited to those expressible in the pre-established frequency basis, this basis must be appropriately selected to include all the solutions involved in the bifurcation.

The convergence of the Newton–Raphson algorithm may be compromised if, for certain parameter value η_b, the Jacobian matrix of the harmonic balance system becomes singular, as is the case in turning points or saddle–node bifurcations. In order to tackle this limitation, continuation techniques based on replacing the parameter η with another circuit variable, for which the Jacobian

matrix is not singular in the region of difficult convergence, have been developed [4]. Although these techniques are not implemented in some commercial harmonic balance simulation packages, they can be externally applied by the user with the aid of auxiliary generators and optimisation processes [4].

The application of pole zero identification techniques to the closed loop transfer function of the circuit, corresponding to different values of the parameter η, provides, along with the required stability information, variation loci for the different solution poles, as a function of η. Once the complete map of coexisting solutions, complemented with the pole information, has been obtained, the qualitative changes associated with bifurcations can be straightforwardly detected.

The mathematical bifurcation conditions that have been established in the time domain are topological descriptions that must be satisfied by the flows or Poincaré maps, in order for the associated system to undergo the bifurcation phenomena. However, the thorough information about the evolution of the different solutions that can be obtained in the frequency domain, enables the direct identification of the different types of bifurcations.

For a constant solution (or equilibrium point), the solution poles agree with the roots of the characteristic determinant of the linearised system in the frequency domain. In the case of a periodic regime, an infinite set of poles $\sigma + jm\omega$, $m \in \mathbb{Z}$ is obtained, due to the non-univocal relationship between the Floquet multipliers and the Floquet exponents (which match the solution poles). Hence, unlike in the time domain, the solution poles provide a common criterion for the stability analysis of steady state solutions, irrespective of the type of operating regime they represent. Taking advantage of this common criterion, the evolution of the solution poles in the different types of local bifurcations is described next, both of equilibrium points and periodic solutions.

Saddle–Node Bifurcation. Due to convergence problems, the solution path is generally obtained versus a circuit parameter for which this curve is not multivalued.

At the saddle–node bifurcation point, a real pole crosses the imaginary axis, dividing the solution path in two parts for which the number of unstable (or stable) poles differs in one. Since the existence of a zero eigenvalue produces a singularity of the Jacobian matrix at the bifurcation point, this condition can also be used for the bifurcation detection.

For the saddle–node bifurcation of a periodic solution of frequency ω_0, an infinite set of poles of the form $\sigma + jm\omega_0$, $m \in \mathbb{Z}$, associated with a single real Floquet multiplier, crosses the imaginary axis at the bifurcation point.

Hopf Bifurcation. A pair of complex conjugate poles $\sigma \pm j\omega$ crosses the imaginary axis at the bifurcation point.

At the bifurcation of an equilibrium point, the pair of complex conjugate poles is transformed into two real multipliers equal to one (or, equivalently, two real poles of the periodic solution equal to zero). As the amplitude of the limit cycle generated increases, one of the poles continues to be equal to zero, corresponding to perturbations tangent to the periodic orbit, whereas the other moves continuously away from the imaginary axis. If this pole moves to the left hand side of the complex plane, it will have negative real part and the periodic solution will be stable (as long as the remaining poles have negative real parts, except for the one equal to zero), giving rise to a supercritical Hopf bifurcation. Conversely, if the pole moves to the right hand side of the complex plane, the periodic solution will be unstable and the bifurcation will be subcritical. The two types of bifurcation can also be distinguished by observing the geometrical variation of the different solutions with the bifurcation parameter.

For the case of a secondary Hopf or Neimark–Sacker bifurcation, a set of complex conjugate poles of the periodic solution of the form $\sigma \pm j(\alpha\omega_0 + m\omega_0)$, $m \in \mathbb{Z}$, crosses the imaginary axis at the bifurcation point. An additional fundamental frequency $\alpha\omega_0$, which is usually dependent on the bifurcation parameter value η, appears in the system.

1.5. Synchronisation or Injection Locking

A non-linear autonomous dynamical system operating in a stable periodic regime $\bar{x}_0(t)$, is usually referred to in the literature as a *self-sustained* or *free running* oscillator. When the operation of such a system is perturbed by the injection of an external periodic signal $\bar{x}_s(t)$, different non-linear phenomena can take place, generally leading to variations in the parameters (amplitude, frequency, phase) of the autonomous solution $\bar{x}_0(t)$.

Under specific conditions, the interaction results in the onset of a constant and stable phase relationship between the autonomous and the external signal, in virtue of a phenomenon known in the bibliography as injection locking or synchronisation[10]. Although, in general, this non-linear phenomenon reflects the *mutual* influence between self-sustained oscillators, the analysis performed here will be restricted to the assumption that the external signal $\bar{x}_s(t)$ is robust and cannot be affected by the interaction, focusing exclusively on its effects upon the autonomous solution $\bar{x}_0(t)$.

Due to the complexity of the non-linear dynamics involved, it is not possible to obtain a closed universal model of the phenomenon, valid for every oscillator and for every level of interaction. However, through the application of different approximations, a simplified phase equation can be derived, providing an

[10] In the related mathematical literature, the terms *phase locking* or *frequency entrainment* are usually more common.

acceptably accurate description of the phase dynamics, under the circumstances associated with the performed approximations. When these assumptions cannot be made, the behaviour in each particular case can be analysed through numerical simulation.

In this section, the simplified phase model will be presented and described, along with the specific conditions in which it is reliable. The operation under these conditions has a substantial practical interest for the purpose of this work, as will be properly justified. In order to illustrate the fundamental operating regimes that can be observed in oscillators with external periodic forcing, simulations of a representative system in different working conditions will be presented, highlighting the main similarities and differences with practical interest.

1.5.1. Weak Forcing: Averaged Phase Equation

Consider a non-linear N-dimensional autonomous system of ordinary differential equations

$$\frac{d\bar{x}}{dt} = \bar{f}(\bar{x}), \tag{1.90}$$

with a stable periodic steady state solution $\bar{x}_0(t)$, with period T_0, such that $\bar{x}_0(t) = \bar{x}_0(t+T_0)$. The instantaneous solution of the system follows a limit cycle in the phase space and it can thus be parameterised in terms of a uniformly growing phase coordinate ϕ, fulfilling

$$\frac{d\phi}{dt} = \frac{2\pi}{T_0} = \omega_0. \tag{1.91}$$

Note that such a uniformly growing phase variable always exists and can be obtained from any 2π periodic angle variable θ, through the transformation [19]:

$$\phi = \omega_0 \int_0^{\theta} \left[\frac{d\theta}{dt}\right]^{-1} d\theta. \tag{1.92}$$

Because the possible perturbations of the system steady state may drive the trajectory away from the limit cycle, it is interesting to extend the phase definition to the vicinity on the limit cycle. This is achieved by considering the mapping

$$\Phi(\bar{x}) : \bar{x}(t) \mapsto \bar{x}(t+T_0), \tag{1.93}$$

for which the points of the limit cycle are fixed points. The set of points in the phase space that are attracted to a specific point in the limit cycle $\bar{x}_a$, under the action of Φ, forms a (N-1)-dimensional hypersurface called *isochrone* [19], that crosses the limit cycle at $\bar{x}_a$. Since a different isochrone can be obtained for every point in the limit cycle $\bar{x}_a$, these hypersurfaces can also be parameterised

by the phase corresponding to the associated point $\bar{x}_a$, thus extending the phase definition to the vicinity of the limit cycle.

When the operation of the self-sustained oscillator is perturbed by the introduction of a small external periodic signal $\varepsilon\bar{p}(\bar{x},t)$, the forced system can be described by the equations

$$\frac{d\bar{x}}{dt} = \bar{f}(\bar{x}) + \varepsilon\bar{p}(\bar{x},t), \tag{1.94}$$

where the signal $\varepsilon\bar{p}(\bar{x},t) = \varepsilon\bar{p}(\bar{x},t+T)$, has a period T, generally different from T_0. Since the amplitude of the external signal is proportional to the small parameter ε, the analysis presented in the following is restricted exclusively to first order effects in ε.

The presence of the external signal drives the trajectory away from the stable limit cycle. However, taking advantage of the weakness of the external force and the stability of the cycle, it can be assumed that the trajectory is only slightly deviated from the original solution $\bar{x}_0(t)$ or, equivalently, that perturbations in the direction transverse to the cycle are relatively small. On the other hand, as has been previously discussed, an autonomous system operating at a stable periodic solution is incapable of recovering from perturbations tangential to the associated limit cycle, for which it has a zero Lyapunov exponent (or a Floquet multiplier equal to one). Note that such a system is invariant with respect to time shifts; an arbitrarily time shifted solution is also a solution. Therefore, unlike amplitude, phase is neutrally stable in autonomous[11] periodic systems, in the sense that its perturbations remain constant; neither grow, nor decay in time. As a result of the fact that forced systems lack this fundamental property, which is the basis of the synchronisation processes, they are not subject to this kind of phenomena.

In the vicinity of the limit cycle $\bar{x}_0(t)$, where the isochrones are defined, equation (1.91) takes the form:

$$\frac{d\phi(\bar{x})}{dt} = \omega_0. \tag{1.95}$$

Alternatively, because the phase is a smooth function of the coordinates $\bar{x}$, its time derivative can be calculated as:

$$\frac{d\phi(\bar{x})}{dt} = \sum_{n=0}^{N} \frac{\partial\phi}{\partial x_n}\frac{dx_n}{dt} = \sum_{n=0}^{N} \frac{\partial\phi}{\partial x_n} f_n(\bar{x}) = \omega_0, \tag{1.96}$$

[11] A non-autonomous system can be formulated as autonomous by introducing an additional state variable that represents time. The periodic solutions of such a system also have a zero Lyapunov exponent, corresponding to perturbations of this time related variable. However, it is obvious that this variable cannot be practically influenced.

where $f_n(\bar{x})$ represents the nth scalar function that composes the vector field $\bar{f}(\bar{x})$ which, by (1.90), is equal to the time derivative of the nth state variable x_n. For the perturbed system, using (1.94) instead of (1.90), an analogous expression is obtained:

$$\frac{d\phi(\bar{x})}{dt} = \sum_{n=0}^{N} \frac{\partial \phi}{\partial x_n} \left[f_n(\bar{x}) + \varepsilon p_n(\bar{x}, t) \right] = \omega_0 + \varepsilon \sum_{n=0}^{N} \frac{\partial \phi}{\partial x_n} p_n(\bar{x}, t). \tag{1.97}$$

Taking advantage of the previous assumption that the perturbations transverse to the limit cycle are small, the second term of equation (1.97) particularised at a generic point $\bar{x}_e$ can be approximated by its value at the closest point in the limit cycle $\bar{x}_0$. As the points of the limit cycle can be parameterised by the phase, the following closed equation for the phase dynamics is obtained:

$$\frac{d\phi}{dt} = \omega_0 + \varepsilon Q(\phi, t), \tag{1.98}$$

where

$$Q(\phi, t) = \sum_{n=0}^{N} \frac{\partial \phi(\bar{x}_0(\phi))}{\partial x_n} p_n(\bar{x}_0(\phi), t). \tag{1.99}$$

Because $Q(\phi, t)$ is 2π periodic function of ϕ and T periodic function of t, it can be expanded in a Fourier series in the general form:

$$Q(\phi, t) = \sum_{k,l} a_{k,l} e^{j(k\phi + l\omega t)}, \tag{1.100}$$

where $\omega = 2\pi/T$ is the frequency of the external signal.

Neglecting the effect of the external signal ($\varepsilon = 0$), equation (1.90) has the solution

$$\phi = \omega_0 t + \phi_0. \tag{1.101}$$

The particularisation of (1.100) for this solution, yields:

$$Q(\phi, t) = \sum_{k,l} a_{k,l} e^{jk\phi_0} e^{j(k\omega_0 + l\omega)t}. \tag{1.102}$$

The function $Q(\phi, t)$ is composed of both fast oscillating terms and slowly varying (or even constant) terms that satisfy the *resonance condition*:

$$k\omega_0 + l\omega \approx 0. \tag{1.103}$$

Replacing (1.102) into (1.98), the fast oscillating terms give rise to deviations of the order of ε, whereas the resonant terms can lead to large (although slow, due to the integration at a rate proportional to the small parameter ε) variations

in the phase, which constitute the principal component of the phase dynamics. Hence, in order to simplify the analysis, the forcing (1.102) is restricted to the resonant terms through averaging. The relationship between the frequency of the external signal ω and the natural frequency ω_0 determines the particular terms that fulfil (1.103). In general, when these frequencies are nearly rationally related, $m\omega_0 \approx n\omega$, where m and n are coprime integers, the resonant terms are associated with the indices $k = m$ and $l = -n$ and their integer multiples. The averaged forcing can thus be written as:

$$\sum_{k,l} a_{k,l} e^{j(k\phi + l\omega t)} = \sum_{s} a_{sm,-sn} e^{js(m\phi - n\omega t)} = q(m\phi - n\omega t), \tag{1.104}$$

where $q(\cdot)$ is a 2π periodic function. Introducing the phase difference $\psi = m\phi - n\omega t$, and the frequency detuning $\nu = n\omega - m\omega_0$, the phase equation can be written as:

$$\frac{d\psi}{dt} = -\nu + \varepsilon m q(\psi). \tag{1.105}$$

Equation (1.105) depends on two parameters: ε, which is related to the amplitude of the external signal, and $\nu = n\omega - m\omega_0$, that represents the frequency detuning. The function $q(\psi)$ is smooth and 2π periodic, therefore it must have a maximum q_{max} and a minimum q_{min} in the interval $[0, 2\pi)$. As shown if Figure 1.15(a), two different types of dynamic behaviour are possible depending on the values of the parameters. If the frequency detuning ν lies in the interval

$$\varepsilon q_{min} < \nu < \varepsilon q_{max}, \tag{1.106}$$

then the phase equation has at least one pair of fixed points (roots of $-\nu + \varepsilon m q(\psi)$); one asymptotically stable and one unstable. Note that more stable fixed points may exist if the function has more than two non-degenerate ($d^2q(\psi)/d\psi^2 \neq 0$) extrema. Hence, in the range of ν where (1.106) is satisfied, the system evolves to one of the stable fixed points $\psi = \psi_s$, and maintains this constant solution. Under these operating conditions, the phase ϕ varies as:

$$\phi = \frac{n}{m}\omega t + \frac{\psi_s}{m}, \tag{1.107}$$

which corresponds to a constant angular frequency Ω, rationally related to the forcing frequency ω, as follows:

$$\Omega = \frac{d\phi}{dt} = \frac{n}{m}\omega. \tag{1.108}$$

This dynamic regime is known as synchronisation or phase locking, as the phase difference $\psi = m\phi - n\omega t$, is *locked* to a constant value ψ_s, or as frequency

entrainment, referring to the fact that the frequency of the oscillator maintains a rational relationship with that of the forcing signal. The interval of values of the frequency detuning (ν_{min}, ν_{max}) for which the injection locked solution exists, or synchronisation region, depends on the forcing amplitude ε, according to (1.106). In the parameter space (ε, ν), this area limited by straight lines that intersect at the point $(\varepsilon, \nu) = (0, 0)$, as depicted in Figure 1.15(b), is known as *Arnold tongue*. Note that, when the frequency detuning is zero, synchronisation takes place even for vanishingly small amplitudes of the forcing signal although, in this case, a long transient period would be required for the phase locked regime to set in. Conversely, as the frequency detuning departs from zero, increasingly high amplitudes of the forcing signal are needed for the synchronisation phenomenon to take place.

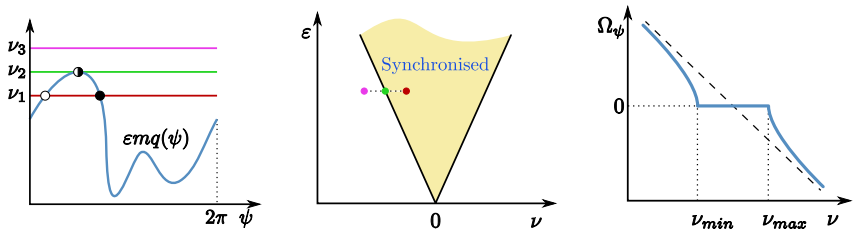

(a) (b) (c)

Figure 1.15: (a) Generic $q(\psi)$ function represented in one period. Depending on the values of the frequency detuning, Equation (1.105) will have at least two fixed points, one stable and one unstable (ν_1), one structurally unstable (ν_2), or none (ν_3). (b) Synchronisation region on the (ε, ν) plane: Arnold tongue. (c) Averaged observed frequency Ω of the oscillator, versus the detuning.

A completely different dynamic behaviour is observed if the frequency detuning lies outside the range (1.106). Then, the time derivative of the phase difference ψ is permanently positive or negative, and therefore, (1.105) does not have any constant steady state solution. The variation of the phase ϕ is given by:

$$\phi = \frac{n}{m}\omega t + \frac{\psi(t)}{m}. \tag{1.109}$$

Since, in this regime, the frequency of the self-sustained oscillator may be time dependent, the *mean* observed frequency Ω is defined as:

$$\Omega = \left\langle \frac{d\phi}{dt} \right\rangle = \frac{n}{m}\omega + \frac{1}{m}\left\langle \frac{d\psi(t)}{dt} \right\rangle = \frac{n}{m}\omega + \frac{1}{m}\Omega_\psi, \tag{1.110}$$

where the angle brackets $\langle\rangle$ denote time averaging. The *beat frequency* Ω_ψ is defined as the averaged time derivative of the phase difference $\psi(t)$. When the

detuning ν lies outside the synchronisation range, the oscillator solution will be quasiperiodic providing the beat frequency is not rationally related to the forcing frequency ω. As the forcing frequency is varied, the solution will become alternatively periodic, when the detuning lies within the synchronisation region associated with a generic pair of integers n_g, m_g, such that $\omega_0 \approx n_g/m_g\omega$, and quasiperiodic otherwise.

In the vicinity of the synchronisation transition, where a stable and an unstable node coalesce and annihilate each other through a saddle–node bifurcation (as illustrated in Figure 1.15(a) for $\nu = \nu_2$), it can be shown that the beat frequency presents approximately a square root variation with the frequency detuning, in the general form [19]:

$$|\Omega_\psi| \approx K\sqrt{|\nu - \nu_{ext}|}, \tag{1.111}$$

where ν_{ext} represents the limit of the synchronisation region, either ν_{min} or ν_{max}. The typical dependence of the observed frequency on the detuning is depicted in Figure 1.15(c). Within the synchronisation region, $\nu \in (\nu_{min}, \nu_{max})$, the beat frequency is equal to zero and the observed frequency remains constant and rationally related to the forcing frequency, as $\Omega = \omega n/m$. Outside this region, the beat frequency initially evolves in accordance to (1.111) in the vicinity of the transition, and progressively tends to the asymptote associated with the isolated behaviour. If the external forcing did not affect the phase of the self-sustained oscillator, it would rotate with its natural frequency ω_0, and the beat frequency would be given by:

$$\Omega_{\psi_{isolated}} = \left\langle \frac{d\psi(t)}{dt} \right\rangle = m \left\langle \frac{d\phi}{dt} \right\rangle - n\omega = m\omega_0 - n\omega = -\nu. \tag{1.112}$$

When the forcing frequency is sufficiently far from the synchronisation region, the phase of the oscillator rotates with its natural undisturbed frequency ω_0. However, as the forcing frequency approaches the phase locking range, the frequency of the self-sustained oscillator gradually tends to the corresponding synchronised frequency, to which it eventually becomes entrained in the synchronisation range. The interval of the detuning ν in which the frequency of the oscillator is progressively attracted to the synchronised frequency is usually referred to as *injection pulling region.*

1.5.1.1. Simplified Fundamental Synchronisation: Adler Equation

The simplest case of phase locking, known as *fundamental synchronisation*, is obtained when $\omega \approx \omega_0$, corresponding to the indices $n = m = 1$ in (1.105). Under these conditions, the generalised phase difference ψ, directly represents the difference between the phase of the oscillator and that of the external signal $\psi = \phi - \omega t$, and the frequency detuning ν, represents the difference between the

frequency of the external forcing and the natural frequency of the self-sustained oscillator $\nu = \omega - \omega_0$.

A simplified model of the phase dynamics of free running oscillators under fundamental synchronisation was obtained in [20]. Through a series of geometrical approximations, a phase equation analogous to (1.105) was derived, in which the generic periodic waveform $q(\psi)$ is a sine function. The resulting expression, usually referred to in the literature as *Adler equation*, can be written as:

$$\frac{d\psi}{dt} = -\nu + \varepsilon \sin \psi. \tag{1.113}$$

The synchronised behaviour is associated with the existence of fixed points in (1.113). The parameters ε and ν must satisfy:

$$-\nu + \varepsilon \sin(\psi) = 0. \tag{1.114}$$

Considering the fact that $|\sin(\psi)| \leq 1$, the synchronisation region can be described as $|\nu| \leq \varepsilon$, which represents the typical Arnold tongue in the parameter space (ε, ν), illustrated in Figure 1.15(b). Within this region, the solution of (1.113) is constant $\psi(t) = \psi_s$, and its value can be obtained from (1.114) as:

$$\psi(t) = \psi_s = \arcsin(\frac{\nu}{\varepsilon}). \tag{1.115}$$

Except for the structurally unstable cases in which $|\sin(\psi)| = 1$, two values of ψ satisfy (1.114) for a given pair of parameter values (ε, ν), in every 2π interval. However, in order for the fixed point ψ_s to be stable, the left hand side of (1.114) must pass through zero at ψ_s, with positive slope. The stable solutions in the $(-\pi/2, \pi/2)$ interval have been depicted in Figure 1.16(a), as a function of the frequency detuning ν.

In the synchronised regime, the phase of the self-sustained oscillator varies in accordance with:

$$\phi = \omega t + \psi_s, \tag{1.116}$$

which corresponds to a constant rotation at the frequency of the external forcing ω, maintaining a constant phase difference ψ_s, that depends on the initial difference between the forcing frequency and the natural frequency of the oscillator $\nu = \omega - \omega_0$.

Therefore, the injection locking phenomenon can be used as the base for variable phase shifting applications, by controlling the frequency detuning ν, which can be straightforwardly achieved through varying the frequency of the external signal ω. Nonetheless, the goal in this type of practical applications, is generally to control the phase shift of a carrier with constant frequency and thus, the frequency of the external signal ω, to which the oscillator is entrained must be kept constant.

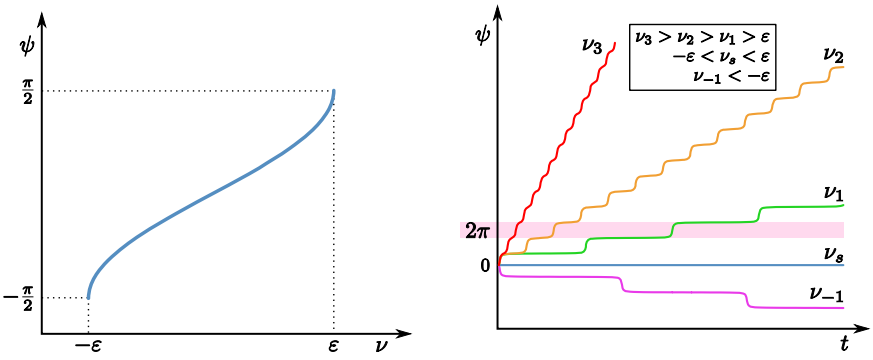

Figure 1.16: (a) Phase difference characteristic versus the frequency detuning according to Adler equation. (b) Time evolution of the phase difference in the injection locked regime and for several values of the detuning ν in the vicinity of the synchronisation transition.

The frequency detuning ν can be equivalently modified if, for certain parameter η of the oscillator, its natural frequency can be swept throughout the synchronisation region $\omega_0 = \omega_0(\eta)$. However, the parameter ε which, as has been commented, is related to the amplitude of the external signal, also depends on certain internal parameters of the oscillator. Under the approximations carried out in [20], this parameter is defined as:

$$\varepsilon = \frac{V}{V_0}\frac{\omega_0}{2Q}, \tag{1.117}$$

where Q is the *quality factor* of the oscillator, V is the amplitude of the external signal and V_0 is the amplitude of the self-sustained oscillations. The internal parameter η of the oscillator, that enables the control of the natural frequency ω_0, may also considerably affect the quality factor Q, or the amplitude of the oscillation V_0, giving rise to potential deviations from the ideal phase shifting characteristic shown in Figure 1.16(a). This approach will be extensively employed throughout this work for the design of multifunctional versatile phase shifting applications.

Outside the phase locking region, (1.113) does not have fixed points and the phase difference is time dependent $\psi(t)$. The evolution of this phase difference $\psi(t)$ is shown in Figure 1.16(b), both within the injection locking area and outside, for different values of the frequency detuning ν, in the vicinity of the synchronisation transition. The dynamics of the phase difference are highly non-uniform in time, when operating close to the limits of the phase locking region, $\nu_{ext} = \nu_{min}, \nu_{max}$. The trajectory spends long periods of time (approximately

proportional to $\sqrt{|\nu - \nu_{ext}|}$) in the neighbourhood of the maximum or minimum phase difference that can be attained in the synchronised regime ψ_{max} or ψ_{min}. These periods of nearly constant phase difference $\psi \approx \psi_{max}$, intermingle regularly with relatively short intervals in which the phase varies (either increases or decreases) in 2π; these events are called *phase slips*. Between the slips, the oscillator is nearly synchronised to the external force and its phase is nearly locked to the external phase, and the phase difference remains in the vicinity of ψ_{max} or ψ_{min}. During the slip, the phase of the oscillator makes a complete additional rotation of 2π or -2π with respect to the external force. As the frequency detuning approaches the synchronisation region, the interval between the slips progressively increases until they completely disappear in the injection locked regime

1.5.1.2. Limitations of the Averaged Phase Equation Approach

The foregoing description of the phase dynamics of a self-sustained oscillator under periodic forcing is based on the assumption that the amplitude of the forcing signal is small. Therefore, the analysis has been limited to a first order approximation in ε, whereby the external signal may significantly influence the phase of the oscillation, whereas its effects upon the amplitude are negligible. The fundamental changes in the dynamics that can be observed when considering moderate and high amplitudes of the external signal are summarised next.

For the case of moderate amplitude of the external signal, the behaviour is not essentially modified; the solution is periodic with a frequency rationally related to that of the forcing signal within the synchronisation region, and quasiperiodic outside. The variation of the beat frequency in the vicinity of the synchronisation transition continues to be smooth and proportional to a square root function of the detuning, as this behaviour is determined by the type of bifurcation, which remains of the saddle–node type. However, the boundaries of the synchronisation region are generally curves, rather than straight lines, for moderate ε. If the resonant terms are not present in the Fourier series (1.102), they can appear in higher order approximations (as terms proportional to $\varepsilon^2, \varepsilon^3, \ldots$) giving rise to extremely narrow synchronisation ranges as ε tends to zero. Furthermore, due to the effect of the non-resonant terms that have been neglected in the averaged approach, the phase difference ψ is not generally constant in the synchronised regime, for moderated amplitudes of the forcing, and becomes periodic with the period of the external force.

For high amplitude values of the external signal, on the other hand, the synchronisation transition may be originated by different types of bifurcations, leading to qualitatively different dynamical properties, or even more complicated regimes, such as transitions to chaos. Under these circumstances, in which the simplified model fails to describe the behaviour accurately, the dynamical prop-

erties can still be studied through numerical simulation, as will be shown in the following section.

1.5.2. Synchronisation Dynamics of a Representative Circuit

The averaged phase equation approach, that has been introduced, is a valuable simplified model for the description of the synchronisation phenomena, under weak forcing conditions. However, the dynamical characterisation of the synchronisation process in the general case, in which no initial assumptions as to the level of the forcing can be made, must be generally carried out through numerical simulation. In order to illustrate the fundamental dynamical features of this phenomenon, which will be extensively exploited throughout this work, the numerical simulations of the behaviour of a simple, yet sufficiently representative, system will be presented and discussed next, both in the cases in which the averaged phase equation can be applied, and when it no longer provides an accurate prediction of the performance.

The circuit chosen to perform the numerical analysis consists of a parallel RLC resonator, connected to a third order current non-linearity, as shown in Figure 1.17. This circuit has a stable periodic solution at a frequency $f_0 = \omega_0/2\pi \approx 1.5876$ GHz, in the neighbourhood of the resonance frequency of the parallel RLC network, given by:

$$f_{RLC} = \frac{\omega_{RLC}}{2\pi} \approx \frac{1}{2\pi\sqrt{LC}} \approx 1.5915 \text{ GHz}. \tag{1.118}$$

An external current generator of amplitude I_s, frequency f_s and phase ϕ_s has been connected in parallel to the free running oscillator, in order to evaluate its performance under external periodic forcing. It will be assumed that the external generator is independent and cannot be perturbed by the interaction with the circuit.

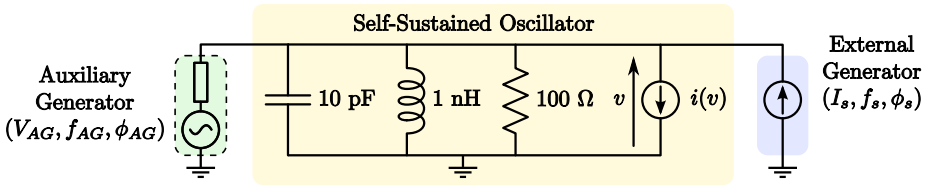

Figure 1.17: Circuit diagram of the free running oscillator used in the numerical simulations. The non-linear element is ruled by the time domain expression: $i(v) = -0.03v + 0.01v^3$. An external current generator of amplitude, I_s, frequency f_s and phase ϕ_s, has been connected to the circuit.

In the following, the case of fundamental synchronisation, in which the frequency of the forcing signal is close to the natural frequency of the self-sustained

oscillator, $f_s \approx f_0$, will be considered in detail first. Different types of rational synchronisation ($f_s \approx m/nf_0$, $m \neq n$, $m, n \in \mathbb{N}$) will be subsequently addressed, focusing on their main similarities and differences with the fundamental case.

1.5.2.1. Fundamental Synchronisation

The injection locked solutions of the considered circuit have been obtained through harmonic balance, for a frequency variation range of the external signal f_s, between 1.3 and 1.9 GHz and for different current amplitudes I_n, from 0.5 to 30 mA. As has been stated, the phase locked solutions share the same frequency as the external signal f_s, and they can thus be described by the amplitude V_n, and phase ϕ_n of the corresponding phasor, $v(t) = \Re\{V_n e^{j\phi_n} e^{j\omega_s t}\}$, $V_n, \phi_n \in \mathbb{R}$. The results are shown in terms of amplitude V_n in Figure 1.18(a), and in terms of phase shift with regard to the external signal $\Delta\phi = \phi_n - \phi_s$, in Figure 1.18(b).

The red traces correspond to amplitude values of the external signal I_s from 0.5 to 12.5 mA, in steps of 4 mA, increasing in the directions indicated by the grey arrows. The red dotted lines in the lower part of Figure 1.18(a) have been calculated with a conventional harmonic balance simulation, without any complementary initialisation process. Because the autonomous oscillation was not properly initialised, the simulation converges to an unstable regime associated with the perturbation of the unstable constant (DC) solution of the circuit. This solution is of the unstable focus type, except in the central region of the considered frequency band (where it coexists with other synchronised solutions), in which it becomes of the unstable node type. The corresponding phase shift $\Delta\phi$ response is represented in red dotted line in Figure 1.18(b). These curves exhibit the characteristic behaviour of a parallel resonant circuit: the phase crosses through 180° at the maximum of the amplitude.

In the central part of the studied frequency range, this solution coexists with a closed solution curve, that evolves from a small loop around the natural frequency of the oscillator f_0, for $I_s = 0.5$ mA, to a loop that spans a frequency range over 100 MHz for $I_s = 0.5$ mA. Each of these closed curves is formed by two solution branches; the upper part, indicated in solid line, consists of stable node type solutions, whereas the lower part, plotted in dashed line, is formed by saddle solutions. These two solutions coalesce and annihilate one another at two saddle–node bifurcations.

The phase shift $\Delta\phi$ associated with these solutions is shown in Figure 1.18(b); each closed amplitude curve corresponds to a 360 degree phase variation. For low amplitudes of the external signal I_s, the behaviour in the stable part—limited by saddle–node bifurcations—is analogous to that predicted by Adler equation, as shown in Figure 1.16(a); a phase variation of about 180 degrees is covered in the synchronisation range. However, this phase shift range progressively increases with I_s, deviating from the results predicted by the simplified model.

For the obtention of these injection locked solutions, the autonomous oscillation has been conveniently initialised in the harmonic balance simulations, by means of a non-perturbing voltage auxiliary generator with the same frequency as the external generator $f_{AG} = f_s$. Taking advantage of the fact that each value of the phase shift $\Delta\phi = \phi_n - \phi_s = \phi_{AG} - \phi_s$, in the range $[0, 360)^\circ$ produces one single solution point, the phase shift has been swept throughout this range in the simulation process, optimising, for each point, the values of amplitude V_{AG} and frequency $f_s = f_{AG}$, that fulfil the non-perturbation condition.

The green traces correspond to amplitude values of the external signal I_s, between 12.6 and 15 mA, in steps of 0.8 mA and from 16 to 18 mA, in steps of 1 mA. The closed and open curves found in the previously considered amplitude range have merged, giving rise to a single continuous trace for each amplitude value, divided into different regions (associated with different types of solutions), by saddle–node bifurcations. Starting from either end of the frequency range and moving towards the centre, only one solution of the unstable focus type can be found for each frequency value—indicated with dotted line—that becomes of the unstable node type at some point, as has been commented. At certain value of the frequency, which varies with the amplitude I_s, two additional coexisting solutions appear at a saddle–node bifurcation; a stable node (solid line) and a saddle (dashed line). The unstable node and the saddle progressively approach each other as the frequency tends to the centre of the range, until they eventually connect and disappear in a turning point, that will be closer to the centre for lower values of the amplitude of the external signal I_s. The behaviour of the phase shift $\Delta\phi$ is similar to the previous case; the range it covers continues to widen as the synchronisation amplitude grows.

Since the curves for this amplitude range are multivalued in amplitude, frequency and phase, they must be obtained in a piecewise approach using continuation techniques. Each trace is thereby divided into three different regions: the part above the saddle–node bifurcation loci, which is not multivalued versus f_s, and the two lateral sectors at either side of the centre of the figure which, individually, are not multivalued versus the amplitude V_n.

The harmonic balance simulations of the injection locked solutions are performed with a non-perturbing auxiliary generator operating at the same frequency as the external generator $f_{AG} = f_s$. For the obtention of the upper part, the frequency of the auxiliary generator $f_{AG} = f_s$ is swept, optimising the amplitude $V_{AG} = V_n$, and phase values $\phi_{AG} = \phi_n$, that minimise the error function associated with the non-perturbation condition. The simulation of either of the lateral parts, on the other hand, is carried out by sweeping the amplitude of the generator $V_{AG} = V_n$ and optimising the phase ϕ_{AG} and the frequency $f_{AG} = f_s$ (restricted to the corresponding lateral part), that fulfil the non-perturbation condition.

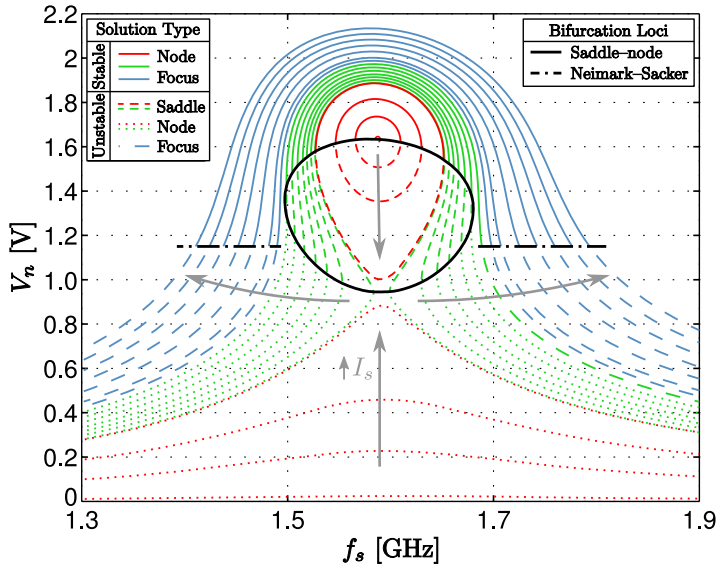

(a)

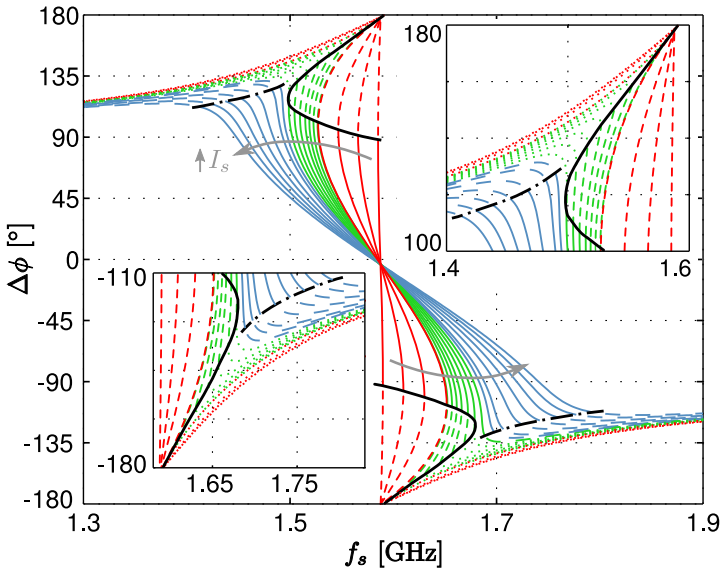

(b)

Figure 1.18: Injection locked solutions versus the frequency of the external forcing f_s, for different values of the current amplitude I_n, from 0.5 to 30 mA. (a) Amplitude of the node voltage V_n and (b) Phase shift with regard to the external reference $\Delta\phi = \phi_n - \phi_s$.

As has been previously discussed, the convergence of the harmonic balance simulation is compromised when approaching a turning point, as the Jacobian matrix becomes progressively singular. Since, in the upper part, this happens at the intersection with the saddle–node bifurcation locus while, in the lateral parts, the only tuning point versus the amplitude takes place at the maximum of the curve, the appropriate combination of the three segments leads to the accurate obtention of the complete solution curve.

Finally, the blue curves have been calculated for the amplitude values $I_s = 19$ mA and from 20 to 30 mA in steps of 2 mA. As no turning points are observed in these traces, they can be straightforwardly calculated by sweeping the frequency of the external signal in conventional harmonic balance simulations, without any complementary techniques. The stable ranges are limited by secondary Hopf or Neimark–Sacker bifurcations, in which the stable periodic solution of the focus type, becomes an unstable focus, as a pair complex conjugate Floquet multipliers crosses the unit circle. Although the Neimark–Sacker bifurcation can be detected through an envelope transient simulation, for this particular circuit, it can be proved [7] that it takes place for $V_n = 1.15$ V.

Note the asymmetrical behaviour of the outermost green trace ($I_s = 18$ mA), in which the stable range is limited by a turning point at the lower frequency end, and by a secondary Hopf bifurcation at the upper end.

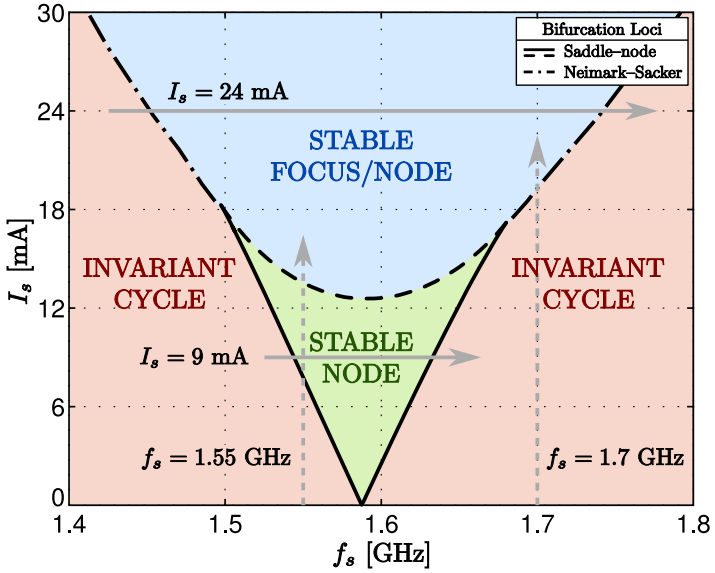

Figure 1.19: Bifurcation loci in the parameter plane (I_s, f_s). The areas with different solution properties have been shaded in different colours.

The bifurcation loci can be represented in the parameter plane (I_s, f_s), as shown in Figure 1.19. In the regions where the saddle–node and the Neimark–Sacker bifurcation loci converge, complex higher order bifurcations may occur [21].

The saddle–node bifurcation locus delimits the area shaded in green, in which the system presents three coexisting solutions: a stable node and a saddle, that compose the closed solution curves of Figure 1.18(a), together with an unstable node corresponding to the central region of the red dotted traces. The parts of the locus in solid line represent the saddle–node bifurcation associated with the stable node and the saddle, whereas the parts in dashed line correspond to the coalescence of the unstable node and saddle.

In the region shaded in blue, delimited by the Neimark–Sacker bifurcation locus and the upper part of the saddle–node locus, the system presents one single solution, which is of node type in the central region of the frequency range, and becomes of focus type when approaching the Neimark–Sacker bifurcation locus. Outside the previously described areas, no stable synchronised solution can be found; the system shows a quasiperiodic regime represented by an invariant cycle in the Poincaré map. Nevertheless, in the vicinity of the frequency values of the external signal that are rationally related to the natural oscillation frequency, $nf_s = mf_0$, the solution will be periodic, although these rational synchronisation regions may be extremely narrow and difficult to detect.

In order to illustrate the synchronisation process under different conditions, the behaviour of the system has been evaluated when varying the amplitude and the frequency of the external generator along the grey arrows shown in Figure 1.19. The results of the simulations are presented and commented next.

Frequency Sweeps. The frequency of the external signal f_s has been varied between 1.3 and 1.9 GHz for two fixed values of the amplitude I_s: 9 and 24 mA.

The results for 9 mA are shown in terms of amplitude in Figure 1.20(a), and averaged observed frequency f_Ω, in Figure 1.20(b). The averaged observed frequency f_Ω is associated with the averaged observed angular frequency $\Omega = 2\pi f_\Omega$, as defined in (1.110), which represents the mean frequency of the oscillator. Note that this frequency is in general different from the natural frequency of the oscillator f_0, due to the effect of the perturbing external signal.

In the central region of the frequency range, a stable phase locked solution has been obtained in a harmonic balance simulation, using a non-perturbing auxiliary generator operating at the same frequency as the external generator. The phase of the auxiliary generator has been swept between 0 and 360° optimising the amplitude and frequency values that fulfil the non-perturbing condition. The amplitude of the synchronised solutions produces a closed curve represented in red, like those shown in Figure 1.18(a), whose upper part is stable (solid line)

and the lower part is unstable (dashed line). Since both parts annihilate each other at a saddle node bifurcation, no synchronised solution can be found outside this region.

The behaviour outside the synchronisation region has been evaluated through a different harmonic balance simulation. Because the observed frequency of the oscillator no longer matches that of the external signal, an additional fundamental must be included in the frequency basis. Furthermore, when the oscillator is not synchronised, it can be analysed as a perturbed autonomous system and thus, the phase of the auxiliary generator can be arbitrarily set to zero, taking advantage of the invariance of the solution versus time shifts. The amplitude and frequency of the auxiliary generator have been optimised to fulfil the non-perturbing condition. The amplitudes of the components of the node voltage V_n at the frequency of the external signal f_s and at the observed frequency of the oscillator f_Ω, have been represented in Figure 1.20(a), and the values of the observed frequency f_Ω in Figure 1.20(b). Note that, in the synchronisation region, the observed frequency matches that of the external signal $f_\Omega = f_s$.

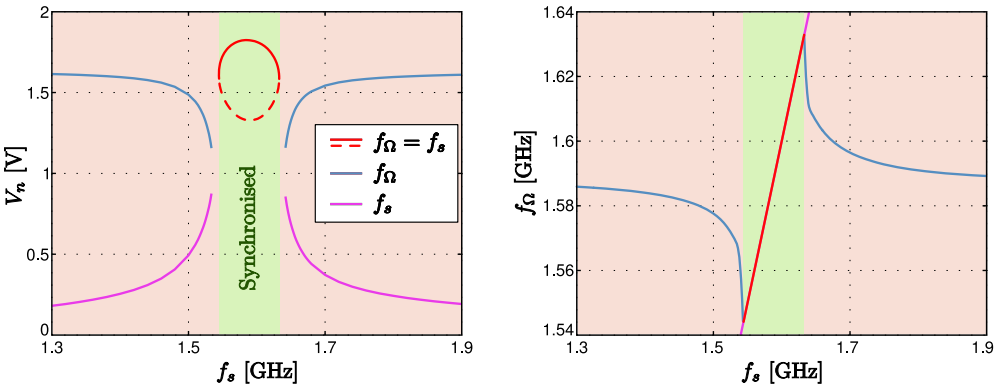

(a) (b)

Figure 1.20: Solutions of the circuit of Figure 1.17 when sweeping the frequency of the external generator for a fixed amplitude value of 9 mA. (a) Node voltage amplitude. (b) Averaged observed frequency f_Ω.

As the frequency of the external generator approaches the natural frequency of the oscillator f_0, the observed frequency f_Ω progressively tends to that of the external signal f_s, until it matches that value $f_\Omega = f_s$, in the synchronisation region. On the other hand, as the perturbed frequency of the oscillator converges to that of the external generator, the amplitudes of the components at f_s and f_Ω respectively increase and decrease their values smoothly, until they eventually undergo an abrupt change in the synchronisation transition.

The result of the corresponding simulations of the frequency sweep with a fixed amplitude value $I_s = 24$ mA are presented in terms of amplitude V_n in Figure 1.21(a), and averaged observed oscillator frequency f_Ω in Figure 1.21(b).

This frequency sweep crosses the blue region of Figure 1.19 where, as has been commented, the system presents a single solution. Therefore, this synchronised solution can be obtained through a conventional harmonic balance simulation without any complementary initialisation technique. As opposed to the previous case, the synchronised solution exists throughout the whole frequency range, although it becomes unstable through two secondary Hopf bifurcations, which set the limits of the synchronisation region. The phase locked solution continues to exist beyond those limits, but it is not robust and therefore unobservable.

The operation of the circuit outside the synchronisation region is evaluated in an analogous manner to that used in the previous case: a harmonic balance simulation with a two fundamental frequency basis (f_s and f_Ω), complemented by a non-perturbing auxiliary generator has been used. The phase of the auxiliary generator can be arbitrarily set to zero and its amplitude and frequency are optimised to satisfy the non-perturbing condition.

As can be seen in Figure 1.21(a), the amplitude of the component at f_s progressively tends to the amplitude of the synchronised solution at the phase locking transitions, until it matches this value smoothly at the limit of the synchronisation region. On the other hand, the amplitude of the component at f_Ω progressively reduces its value until it vanishes at the synchronisation transition. This behaviour corresponds to a Neimark–Sacker bifurcation, as described in Section 1.4.1.2.

When the frequency of the external signal is far apart from the synchronisation region, the observed frequency f_Ω is close to the natural frequency of the oscillator f_0 and, as it approaches the synchronisation region, the observed frequency first tends to the frequency of the external signal at the limit of the phase locking region, and then slightly deviates from it. At the limit of synchronisation region, the component at frequency f_Ω has completely vanished, and the solution presents a single frequency component at f_s. This kind of phase locking for relatively high amplitude values of the external signal is usually referred to in the bibliography as *suppression of the natural dynamics*, as opposed to the conventional phase locking or synchronisation, that takes place for lower amplitudes [21].

Amplitude Sweeps The amplitude of the external generator has been swept along the grey arrows shown in dashed line in Figure 1.19, corresponding to 1.55 and 1.7 GHz.

The behaviour of the system has been evaluated through envelope transient simulations, obtaining samples of the envelopes of the circuit variables, about

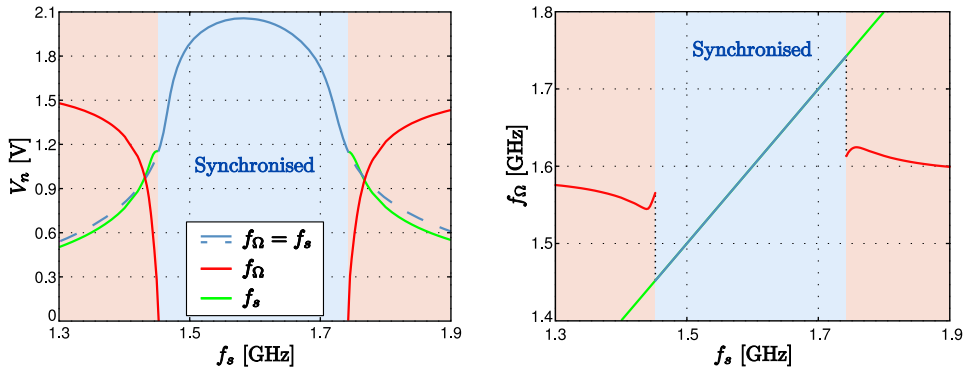

(a) (b)

Figure 1.21: Solutions of the circuit of Figure 1.17 when sweeping the frequency of the external generator for a fixed amplitude value of 24 mA. (a) Node voltage amplitude. (b) Averaged observed frequency f_Ω.

the components of the pre-established frequency basis. Because the frequency of the external signal f_s is close to the natural frequency of the oscillator f_0, the simulations are performed with f_s as the only fundamental of the frequency basis, while setting a sufficiently high sampling rate to detect the possible coexisting frequency components.

The Poincaré map is a useful tool for the simplified representation of the system solutions, transforming a N dimensional continuous solution into a discrete solution of dimension $N-1$. As has been explained in Section 1.2.4, for a system under periodic forcing with period T_s, an angular magnitude $\theta = \frac{2\pi t}{T_s} \pmod{2\pi}$, can be introduced in the state vector, enabling the definition of a global cross section through simply selecting a fixed value $\theta = \theta_0$, of this angular magnitude. The evaluation of the state variables at this constant value of the angular magnitude is equivalent to a sampling at the period of the forcing T_s, with an initial offset that depends on the particular value θ_0.

Given the envelope of a state variable $X(t)$, whose samples are obtained as the result of an envelope transient simulation, the corresponding time domain signal $x(t)$ can be calculated as

$$x(t) = \Re\{X(t)e^{j\omega_s t}\}. \tag{1.119}$$

At integer multiples of the forcing period $t = kT_s$, $k \in \mathbb{N}$, the exponential term of (1.119) is equal to unity and therefore, the time domain signal can be evaluated as $x(kT_s) = \Re\{X(kT_s)\}$. By setting up the envelope transient simulation to calculate samples of the envelope at integer multiples of the period $X(kT_s)$, the Poincaré maps of the solutions can be straightforwardly obtained. The computational cost of the simulation can be reduced by decreasing the number of

calculation points to $X(nT_s)$), $n = 2k, 3k, \ldots$, leading to the Poincaré second, third and successive return maps, as long as the sampling rate remains high enough to correctly represent all the frequency components involved.

The results for the amplitude sweep corresponding to $f_s = 1.55$ GHz are presented in Figure 1.22, for six different values of the amplitude of the synchronisation signal I_s. For each amplitude value, the Poincaré map, calculated through the foregoing procedure, is shown in the upper part, and the normalised envelope spectrum centred at the carrier at f_s on the lower part. For the Poincaré map, the unstable solutions are calculated using harmonic balance simulations.

In the absence of the synchronisation signal ($I_s = 0$ mA) the results are shown in Figure 1.22(a). Exceptionally, in this case the envelope transient simulation has been performed with the natural frequency f_0 as the only fundamental. A stable periodic solution is obtained, giving rise to a limit cycle in the phase space represented by the red filled circle in the Poincaré map. The envelope spectrum has been centred at $f_s = 1.55$ GHz to simplify the comparison with the remaining cases. This solution coexists with an unstable constant solution of the circuit with $v = i_L = 0$, which is indicated by a triangle instead of a circle, in order to highlight the fact that it represents a constant solution, rather than a periodic orbit.

Due to the injection of the external signal, the constant solution has become an unstable periodic orbit, indicated by the red empty circle of Figure 1.22(b). If the observed frequency of the oscillator (which corresponds to the perturbation of the previously stable periodic orbit) and the frequency of the external signal are not rationally related, the solution will be quasiperiodic, giving rise to an invariant cycle in the Poincaré map. The envelope spectrum is formed by two main peaks, along with their intermodulation products; the peak at 0 MHz corresponds to the frequency of the external signal f_s, while the other main peak is associated with the observed frequency of the oscillator. The observed frequency of the oscillator has slightly shifted from the natural frequency f_0, indicated by the grey dashed line, towards the forcing frequency f_s (offset frequency 0).

As the limit of the phase locking region is approached, the solution spends most of the time in the vicinity of a particular point of the invariant cycle, although it periodically completes a turn around the invariant cycle quickly, as shown in Figure 1.22(c). This is in total agreement with the phase slips predicted by Adler equation and depicted in Figure 1.16(b). In the envelope spectrum, the observed frequency of the oscillator is extremely close to the frequency of the external signal, giving rise to a *dense* spectrum.

In the synchronisation transition, a saddle–node bifurcation takes place at the point of the invariant cycle around which the solution used to spend most of the time. The situation slightly after the bifurcation is shown in Figure 1.22(d), where the previous invariant cycle has been represented in grey. Two periodic

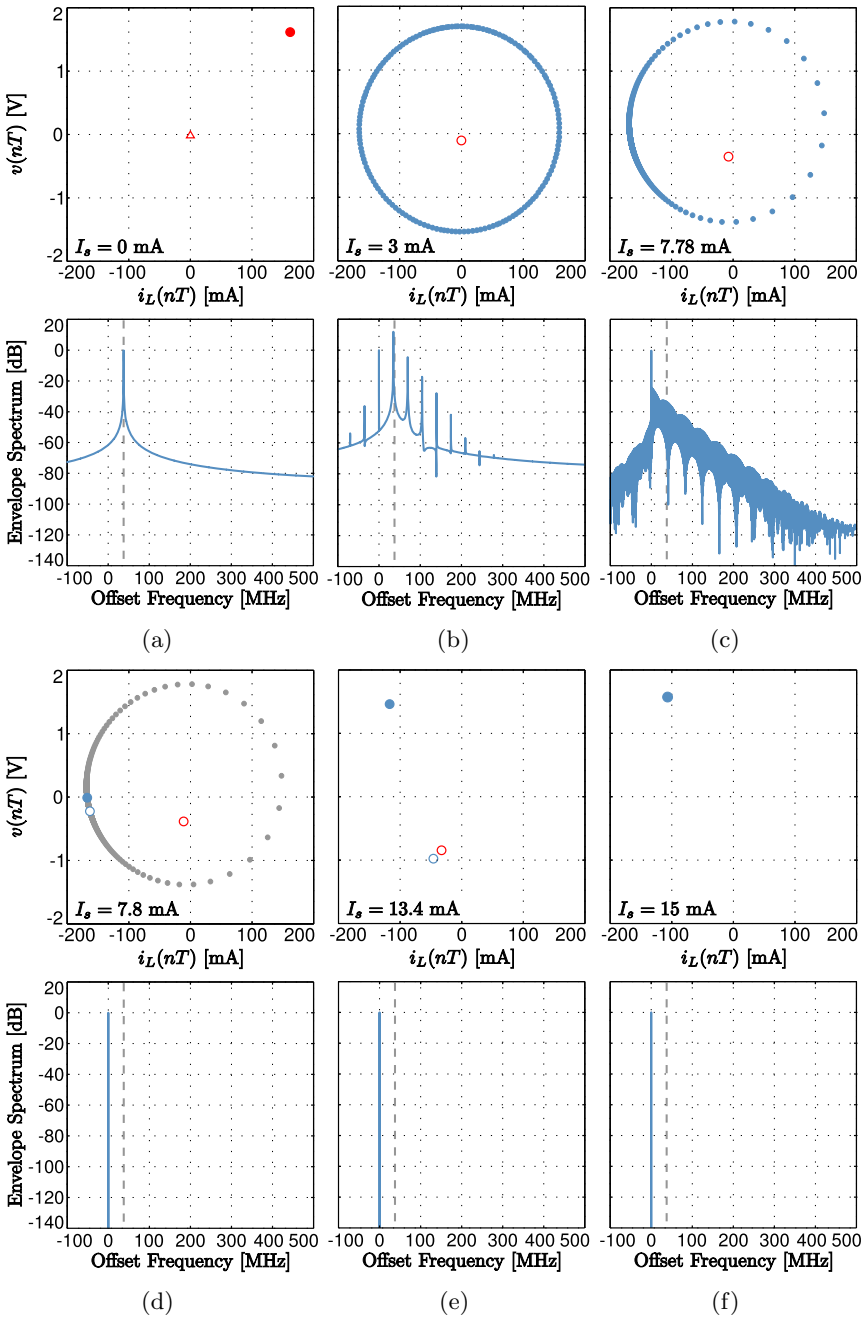

Figure 1.22: Simulation of the circuit of Figure 1.17 for a fixed frequency of the external signal $f_s = 1.55$ GHz and for six different values of its amplitude I_s. In each subfigure, (a) to (f), the Poincaré map of the solution is shown on the upper side and the envelope spectrum centred at f_s on the lower side. Except in (a), the envelope spectrum is normalised versus its value at f_s.

orbits have been generated at the bifurcation: one of the stable node type and the other of the saddle type. These solutions are indicated in the Poincaré map with the blue filled circle and the blue empty circle, respectively. The solution is periodic and, consequently, the spectrum shows a single tone at f_s.

When approaching the upper limit of the phase locking region shaded in green in Figure 1.19, the saddle type solution generated in the bifurcation (blue empty circle) progressively closes on the unstable node type solution (red empty circle), as shown in Figure 1.22(e). These solutions merge and disappear in a new saddle-node bifurcation, leaving the stable node type solution, represented by the blue filled circle in Figure 1.22(f), as the only solution of the system; the system is now operating in the region of suppression of the natural dynamics (blue region in Figure 1.19).

It is important to focus on the noteworthy properties of the saddle–node bifurcation that originates the synchronisation transition. In a typical saddle–node bifurcation of periodic solutions, as described in Section 1.4.1.2, two periodic solutions: one of node type and one of saddle type, like those represented in Figure 1.22(d), coalesce and annihilate each other. If the node type solution involved was stable, the system evolves to a different steady state solution beyond the bifurcation point, that cannot be locally determined. However, in this case, the quasiperiodic solution that appears after the bifurcation is such that the torus that represents it in the phase space, contains the periodic orbits that merged at the turning point (the invariant cycle in Figure 1.22(c) contains the fixed points associated with the saddle and node periodic solutions).

This kind of behaviour, first discovered in the Van der Pol oscillator, is associated with a global bifurcation: the saddle–node homoclinic bifurcation, as introduced in Section 1.4.2.2 [22]. Before the bifurcation point, the unstable manifold of the saddle forms a closed connection passing through the stable node, that leads to a homoclinic orbit with infinite period at the bifurcation point. This homoclinic orbit brings about a limit torus beyond the bifurcation point, as the period of the newly generated fundamental progressively decreases. Immediately after the desynchronisation, the fundamental of the solution associated with the previous stable periodic regime coexists with a new fundamental originated in the homoclinic orbit, which has a large period. The solution spends most of the time in the vicinity of the previously stable periodic orbit and occasionally completes a quick turn around the other dimension of the torus, which explains the behaviour shown in Figure 1.22(c). Further beyond the bifurcation point, the rotation period around the newly created dimension of the torus continues to decrease steadily.

The results of the amplitude sweep for a fixed frequency $f_s = 1.7$ are presented in Figure 1.23, for six different values of the amplitude I_s. The envelope transient simulations have been performed with a single fundamental frequency

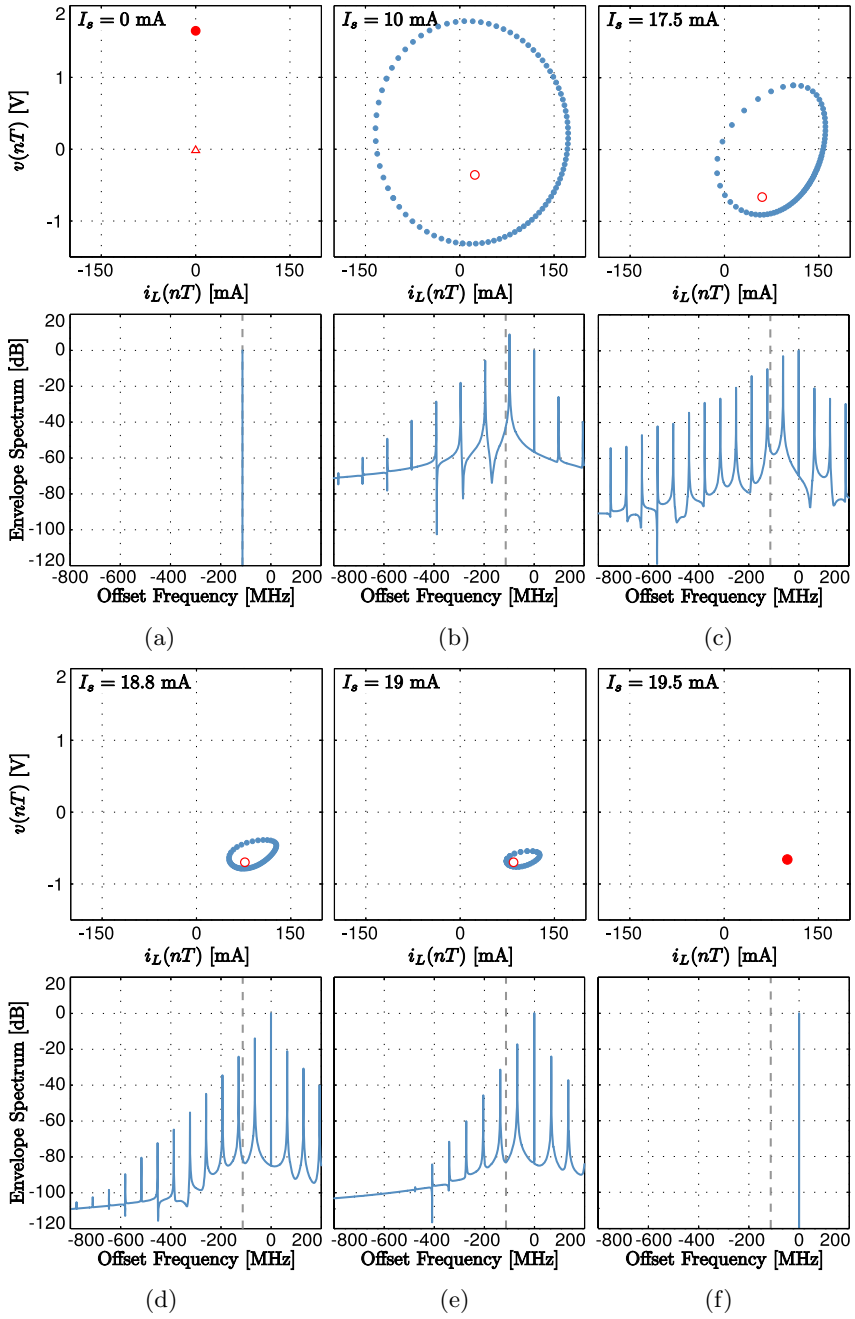

Figure 1.23: Simulation of the circuit of Figure 1.17 for a fixed frequency of the external signal $f_s = 1.7$ GHz and for six different values of its amplitude I_s. In each subfigure, (a) to (f), the Poincaré map of the solution is shown on the upper side and the envelope spectrum centred at f_s on the lower side. Except in (a), the envelope spectrum is normalised versus its value at f_s.

basis, which is f_0 for the first case without synchronisation signal, and f_s for the remaining cases. The envelope spectrum is centred at f_s for all the cases, in order to simplify the comparison.

Without external synchronisation signal (Figure 1.23(a)), the solution is a periodic orbit with natural frequency of the oscillator f_0, which is represented by a red filled circle in the Poincaré map. This periodic solution coexists with a constant solution that is indicated with an empty triangle. The natural frequency f_0 is indicated in all the spectra by a grey dashed line.

As a result of the injection of the external synchronisation signal, the previous unstable constant solution becomes an unstable periodic orbit, represented by a red empty circle in Figure 1.23(b). The envelope spectrum consists of two main peaks, together with their intermodulation products: the peak at 0 corresponds to the component at f_s, and the other main peak is associated with the observed frequency of the oscillator, which has slightly shifted from the natural value f_0 towards f_s. When these two fundamentals are not rationally related, the solution yields an invariant cycle in the Poincaré map (equivalent to a limit torus in the phase space).

With the increasing amplitude of the external signal I_s (Figures 1.23(c) and 1.23(d)), the observed frequency of the oscillator continues to approach the frequency of the external signal f_s, while it gradually reduces its oscillation amplitude. Consequently, the area of the invariant cycle in the Poincaré map progressively reduces.

At some point close to the limit of the phase locking region, as was detected in the results of the frequency sweep for $I_s = 24$ presented in Figure 1.21(b), the observed frequency of the oscillator starts to depart from the frequency of the external signal f_s. In the envelope spectrum shown in Figure 1.23(e), it can be seen that the peak corresponding to the oscillator operation has slightly moved away from f_s, with regard to the previous case, while its amplitude has further decreased. The invariant cycle in the Poincaré map has shrunk to a small loop around the unstable periodic orbit corresponding to the perturbation of the DC solution of the self-sustained oscillator.

At the synchronisation transition, the area of the invariant cycle has decreased to zero; the oscillating component has completely vanished from the spectrum, and the periodic orbit becomes stable in a supercritical secondary Hopf or Neimark–Sacker bifurcation. Due to this progressive extinction of the oscillating component of the circuit, this type of synchronisation is also referred to in the literature as suppression of the natural dynamics. Beyond the bifurcation, a single periodic orbit exists, as can be seen in Figure 1.22(f).

The practical interest of the synchronisation phenomena has traditionally lain in the capability to stabilise the frequency of a powerful oscillator by means of a very precise but weak signal [19]. More recently, these phenomena have been

applied to a wider range of practical purposes, such as the development of multifunctional oscillator based phase shifting topologies, to which the present work is devoted. For these applications, it is usually sought to reduce the required synchronisation power, in order to improve the efficiency and to enable the entrainment of multiple oscillators with the same external signal. Hence, for these particular purposes, the phase locking with low amplitude (the green area of Figure 1.19) is usually preferred over the suppression of the natural dynamics (blue area), which requires higher amplitude values.

1.5.2.2. Rational Synchronisation

The rational synchronisation describes the phenomenon whereby the oscillator frequency is entrained to a frequency rationally related to that of the external signal. Under these conditions, as has been previously derived, the phase of the oscillator is described by the expression

$$\phi = \frac{n}{m}\omega t + \frac{\psi_s}{m}, \tag{1.120}$$

where $\psi_s \in [0, 2\pi)$ is a fixed point of the averaged phase equation. Although there exists a fixed point of the averaged phase equation for every value of this interval, normally only a subset of these are stable. According to Adler equation, which has proved to be accurate for fundamental phase locking with low amplitude of the external signal, only half of this interval consists of stable equilibria. Outside the 2π interval, the fixed points repeat themselves. The phase evolution described by (1.120) corresponds to a oscillation at a frequency $f_\Omega = \frac{n}{m} f_s$, with a constant phase shift given by $\Delta\phi = \frac{\psi_s}{m}$. Note that the range of constant phase shift values $\Delta\phi$, that can be obtained is restricted to $\Delta\phi \in [0, \frac{2\pi}{m})$.

This operating regime can be thought of as the entrainment of the mth harmonic component of the oscillation by the nth harmonic component of the external signal ($nf_s = mf_\Omega$). Therefore, these harmonic components must be present in the circuit, with the appropriate levels, in order for the synchronisation to occur. Theoretically, the phase locking phenomenon would take place even for vanishingly small values of the external signal, although the synchronised regime would take a long time to set in. However, the synchronisation region under these conditions would be extremely narrow, making it extraordinarily difficult to detect in simulation, and nearly impossible to observe in practice.

Different representative types of rational synchronisation have been obtained through an analogous procedure to that followed in the previous section. The bifurcation loci represented in the parameter plane $(I_s, f_s/f_0)$ are depicted in Figure 1.24. For the sake of clarity, the frequency of the external signal f_s has been normalised by the natural frequency of the oscillator f_0. Although the phase locking phenomenon would theoretically take place for every rational number

$\frac{n}{m}$, $n, m \in \mathbb{N}$, the analysis has been restricted to four representative cases: $n = 3, m = 1$ ($3f_s = f_\Omega$), $n = m = 1$ ($f_s = f_\Omega$, fundamental synchronisation), $n = 2, m = 4$ ($2f_s = 4f_\Omega$) and $n = 1, m = 3$ ($f_s = 3f_\Omega$).

The Neimark–Sacker bifurcation locus delimits the common area of suppression of the natural dynamics, shaded in blue, whereas the saddle–node bifurcation locus associated to each particular type of rational synchronisation defines an individual Arnold tongue. The remaining area, shaded in light red, corresponds to quasiperiodic solutions, except in the vicinity of the rational values $\frac{n}{m}$, $n, m \in \mathbb{N}$ (in the corresponding rational synchronisation regions), where the solutions will be periodic.

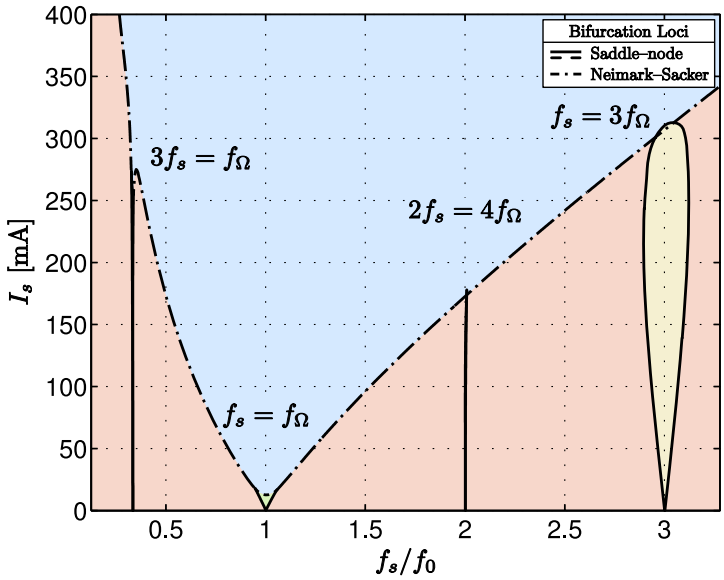

Figure 1.24: Bifurcation loci in the parameter plane $(I_s, f_s/f_0)$ for four different types of rational synchronisation: $n = 3, m = 1$ ($3f_s = f_\Omega$), $n = m = 1$ ($f_s = f_\Omega$, fundamental synchronisation), $n = 2, m = 4$ ($2f_s = 4f_\Omega$) and $n = 1, m = 3$ ($f_s = 3f_\Omega$).

The rational synchronisation region associated with $n = 3, m = 1$ ($3f_s = f_\Omega$) has been magnified in Figure 1.25(a). The saddle–node bifurcation locus has a curvy triangular shape analogous to that corresponding to the fundamental synchronisation, shown in Figure 1.19. The rationally synchronised solutions have been calculated through harmonic balance simulations, complemented with a non-perturbing auxiliary generator operating at a fixed frequency $f_{AG} = 3f_s$. The phase of the auxiliary generator ϕ_{AG} is swept between 0 and 2π, optimising the amplitude and frequency values that fulfil the non-perturbation condition.

The synchronisation region for $n = 1, m = 3$ ($f_s = 3f_\Omega$) has been magnified in Figure 1.25(c). Since $m = 3$, the phase shift range that can be obtained in this case is limited to the interval $[0, \frac{2\pi}{3})$. Therefore, the phase locked solutions are calculated through the same simulation set-up, by sweeping the phase of the auxiliary generator ϕ_{AG} between 0 and $\frac{2\pi}{3}$, as the solution repeats itself thereafter.

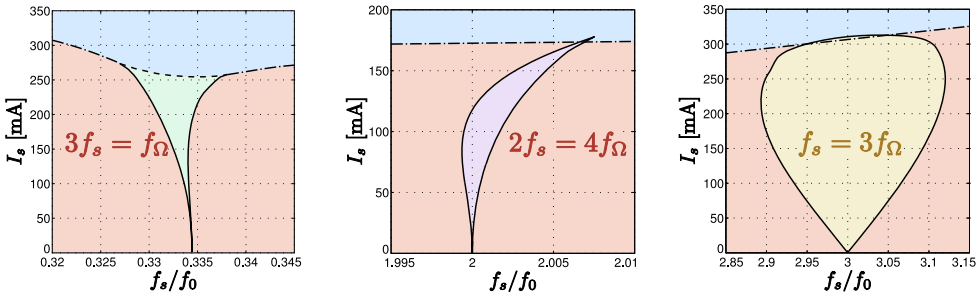

(a) (b) (c)

Figure 1.25: Magnification of the bifurcation loci associated with several rational phase locking. (a) $n = 3, m = 1$ ($3f_s = f_\Omega$). (b) $n = 2, m = 4$ ($2f_s = 4f_\Omega$). (c) $n = 1, m = 3$ ($f_s = 3f_\Omega$)

In the vicinity of $f_s/f_0 = 2$ the rational phase locking for $n = 1, m = 2$ ($f_s = 2f_\Omega$) might be expected. Nonetheless, since the non-linear element of the circuit of Figure 1.17 has a describing function $i(v) = -0.03v + 0.01v^3$, which lacks the second order term, no second order harmonics or second order intermodulation products are generated. Therefore, a higher order phase locking $n = 2, m = 4$ takes place instead. In this case, the third harmonic component of the self oscillation at $3f_\Omega$ is entrained by the third order intermodulation product $2f_s - f_\Omega$, leading to a synchronised solution at $2f_s - f_\Omega = 3f_\Omega$ or, equivalently $2f_s = 4f_\Omega$.

The appearance of this higher order synchronisation is proved by the fact that the solution repeats itself after a $\frac{2\pi}{4}$ interval, rather than π interval, as would be the case in a $n = 1, m = 2$ entrainment. Moreover, if the frequency component at $4f_\Omega$ is not included in the frequency basis for the harmonic balance simulation, the synchronised solution cannot be obtained. The saddle–node bifurcation locus for this type of synchronisation is magnified in Figure 1.25(b).

The synchronisation region that has been obtained for $n = 2, m = 4$ is extremely narrow due to the weakness of the high order components involved. In general, the width of the phase locking range is determined by the levels of the frequency components that take part in the process.

Bibliography

[1] J. Guckenheimer and P. Holmes. *Nonlinear Oscillations, Dynamical Systems and Bifurcations of Vector Fields*. Springer-Verlag, New York, 1990.

[2] T.S. Parker and L.O. Chua. Chaos: A tutorial for engineers. *Proceedings of the IEEE*, 75(8):982–1008, aug. 1987.

[3] M. Koksal. On the state equations of nonlinear networks and the uniqueness of their solutions. *Proceedings of the IEEE*, 74(3):513–514, march 1986.

[4] A. Suárez and R. Quéré. *Stability Analysis of Nonlinear Microwave Circuits*. Artech House, Norwood, MA, 2003.

[5] Harald Bohr. *Almost Periodic Functions*. Chelsea, 1947.

[6] A. Suarez and J.-M. Collantes. Chaos detection in microwave circuits using harmonic balance commercial simulations. In *Microwave Symposium Digest, 1998 IEEE MTT-S International*, volume 1, pages 271–274 vol.1, 7-12 1998.

[7] A. Suárez. *Analysis and Design of Autonomous Microwave Circuits*. IEEE, 2008.

[8] G. Teschl. *Ordinary Differential Equations and Dynamical Systems*. Wien, 2010.

[9] C. Chicone. *Ordinary Differential Equations with Applications*. Springer, New York, 2006.

[10] P. Hartman. *Ordinary Differential Equations*. Wiley, New York, 1964.

[11] A. S. Willsky A. V. Oppenheim and W. T. Young. *Signals and Systems*. Prentice-Hall, Englewood Cliffs, NJ, 1983.

[12] V. Rizzoli and A. Lipparini. General stability analysis of periodic steady-state regimes in nonlinear microwave circuits. *Microwave Theory and Techniques, IEEE Transactions on*, 33(1):30–37, jan. 1985.

[13] K. Ogata. *Modern Control Engineering*. Prentice-Hall Inc., NJ, 1997.

[14] J. Jugo, J. Portilla, A. Anakabe, A. Suarez, and J.M. Collantes. Closed-loop stability analysis of microwave amplifiers. *Electronics Letters*, 37(4):226–228, feb. 2001.

[15] Vittorio Rizzoli, Andrea Neri, and Franco Mastri. A modulation-oriented piecewise harmonic-balance technique suitable for transient analysis and digitally modulated signals. volume 2, pages 546 –550, sep. 1996.

[16] E. Ngoya and R. Larcheveque. Envelop transient analysis: a new method for the transient and steady state analysis of microwave communication circuits and systems. volume 3, pages 1365 –1368 vol.3, jun. 1996.

[17] J.C. Pedro and N.B. Carvalho. Simulation of rf circuits driven by modulated signals without bandwidth constraints. volume 3, pages 2173 –2176, 2002.

[18] S. Wiggins. *Introduction to Applied Nonlinear Dynamical Systems and Chaos*. Springer-Verlag, New York, 1990.

[19] A. Pikovsky, M. Rosenblum, and J. Kurths. *Synchronization. A Universal Concept in Nonlinear Sciences*. Cambridge University Press, Cambridge, 2001.

[20] R. Adler. A study of locking phenomena in oscillators. *Proceedings of the IEEE*, 61(10):1380 – 1385, 1973.

[21] Alexander Balanov, Natalia Janson, Dmitry Postnov, and Olga Sosnovtseva. *Synchronization: From Simple to Complex*. Springer, Berlin Heidelberg, 2009.

[22] Leonid P. Shilnikov, Andrey L. Shilnikov, and Dmitry V. Turaev. *Methods Of Qualitative Theory In Nonlinear Dynamics, Part 2*. World Scientific Publishing Company, 2002.

Chapter 2

Receiving Phased Antenna Array based on Injection Locked Third Harmonic Self Oscillating Mixers

Contents

2.1. Introduction

Antenna arrays have been widely employed in a great variety of applications, taking advantage of their well known beam forming, pattern nulling or comformation capabilities, among many others. Additionally, the behaviour of the arrays can be completely modified in real time, giving rise to adaptive solutions.

For the implementation of these adaptive topologies, the contributions transmitted or received by each of the individual elements composing the array, must be separately tuned in amplitude and phase.

As opposed to the amplitude tuning, which can be straightforwardly achieved through variable gain amplifiers, the practical implementation of versatile and efficient phase shifting solutions represents a noteworthy technological challenge, especially at high frequencies.

For this purpose, multiple phase shifting topologies based on oscillator circuits have been presented in the literature [1; 2; 3; 4]. Solutions based on fundamentally injection locked oscillators are limited to a 180° theoretical phase shift range [5]. This range can be doubled by using a two stage solution in which the second oscillator is injection locked to the second harmonic component of the first oscillator [6], when using a configuration based on master–slave cascaded oscillators [7], or by extracting the second harmonic component of a synchronised oscillator [8].

In this work, in order to assure a practically usable phase shift range of at least 360°, an injection locked harmonic self oscillating mixer circuit [9], has been chosen. This topology integrates the downconversion and continuous range

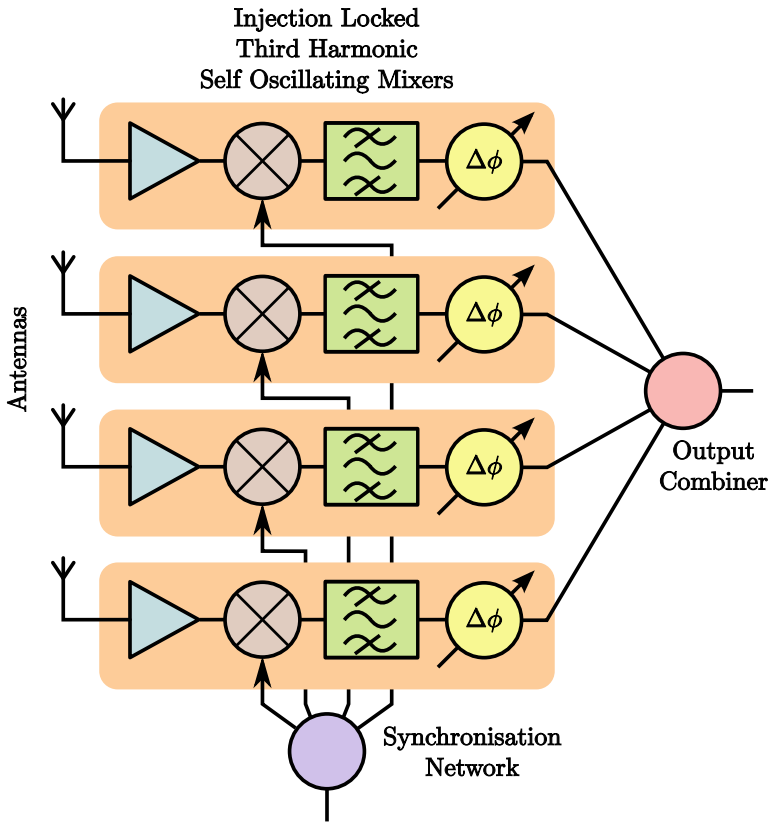

Figure 2.1: Block Diagram of the receiving phased antenna array based on injection locked third harmonic self oscillating mixers.

phase shifting operations, together with the local oscillator, providing an overall positive conversion gain.

As shown schematically in Figure 2.1, this topology will be used to control a receiving four element linear antenna array. The isolated performance of the circuits will be first analysed, both as a function of the control voltages and versus frequency. The antenna array, along with the required auxiliary microwave networks will be designed and experimentally validated separately. Finally, a prototype of the complete system will be manufactured, and its performance will be assessed through measurements in the anechoic chamber.

2.1.1. Third Harmonic Self Oscillating Mixer

The design of the third harmonic self oscillating mixer used in the present chapter was prior to this work [9] and therefore, it has not been part of it.

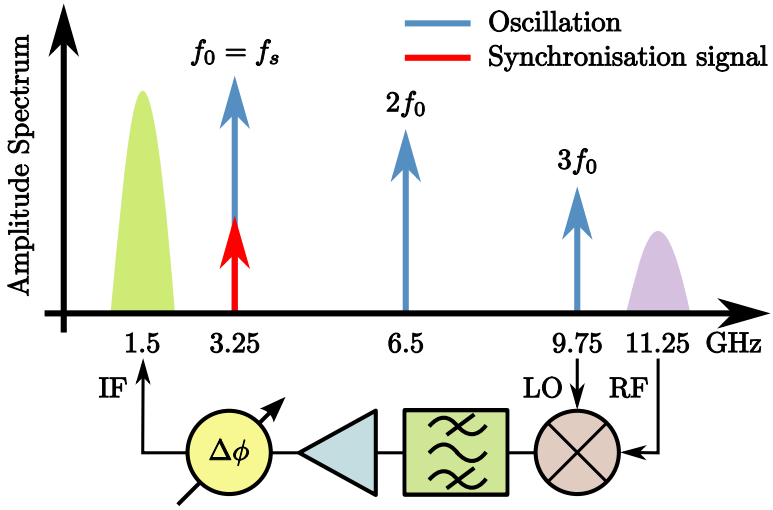

Figure 2.2: Frequency components involved in the operation of the injection locked harmonic self oscillating mixer.

Nonetheless, in the interest of self-containment, the main features of this circuit are briefly described in this introductory section.

The harmonic self oscillating mixer circuit is firstly designed as a voltage controlled oscillator at a frequency $f_0 = 3.25$ GHz. Under injection locked operating conditions, as explained in Section 1.5, the phase of the output signal with respect to the external reference can be varied within a continuous range of about 180°. However, since this phase shift range is not sufficient for the effective control of an antenna array, a harmonic component of the fundamentally synchronised self oscillation must be used instead.

Even though the second harmonic component would theoretically yield a 360° phase shift range, this theoretical range is usually reduced in practice as a result of the appearance of noisy precursors when the circuit is operated close to the limits of the synchronisation region [10]. Thus, in order to assure that a full 360° phase shift range is effectively available in practice, the third harmonic component of the oscillation, with a theoretical phase shift range of 540°, was chosen for this design.

The operation of the circuit is illustrated in Figure 2.2. The input RF signal in the band $f_{in} = 11.1-11.4$ GHz is mixed with the third harmonic component of the fundamentally injection locked self oscillation. Using the techniques presented in [11], the circuit was optimised to carry out an efficient mixing operation $f_{IF} = f_{in} - 3f_0$, providing an overall positive conversion gain.

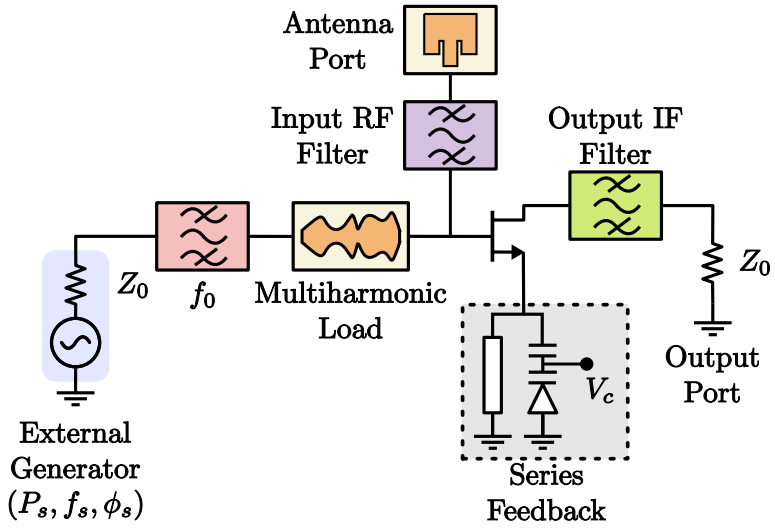

Figure 2.3: Schematic topology of the harmonic self oscillating mixer.

2.1.1.1. Circuit Topology

The electrical diagram of the third harmonic self oscillating mixer design is shown schematically in Figure 2.3. The topology comprises the following fundamental parts:

- ***Transistor:*** A Hewlett-Packard ATF-36077 Pseudomorphic High Electron Mobility Transistor (pHEMT) has been chosen for this design, owing to its ultra low noise performance capabilities in its operating band, from 2 to 18 GHz.

- ***Series Feedback:*** A resonant network is connected to the source terminal of the transistor in order to synthesise the required oscillation start-up conditions at the operating frequency $f_0 = 3.25$ GHz. A varactor diode is integrated in this series feedback network, enabling the tuning of the oscillation frequency f_0.

- ***Varactor:*** The chosen device is a Microsemi-GC15007, which provides a capacitance range between 0.2 and 2.8 pF, for control voltages from 20 to 0 V.

- ***Synchronisation Filter:*** An external generator is connected to the circuit for injection locking purposes. The external signal at frequency $f_s = f_0 = 3.25$ GHz is routed through a bandpass filter in order to block out other undesired external signals that might lead to spurious synchronisations.

- ***Input Filter:*** The input RF signal in the band $f_{in} = 11.1 - 11.4$ GHz is selected using a hairpin bandpass filter and delivered to the transistor gate terminal.

- ***IF Filter:*** The output signal of the harmonic self oscillating mixer is the intermodulation product generated in the mixing operation between the input signal in the band $11.1 - 11.4$ GHz, and the third harmonic component of the oscillation at $3f_0 = 9.75$ GHz. The product, in the intermediate frequency band $f_{IF} = 1.35 - 1.65$ GHz, is extracted from the transistor drain terminal through the IF bandpass filter.

- ***Multiharmonic Load:*** A transmission line structure whose parameters can be optimised to control the harmonic content present in the circuit is connected to the transistor gate terminal.

2.2. System Overview

A diagram of the receiving active antenna array based on injection locked harmonic self oscillating mixers that has been designed is shown in Figure 2.4. The signal received by each of the four elements of the antenna array in the band $f_{in} = 11.1 - 11.4$ GHz, is delivered to the input port of an independent third harmonic self oscillating mixer, which is injection locked to an external reference signal at frequency $f_s = f_0 = 3.25$ GHz. A synchronisation network has been designed to deliver this reference signal with equal power P_s and phase ϕ_s, to each of the harmonic self oscillating mixer circuits.

As has been previously explained, the third harmonic self oscillating mixer circuit performs a mixing operation between the input signal and the third harmonic component of the self oscillation, downconverting the input signal to the corresponding intermediate frequency band $f_{IF} = 1.35 - 1.65$ GHz. In the process, the circuit introduces a phase shift that can be arbitrarily varied within a continuous range wider than 360°, adding an overall positive conversion gain.

For monitoring purposes, an individual low power sample is extracted from the output of each of the individual harmonic self oscillating mixers through a directional coupler. Each of these samples can be selected through a 4×1 microwave switch and separately measured using an Agilent 89600 Vector Signal Analyser. The output signals of the harmonic self oscillating mixer circuits at intermediate frequency are finally combined to obtain the overall system output.

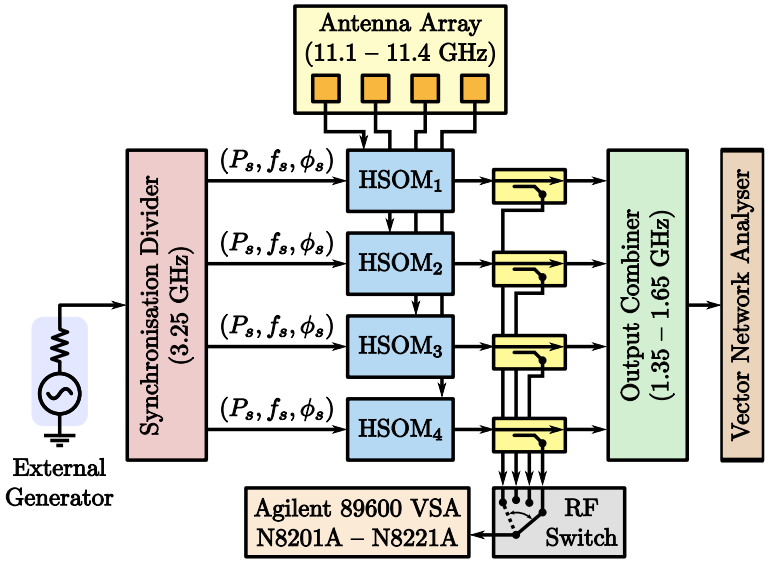

Figure 2.4: Topology of the receiving phased antenna array based on injection locked third harmonic self oscillating mixers.

2.3. Behaviour of the Injection Locked Harmonic Self Oscillating Mixer Circuits

The design criteria for the different functional blocks involved in the system topology that has been described in the foregoing section are primarily determined by the core active circuit. Thus, a thorough evaluation of the performance of the injection locked harmonic self oscillating mixer circuit was initially performed, focusing on the specific parameters that are directly related to its application in the active antenna array system.

As has been previously mentioned, the IL3HSOM circuit is injection locked at the fundamental oscillation component. Hence, the phase of the fundamental component with regard to that of the external signal $\Delta\phi = \phi - \phi_s$, varies with the frequency detuning $\nu = \omega_s - \omega_0 = 2\pi(f_s - f_0)$, while the frequency remains equal to that of the external signal $f_\Omega = f_s$.

In the analysis presented in Section 1.5, the phase variation of the oscillation signal was evaluated while sweeping the frequency of the external signal f_s. However, using that approach, the frequency of the oscillation follows that of the external signal, which rarely has practical interest.

For the purpose of this application, the oscillation signal—specifically its third harmonic component—will be used as the local oscillator for the downconversion, whose frequency must be constant. Therefore, the frequency of the synchroni-

sation generator ω_s cannot be swept to tune the phase shift introduced by the circuit, and the frequency detuning $\nu = \omega_s - \omega_0$ must be varied otherwise.

The circuit can be designed as a Voltage Controlled Oscillator (VCO), integrating a tuning device in its resonant network (e.g. a varactor diode), in such a way that its fundamental oscillation frequency ω_0 can be varied by tuning the bias voltage of the device. Thus, the frequency detuning $\nu = \omega_s - \omega_0$, which—under injection locked conditions—determines the phase shift of the oscillation with regard to the external signal, can be modified while keeping its frequency $f_\Omega = f_s$ constant.

As shown in Figure 2.3, a varactor diode was integrated in the series feedback network of the IL3HSOM circuit, enabling the tuning of its fundamental oscillation frequency f_0 which, in turn, varies the frequency detuning $\nu = \omega_s - \omega_0$. Hence, the phase shift $\Delta\phi$ introduced by the circuit, can be directly controlled through the bias voltage of the varactor diode.

2.3.1. Injection Locked Solutions

As has been discussed in Section 1.5, for an external signal with a given power value P_s, there will be a range of values of its frequency f_s around the fundamental oscillation frequency of the circuit f_0, known as fundamental synchronisation region, where the oscillation frequency of the circuit follows that of the external signal $f_\Omega = f_s$. Within the synchronisation region, the phase shift between the oscillation and the external signal $\Delta\phi = \phi - \phi_s$ is determined by the frequency detuning $\nu = \omega_s - \omega_0$.

However, in the operation regime of the IL3HSOM circuit that has been described, the frequency of the external signal f_s is kept constant, and the frequency detuning is modified through the variation of the fundamental oscillation frequency of the circuit. In an analogous manner, for a given power value of the synchronisation signal P_s, there will be a range of values of the fundamental oscillation frequency f_0 in which the circuit will be injection locked, that defines the synchronisation region in this case.

In order to take advantage of the complete theoretical phase shift range available, the frequency tuning range achieved by the voltage controlled oscillator design must cover the entire synchronisation region at the desired power level of the external signal P_s. In case the frequency cannot be tuned throughout the complete synchronisation range, only a limited fraction on the theoretical phase shift range will be practically usable.

The injection locked solutions of the circuit for different values of the synchronisation power P_s have been evaluated through harmonic balance simulations, carried out using the commercial software package *Advanced Design System* (ADS). A frequency basis with one fundamental component at the frequency of the external generator f_s, along with its first 10 harmonic components has been

considered in those simulations. To initialise the correct autonomous solution, a voltage auxiliary generator directly connected to the gate port of the transistor has been used. The injection locked solutions are obtained by sweeping the phase of the auxiliary generator ϕ_{AG} between 0 and 360°, while the phase of the external signal ϕ_s can be arbitrarily set to 0. At each point of the sweep, the frequency of the auxiliary generator is set to be equal to that of the external signal $f_{AG} = f_s$, and the voltage V_{AG} and capacitance of the varactor diode C_{var} are optimised to fulfil the corresponding non-perturbation condition.

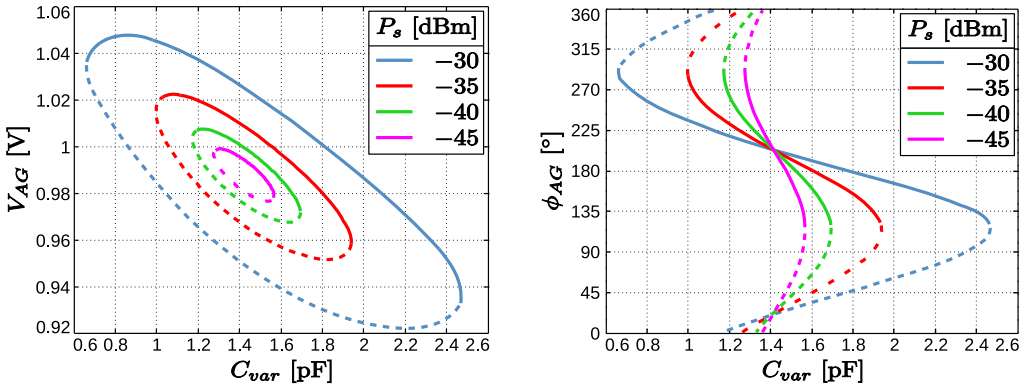

(a) (b)

Figure 2.5: Injection locked solutions for four different synchronisation power levels. (a) Amplitude. (b) Phase shift.

The synchronised solutions, calculated for four different power values of the external signal, are shown in terms of amplitude of the auxiliary generator V_{AG}, in Figure 2.5(a), and in terms of phase ϕ_{AG}, in Figure 2.5(b), both versus the capacitance of the varactor diode C_{var}.

As expected, for higher power levels of the external signal P_s, there is a wider range of values of the fundamental oscillation frequency f_0 which corresponds to injection locked solutions and therefore, a wider variation of the capacitance of the varactor diode C_{var} is required to cover the synchronisation range. The varactor diode that has been chosen for this design provides capacitance values between 0.2 and 2.8 pF, which is sufficient for the synchronisation power levels that have been studied.

Although the synchronisation loci calculated through harmonic balance are mathematical solutions of the circuit, no information is obtained regarding their stability properties. Envelope transient simulations have been used to determine the stable regions, which are indicated in solid line in Figure 2.5, while the unstable parts are represented in dotted line.

For the power values of the external signal P_s that have been considered, the phase of the fundamental oscillation can be varied in a continuous range of about 180°, by tuning the capacitance of the varactor diode C_{var}. The amplitude of the oscillation V_{AG} shows a slight dependence on the capacitance of the varactor diode, and thus it varies with the phase shift selected. Nevertheless, this variation is very limited and it can be neglected for most applications.

In the IL3HSOM topology that has been presented, the third harmonic component of the oscillation is used as the local oscillator signal for the downconversion. Therefore, the phase shift introduced in this frequency component $\Delta\phi_3 = \phi_3 - \phi_s$, will be imposed on the output signal at intermediate frequency, giving rise to the desired phase shifting behaviour.

The phase shift of the third frequency component of the oscillation is presented in Figure 2.6, as a function of the capacitance of the varactor C_{var}, for four different values of the synchronisation power P_s. A continuous phase shift range of about 540° is available, which assures a practically usable range wider than 360°.

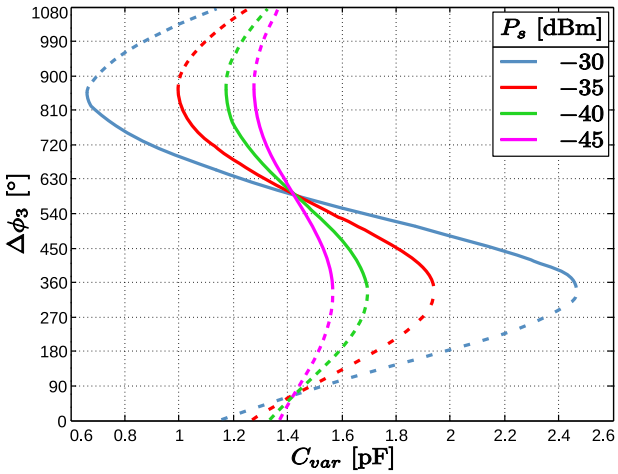

Figure 2.6: Synchronised solutions of the IL3HSOM circuit versus the capacitance of the varactor diode C_{var}. (a) Amplitude of the auxiliary generator (b) phase of the auxiliary generator. The stable parts are represented in solid line and the unstable part in dotted line.

2.3.1.1. Characterisation as a Variable Phase Shifter

The IL3HSOM circuit has been conceived to introduce a variable phase shift while performing the downconversion operation. Thus, in order to characterise its phase shifting performance, the behaviour of the circuit must be analysed

when introducing an external signal at frequency f_{in}, through the antenna port indicated in Figure 2.3.

Harmonic balance simulations have been performed introducing a tone at the centre frequency of the input RF band $f_{in_c} = 11.25$ GHz. The frequency basis for these simulations must include this new frequency component and the intermodulation products up to, at least, the 4^{th} order (note that the intermediate frequency is obtained through the mixing of the input signal with the 3^{rd} harmonic component of the self oscillation). Intermodulation products up to the fifth order have been included in the basis. Nonetheless, assuming that the level of the input signal is low and consequently, that the response of the circuit to this signal can be considered approximately linear, no harmonic components of this fundamental have been considered.

The output signal of the circuit is obtained at intermediate frequency $f_{IF} = f_{in} - 3f_s$. The *conversion gain* can thus be defined as the ratio between the power of the output signal at intermediate frequency P_o, and the input RF power P_{in}, as follows

$$G_c = \frac{P_o}{P_{in}}. \tag{2.1}$$

The phase shift introduced by the circuit is defined as the difference between the phase of the output signal at intermediate frequency ϕ_o and that of the input RF signal ϕ_o:

$$\Delta\phi = \phi_o - \phi_{in}. \tag{2.2}$$

The conversion gain of the circuit calculated for three different values of the synchronisation power are presented in Figure 2.7(a). In this case, the results have been represented as a function of the control voltage of the varactor diode V_c using the varactor model provided by the manufacturer. The corresponding phase shift $\Delta\phi$ is shown in Figure 2.7(b), also versus the varactor bias voltage.

A continuous variable phase shift range of about 540° has been obtained for the three power values of the synchronisation power that have been analysed. For the sake of clarity, the phase reference ϕ_s has been adjusted for the traces to intersect at 0°.

The conversion gain is slightly dependent on the control voltage and thus, on the imposed phase shift. Although the variation increases with the synchronisation power level, it remains under 0.7 dB for the synchronisation power levels that have been considered.

Hence, the injection locked harmonic self oscillating mixer can effectively perform the local oscillator signal generation, together with the frequency down-conversion and the continuous range variable phase shifting operations, while providing a positive conversion gain, barely dependent on the phase shift value selected.

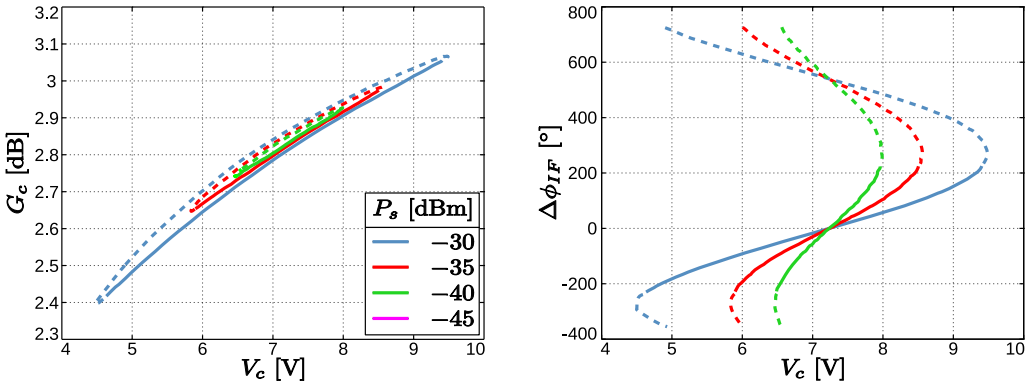

(a) (b)

Figure 2.7: Characterisation of the IL3HSOM circuit versus the varactor bias voltage V_c, for different values of the synchronisation power. (a) Conversion gain (b) Phase shift. The stable ranges calculated through harmonic balance simulations are indicated in solid line.

2.3.2. Frequency Response

As has been shown, the injection locked harmonic self oscillating mixer introduces a phase shift value that can be accurately controlled within a continuous range greater than 360°. Nonetheless, this phase shift value can only be imposed at a single frequency (note that the figures shown in the previous section correspond to the the centre frequency $f_{in_c} = 11.25$ GHz). The phase shift introduced at other frequencies cannot be controlled simultaneously, as it is determined by the frequency response of the circuit.

The frequency performance of the circuit has been evaluated through harmonic balance simulations in which the frequency of input signal f_{in}, has been swept throughout the input frequency band (11.1–11.4 GHz). In order to analyse the influence of the phase shift value imposed at the centre of the band $\Delta\phi(f_{in_c})$ in the frequency response of the circuit, the simulations have been carried out for six uniformly distributed values across the stable range: $\Delta\phi(f_{in_c}) = \Delta\phi_n = -225° + n90°$, $n \in [0, 5]$.

The frequency response calculated for two different values of the synchronisation power P_s is presented in terms of conversion gain in Figure 2.8(a), and in terms of phase shift in Figure 2.8(b).

The conversion gain presents a wider variation range both with frequency and with the phase shift imposed at the centre frequency $\Delta\phi(f_{in_c})$, for higher values of the synchronisation power. Even though these fluctuations are more pronounced at the ends of the frequency band, the maximum variation is about 2 dB in the worst case.

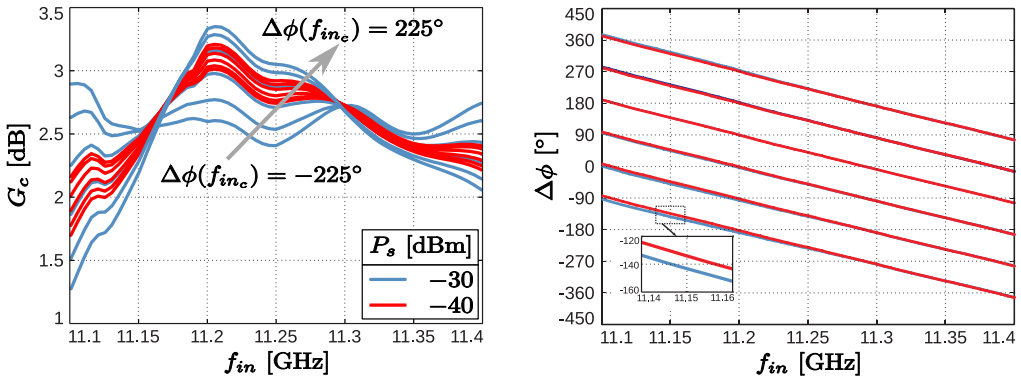

(a) (b)

Figure 2.8: Frequency response of the IL3HSOM circuit for six different values of the phase shift established at the centre frequency $\Delta\phi(f_{in_c})$. (a) Conversion gain (b) Phase shift.

The phase shift at intermediate frequency $\Delta\phi$ shows a steep slope versus frequency that disguises the small variations for the different the phase shift values imposed at the centre frequency. This slope is caused by the propagation of the signals throughout the circuit. The phase shift undergone by an electromagnetic wave traveling in an ideal and lossless transmission line of length L is known to be given by

$$\Delta\phi_L = -\frac{2\pi}{\lambda_L}L = -\frac{2\pi}{v_L}fL, \tag{2.3}$$

where λ_L and v_L are respectively the wavelength and the propagation velocity in the transmission line. Therefore, the propagation through the transmission line gives rise to a linear variation of the phase shift with frequency, analogous to the behaviour observed in Figure 2.8(b).

As was the case with the conversion gain, the phase shift also shows a wider range of variation with frequency for higher values of the synchronisation power P_s. A more detailed analysis, eliminating the slope and particularising the results for a practical antenna array, will be performed later in this chapter.

2.4. Antenna Array Design

The design process of the four element antenna array that will be controlled by means of the injection locked harmonic self oscillating mixer circuits is addressed in this section.

The elements of the array will be disposed in a linear arrangement. In this configuration, the radiation pattern in the plane perpendicular to the axis of the array cannot be controlled, as it directly matches that of the individual element.

The antenna array will be designed and manufactured in microstrip technology, taking advantage of the robustness, versatility and ease of design of these implementations.

2.4.1. Individual Radiating Element

The antenna elements for the array must necessarily cover the input frequency band (11.1–11.4 GHz), with a return loss greater than 10 dB. Nonetheless, it would be desirable to obtain a slightly wider bandwidth, in order to prevent small deviations that might appear between simulated and measured performance (due to errors in the manufacturing process, simulation inaccuracies, mismatches in the physical properties of the material, etc.), from completely invalidating the design for the target application.

Since no further specifications are imposed on the performance of the antenna element in addition to the relatively lax bandwidth requirement, keeping the element complexity to a minimum has been adopted as an additional goal for the design process.

The first choice to make when it comes to microstrip technology is the type of substrate to employ. In this case, the same multipurpose laminate used to implement the injection locked harmonic self oscillating mixer circuits—Arlon 25N—has been chosen for the individual antenna element. The datasheet properties of this material are summarised in Table 2.1.

Symbol	Parameter	Value	Unit
ε_r	Relative Permittivity	3.38	
$\tan(\delta)$	Loss Tangent	0.0025	
h	Thickness	0.762	mm
h_c	Cladding Thickness	18	µm

Table 2.1: Datasheet specification of the Arlon 25N substrate. Electrical properties measured at 10GHz.

Multiple antenna designs implemented in microstrip technology have been presented in the literature, optimised for different purposes and applications. For simplicity, a rectangular patch has been chosen as the first approach to this design. An important aspect to address in the design of this type of antenna topologies is the feeding technique. For the modular assembly of the different parts of the system, it is advantageous to install the connectors to feed the array

in the edge of the printed circuit board, as it simplifies its connection to the IL3HSOM circuits.

By implementing the feeding line in the in the same layer as the patch, the complete array can be designed in a single layer substrate structure, which makes the design cheaper and easier to manufacture. This approach also presents several technical shortcomings, such as the fact that the radiation of the feeding line may disturb the radiation pattern of the antenna. Nevertheless, since this substrate is not particularly thick or its dielectric constant particularly low, the impact of this effect on the overall radiative performance of the patch should be fairly limited.

In order to obtain an estimate to the dimensions of the rectangular patch, the following set of approximate design equations can be found in [12]:

$$W = \frac{1}{2f\sqrt{\mu_0\varepsilon_0}}\sqrt{\frac{2}{\varepsilon_r+1}}, \tag{2.4}$$

$$\varepsilon_{reff} = \frac{\varepsilon_r+1}{2} + \frac{\varepsilon_r-1}{2}\left[1+12\frac{h}{W}\right]^{-1/2}, \tag{2.5}$$

$$\frac{\Delta L}{h} = 0.412\frac{(\varepsilon_{reff}+0.3)\left(\frac{W}{h}+0.264\right)}{(\varepsilon_{reff}-0.258)\left(\frac{W}{h}+8\right)}, \tag{2.6}$$

$$L = \frac{1}{2f\sqrt{\varepsilon_{reff}}\sqrt{\mu_0\varepsilon_0}} - 2\Delta L, \tag{2.7}$$

where W and L are the width and length of the patch. Although these approximate equations were derived under certain simplifying assumptions, they usually provide a good starting point for the design process. By particularising the equations for the substrate parameters and desired centre operating frequency in this case, the initial dimensions of the patch shown in Table 2.2 have been obtained.

Frequency [GHz]	W_i [mm]	L_i [mm]
11.25	9	6.9

Table 2.2: Approximate dimensions of the resonant rectangular microstrip patch.

A rectangular patch with the initial dimensions that have been calculated is simulated using the Method of Moments (MoM) electromagnetic simulator included in the software package *Advanced Design System*.

As has been commented, the patch is fed through a transmission line etched on the same layer. If the line is directly connected to the edge of the patch, the input impedance will be very high and thus difficult to match. However, the

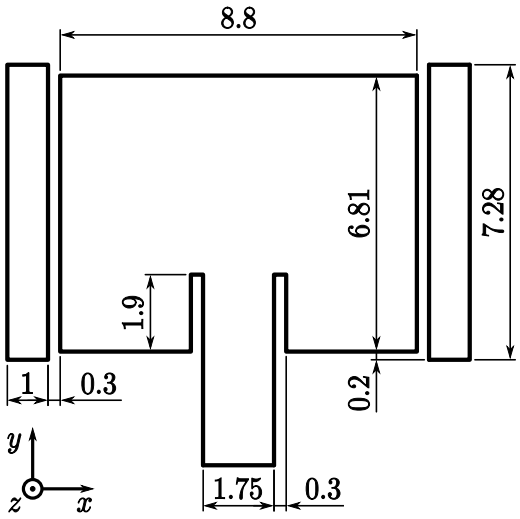

Figure 2.9: Schematic diagram of the final individual microstrip antenna element. Dimensions in millimetres.

impedance will progressively decrease from the radiating edge towards the centre of the patch, where it will reach 0 Ω. The simplest method to match the input impedance of the patch to the feeding line is known as *inset feeding*, and it entails cutting a slot in the patch at either side of the line, in such a way that, rather than connecting it to the edge of the patch, it is connected to an inner point where the input impedance is similar to that of the line.

The patch will be fed using a transmission line with a characteristic impedance of 50 Ω. Using the tool *LineCalc*, included in the ADS package, and taking into account the properties of the substrate, the width of the transmission line corresponding to a characteristic impedance of 50 Ω at 11.25 GHz was found to be $W_{line} = 1.75$ mm.

By tuning the design parameters: lengths, widths of the patch and of the matching slots, the patch was matched to an input impedance of 50 Ω, achieving a maximum bandwidth of about 300 MHz centred at 11.25 GHz. Although this bandwidth would be just enough to cover the input frequency band between 11.1 and 11.4 GHz, as has been justified, it would be advisable to have certain margin over the requirements, in order for the design to tolerate small deviations from the expected behaviour.

Hence, certain modifications in the structure of the patch were considered to increase its bandwidth. A rectangular microstrip antenna is a resonant system whose operating frequency is closely related to its geometrical dimensions, specifically to its length. A common approach to increase the bandwidth consists in generating additional resonances at frequencies close to the fundamental, giving

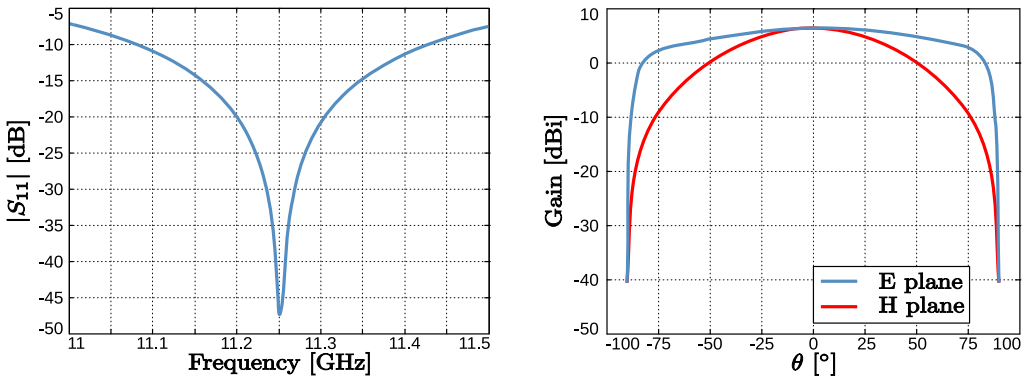

(a) (b)

Figure 2.10: Simulated performance of the final microstrip antenna design (a) S_{11} parameter (b) Copolar component of the radiation pattern in the H (xz) and E (yz) planes.

rise to a widened band. This can be attained by delimiting separate areas that resonate at different frequencies, either inside the patch, through cutting slots and/or holes, or outside, introducing parasitic patches.

The influence of the inclusion of a rectangular parasitic patch at either side of the main patch has been evaluated. To prevent the appearance of asymmetries in the radiation pattern, the dimensions of the patches were kept identical. As was the case with the main patch, the length of the parasitic patches has a strong connection to their resonant frequency, whereas their width is less influential. The separation between the main patch and the parasitic, whose lower limit is set by the precision of the fabrication equipment, determines the coupling between them.

The design parameters were conveniently modified in method of moments simulations to maximise the bandwidth. A schematic diagram of the optimised design is shown in Figure 2.9, including dimension lines. The best performance was attained when the length of the main patch is slightly smaller than that of the single resonant patch, shifting its resonance to a higher frequency, while the parasitic patches are slightly longer, decreasing their resonant frequency. Consequently, these close resonances merge together, giving rise to an extended operating band of about 350 MHz, as shown in Figure 2.10(a).

The radiation patterns of the final design are presented in Figure 2.10(b), both in the E (yz) and H (xz) planes. A gain value of 6.34 dB was obtained, with a negligible cross polar component. This final optimised design will be used as the individual element for the antenna array.

2.4.2. Array Design

The joint behaviour of a group of antennas working together in an array is primarily determined by the way the signals received by the individual elements are combined. By conveniently weighting and/or phase shifting those individual signals prior to the combination, the radiation pattern of the array can be effectively governed.

Depending on its position in space with regard to the incoming wavefront, each individual element will receive the impinging signal with a given phase shift. A schematic diagram of a four element linear antenna array with an incoming wavefront forming and angle θ with the axis of the array, is shown in Figure 2.11. The elements of the array are uniformly distributed along the x axis and separated a distance d.

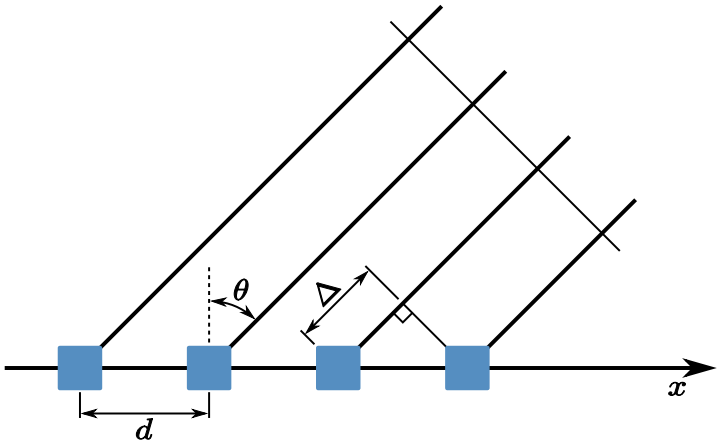

Figure 2.11: Schematic diagram four element antenna array.

Under *far field*[1] conditions, the additional distance that the wave needs to cover between one individual element and the next is given by $\Delta = d \sin\theta$. This difference in distance causes a phase shift

$$\Delta\phi_p = kd \sin\theta, \tag{2.8}$$

[1]When the wave that reaches the array is generated at a point source located far away from it, the rays that impinge upon the different individual elements can be considered to be parallel, and the associated wavefront, plane. This approximation brings about an error in the distance to the different elements, that decreases with the distance to the source of the wave. When the source is located at a distance far greater than the wavelength $d_{source} >> \lambda$, such that $d_{source} > 2D^2/\lambda$, where D is the greatest dimension of the antenna, the phase error associated with this approximation is smaller than $\pi/8$, which is usually regarded as acceptable. The area where these conditions are fulfilled is generally referred to in the literature as *far field* or Fraunhofer region [12].

where $k = 2\pi/\lambda$, is the wave number and λ, the wavelength, both in the free space.

The radiation pattern of the array can be calculated as the superposition of the individual contributions. Assuming all the antennas are identical and neglecting any mutual coupling, the complete radiation pattern can be written as

$$\vec{E}(\vec{r}) = \vec{E}_0(\vec{r}) \left[A_1 e^{-jk\frac{3d}{2}\sin\theta} + A_2 e^{-jk\frac{d}{2}\sin\theta} + A_3 e^{jk\frac{d}{2}\sin\theta} + A_4 e^{jk\frac{3d}{2}\sin\theta} \right], \quad (2.9)$$

where the centre of the array has been chosen as the phase reference and $\vec{E}_0(\vec{r})$, represents the radiation pattern of the individual element located at the origin of the coordinate system. As has been commented, the radiation pattern of the array can be controlled by conveniently weighting and phase shifting the different contributions before combining them. The complex factors $A_n = a_n e^{j\alpha_n}$, represent the phase shift α_n, and the weight a_n, applied to each of the individual components.

The design parameters for the antenna array are the separation between elements d, and the set of factors A_n, that needs to by applied to the individual contributions in order to produce the desired radiation pattern. The variety of factors that can be selected is usually limited by the practical implementation of the array. In this case, as has been studied, the injection locked harmonic self oscillating mixers enable the phase shift tuning of the received signals in a continuous range greater than 360°. The slight variation of the conversion gain with the phase shift selected is negligible, and a uniform amplitude distribution $a_n = 1$, $\forall n \in [1, 4]$, can be assumed for the purpose of this analysis.

For simplicity, ease of design and good performance, progressive phase shift distributions, in which the difference in phase shift between adjacent elements is constant $\alpha = \alpha_n - \alpha_{n-1}$, $\forall n \in [2, 4]$, are widely employed in antenna arrays. In this configuration, (2.9) can be rewritten as

$$\vec{E}(\vec{r}) = \vec{E}_0(\vec{r}) \sum_{n=1}^{4} a_n e^{j\left[n-\frac{5}{2}\right](kd\sin\theta+\alpha)} = \vec{E}_0(\vec{r}) F_A(\theta), \quad (2.10)$$

where $F_A(\theta)$ is usually referred to as the *array factor* and defined as

$$F_A(\theta) = e^{-j\frac{5}{2}(kd\sin\theta+\alpha)} \sum_{n=1}^{4} a_n e^{jn(kd\sin\theta+\alpha)}. \quad (2.11)$$

If the magnitude of the array factor is plotted as a function of $\Psi = kd\sin\theta+\alpha$, a 2π periodic function is observed, with a maximum for $\Psi = 0$. Therefore, the maximum of the array factor will be obtained for the incidence angle θ_m, that

satisfies $\Psi = kd\sin\theta_m + \alpha = 0$, namely:

$$\theta_m = -\arcsin(\frac{\alpha}{kd}). \tag{2.12}$$

The radiation pattern can be estimated according to (2.10), as the product between the radiation pattern of the individual element, as shown in Figure 2.10(b), and the array factor. To illustrate the influence of the design parameters, the magnitude of the radiation pattern thus estimated is represented in Figure 2.12(a) for three values of the separation d, when the same phase shift is applied to all the elements $\alpha = 0$. As the separation d increases, the main lobe becomes narrower improving the directivity of the array, while worsening the side lobe level. However, at some point, copies of the main lobe known as *grating lobes* will appear in the radiation pattern, limiting its practical interest.

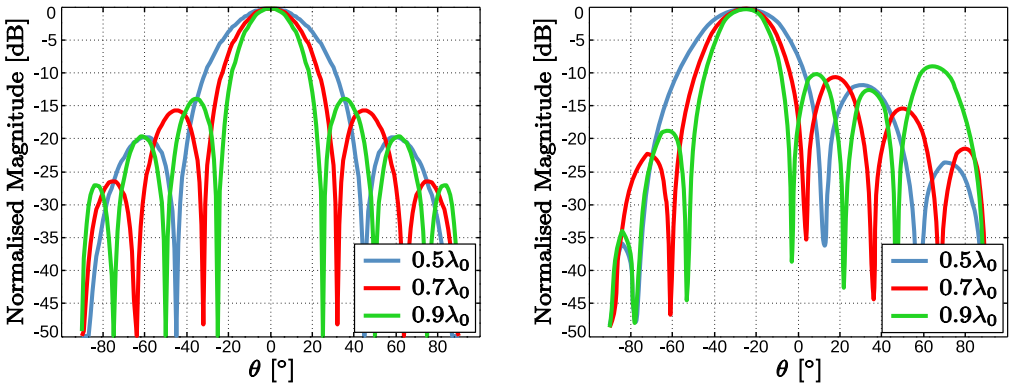

(a) (b)

Figure 2.12: Estimation of the radiation pattern for different values of the separation between elements d: (a) Broadside configuration (b) Main beam shifted to $\theta_m = -25°$.

For $d < \lambda/2$, there will be one single main lobe in the array factor, whereas for $d > \lambda$, there will be more than one regardless of the value of the progressive phase shift α selected. In between, the level of the grating lobes will be directly dependent on the progressive phase shift applied α.

A design requirement of a side lobe level smaller than -10 dB for angles of the main lobe $|\theta_m| < 20°$, is imposed on the antenna array. In order to meet this requirement, the properties of the individual element must be taken into account, along with the array factor, in accordance with (2.10). As shown in 2.10(b), the radiation pattern of the individual element has its maximum for $\theta = 0°$ and progressively decreases with the incidence angle until it practically vanishes for $\theta = \pm 90°$.

For a separation $d = 0.9\lambda$, the outermost secondary lobes shown in Figure 2.12(a), are actually grating lobes, which are severely attenuated by the pattern of the individual element. Nonetheless, as the progressive phase shift is incremented $\alpha \neq 0°$, the main lobe starts to shift from the direction perpendicular to the axis of the array $\theta = 0°$, thus being multiplied by the increasingly low value of the radiation pattern of the individual element. Conversely, the grating lobe, which was initially highly attenuated by the pattern of the individual element, gains significance rapidly as it correspondingly shifts towards $\theta = 0°$.

To illustrate this behaviour, the estimated radiation patters for the same three values of the separation d, are presented in Figure 2.12(b) when the main lobe is shifted to $\theta_m = -25°$, which corresponds to the progressive phase shift values $\alpha(0.5\lambda) = 65°$, $\alpha(0.7\lambda) = 80°$ and $\alpha(0.9\lambda) = 100°$.

For $d = 0.9\lambda$, the side lobe level when $\theta_m = -25°$ is higher than -10 dB. On the other hand, the side lobe level specification is fulfilled with $\theta_m = -25°$, both for $d = 0.7\lambda$ and $d = 0.5\lambda$. Although there would be margin to further shift the main lobe with $d = 0.5\lambda$, this option brings about a significant reduction in the directivity. Hence, the separation value $d = 0.7\lambda$ will be chosen for this work as a trade-off solution.

The analysis that has been carried out thus far is based on the array factor formulation, which includes a set of approximations, such as neglecting the coupling between the individual elements, that may compromise the accuracy of the results obtained. Therefore, the microstrip antenna array with an element separation $d = 0.7\lambda$ which, in free space, corresponds to $d = 18.67$ mm, has been studied using method of moments simulations. The simulated radiation patterns in the H plane when the elements are fed in phase $\alpha = 0$, are presented in Figure 2.13(a). The side lobe level is about -13 dB and the cross polar component is more than 35 dB under the copolar. The gain obtained in the simulation was $G = 11.81$ dB.

The maximum deviation of the main lobe corresponding to a side lobe level under -10 dB has also been determined through simulation. With a progressive phase shift $\alpha = 104°$, a deviation of the main lobe of $\theta_m = 23.5$ dB was obtained, while meeting this requirement. In this situation, the level of the crosspolar component increases to nearly -25 dB, as shown in Figure 2.13(b).

Finally, in order to validate the simulated results, a prototype of the four element antenna array fed in phase with a conventional power divider implemented in microstrip technology has been manufactured. An image of the prototype is presented in Figure 2.14. The H plane radiation patterns measured in the anechoic chamber are compared with the simulated results in Figure 2.15(a) for the copolar component and in Figure 2.15(b) for the crosspolar.

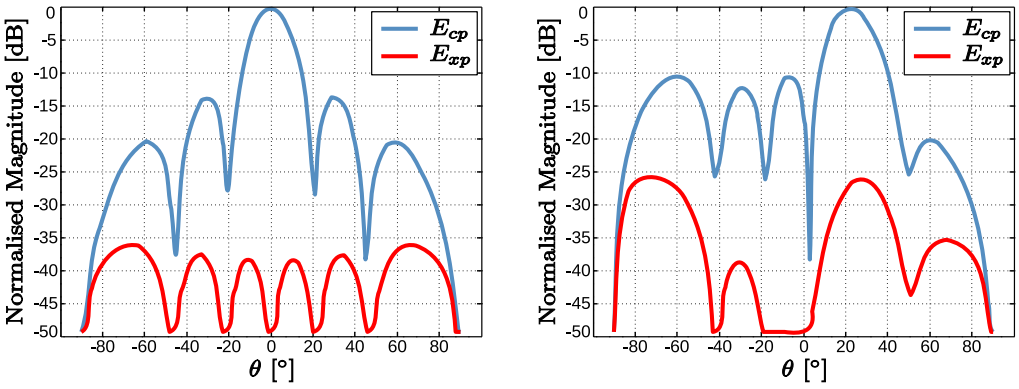

Figure 2.13: Method of moments simulation of the array radiation pattern corresponding to an element separation $d = 0.7\lambda$: (a) Broadside configuration (b) Main beam shifted to $\theta_m = -23.5°$.

The good agreement that has been obtained between simulations and measurement validates the antenna array design for the target application for which it has been conceived.

2.5. Auxiliary Networks

For the interconnection of the different functional blocks that compose the receiving antenna array topology, as shown schematically in Figure 2.4, several microwave networks are required.

In addition to the signal routing and distribution purposes, these networks will also be used to physically assemble the different parts of the system in the final prototype. Therefore, both electrical and mechanical specifications need to be imposed on their design process.

The required networks have been developed in microstrip technology, using the substrate laminate Arlon 25N, whose datasheet properties have been specified in Table 2.1. The design process leading to the final solutions, which are manufactured and measured for their experimental validation, is illustrated in this section.

2.5.1. Synchronisation Power Divider

The injection locked harmonic self oscillating mixer circuits require an external synchronisation signal at the frequency of the fundamental oscillation $f_s = 3.25$ GHz. As shown in Figure 2.4, this signal is produced for the four

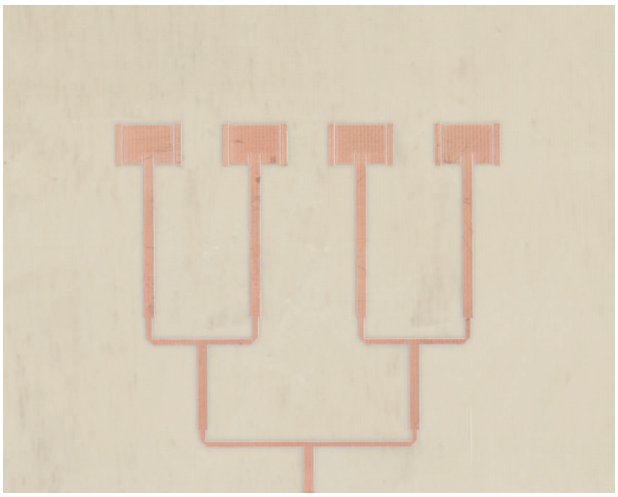

Figure 2.14: Prototype of the antenna array.

circuits by a single signal generator, and delivered to them by means of a four port power divider.

Inasmuch as the synchronisation signal constitutes the reference for the phase shifting operation of the circuits, it must be delivered with equal phase and, more importantly, it must be robust and independent on their operation regime. Therefore, high isolation levels are required between the output ports of the network, in order to conveniently attenuate the spurious signals produced by the circuits and delivered through their synchronisation port, that might otherwise perturb the synchronisation signal of adjacent circuits.

Furthermore, as has been previously discussed, the power level of the synchronisation signal has a strong influence on the performance of the circuits. Hence, for the circuits to present a similar behaviour, the synchronisation signal must be delivered with equal power level.

In the final prototype, the physical separation between injection locked harmonic self oscillating mixer circuits is determined by the antenna array that has been designed. For mechanical compatibility, the same separation $d = 18.66$ mm, must be established between the output ports of the synchronisation power divider.

In consideration of the equal split and high isolation requirements, the well-known *Wilkinson* power divider topology, shown schematically in Figure 2.16, is a simple and versatile solution [13]. It is designed as a conventional quarter wavelength power divider in which a resistor of twice the value of the input impedance Z_0, is connected between the output ports.

The connection of the resistor turns the design into a three port lossy network which is matched in all the ports and significantly improves the isolation between

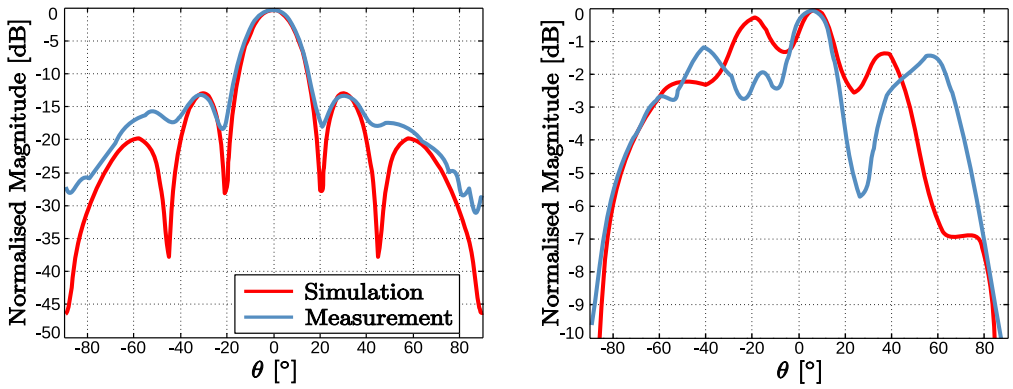

Figure 2.15: Measured H-plane radiation patterns of the manufactured prototype: (a) Copolar component (b) Crosspolar component.

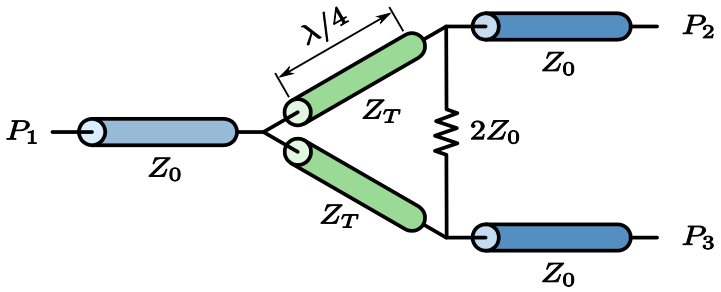

Figure 2.16: Schematic transmission line diagram of the Wilkinson power divider.

output ports. Moreover, it can be shown that, when Z_0 loads are connected to the output ports, no power dissipation takes place in the network [13].

To provide the synchronisation signal to the four IL3HSOM circuits a two stage topology using three Wilkinson power dividers has been designed at $f_s = 3.25$ GHz. The lengths of the interconnecting lines involved have been adjusted to obtain the desired separation $d = 18.66$ mm between the output ports.

Once the final design was obtained, the prototype shown in Figure 2.17 was manufactured for its experimental validation. The measurements are compared to the simulated results in the following.

As can be observed in Figure 2.18, the input port of the power divider (port 1), as well as the output ports (port 2 to 5), present a relatively high return loss throughout a wide band around the operating frequency $f_s = 3.25$ GHz.

The scattering parameters S_{i1}, $i \in [2, 5]$, that describe the transmission between the input and each of the outputs are presented in Figure 2.19(a), in amplitude and in Figure 2.19(b), in phase. The measured loss is slightly higher

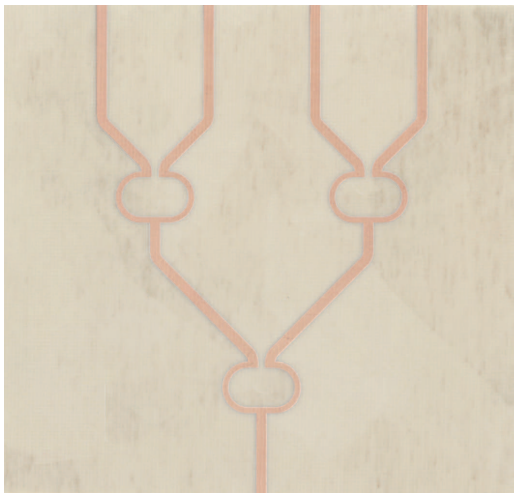

Figure 2.17: Circuit board of the synchronisation power divider.

than the result obtained in the electromagnetic simulation, due to the fact that the connectors were not modelled in the simulation. Nevertheless, a practically equal split among the four output ports has been obtained.

As has been justified, the isolation between the output ports is also an important parameter for the synchronisation power divider. The isolation between two non-consecutive ports is represented in Figure 2.20. Despite the fact that the isolation between consecutive ports could not be measured, due to the close proximity between them, which made it physically impossible to connect the cables of the vector network analyser, a sufficiently high value of about 30 dB is expected according to the simulations.

2.5.2. Output Power Combiner and Sampling Network

The downconverted and conveniently phase shifted signals obtained at the output of the injection locked harmonic self oscillating mixers must be combined to produce the global output of the system. A four port power combiner operating in the intermediate frequency band $1.35 - 1.65$ GHz, is required for this purpose.

The input ports must be matched to 50 Ω to maximise the power transfer from the IL3HSOM circuits, and high isolation levels between them are necessary to prevent the injection of spurious signals through the output port of the circuits, that might disturb their operation regime.

Once again, in order for the network to be mechanically compatible with the rest of the prototype from an assembly standpoint, the separation between the input ports must be $d = 18.66$ mm.

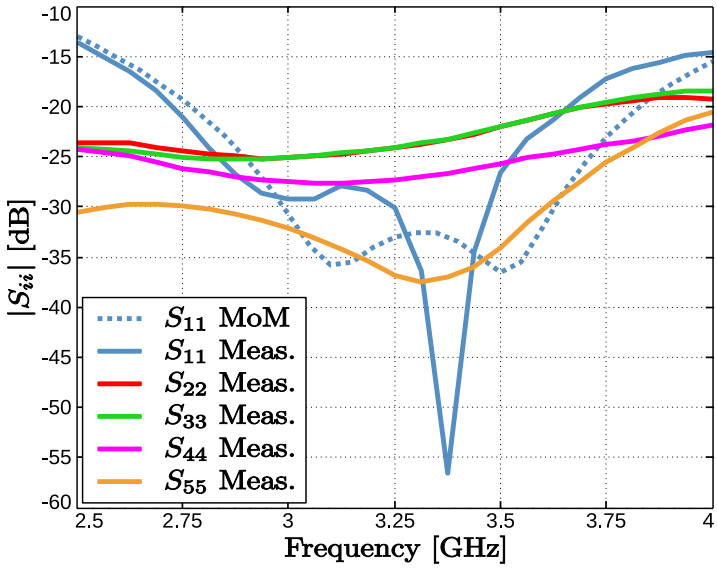

Figure 2.18: Measured reflection coefficients at the ports of the synchronisation power divider.

Furthermore, prior to the combination, low power samples must be extracted from the output of each IL3HSOM circuit, for individual phase shift monitoring purposes. These samples must be routed to independent connectors installed underneath the ground plane of the structure, in such a way that the phase shift introduced from the each of the input ports to its corresponding sample port is identical, not perturbing the measurement.

The sample ports will be connected to an 8 port ACSW−5034 microwave switch, that enables the selection, through a digital control signal, of the individual sample to measure with an Agilent 89600 vector signal analyser N8201A–N8221A.

Since the input ports of the switch are separated 12.9 mm, the sample connectors must be geometrically disposed to fit four of these ports. This specification, together with the distance between the input ports of the network and the requirement to introduce the same phase shift between each input port and the corresponding sampling port, add an additional challenge to the design process.

2.5.2.1. Power Combiner

The Wilkinson power divider used in the previous section presented a set of interesting properties, such as impedance matching in all ports and high isolation level between outputs. Taking into account the reciprocity of the network, these

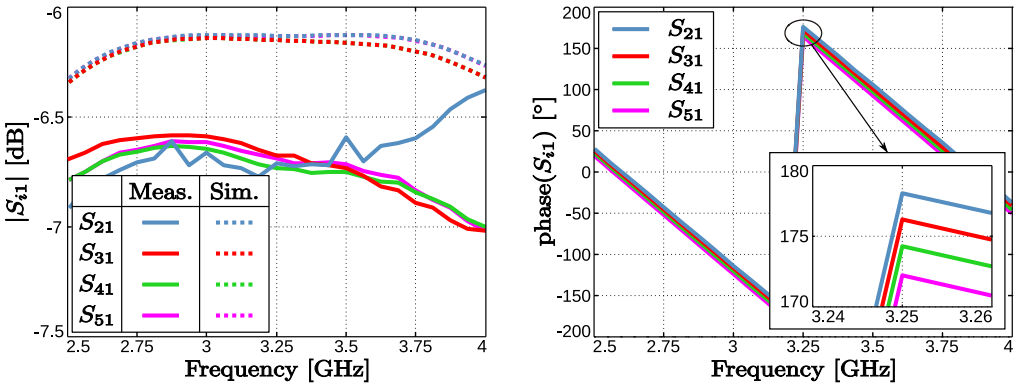

(a) (b)

Figure 2.19: Transmission coefficients measured from the input to each of the output ports of the synchronisation power divider: (a) Magnitude (b) Phase.

same properties are observed if inputs and outputs are interchanged, using it as a power combiner.

Likewise, the transmission coefficients are the same, giving rise to a total combination loss slightly higher than 6 dB, which fundamentally corresponds to the power dissipated in the resistors.

An analogous topology to the power divider described in the last section has been designed to operate at the intermediate frequency band $1.35 - -1.65$ GHz.

2.5.2.2. Sampling

The extraction of a fraction of the power travelling through a transmission line can be achieved using multiple microwave solutions. Since only a low power sample (below 10%) is required in this case, a topology based on a coupled line directional coupler seems to be appropriate.

The component consists of two transmission line segments disposed in close proximity, giving rise to certain degree of coupling between them. A schematic diagram of a directional coupler is shown in Figure 2.21. Most of the power injected through port ① continues to port ②, while a small fraction is derived to port ③. Although, theoretically, ④ is isolated, the isolation that can be practically attained in microstrip implementations is fairly limited, and this port must be terminated with a 50 Ω load.

The coupling factor between the lines is primarily determined by the separation between them, which is usually constrained by the accuracy that can be achieved in the fabrication process. Nonetheless, according to the electromagnetic simulations of the structure, a tap loss of 13 dB corresponds to a separation of 0.28 mm, which can be straightforwardly manufactured.

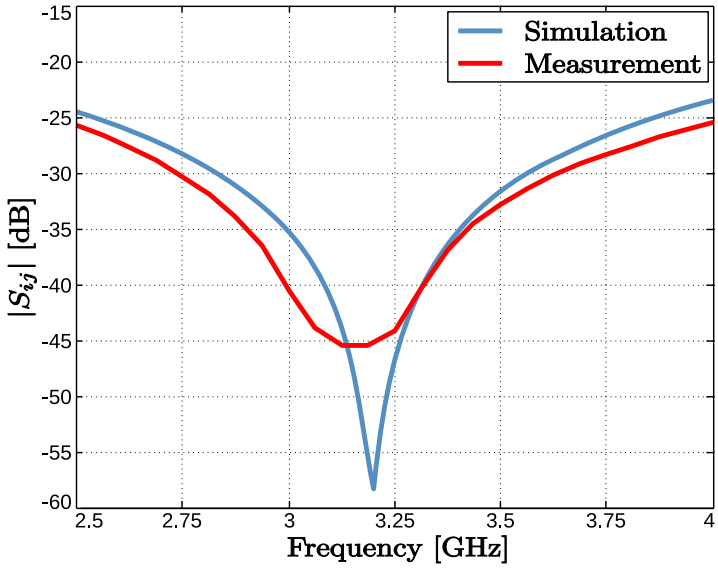

Figure 2.20: Measured isolation between non-consecutive output ports of the synchronisation power divider.

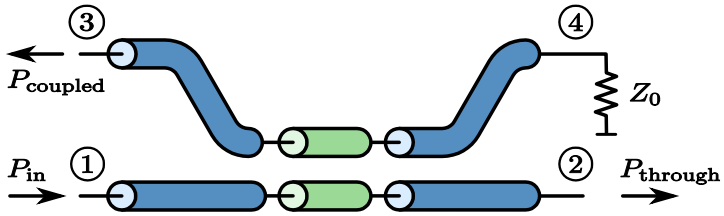

Figure 2.21: Schematic diagram of the coupled line directional coupler.

2.5.2.3. Layout

As has been pointed out, several geometrical constraints have been imposed on the power combiner and sampling network. The separation between the input connectors must be 18.66 mm and the sampling connectors must match four ports of the switch, which are separated 12.9 mm. Furthermore, the phase shift introduced between each of the input ports and the corresponding sample port must be identical and the input signals must be combined in phase.

At a single frequency, this requirement can be satisfied if the lengths of the transmission line segments associated with the different branches differ an integer multiple of the guided wavelength. However, the only way to fulfil this condition throughout the intermediate frequency band is by assuring that the electric path between each of the input port and the corresponding sample port is the same.

To meet this requirement, the sample connectors can be arranged to match any four of the eight input ports of the switch.

The solution based on symmetrical curves, which guarantees their equal lengths, that has been adopted is depicted in Figure 2.22. The sample connectors have been arranged to match the ports 1, 4, 5 and 8 of the switch, in order to maximise the separation between the different branches.

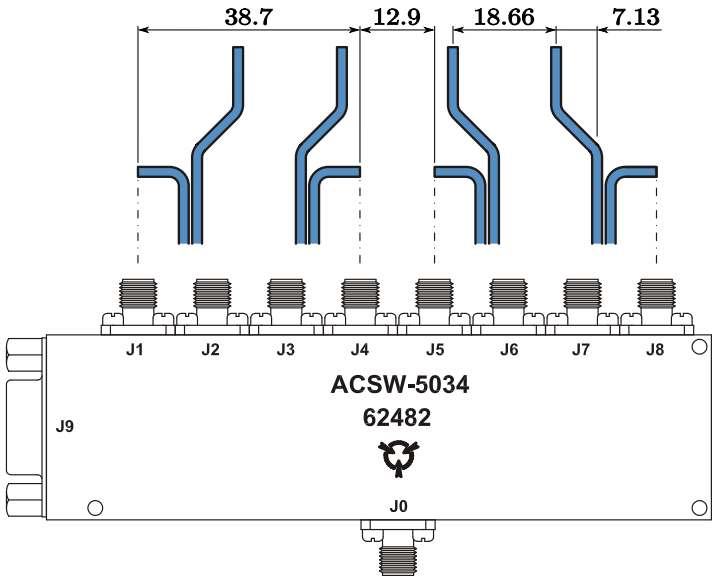

Figure 2.22: Layout of the power combiner to match the ports of the ACSW−5034 microwave switch.

The procedure to install the connectors underneath the ground plane is analogous to the well-known probe feeding technique, widely used in microstrip patch antennas [12]. The outer conductor of the coaxial connector is soldered to the ground plane of the structure, while the inner conductor—or probe—is connected to the corresponding transmission line in the upper metal layer through a hole in the substrate with diameter of 0.8 mm. A small area of the ground plane around the hole must be removed to avoid the shorting of the connector.

Additionally, four 2 mm holes have been drilled to accommodate the mounting pins of the connector, conceived to install it on the edge of the circuit board. A metal region is laid out around these holes and grounded using via holes. Likewise, grounded areas are introduced to connect the 50 Ω loads to the isolated ports of the directional couplers.

An image of the circuit board of the final design, where labels for the main composing parts have been superimposed, is shown in Figure 2.23.

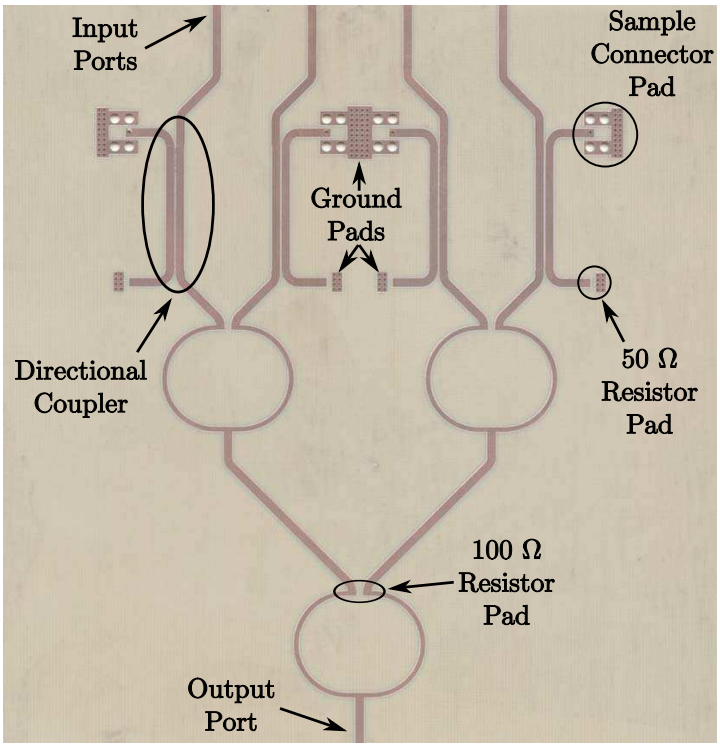

Figure 2.23: Circuit board of the output power combiner and sampling network. Labels for the main composing parts have been superimposed.

2.5.2.4. Results

The design process that has been described was carried out using method of moments simulations. In the following, the simulations of the the different parameters of interest, are compared with measurements of the prototype that has been manufactured for the experimental validation of the design.

The impedance matching of the input ports can be evaluated through the S_{22} to S_{55} parameters, presented in Figure 2.24. The network exceedingly covers the intermediate frequency band with a return loss greater than 10 dB.

The combination loss of the network can be assessed through the parameters S_{i1}, shown in Figure 2.25(a). The variation of the simulated and measured parameters follow a similar trend, although with approximately a 1 dB offset. The coefficients for the different ports vary in a range of about 0.2 dB, which is negligible. The total combination loss of the network, including the sampling, is under 7.35 dB.

To verify that the input signals are combined in phase, the phase of the same S_{i1} parameters is shown in Figure 2.25(b). In this case, the simulated results are

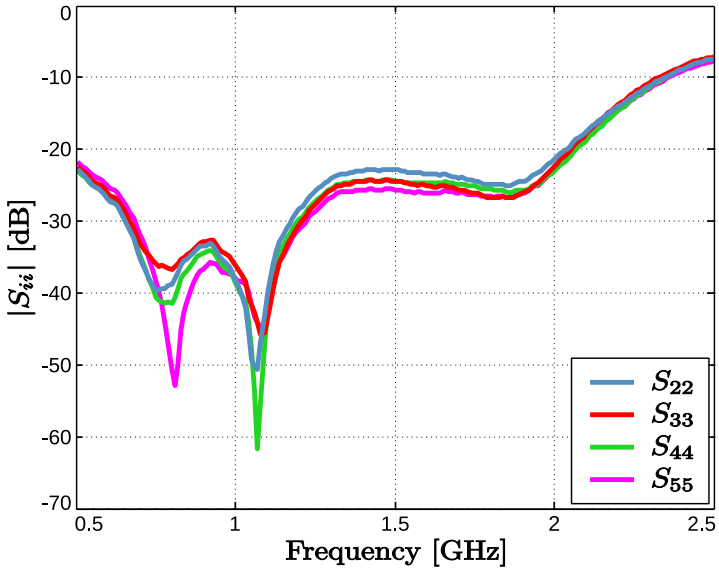

Figure 2.24: Measured reflection coefficients at the ports of the output power combiner.

not included, since the connectors were not modelled in the simulations. The maximum phase deviation observed is about 2°, which is perfectly acceptable.

The fraction of power extracted from each input and delivered to the corresponding sample port is given by the transmission parameters S_{ij}, measured from each input port to its associated sample port, which are plotted in Figure 2.26(a). The simulation shows a transmission coefficient of -13 dB, which was the design goal, whereas the measured values are about 1.5 dB below, showing reasonably similar results for all the branches (the maximum variation is about 0.5 dB).

As has been explained, the sample ports are used to monitor the phase shift introduced by the individual IL3HSOM circuits. Hence, an important design requirement is that the phase shift introduced between each input and its sample port is the same. This feature can be verified through the phase of the same S_{ij} parameters shown in Figure 2.26(b). As required, the maximum variation is about 4°.

Finally, the isolation between non-consecutive input ports is under -35 dB, as shown in Figure 2.27. Although the isolation between consecutive ports could not be measured, it is expected to be sufficiently high, in accordance with the simulations.

Thus, the network effectively satisfies both the electrical and the mechanical specifications imposed, which validates it for its inclusion in the complete antenna array prototype.

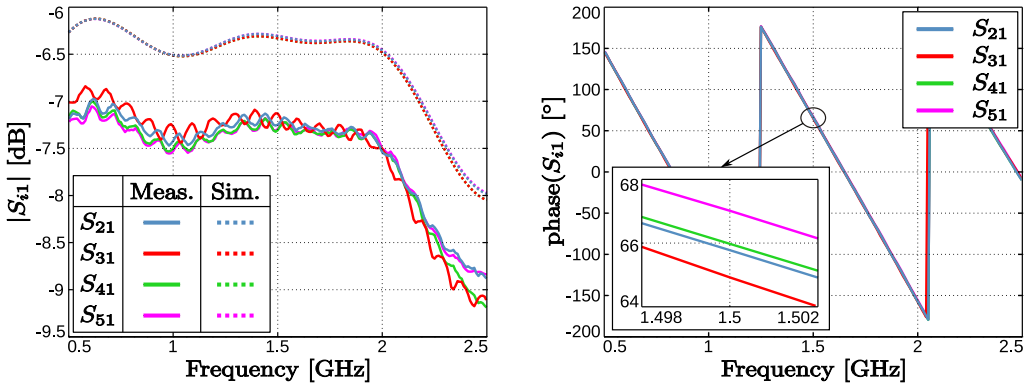

(a) (b)

Figure 2.25: Transmission coefficients measured from each of the inputs to the output port of the output power combiner: (a) Magnitude (b) Phase.

2.6. Global Frequency Response

In previous sections, the fundamental features of the injection locked harmonic self oscillating mixers have been studied, evaluating the feasibility of using these circuits to control an active phased antenna array.

During the design process of the antenna array, the different parameters were adjusted to meet the specifications imposed in terms of side lobe level and beam scanning angle. Nonetheless, all the analyses were performed at the centre frequency of the input band $f_{in_c} = 11.25$ GHz, disregarding the behaviour at other frequencies.

The present section is devoted to the analysis of the frequency response of the system. Initially, the isolated behaviour of the antenna array is addressed, and the frequency response of the injection locked harmonic self oscillating mixers is particularised for the case of a progressive phase shift distribution. The overall frequency response of the system will be subsequently analysed, evaluating the influence of the operating regime of the circuits on the global performance.

2.6.1. Antenna Array

As has been justified in Section 2.4.2, due to the difference in propagation distance, an incident wave impinging with an angle θ, on a linear antenna array with uniformly distributed elements, will be received by consecutive elements with a phase shift given by

$$\Delta\phi_p = kd\sin\theta. \tag{2.13}$$

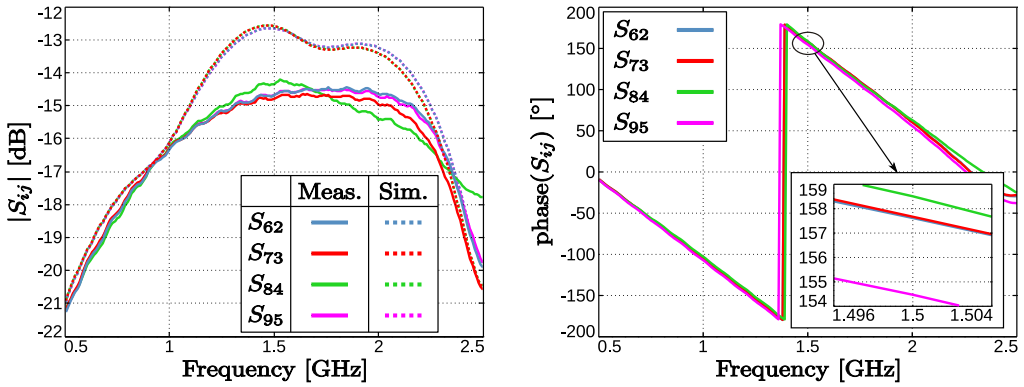

(a) (b)

Figure 2.26: Transmission coefficients measured from each of the input ports to its corresponding sample port: (a) Magnitude (b) Phase.

When using a progressive phase shift distribution, a phase shift α, such that $\Delta\phi_p + \alpha = 0$, is introduced between the individual contributions prior to combining them, thus creating a maximum of the radiation pattern in the direction given by θ.

In (2.13), the wave number $k = \frac{2\pi}{\lambda}$, is directly dependent on frequency through the speed of light c, as follows

$$\Delta\phi_p = \frac{2\pi}{\lambda} d \sin\theta = \frac{2\pi}{c} f d \sin\theta. \tag{2.14}$$

The incident signal is received in consecutive elements of the array with a phase shift $\Delta\phi_p$, which is linearly dependent on frequency. Consequently, in order to keep the maximum of the radiation pattern of the array at the same angle θ_m, throughout the input frequency band, a phase distribution with the opposite variation trend should be imposed, such that $\Delta\phi_p(f) + \alpha(f) = 0$.

Conversely, if the required phase shift is calculated at a single frequency (at the centre of the band, for instance) and imposed throughout the band, the maximum of the radiation pattern will shift with frequency, giving rise to a phenomenon known as *frequency scanning* [14].

Therefore, according to (2.14), the progressive phase shift required for the main beam to be pointed at an angle θ_{m_c} at the centre of the band f_c will be

$$\alpha = -\frac{2\pi}{c} f_c d \sin\theta_{m_c}. \tag{2.15}$$

Solving (2.14) for θ_m, and substituting the progressive phase shift calculated at the centre of the band (2.15), the angle of the main beam as a function of

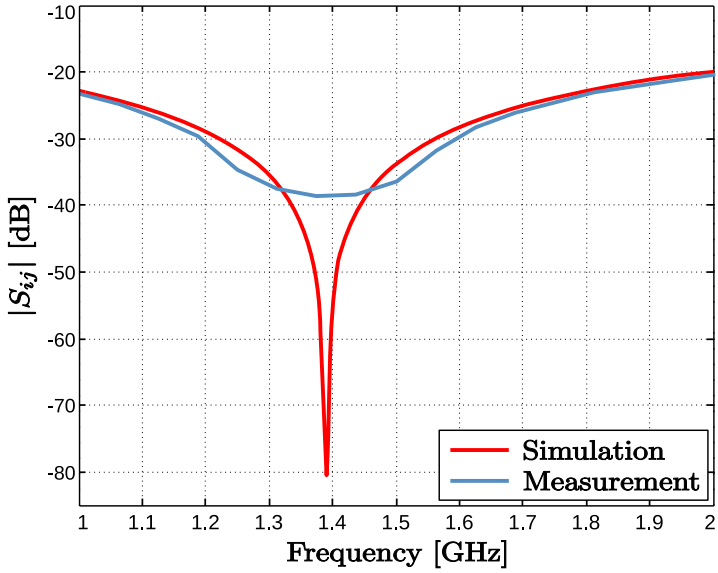

Figure 2.27: Measured isolation between non-consecutive input ports of the output power combiner.

frequency can be obtained:

$$\theta_m(f) = \arcsin\left(-\frac{\alpha}{2\pi f d}c\right) = \arcsin\left(\frac{f_c}{f}\sin\theta_{m_c}\right). \tag{2.16}$$

For certain sets of values of f, f_c and θ_{m_c}, the argument of the inverse sine function in (2.16) is greater than 1, and therefore it cannot be solved in $\mathbb{R}$. This is because (2.16) was derived in Section 2.4.2 under the assumption that the maximum of the array factor (2.11), takes place when the argument of the exponential terms cancels out. However, for specific values of the parameters, the exponent never becomes zero, in which case, the maximum of (2.11) is reached for a different value of the exponents.

Nevertheless, for the particular cases addressed in this work, with relatively small scanning angles of the main lobe θ_m, and restricting the analyses to the relatively narrow input band, a real solution will always exist for (2.16).

The deviation of the main beam with regard to the angle imposed at the centre of the band $\Delta\theta_m(f) = \theta_m(f) - \theta_{m_c}$, is represented versus frequency in Figure 2.28. According to (2.16), the variation of the scanning angle $\theta_m(f)$ with frequency increases with the angle imposed at the centre of the band θ_{m_c}. Hence, the deviation has been represented for the maximum angle of the main beam that can be achieved with the array that has been designed $\theta_{m_c} = 23.5°$.

The frequency scanning observed $\Delta\theta_m(f)$, presents a nearly linear behaviour, crossing through zero at the centre of the band and progressively increasing

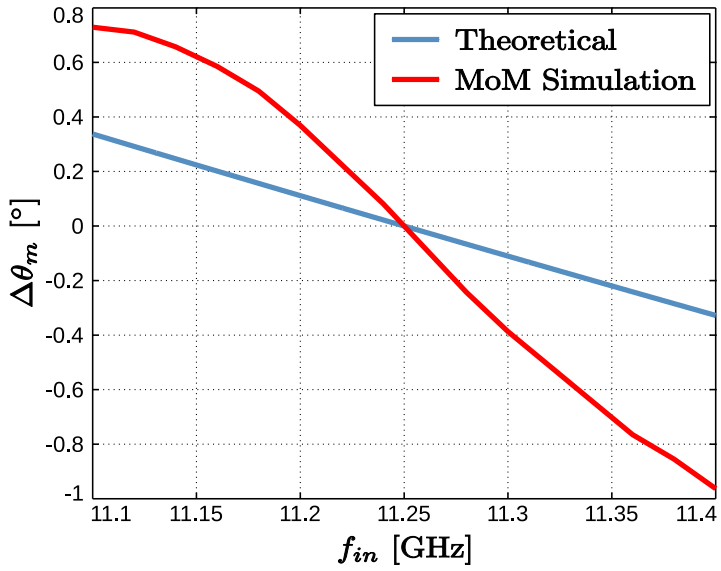

Figure 2.28: Deviation of the main beam $\Delta\theta_m$ with regard to the angle imposed at the centre of the band, as a function of frequency.

towards the ends, where it reaches a maximum deviation of about 0.35°, in absolute value.

As has been discussed in Section 2.4.2, the array factor approach to modelling antenna array, on which the foregoing analysis is based, relies on several simplifying assumptions that may lead to certain inaccuracies in the results. Thus, the frequency performance of the array has been analysed using method of moments electromagnetic simulations for the same steering angle at the centre of the band, $\theta_{m_c} = 23.5°$. A wider variation with frequency (of nearly 2°) can be observed in Figure 2.28.

2.6.2. Injection Locked 3rd Harmonic Self Oscillating Mixers

The frequency response of the IL3HSOM circuits has been described, from a general standpoint, in Section 2.3.2. However, to precisely evaluate its influence on the overall behaviour of the active antenna array topology, this response must be particularised for that scenario.

Firstly, depending on the desired offset angle of the main beam θ_m, a progressive phase shift α, must be introduced between consecutive elements of the array. The imposition of that progressive phase shift distribution throughout the array requires, in general, a different absolute phase shift $\Delta\phi$ for each circuit, which is associated with a different control voltage, a different operation point and thus, a different frequency response.

Although there exist infinitely many absolute phase shift distributions that produce the same progressive phase shift, in this work, a progressive phase shift α, will be introduced through an absolute phase shift distribution $\Delta\phi_i$, $i \in [1,4]$, of the IL3HSOM circuits given by $\left[-\frac{3\alpha}{2}, -\frac{\alpha}{2}, \frac{\alpha}{2}, \frac{3\alpha}{2}\right]$.

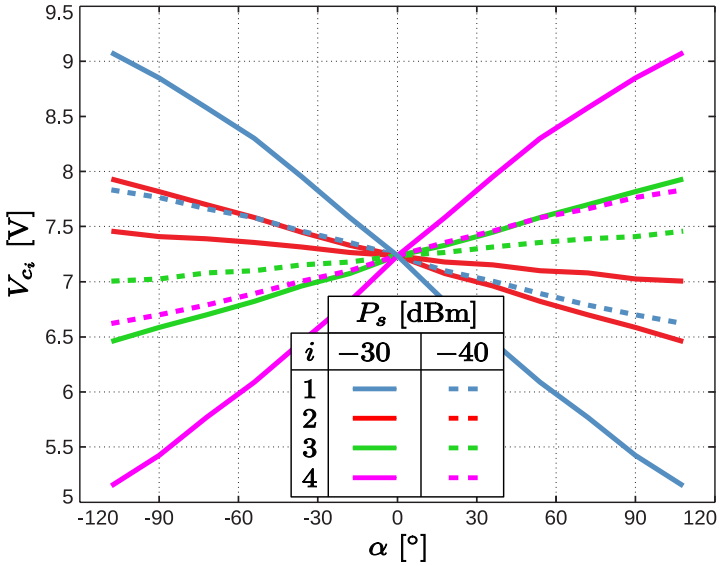

Figure 2.29: Control voltage required for the IL3HSOM circuits, as a function of the intended progressive phase shift value α.

In Figure 2.29, the control voltages for the IL3HSOM circuits V_{c_i}, $i \in [1,4]$, is presented as a function of the progressive phase shift α, for two values of the synchronisation power level. As could be concluded from the phase shift characteristics of the circuit shown in Figure 2.7(b), a wider variation of the control voltages is required for higher values of the synchronisation power.

The control voltages presented in Figure 2.29 have been calculated at the centre frequency $f_{in_c} = 11.25$ GHz. For these control voltages, the variation of the conversion gain and the phase shift for each of the circuits will be analysed throughout the band. This analysis will be performed when imposing the progressive phase shift α, associated with the maximum steering angle of the main beam that can be achieved in the antenna array with a side lobe level better than -10 dB, $\theta_{m_c} = 23.5°$.

The deviation of the conversion gain for the i-th circuit, at the frequency f_{in} for a steering angle of the main beam at the centre of the band θ_{m_c} , with regard to the conversion gain corresponding to a broadside pattern ($\alpha = \theta_{m_c} = 0°$), is defined as

$$DG_{c_i}(f_{in}, \theta_{m_c}) = G_{c_i}(f_{in}, \theta_{m_c}) - G_{c_i}(f_{in}, \theta_{m_c} = 0°), \tag{2.17}$$

where the conversion gains and the deviation are expressed in dB. The gain deviation $DG_{c_i}(f_{in}, \theta_{m_c}, \theta_{m_c})$ for the four circuits and for two values of the synchronisation power has been plotted in Figure 2.30(a). The variation increases with the synchronisation power level, although it remains under 0.75 dB, in absolute value.

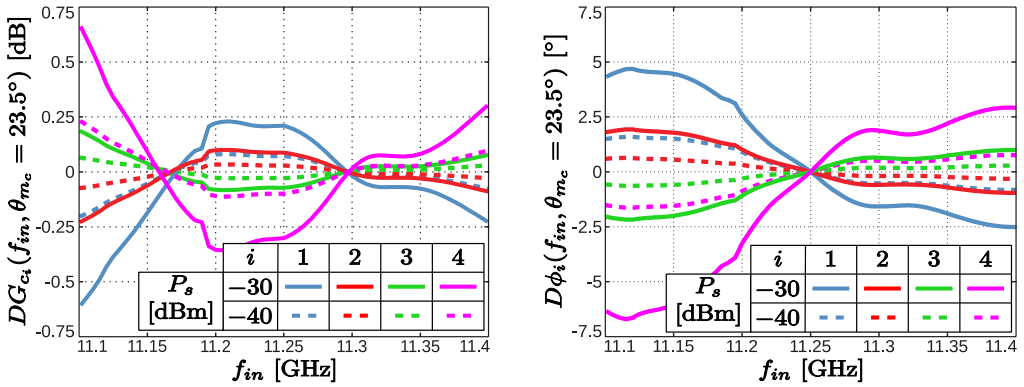

(a) (b)

Figure 2.30: (a) Deviation of the conversion gain of the four HSOM circuits versus frequency, for two power values of the synchronisation signal. (b) Deviation of the phase shift of the four HSOM circuits versus frequency, for two power values of the synchronisation signal.

On the other hand, as was shown in Figure 2.8(b), the phase shift at intermediate frequency presents a steep slope versus frequency that conceals the features of the frequency response. For the sake of clarity, this slope is cancelled out in the definition of the phase shift deviation for the i-th circuit, by subtracting the frequency response of the circuit for a phase shift $\alpha = 0°$, as follows

$$\begin{aligned} D\phi_i(f_{in}, \theta_{m_c}) =& [\Delta\phi_i(f_{in}, \theta_{m_c}) - \Delta\phi_i(f_{in}, \theta_{m_c} = 0°)] \\ & - [\Delta\phi_i(f_{in_c}, \theta_{m_c}) - \Delta\phi_i(f_{in_c}, \theta_{m_c} = 0°). \end{aligned} \tag{2.18}$$

The two terms in the second square brackets are offset constants to impose that the deviation at the centre frequency and for a broadside radiation pattern ($\alpha = \theta_{m_c} = 0$) is zero: $D\phi_i(f_{in_c}, \theta_{m_c} = 0°)$.

The phase shift deviation for a steering angle $\theta_{m_c} = 23.5°$, $D\phi_i(f_{in}, \theta_{m_c} = 23.5°)$, and for two values of the synchronisation power is shown in Figure 2.30(b). The deviation increases with the synchronisation power, nearly reaching 7.5° in absolute value, for $P_s = -30$ dBm.

Consequently, the frequency response of the injection locked harmonic self oscillation mixers presents a wider variation, both in conversion gain and in phase shift, for higher values of the synchronisation power.

2.6.3. Overall Behaviour

According to the analyses that have been carried out thus far, when certain amplitude and phase distributions—constant in frequency—are applied to the signals received by the individual elements of an antenna array, a variation of the steering angle of the main beam known as frequency scanning, is observed.

On the other hand, it has been shown that the conversion gain and phase shift of the IL3HSOM circuits do not present a flat frequency response, but rather they exhibit certain variations throughout the band, which are more apparent for higher values of the synchronisation power.

Nonetheless, solely based on these individual analyses, no assumption can be made as to the overall frequency response of the system. It is obvious that, if the variations of the conversion gain and the phase shift were reduced to negligible values, the frequency scanning phenomenon observed in the isolated antenna would be reproduced, but it is yet to be determined whether the actual frequency response of the circuits will aggravate, or rather mitigate, this error.

Hence, in order to evaluate the overall behaviour of the system, as well as to determine the operation point that minimises the frequency scanning, the response of the complete antenna array topology is studied next.

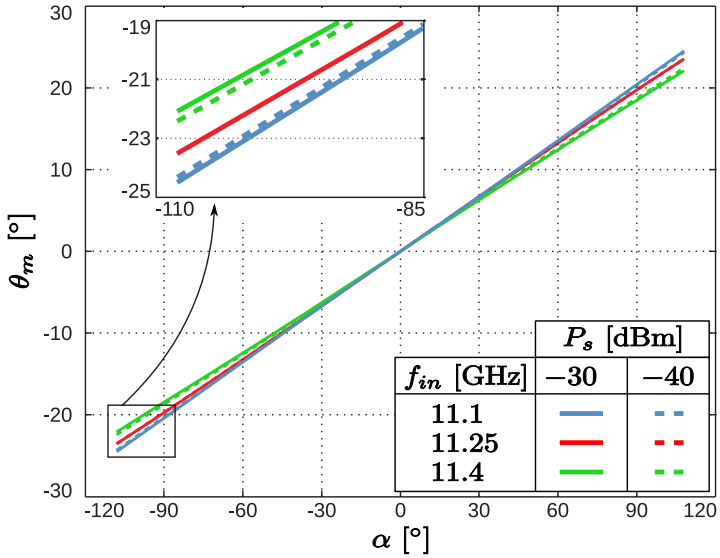

Figure 2.31: Steering angle of the main beam evaluated at the centre and at both ends of the input frequency band, as a function of the progressive phase shift α, imposed at the centre frequency f_{in_c}.

In Figure 2.31, the steering angle of the main beam θ_m, is represented versus the progressive phase shift α, imposed at the centre frequency $f_{in_c} = 11.25$ GHz.

The simulations have been performed at three frequency points: both ends and the centre of the input frequency band (11.1, 11.25 and 11.4 GHz). The steering angle θ_m shows a nearly linear dependence on α, crossing through zero for $\alpha = 0°$, where all the circuits work at the same operating point, and they thus present identical conversion gain and phase shift at every frequency.

For $\alpha \neq 0°$, a deviation in the steering angle of the main beam is observed at both ends of the input frequency band, which increases with the progressive phase shift applied, in such a way that, for the lower frequency, the main beam shifts towards greater angles in absolute value whereas, at the upper frequency, it shifts towards smaller absolute angles.

With regard to the synchronisation power level P_s, a greater deviation is obtained for $P_s = -40$ dBm, while for $P_s = -30$ dBm, the deviation is slightly smaller at those frequency points.

In order to gain an insight into the frequency performance of the system, the simulations must be performed at more frequency points, distributed throughout the input band. Inasmuch as the simulations that have been performed thus far, both of the isolated antenna array and of the complete system at the ends of the band, agree in predicting that the deviation of the steering angle with frequency increases with the steering angle imposed at the centre of the band, the simulations will henceforth be carried out for $\theta_{m_c} = 23.5°$.

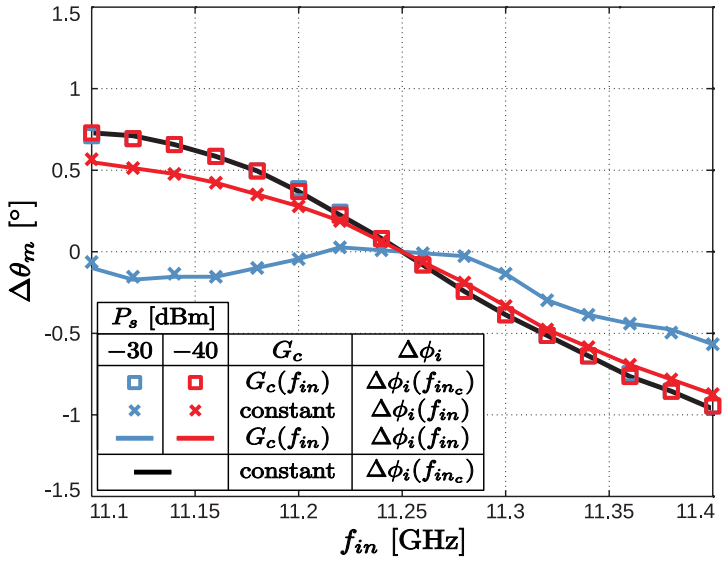

Figure 2.32: Overall deviation of the main beam considering the intrinsic frequency scanning of the antenna array and the conversion gain and phase shift frequency response of the HSOM circuits (both separately and jointly).

The results of multiple simulations have been plotted together in Figure 2.32, for ease of comparison. Moreover, for convenience, the frequency scanning corresponding to the isolated antenna array, when both a gain and a phase shift distribution constant in frequency are applied, that was shown in Figure 2.28, has also been represented as a reference.

Starting from the case with both a conversion gain and a phase shift distribution with a flat frequency response are applied (black trace), the actual frequency responses that have been calculated for the IL3HSOM circuits, are introduced separately in terms of conversion gain and phase shift.

Considering the phase shift distribution flat in frequency and introducing the real values of the conversion gain (square markers, red for $P_s = -40$ dBm and blue for $P_s = -30$ dBm), the behaviour is practically indistinguishable from the reference, for both power levels.

Nevertheless, when assuming a constant conversion gain and taking into account the calculated values for the frequency response of the the phase shift distribution, a reduction of the frequency scanning is observed throughtout the band for $P_s = -40$ dBm. Furthermore, a significant mitigation of the frequency scanning $\Delta\theta_m(f_{in})$, which is over 75% througtout two thirds of the input frequency band, has been attained for $P_s = -30$ dBm. Once again, the results barely change when incorporating the calculated frequency response of the consversion gain (note the small value of the variation).

As a conclusion, taking advantage of the fact that the frequency response of the injection locked harmonic self oscillating mixers tends to compensate for the frequency scanning phenomenon, which is intrinsic to antenna arrays, the overall performance of the system can be improved with regard to an antenna array driven by circuits with an ideal (flat) frequency response. Furthermore, the adequate choice of the synchronisation power level enables a significant reduction of this effect.

2.7. Experimental Results

Once the different parts that compose the active antenna array topology based on injection locked harmonic self oscillating mixers have been designed, analysed and experimentally validated separately, they can be put together in a prototype of the complete system.

This section is focused on the development of the prototype and on the obtention of experimental results to evaluate the practical performance of the system.

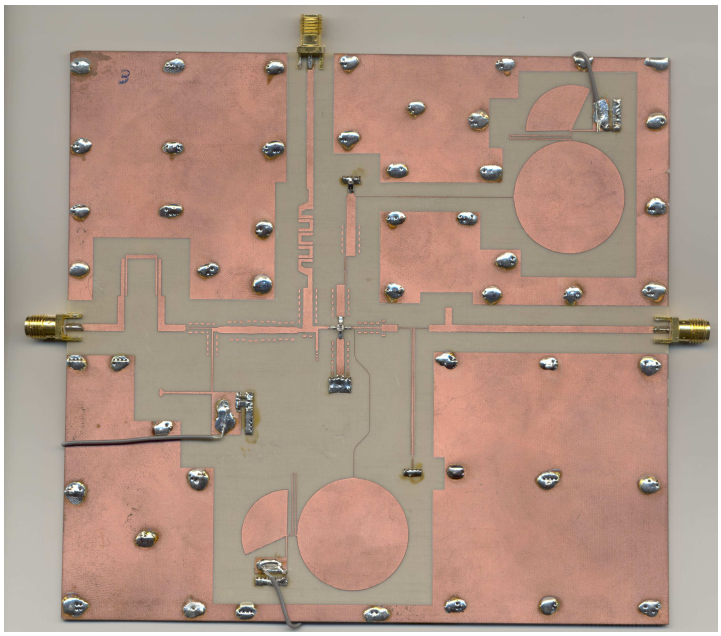

Figure 2.33: Image of one of the manufactured harmonic self oscillating mixers.

2.7.1. Prototype Assembly

The composing blocks of the active antenna array based on injection locked 3^{rd} harmonic self oscillating mixers were schematically outlined in Figure 2.4.

According to the block diagram shown in Figure 2.4, the active antenna array topology is operated by four independent injection locked 3^{rd} harmonic self oscillating mixers, like the one presented in Figure 2.33. Three connectors have been installed at the edges of the circuit board in order to introduce the synchronisation and input RF signals (left hand and upper sides, respectively), as well as to extract the downconverted output at intermediate frequency (right hand side).

A prototype of the four element antenna array has been manufactured, as shown in Figure 2.34(a).The synchronisation signal produced by an external generator is delivered, with equal power level and phase, through the synchronisation power divider that has been described, shown in Figure 2.34(b).

The sampling network that must extract a small fraction of the output signal of each of the HSOM circuits prior to combining them has been integrated with the output combiner, leading to the prototype presented in Figure 2.35(a). The sample ports are located on the opposite side of the board, as shown in Figure 2.35(b).

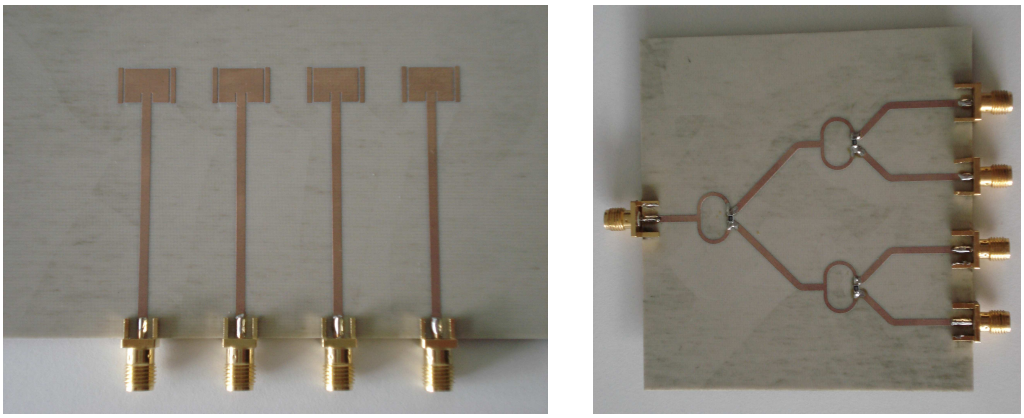

(a) (b)

Figure 2.34: (a) Prototype of the four element microstrip antenna array. (b) Synchronisation power divider.

The aforementioned functional blocks have been implemented in separate circuit boards, conveniently provided with SMA end launchers, which enable the circuit interconnection. The prototype is thus assembled using SMA plug-plug straight adaptors.

In order to limit the mechanical stress on the connectors and to enable the appropriate suspension of the prototype in the anechoic chamber, a tailor-made wooden support structure has been fabricated. An image of the system prototype fitted into the support structure and mounted on the azimuthal positioner of the anechoic chamber is shown in Figure 2.36.

A closer image of the prototype is shown in Figure 2.37, where the main composing parts are indicated.

2.7.2. Measurement Set-up

For the experimental characterisation of the complete system, the measurement set-up represented schematically in Figure 2.38 has been employed.

The fundamental equipment and accessories that compose this set-up are briefly described in the following:

- ***DC Power Supplies Hameg HM7044 and HM7042-5:*** In order to control the three DC bias signals of each of the four HSOM circuits independently, 12 separate power supply channels are required. The ammeters of the power sources enable the real time monitoring of the power consumption of the circuits, which is closely related to their operating regimes.

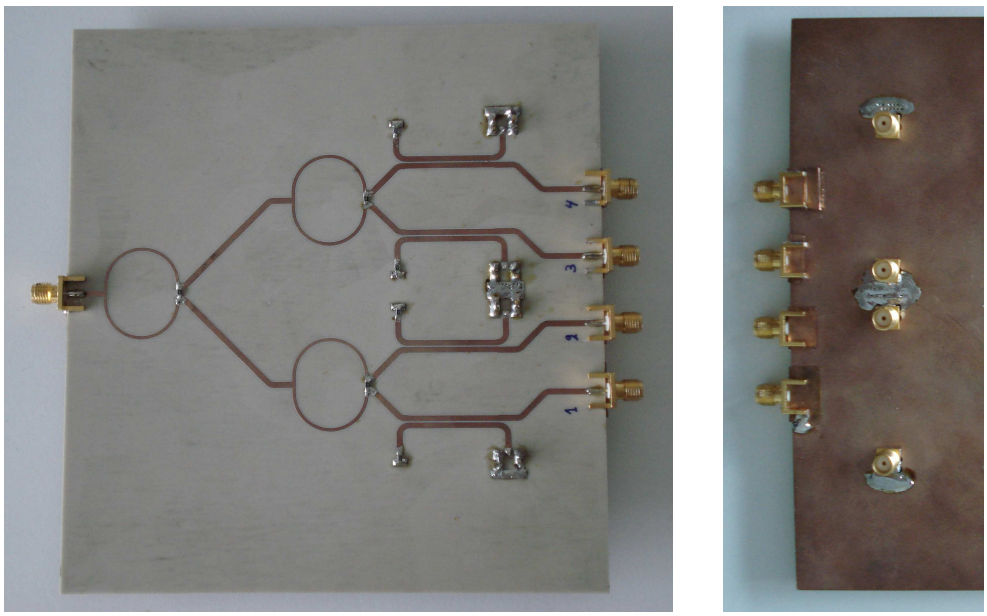

(a) (b)

Figure 2.35: Prototype of the output power combining and sampling network. (a) Upper side. (b) Lower side: sample connectors.

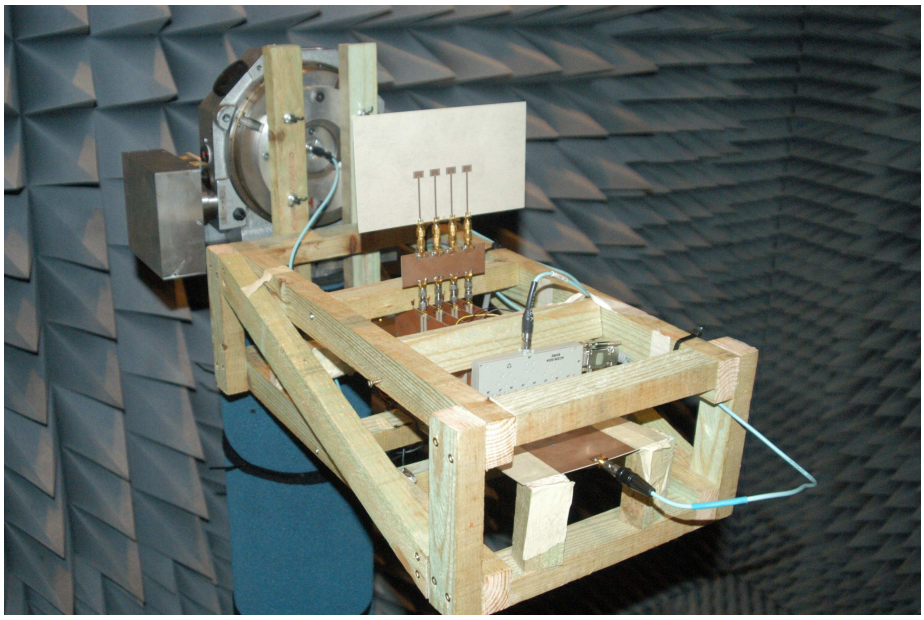

Figure 2.36: Prototype of the complete receiving active antenna array mounted on the rotary platform of the anechoic chamber.

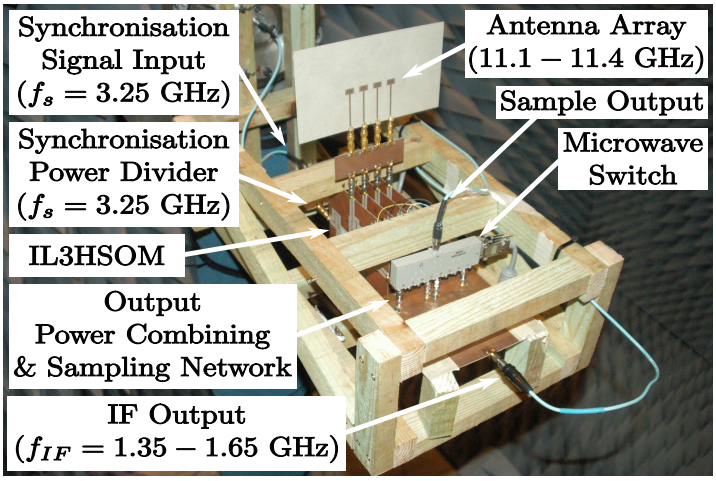

Figure 2.37: Image of the prototype of the active antenna array in which the main composing parts are indicated.

- ***Microwave Signal Generator Rohde & Schwarz SMR40:*** This generator produces the synchronisation signal at $f_s = 3.25$ GHz for the circuits. A second generator produces the RF signal in the input frequency band (11.1–11.4 GHz). The phase locked loops of all the generation and measurement equipment share a 10 MHz reference signal which sets a common frequency reference.

- ***Microwave Switch ACSW-5034:*** As has been described, the sample ports of the power combining network are multiplexed using this device. Through a digital input, the sample signal that is connected to the output port can be selected.

- ***Vector Signal Analyser Agilent 89600 N8201A–N8221A:*** This device measures the sample signal selected through the switch, determining the relative phase shift and conversion gain introduced by the corresponding HSOM circuit.

- ***Pyramidal Horn Antenna:*** Fed by the second signal generator, this antenna will be used to transmit the test signal in the input frequency band (11.1–11.4 GHz), that will be received by the system.

- ***Spherical Range in Anechoic Chamber:*** In order to minimise the impact of reflections and spurious signals in general, the complete measurement process has been carried out in an anechoic environment.

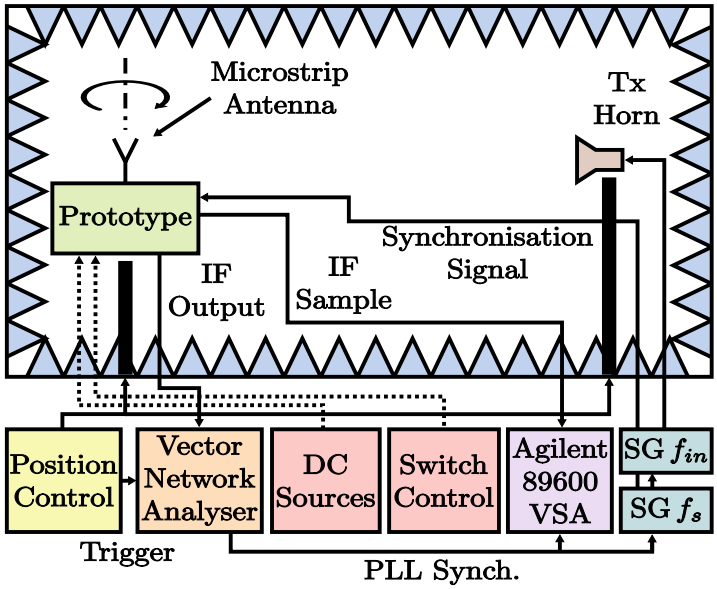

Figure 2.38: Schematic diagram of the measurement set-up in the anechoic chamber.

- ***Vector Network Analyser Rohde & Schwarz ZVK 10 MHz–40 GHz:*** This analyser is part of the equipment of the anechoic chamber and, as such, it is triggered by the control system of the different rotary platforms.

- ***RF Cables:*** In addition to the anechoic chamber semi-rigid cabling, two new flexible coaxial cables were required to connect the prototype to the measurement equipment.

- ***DC wiring:*** For the independent power supply and control of the HSOM circuits, multiple DC circuits are required. A purpose-built VGA cable was used to route these circuits and a VGA jack was installed on the support structure to simplify the connection and disconnection.

2.7.3. System Start-up

Once the prototype has been appropriately connected to ground, the transistors can be biased with the voltages associated with the selected operation point. The gate terminal of the common source topology is initially biased with 0 V, while the drain voltage is progressively increased to about 1.9 V, leading to the onset of an oscillatory regime with a fundamental frequency close to 3.25 GHz. This fundamental frequency can be varied by tuning the varactor bias voltage

V_c. At the desired operation point, about 22 mA will be drawn from the power supply.

As soon as the four circuits are oscillating at similar frequencies, the external synchronisation signal at $f_s = 3.25$ GHz can be introduced. If the fundamental frequencies of the circuits are not close enough to f_s, or if its power level P_s, is low, these frequencies will coexist with f_s giving rise to intermodulation products.

However, by adjusting the varactor bias voltages V_{c_i}, to bring the oscillation frequencies closer to f_s, or by increasing the power level P_s, the circuits will become injection locked.

Under these conditions, the only fundamental component present in the circuits will be f_s, and they will be prepared to downconvert the signal introduced through the input RF port to intermediate frequency, introducing variable phase shifts that can be separately controlled through the varactor bias voltages V_{c_i}.

2.7.4. Coexistence of IL3HSOM Circuits

For the purpose of this work, it has been assumed that the reference signal for all the IL3HSOM circuits is common and independent. Under this assumption, each circuit would preserve the same properties that have been observed in its isolated operation, providing an independent continuous phase shift range exceeding 360°.

Nevertheless, the mutual interaction between practical circuits may lead to significant degradations in their performance. In case the fundamental oscillation of one of the circuits—at the synchronisation frequency f_s—is coupled onto another, the reference signal of the latter would be determined by the vector sum of the external reference and the contribution coupled from the former.

Hence, when the control voltage of a circuit is tuned, the amplitude and phase of its oscillation changes, as does the contribution coupled onto the neighbouring circuits. That coupled contribution will in turn modify the power and phase of the reference signal for these circuits.

The outcome of this effect is twofold. On the one hand, for a given control voltage V_c, the HSOM circuit introduces a fixed phase shift $\Delta\phi$, referred to the synchronisation signal it receives, which is influenced by the coupled contributions. Thus, the actual phase shift introduced by the circuit, with regard to the external unperturbed reference, will be dependent not only on its own control voltage, but also on the phase shift introduced by the neighbouring circuits.

On the other hand, as has been shown in Figure 2.7(b), the response of the HSOM circuit to the control voltage is determined by the reference signal power. For a given control voltage V_c, except for the value corresponding to the intersection of the traces ($\Delta\phi_{IF} = 0$ in Figure 2.7(b)), the variation of the synchronisation power affects the operation of the circuit, to the point that it might even bring it to an unstable region, where it would lose the synchronisation.

Coupled topologies have also been presented in the literature both using oscillators [15], and more complex oscillator based designs [8]. In these solutions, the coupling effects between the circuits are deliberately increased through a purpose-built network, designed to control the output phase of some of the circuits by generating the appropriate reference signal.

In [16], mutually coupled harmonic third oscillating mixers have been used to control a four element antenna array. Through the variation of the varactor bias voltages of the two outer circuits—which are injection locked to an external reference—the progressive phase shift throughout the array can be controlled. In order to minimise the variation of the phase shift with the synchronisation power level on the inner circuits, they are operated at the intersection point of the traces ($\Delta\phi_{IF} = 0$ in Figure 2.7(b)) [17].

This approach allows a reduction in the number of required DC control signals (corresponding to the circuits that are controlled through the reference signal), at the expense of reducing the range of phase distributions that can be obtained, with regard to the case of individually injection locked circuits.

In this work, the individually injection locked topology has been chosen so as to preserve the total flexibility in the phase distributions that can be imposed, whereby each circuit can independently apply any phase shift value within a continuous range of at least 360°.

As has been justified, any mutual coupling between circuits leads to a situation where changes in the control signal of one circuit brings about variations of the output phase of the neighbouring circuits. These variations, whose magnitude will be determined by the power ratio between the injected external reference and the coupled contributions, could be compensated through the joint adjustment of the control voltages of the different circuits.

Nonetheless, this phenomenon gives rise overlapped phase shift ranges in which, while certain phase shift distributions can be achieved with several combinations of control voltages, others become unavailable, resulting in an effective contraction of the usable phase shift ranges [18]. Therefore, the mutual coupling is an utterly detrimental effect that must be kept under control in this type of systems.

For the physical disposition of the HSOM circuits in the manufactured prototype and for the separation between them, the radiative mutual coupling that has been observed is negligible. Hence, any effective coupling can only take place through the antenna array and auxiliary networks.

In fundamental oscillator based topologies, the relatively high output power at the fundamental oscillation frequency generally leads to high coupled components [18], which are difficult to reduce in practice.

Conversely, the architecture of the third harmonic self oscillating mixer strongly limits its vulnerability to this phenomenon. Since both the input RF

signal and the IF output are at different bands, separated from the fundamental oscillation frequency, the fundamental coupling can be severely reduced through filtering, without significantly affecting the desired input and output signals present in the corresponding ports.

Moreover, the purposeful assignment of the input RF and output IF bands of the circuit so as to avoid the harmonic components of the fundamental oscillation frequency Nf_0, $N \in \mathbb{N}$, enables the strong attenuation of these components by means of filtering, which prevents potential harmonic synchronisations from taking place through these ports.

Likewise, the fact that no harmonic component of the fundamental oscillation frequency lies within the input RF band also prevents the potential synchronisation between the input signal and one of these harmonic components $Nf_0 = f_{in_s}$, $N \in \mathbb{N}$, which may result in dysfunctional behaviour.

Although rational synchronisations $Nf_0 = Mf_{in_s}$, $N, M \in \mathbb{N}$, might still occur, unless this feature is deliberately optimised [19], the associated synchronisation ranges are generally extremely narrow and thus impossible to observe in practice, especially for high rational indices N and M.

Hence, owing to the HSOM architecture, the possible mutual coupling between circuits is fundamentally restricted to the synchronisation network.

Consequently, this network must be designed to guarantee sufficiently high isolation levels. However, this is not generally a particularly challenging task since, even if a lossy topology needs to be adopted, the absolute power losses are usually limited, due to the relatively low synchronisation power required by the circuits.

2.7.5. Measurements

The characterisation of the system has been carried in the anechoic chamber, using the measurement set-up that has been described. The receiving antenna array is illuminated with a wave in the input frequency band (11.1–11.4 GHz), with constant power, using a pyramidal horn.

In order to obtain the radiation patterns synthesised by the system, the measurements must be carried out in the far field region of the antenna array which, in this case, starts at a distance of about[2] 0.35 m. The distance between the transmitting horn and the axis of the azimuthal rotary platform is about 5 m, which exceedingly satisfies this condition.

When the circuits are at the selected operating regime and the antenna array is illuminated with the input RF signal, the desired phase shift distribution can

[2]The Fraunhofer region is considered when the following conditions are fulfilled:
$d >> \lambda = 27.03$ mm
$d \geq \frac{2D^2}{\lambda} \approx 350$ mm
$D = 67.4$ mm is the maximum dimension of the antenna array.

be imposed by tuning the varactor bias voltages V_{c_i}, $i \in [1,4]$. By selecting the appropriate input of the sample switch, the output signal of each HSOM circuit can be separately monitored. The phase shift distribution can thus be determined by comparing the phase of the output signal of the different circuits, when they receive the impinging signal in phase. Since this condition is only satisfied[3] when the incidence is perpendicular to the plane of the array ($\theta = 0°$), the phase distribution must be established with the system in that azimuthal position.

2.7.5.1. Radiation Patterns

The radiation patterns that have been measured at $f_{in_c} = 11.25$ GHz, for progressive phase shift distributions corresponding to steering angles $\theta_m = 0, \pm 5, \pm 10, \pm 15, \pm 20, \pm 25°$, are presented in Figure 2.39.

The main lobe of the synthesised radiation pattern can be steered in the desired range, which validates the system for the proposed application. As was pointed out in the design process, for $\theta_m = 25° > 23.5°$, the side lobe level is higher than -10 dB.

The asymmetry that can be observed in the radiation patterns may be justified by the fact that the HSOM circuits are facing one side of the prototype, with the ground plane facing the opposite side. Therefore, when the incoming signal impinges on the circuit side of the prototype, a fraction of the power can be directly coupled onto the circuits, while this effect may be less apparent when it impinges on the ground plane side.

2.7.5.2. Power at Intermediate Frequency

The measured radiation patterns have been presented normalised to simplify the comparison. However, by representing the maximum level received for each steering angle, valuable information about the overall response of the system can also be obtained. The maximum power received at intermediate frequency as a function of the steering angle imposed θ_m, is shown in Figure 2.40, normalised by the maximum power received for $\theta_m = 0°$.

The maximum power measured corresponds to $\theta_m \approx 10°$, and it decreases monotonically when departing from that value, reaching a maximum variation range smaller than 3.5 dB. This behaviour is caused by the radiation pattern of the individual antenna element, together with the deviations in the conversion gain of the circuits in the different operation points.

[3] Although, strictly speaking, the spherical wavefront would reach the different elements of the array with certain phase deviations, these can generally be neglected under far field conditions.

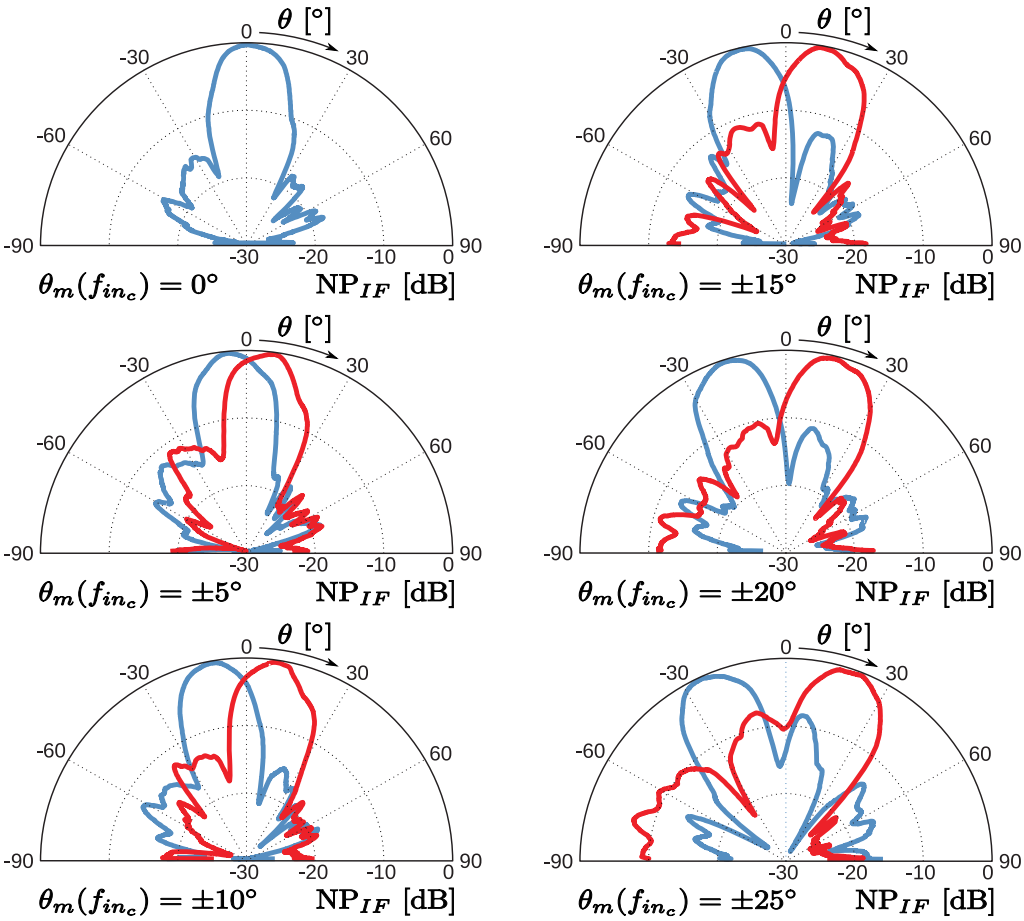

Figure 2.39: Radiation patterns measured at $f_{in_c} = 11.25$ in the anechoic chamber for the steering angles: $\theta_m(f_{in_c}) = 0, \pm 5, \pm 10, \pm 15, \pm 20 \pm 25°$.

2.7.5.3. Frequency Response

In order to experimentally validate the conclusions drawn in Section 2.6.3, regarding the system frequency response, the radiation patterns corresponding to a steering angle imposed at the centre frequency $\theta_m(f_{in_c}) = 23°$, have been measured at the ends of the input frequency band, 11.1 and 11.4 GHz, for two values of the synchronisation power, –40 and –30 dBm. The measurements are compared in Figure 2.41.

As was predicted by the simulations, the main lobe shifts towards greater absolute angles for lower frequencies, and towards smaller angles for greater fre-

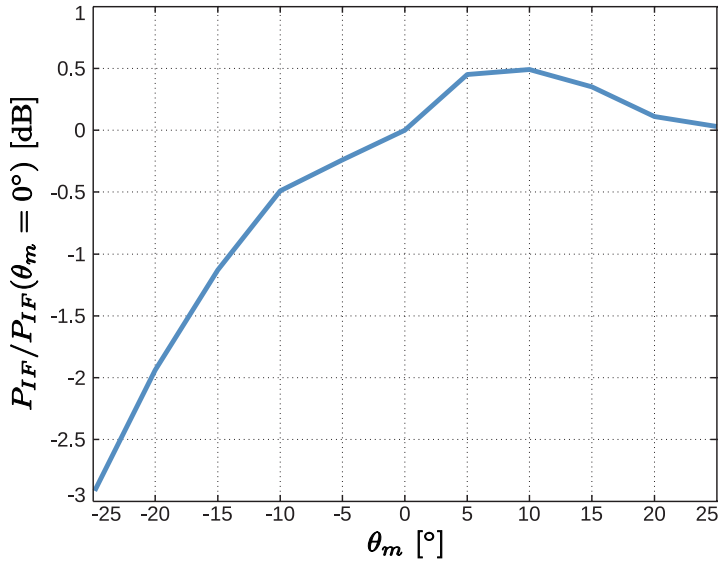

Figure 2.40: Received power at intermediate frequency as a function of the steering angle θ_m, normalised by the power received for $\theta_m = 0°$.

quencies. Furthermore, the deviation observed is clearly smaller for $P_s = -30$ dBm.

Thus, it has been shown that the synchronisation power level has a direct influence on the frequency scanning and how, by the appropriate selection of this level, the intrinsic frequency scanning of the antenna array can be mitigated.

2.8. Conclusions

A receiving four element linear antenna array based on injection locked third harmonic self oscillating mixers has been presented. It has been shown that the multifunctional nature of the IL3HSOM circuits, whereby the downconversion and continuous range phase shifting operations can be integrated with the local oscillator generation, makes them an advantageous choice for the control of receiving antenna array systems. Furthermore, as opposed to other oscillator based topologies, the architecture of the IL3HSOM circuit enables the efficient reduction of the coupling phenomena between adjacent circuits through filtering, without affecting the IF output power of the antenna array.

The frequency response of the complete antenna array system has been evaluated. Through the appropriate selection of the synchronisation power level of the IL3HSOM circuits, the intrinsic frequency scanning effect of the antenna array can be significantly mitigated throughout the input frequency band.

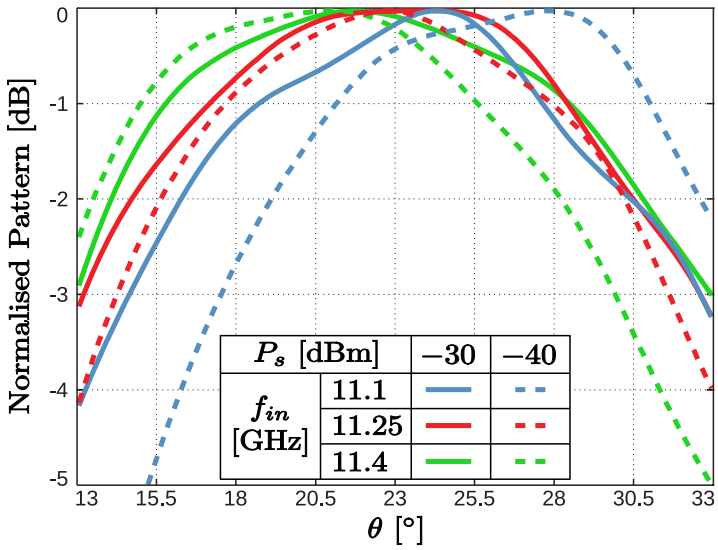

Figure 2.41: Magnification of the main lobe at the ends of the input frequency band, for a steering angle imposed at the centre frequency $\theta_m(f_{in_c}) = 23°$.

The performance of the manufactured prototype of the receiving antenna array topology has been experimentally assessed through measurements in the anechoic chamber. A continuous beam scanning range between -23.5 and $23.5°$ has been attained at the central frequency $f_{in_c} = 11.25$ GHz. The reduction of the frequency scanning effect through the proper selection of the synchronisation power level has also been verified.

Bibliography

[1] K.D. Stephan. Inter-injection-locked oscillators for power combining and phased arrays. *Microwave Theory and Techniques, IEEE Transactions on*, 34(10):1017 – 1025, oct 1986.

[2] A.S. Daryoush, M. Francisco, R. Saedi, D. Polifko, and R. Kunath. Phase control of optically injection locked oscillators for phased arrays. In *Microwave Symposium Digest, 1990., IEEE MTT-S International*, pages 1247 –1250 vol.3, may 1990.

[3] R.J. Pogorzelski. A 5-by-5 element coupled oscillator-based phased array. *Antennas and Propagation, IEEE Transactions on*, 53(4):1337 – 1345, april 2005.

[4] Jinjin Shen and L.W. Pearson. A design for a two-dimensional coupled oscillator beam-steering antenna array. *Antennas and Wireless Propagation Letters, IEEE*, 2(1):360 –362, 2003.

[5] Shih-Chieh Yen and Tah-Hsiung Chu. A beam-scanning and polarization-agile antenna array using mutually coupled oscillating doublers. *IEEE Trans. Antennas Propagat.*, 53(12):4051–4057, Dec. 2005.

[6] X. Zhang and A.S. Daryoush. Full 360 degrees phase shifting of injection-locked oscillators. *Microwave and Guided Wave Letters, IEEE*, 3(1):14 –16, jan. 1993.

[7] I.L. Morrow, P.S. Hall, and J.R. James. Measurement and modeling of a microwave active-patch phased array for wide-angle scanning. *Antennas and Propagation, IEEE Transactions on*, 45(2):297 –304, feb 1997.

[8] Shih-Chieh Yen and Tah-Hsiung Chu. A beam-scanning and polarization-agile antenna array using mutually coupled oscillating doublers. *Antennas and Propagation, IEEE Transactions on*, 53(12):4051 – 4057, dec. 2005.

[9] Samuel Ver Hoeye, Luis Fernando Herrán, Miguel Fernández, and Fernando Las Heras. Design and analysis of a microwave large-range variable phase-shifter based on an injection-locked harmonic self-oscillating mixer. *IEEE Microwave Wireless Compon. Lett.*, 16(6):342–344, June 2006.

[10] Samuel Ver Hoeye, Almudena Suárez, and Sergio Sancho. Analysis of noise effects on the nonlinear dynamics of synchronized oscillators. *Microwave and Wireless Components Letters, IEEE*, 11(9):376–378, Sep 2001.

[11] M. Fernandez, S. Ver Hoeye, L.F. Herran, and Fernando Las Heras. Nonlinear optimization of wide-band harmonic self-oscillating mixers. *Microwave and Wireless Components Letters, IEEE*, 18(5):347–349, May 2008.

[12] Constantine A. Balanis. *Antenna Theory: Analysis and Design*. John Wiley & Sons, Inc., New York, 1982.

[13] G. M. Pozar. *Microwave Engineering*. Wiley, 2005.

[14] A. Ishimaru and H.-S. Tuan. Theory of frequency scanning of antennas. *Antennas and Propagation, IRE Transactions on*, 10(2):144–150, March 1962.

[15] P. Liao and R.A. York. A new phase-shifterless beam-scanning technique using arrays of coupled oscillators. *Microwave Theory and Techniques, IEEE Transactions on*, 41(10):1810 –1815, oct 1993.

[16] L.F. Herran, S. Ver Hoeye, C. Vazquez, M. Fernandez, and F. Las-Heras. A receiving phased array antenna topology based on mutually coupled harmonic self-oscillating mixers. In *Antennas and Propagation Society International Symposium, 2009. APSURSI '09. IEEE*, pages 1 –4, june 2009.

[17] L.F. Herran, S. Ver Hoeye, M. Fernandez, C. Vazquez, and F. Las Heras. Analysis of phase distribution errors in mutually coupled harmonic self-oscillating mixers. *Microwave Theory and Techniques, IEEE Transactions on*, 57(12):2853 –2861, dec. 2009.

[18] C. Vazquez, S. Ver Hoeye, M. Fernandez, L.F. Herran, and F. Las Heras. Analysis of the performance of injection locked oscillators in a data transmitting polarisation agile antenna application. *Progress in Electromagnetics Research Letters*, 12:1 – 10, 2009.

[19] M. Fernandez Garcia, S. Ver Hoeye, C. Vazquez, G.R. Hotopan, R. Camblor, and F. Las Heras. Analysis of the locking range of rationally synchronized oscillators with high reference signal power. *Microwave Theory and Techniques, IEEE Transactions on*, 60(8):2494 –2504, aug. 2012.

Chapter 3

Receiving Polarisation Agile Active Antenna based on Injection Locked Third Harmonic Self Oscillating Mixers

Contents

3.1. Introduction

Reconfigurable antennas have become widespread in recent years, owing to their capability to dynamically adjust some of their properties to the requirements of each particular scenario. In this context, polarisation agility is an interesting feature for an antenna, since it simplifies the implementation of frequency reuse techniques—which can nearly double the channel capacity—and allows the polarisation matching between transmitter and receiver, minimising the associated link losses.

A wide variety of works on polarisation agile antennas have been presented in the literature. Some passive topologies enable the selection of a discrete number of polarisation states by altering the antenna layout through solid state [1; 2], or piezoelectric [3] switches. Others implement a continuous range of polarisation tuning by attaching varactor loads to the radiating patch [4].

Most of the active topologies available in the literature rely on feeding two orthogonal linearly polarised radiating modes of the antenna with the same original signal, conveniently modified through phase shifting circuitry, in order to provide the polarisation tuning capability. As has been commented, phase shifting solutions based on a single oscillator circuits injection locked at the first harmonic component of the oscillation, enable a theoretical phase shift range limited to 180°. This phase shift range can be doubled by feeding each of the radiating modes with an independent oscillator [5], although the appearance of coupling effects between the circuit may lead to severe reductions of the practically usable phase shift ranges [6]. Mutually coupled topologies maintain the same 180° theoretical phase shift range, which can be doubled, as in [7], by extracting the second harmonic component of the oscillation.

With regard to receiving topologies, as has been discussed in detail in Chapter 2, the phase shifting functionality can be attained through an Injection Locked 3^{rd} Harmonic Self Oscillating Mixer (IL3HSOM), in which the output signal is generated through mixing the input signal at frequency f_{in}, with the third harmonic component at frequency $3f_0$ of the HSOM self oscillation fundamental frequency f_0. As a result of this operation, a downconverted signal at $f_{IF} = f_{in} - 3f_0$ is obtained in a single stage, with the desired phase shift within a practically usable range of at least 360°.

In this chapter, a receiving polarisation agile microstrip antenna based on the IL3HSOM circuit topology is presented, enabling the polarisation tuning within

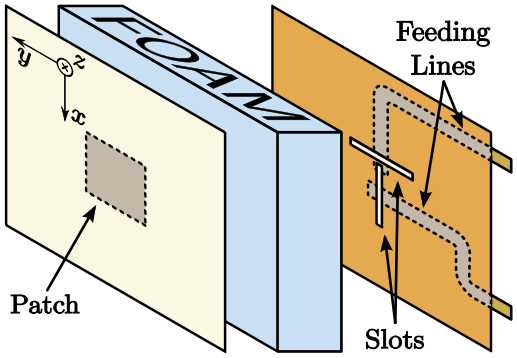

Figure 3.1: Schematic diagram of the two port aperture coupled antenna with dual polarisation.

a continuous range, comprising two orthogonal linear polarisations and both left hand and right hand circular polarisation (LHCP and RHCP). Additionally, another two linear polarisations might be produced by alternatively activating one circuit at a time. However, these are not considered in this work since the received power would be halved, as it would be with any other of the available polarisations.

3.1.1. Two Port Dual Polarisation Microstrip Antenna

The polarisation agile active antenna solution addressed in the present chapter was developed in collaboration with Dr. Germán León [8], who performed the design of the two port microstrip antenna with dual polarisation that will be employed in the system. Therefore, this antenna topology—whose design has not been part of this work—is only briefly described in this introductory section, for completeness.

The antenna, as depicted schematically in Figure 3.1, consists of a square patch designed in the bottom layer of a 0.762 mm thick ARLON 25N substrate, and placed inverted on top of a 2.6 mm thick foam layer ($\epsilon_r = 1.07$ and $\tan\delta = 0.0041$ at 10 GHz). The power received in each of the two orthogonal linearly polarised fundamental modes of the patch is electromagnetically coupled through two perpendicular slots etched on the ground plane of the distribution network, onto the corresponding microstrip transmission line, connected to one of the output ports. These transmission lines are designed to have the necessary length difference, in order for the output signals to be in phase when the incident radiation presents right hand circular polarisation.

A prototype of the antenna was manufactured and measured, showing an impedance matched ($|S_{xx}|, |S_{yy}| < -10$ dB) frequency band from 10.5 to 12

GHz. High isolation levels between the ports ($|S_{xy}| < -30$ dB), are observed throughout the same band.

3.2. System Overview

The topology of the receiving polarisation agile active antenna is presented in Figure 3.2. A two port aperture coupled microstrip antenna, receives two orthogonal linearly polarised fundamental modes of the incident electromagnetic wave, in the band $f_{in} = 11.15 - 11.35$ GHz. The mode with linear polarisation along the x axis is coupled onto the output port labelled as *port* x, while its counterpart with linear polarisation along the y axis, is delivered through *port* y.

These output ports are connected to the input RF ports of two third harmonic self oscillating mixers, injection locked to an external signal of power P_s, frequency $f_s = 3.25$ GHz and phase ϕ_s, through a Wilkinson power divider, providing equal power and phase in both branches.

As has been described in Chapter 2, the injection locked harmonic self oscillating mixer circuit performs the mixing operation $f_{IF} = f_{in} - 3f_0$, and delivers the conveniently phase shifted and downconverted signal at intermediate frequency $f_{IF} = 1.4 - 1.6$ GHz, to its output port.

The phase shifts introduced by the IL3HSOM circuits at intermediate frequency, with respect to the external phase reference ($\Delta\phi_i = \phi_{IF_i} - \phi_s$, $i \in \{x, y\}$), can be separately controlled through two DC signals, enabling the polarisation tuning capability. Low power samples of the output signals of both circuits are extracted through microstrip directional couplers for phase shift monitoring purposes. The sampled signals are simultaneously measured with two Agilent 89600 Vector Signal Analysers (N8201A - N8221A). The output signal of the polarisation agile antenna is finally obtained through a Wilkinson combiner and measured with the vector network analyser of the anechoic chamber measurement set-up.

In order to prevent detrimental reductions in the phase shift ranges of the IL3HSOM circuits and to assure their independent performance, mutual coupling between them at the harmonic components of the self oscillation frequency, (Nf_0, $N \in \mathbb{N}$), must be avoided. The required isolation levels through the input and output ports are achieved by filtering, taking advantage of the fact that none of these harmonic components falls into either the input or output frequency bands. Mutual coupling through the synchronisation port at the harmonic components (Nf_0, $N = 2, \ldots, 8$) is avoided by the bandpass filter centred at $f_s = f_0$. However, the synchronisation power divider must be designed to feature high isolation levels, so that the synchronisation signal for both circuits is nearly exclusively determined by the external generator.

Except for the fact that two, instead of four, IL3HSOM circuits are employed in the polarisation agile active antenna presented in Figure 3.2, this new system

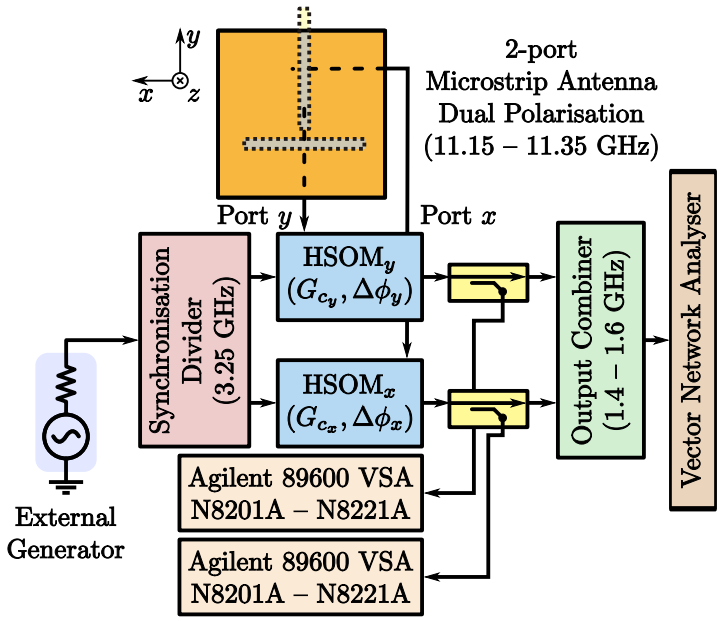

Figure 3.2: Topology of the polarisation agile active antenna based on injection locked third harmonic self oscillating mixers.

is topologically analogous to the active phased antenna array design addressed in Chapter 2. Moreover, the frequency bands involved are compatible, as are the design requirements that have been imposed on the different composing parts.

Therefore, the auxiliary networks that were developed for the antenna array prototype, described in detail in Section 2.5, can be reused here for the polarisation agile active antenna design. Since these networks were designed to drive four IL3HSOM circuits, and only two are employed in this new topology, the remaining ports are terminated with 50 Ω loads.

Consequently, the power losses, both in the synchronisation divider and output combiner, will be about 3 dB higher than the values that could be achieved with purpose-built networks. Nevertheless, inasmuch as this excess of power loss does not affect the operation dynamics of the system, beyond a tantamount reduction of the overall output power and an increment in the external synchronisation power level required, the design and fabrication of new networks is not justified for this first proof of concept prototype.

Similarly, the injection locked third harmonic self oscillating mixer design used in Chapter 2 will also be employed here with certain minor modifications, as will be discussed in a subsequent dedicated section.

3.3. Polarisation Fundamentals

As has been justified, under far field conditions, the electromagnetic wave radiated by an antenna can be locally approximated by a plane wave with the same field amplitude, propagating in the radial direction from the antenna. For plane waves, it can be shown [9] that the electric and magnetic fields are perpendicular to the direction of propagation. Therefore, this type of waves can be described by their electric field, as the magnetic field is perpendicular and proportional to it.

Let $\bar{E}(z,t)$ be the electric field of a plane monochromatic wave propagating along the positive z direction, in an unbounded lossless medium, defined as follows:

$$\vec{E}(z,t) = E_x \cos(\omega t - kz + \alpha_x)\hat{x} + E_y \cos(\omega t - kz + \alpha_y)\hat{y}, \tag{3.1}$$

where $\hat{x}$ and $\hat{y}$ are the unit vectors in the directions x and y, k is the wave number and ω, the angular frequency. The electric field can thus be expressed in terms of two orthogonal components in the directions x and y, characterised by their amplitudes, E_x and E_y, and phases, α_x and α_y, respectively.

The polarisation of the electromagnetic wave defined in (3.1) is determined by the trajectory described by the electric field vector at a fixed point in space in one period, and the sense in which it is traced, as observed along the direction of propagation [10].

Particularising (3.1) for a fixed point $z = z_0$, the electric field can be rewritten as:

$$\vec{E}(z_0,t) = E_x \cos(\omega t + \varphi_x)\hat{x} + E_y \cos(\omega t + \varphi_y)\hat{y}, \tag{3.2}$$

where the constants $\varphi_x = kz_0 + \alpha_x$ and $\varphi_y = kz_0 + \alpha_y$ have been introduced.

Since (3.2) is the parametric equation of an ellipse, the polarisation of the wave is defined in terms of the geometrical parameters of this figure, known as *polarisation ellipse*.

The polarisation of the wave is usually characterised by the *ellipticity* ε, or *axial ratio* AR, defined as the ratio between the major and the minor axes of the ellipse, and by the angle ψ, between the major axis of the ellipse and the x axis, as shown schematically in Figure 3.3.

Due to their practical relevance, two particular cases are usually considered. When the phase difference between the two components of (3.2) is

$$\Delta\varphi = \varphi_y - \varphi_x = \alpha_y - \alpha_x = n\pi, \quad n \in \mathbb{Z}, \tag{3.3}$$

then corresponding ellipse becomes a straight line, and the polarisation is referred to as *linear*.

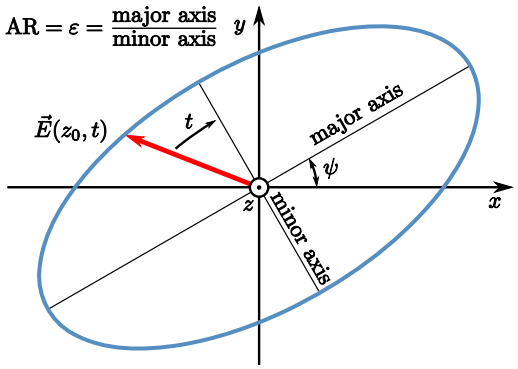

Figure 3.3: Polarisation ellipse and its fundamental parameters.

On the other hand, when both components have identical amplitude, $E_y = E_x$, and the phase difference is an odd multiple of $\pi/2$:

$$\Delta\varphi = \varphi_y - \varphi_x = \alpha_y - \alpha_x = \pm\left(\frac{1}{2} + 2n\right)\pi, \quad n \in \mathbb{Z}, \tag{3.4}$$

the associated ellipse becomes a circumference, and the polarisation is known as *circular*. Depending on the sense of rotation as the wave travels away from the observer, circular polarisation is classified as Left Hand Circular Polarisation (LHCP) for $\Delta\varphi > 0$, and as Right Hand Circular Polarisation (RHCP) for $\Delta\varphi < 0$.

If the polarisation is neither linear nor circular, then it is called *elliptical*. Although, in practice, the polarisation is generally elliptical, by convention, it is considered linear when the axial ratio is very high ($AR > 30$ dB), and circular when it is close to unity ($AR < 3$ dB). This is the criterion that has been adopted for the present work.

The polarisation of a transmitting antenna in a specified direction is defined as the polarisation of the plane wave by which the radiated wave can be locally approximated at a point in that direction within the far field region of the antenna [10].

Analogously, the polarisation of a receiving antenna in a given direction is defined as the polarisation of a plane wave, with fixed power flux density, incident from that direction, which results in maximum available power at the antenna output [10].

3.3.1. Polarisation Tuning

As has been commented, the antenna separates two independent perpendicular linearly polarised components of the incident electromagnetic wave. The

polarisation state of the complete active antenna will be determined by the relative gain and phase shift applied to these components, prior to combining them to obtain the overall antenna output.

Taking advantage of the phase shifting capabilities of the IL3HSOM circuits, the relative phase between the components can be arbitrarily modified, thus controlling the polarisation state.

According to the system topology presented in Figure 3.2, the output signal of the active antenna is given by the combination of the output signals of the IL3HSOM circuits, as follows:

$$V_{out} = g_x V_x + g_y V_y e^{j(\Delta\phi - 90)}, \tag{3.5}$$

where V_y and V_x are voltage phasors that represent the two perpendicular linearly polarised modes received, as they are excited on the antenna patch. The voltage gain terms g_y and g_x are associated with the conversion gain of the circuits, G_{c_y} and G_{c_x}, which are assumed to be equal $G_{c_y} = G_{c_x}$. The phase term $\Delta\phi = \Delta\phi_y - \Delta\phi_x$, represents the relative phase shift between both components, introduced by the IL3HSOM circuits. Note that the antenna introduces an additional 90° phase shift in the V_y component, in order to produce right hand circular polarisation when its output signals are combined in phase.

In fact, the model described by (3.5) is incomplete. On the one hand, the response of the antenna may not be identical for both modes, affecting the polarisation state. Moreover, the responses of both the antenna and the IL3HSOM circuits are frequency dependent, as will be studied in later sections. Nevertheless, this preliminary simplified analysis can still be used to illustrate the approximate polarisation tuning capabilities of the system.

The variation of the polarisation state and the changes in the corresponding polarisation ellipse, versus the relative phase shift $\Delta\phi$, are shown schematically in Figure 3.4, assuming the incident wave propagates in the $+z$ direction. The tuning of the relative phase shift in a 360° range enables the obtention of two orthogonal linear polarisations, together with right hand and left hand circular polarisation.

The polarisation state of the antenna can also be described in terms of the axial ratio, as represented in Figure 3.5, versus the relative phase shift $\Delta\phi$. When both components are combined in phase ($\Delta\phi = 0°$), the axial ratio drops to zero, corresponding to right hand circular polarisation (RHCP). The axial ratio is likewise zero for $\Delta\phi = \pm 180°$, obtaining left hand circular polarisation (LHCP). For $\Delta\phi = 90°$ and $\Delta\phi = -90°$, two linear polarisations ($AR > 30$ dB) are achieved in the $\psi = +45°$ and $\psi = -45°$ orientations respectively (henceforth referred to as LP+ and LP−).

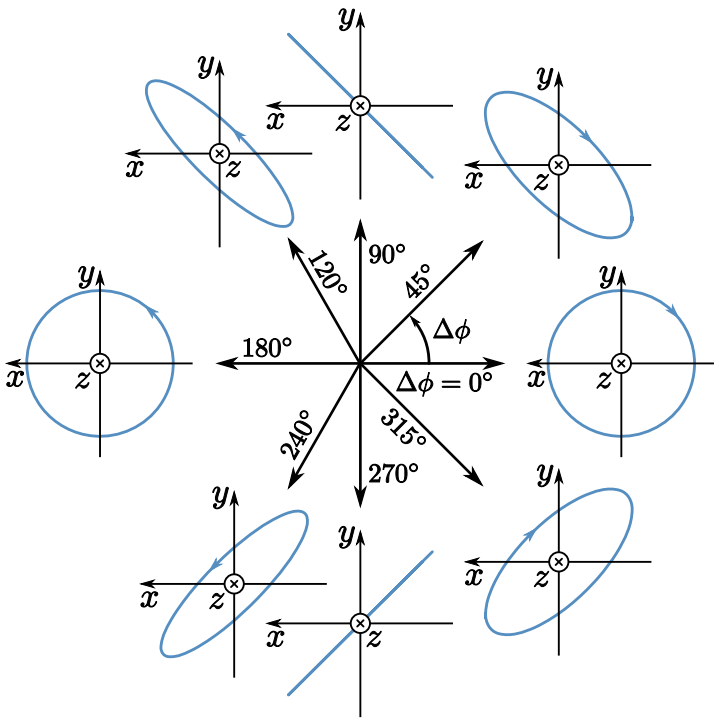

Figure 3.4: Polarisation states associated with different relative phase shifts $\Delta\phi$.

3.3.2. Frequency Response

As has been discussed in Section 2.3.2, even ideal antenna arrays exhibit an intrinsic frequency response, associated with the spatial distribution of the composing individual elements, whereby the steering angle of the main beam varies with frequency.

Nonetheless, in the case of the polarisation agile topology addressed here, since the same microstrip patch is used to receive the two perpendicular linearly polarised components of the incident wave, no frequency dependent phase shift is observed between both components due to propagation effects.

Therefore, as opposed to the antenna array case, if the polarisation agile antenna topology were implemented using a phase shifter with a completely flat frequency response, the polarisation state would in principle be frequency independent.

However, as can be seen in Figure 3.1, the coupling slot and microstrip line associated with either linearly polarised component of the incident wave are not placed symmetrically and therefore, the modifications—in terms of both amplitude and phase—undergone by these components as they are coupled onto their corresponding output ports, may not necessarily be identical, giving rise to dif-

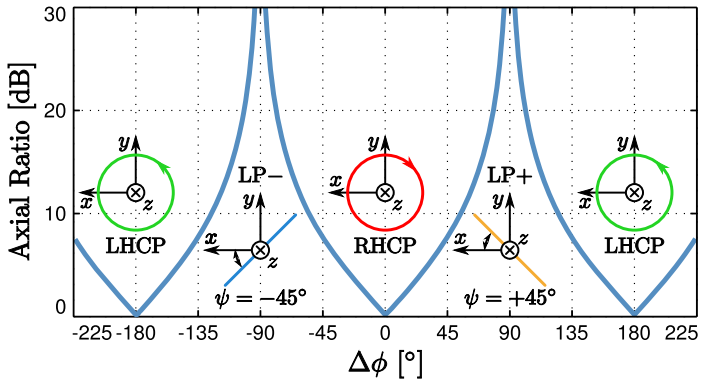

Figure 3.5: Axial ratio as a function of the relative phase shift $\Delta\phi$.

ferent frequency responses. Furthermore, the lengths of the transmission lines corresponding to either component were subsequently adjusted to produce right hand circular polarisation when the output signals are combined in phase, which further affects the frequency response of the antenna.

The polarisation of the antenna is determined by the relative phase shift introduced between the signals associated with the two perpendicular components of the incident wave, prior to combining them. Thus, if the antenna exhibits a different frequency response for either component, these frequency responses must be taken into account, as they will affect the overall polarisation behaviour of the active antenna system.

The two port antenna with dual polarisation has been modelled through electromagnetic MoM simulations. When the antenna is illuminated with an electromagnetic field linearly polarised along the x axis, $\vec{E} = E_x\hat{x}$, the voltage waves delivered to the output ports V_x and V_y, have been obtained, enabling the calculation of the following complex transfer functions:

$$\begin{aligned} T_{xx} &= \frac{V_x}{E_x}, \\ T_{yx} &= \frac{V_y}{E_x}. \end{aligned} \tag{3.6}$$

When the antenna is illuminated with an electromagnetic field linearly polarised along the y axis, the transfer functions T_{xy} and T_{yy}, can be analogously calculated.

To illustrate the behaviour of the antenna, the transfer functions associated with the coupling of either linearly polarised mode onto its corresponding port, T_{xx} and T_{yy}, are compared in Figure 3.6(a), in terms of amplitude and in Figure 3.6(b), in terms of phase.

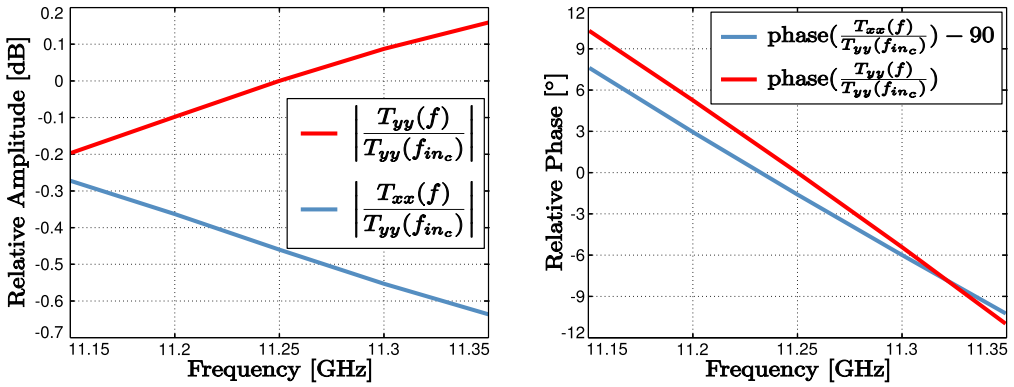

(a) (b)

Figure 3.6: Coupling between either linearly polarised mode of the incident wave onto its corresponding port. (a) Relative amplitude. (b) Relative phase.

The amplitude traces have been normalised by the value of the transfer function T_{yy}, evaluated at the centre of the input frequency band f_{inc}. The maximum relative variation is about 0.75 dB. The phase traces, shown in Figure 3.6(b), are also referred to the value of the transfer function T_{yy} at the centre of the input frequency band f_{inc}. Additionally, for ease of comparison, 90° have been subtracted from the trace corresponding to the transfer function T_{xx}, to compensate for the phase shift introduced to obtained right hand circular polarisation.

The remaining transfer functions, T_{xy} and T_{yx}, correspond to the cross-polar components of the antenna. Although these contributions will also be taken into account in the calculations performed in later sections, their influence on the overall polarisation is far less significant, due to their low amplitude.

3.4. Enhancement of the IL3HSOM Circuit Frequency Performance

The topology of the injection locked third harmonic self oscillating mixer has been shown and described in Chapter 2. The circuit integrates the continuous range phase shifting and downconversion operations, together with the local oscillator generation, providing a positive global conversion gain. Furthermore, the possibility to effectively adjust its frequency response to compensate for the frequency scanning effect in antenna arrays, has also been demonstrated.

In the case of the polarisation agile antenna topology addressed in this chapter, the differences in the coupling performance of the two antenna ports that have been evaluated, show a very mild relative frequency variation. Therefore,

as opposed to the antenna array case, when using ideal phase shifters with a flat frequency response, the polarisation state of the active antenna would naturally exhibit a limited frequency dependence.

On the other hand, the frequency response of the IL3HSOM circuit varies with the phase shift selected at the centre of the band. When the phase shift selected for both ports is not the same, this variation results in the frequency response of the circuits being different, which ultimately brings about a mismatch in the conversion gain and phase shift applied to either port. Since this mismatch is frequency dependent, it cannot be compensated for through calibration.

Hence, in order to reduce the variation of the frequency response of the IL3HSOM circuit with the selected phase shift, which would otherwise result in a frequency dependence of the polarisation state of the active antenna, an re-optimisation of the IL3HSOM circuit design to improve its frequency behaviour has been addressed.

Since the purpose of this process is not to undertake a full redesign of the circuit, but to reduce the fluctuation of the frequency response with the control voltage, stringent constraints must be imposed on the optimisation.

Firstly, only a limited set of parameters is defined as optimisation variables, such as the parameters of the multiharmonic load, the amplitude of the auxiliary generator V_{AG} and the varactor capacity C_{var}. The DC bias point of the transistor and the vast majority of the geometrical design parameters of the circuit are kept constant.

Although the circuit employed for the antenna array topology presented in Chapter 2 was already optimised, using the techniques described in [11], to maximise the conversion gain G_c, the reduction of the input frequency band in this case to $f_{in} = (11.15-11.35)$ GHz, leaves room for further optimisation. Moreover, the requirements in terms of conversion gain are slightly relaxed here, enabling the flattening of the frequency response, at the expense of a limited reduction of the absolute conversion gain.

The circuit is analysed using harmonic balance simulations, duly initialised with a complementary voltage auxiliary generator. In each iteration of the optimisation process, the circuit is simulated for three values of the input frequency f_{in}: the two ends and the centre of the band. The set of goals for the optimisation are composed by the non-perturbation conditions, the phase shift value to establish at the centre of the band $\Delta\phi(f_{in_c})$, and maximum fluctuation limits for both the phase shift and the conversion gain at the three frequency points considered.

Since the fluctuation of the frequency response increases as the established phase shift at the centre of the band approaches the limits of the synchronisation range, the optimisations are initially performed for those values. As the successive optimisation converge, the maximum fluctuation limits imposed are progressively

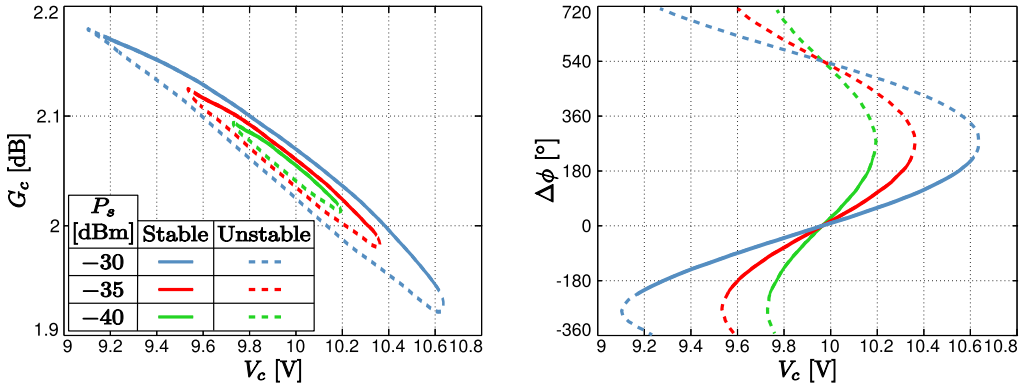

(a) (b)

Figure 3.7: Injection locked solutions of the isolated IL3HSOM circuit for three different synchronisation power levels P_s, as a function of the control voltage V_c, for (a) the conversion gain G_c, and (b) the phase shift at intermediate frequency $\Delta\phi$. The stable and unstable regions have been determined through envelope transient simulations.

tightened. The complete frequency response must be periodically simulated, in order to prevent undesirable abrupt changes in the behaviour of the circuit.

After a few iterations, the frequency response has been effectively flattened, thus reducing its dependence on the phase shift established at the centre of the band. The behaviour of the optimised design that has been obtained is shown and commented next.

3.4.1. Injection Locked Solutions

The injection locked solutions of the IL3HSOM circuit, have been evaluated using harmonic balance simulations, initialised through a non-perturbing voltage auxiliary generator.

The solutions of the circuit have been calculated with an input RF signal at the centre of the band f_{in_c}, and for three different power values of the synchronisation signal P_s. The stable ranges of the synchronisation loci have been determined using envelope transient simulations.

The conversion gain G_c, as a function of the varactor control voltage V_c, is represented in Figure 3.7(a). The conversion gain is slightly dependent on the control voltage and, although this dependence increases with the synchronisation power level P_s, it is not significant for this application since, in the worst case ($P_s = -30$ dBm), its variation range remains under 0.3 dB.

The phase shift $\Delta\phi$ introduced in the downconverted signal has been represented in Figure 3.7(b). By tuning the varactor control voltage V_c, the phase shift

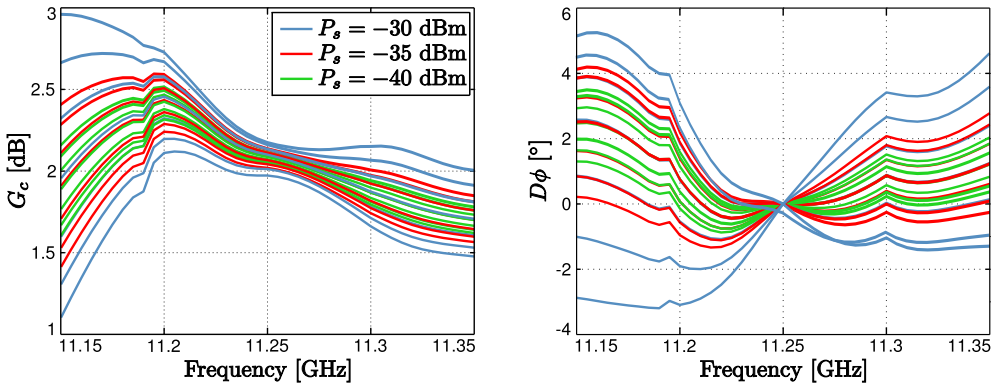

(a) (b)

Figure 3.8: Frequency response of the IL3HSOM circuit for three different synchronisation power levels and for seven working points, uniformly distributed throughout the stable ranges (a) Conversion gain. (b) Phase deviation $D\phi$, as defined in (3.7).

$\Delta\phi$ can be controlled within a stable range of about 450 degrees. Even though the sensitivity to the control signal is higher for lower synchronisation power levels, the stable range of variation is approximately the same for the three cases studied.

3.4.2. Frequency Response

The phase shift introduced at a particular frequency, such as the centre of the band, $\Delta\phi(f_{inc})$, can be arbitrarily selected within the synchronisation ranges through the varactor bias voltage V_c. However, once the phase shift is fixed at a specific frequency point $\Delta\phi(f_{inc})$, the phase shifts introduced at other frequencies cannot be controlled, as they are determined by the frequency response of the circuit.

For three synchronisation power levels, this frequency response has been calculated through harmonic balance and envelope transient simulations, considering seven different phase shift values set at the centre frequency $\Delta\phi(f_{inc})$, uniformly distributed throughout the corresponding stable ranges (Figure 3.7(b)).

The frequency response of the conversion gain G_c, is represented in Figure 3.8(a). For higher synchronisation power levels, a stronger variation is observed, both with frequency and with the operation point selected ($\Delta\phi(f_{inc})$), especially when approaching the limits of the input frequency band.

With regard to the phase shift, in order to simplify the comparison between the multiple traces represented, the phase deviation $D\phi$ can be defined as:

$$D\phi(f, V_c, P_s) = \Delta\phi(f, V_c, P_s) - \Delta\phi(f_{in_c}, V_c, P_s) - L(f, P_s) + L(f_{in_c}, P_s), \tag{3.7}$$

wherein the first term is the actual frequency response of the circuit, for the different control voltages V_c considered. By subtracting the second term (the phase shift value established at the centre frequency $\Delta\phi(f_{in_c}, V_c, P_s)$, for each different trace), the offset between traces is eliminated, bringing them together at the centre frequency.

Due to the propagation throughout the circuit, the phase response presents the characteristic strong slope as a function of frequency which, in this case, conceals the small differences between the traces. Thus, for each of the considered synchronisation power levels, the linear least squares fitting of the trace corresponding to the centre of the stable phase shift range (Figure 3.7(b)), $L(f, P_s)$, is calculated to cancel out this slope. The last term of (3.7) sets the deviation to zero at the centre frequency ($D\phi(f_{in_c}, P_s) = 0$).

As shown in Figure 3.8(b), the phase deviation $D\phi$ also increases its variation, both with frequency and with the operation point selected ($\Delta\phi(f_{in_c})$), for higher synchronisation power levels. The impact of the frequency performance of the circuit on the present application is studied in the next section.

3.5. Polarisation Tuning of the Complete Active Antenna System

The polarisation tuning capability of the active antenna is attained by introducing a relative phase shift between the signals corresponding to the two orthogonal linearly polarised modes received, by means of the IL3HSOM circuits.

Apart from the relative phase shift introduced by the circuits, which can be arbitrarily controlled at the centre frequency f_{in_c}, the polarisation state is also influenced by other factors. The conversion gain G_{c_x} and G_{c_y}, as well as the frequency response of the antenna, modelled through the complex transfer functions T_{xx} and T_{yy}—which have been shown to be slightly different for either port—must be jointly considered to determine the overall polarisation state of the system.

Furthermore, the coupling of undesired cross-polar components onto the output ports, quantified through the transfer functions T_{yx} and T_{xy}, must also be taken into account, as it also affects the polarisation state of the antenna.

Therefore, taking into consideration all the effects involved, the overall output signal of the active antenna can be expressed as:

$$\begin{aligned} V_{out} =& g_x(f_{in})T_{xx}(f_{in})E_x + g_y(f_{in})T_{yy}(f_{in})E_y e^{j\Delta\phi(f_{in})} \\ &+ g_x(f_{in})T_{xy}(f_{in})E_y + g_y(f_{in})T_{yx}(f_{in})E_x e^{j\Delta\phi(f_{in})}, \end{aligned} \tag{3.8}$$

where $g_x, g_y \in \mathbb{R}$ are the voltage gain factors associated with the conversion gain terms G_{c_x} and G_{c_y} of the IL3HSOM circuits, and $\Delta\phi \in \mathbb{R}$, is the relative phase shift introduced $\Delta\phi = \Delta\phi_y - \Delta\phi_x$. Note that the transfer functions T_{xx}, T_{yy}, T_{yx} and T_{xy} are complex quantities.

By regrouping the terms of (3.8), separating those multiplying either mode, the expression can be rewritten as:

$$\begin{aligned} V_{out} =& \left(g_x(f_{in})T_{xx}(f_{in}) + g_y(f_{in})T_{yx}(f_{in})e^{j\Delta\phi(f_{in})}\right) E_x \\ &+ \left(g_y(f_{in})T_{yy}(f_{in})e^{j\Delta\phi(f_{in})} + g_x(f_{in})T_{xy}(f_{in})\right) E_y. \end{aligned} \tag{3.9}$$

For convenience, the parameters $p_x, p_y, \alpha_x, \alpha_y \in \mathbb{R}$, can be introduced and substituted for the factors in brackets in (3.9), as follows:

$$V_{out} = p_x e^{j\alpha_x} E_x + p_y e^{j\alpha_y} E_y. \tag{3.10}$$

Note that those parameters are dependent on both the input frequency f_{in}, and the relative phase shift $\Delta\phi$, imposed.

Through the geometrical analysis of the polarisation ellipse associated with (3.10), the axial ratio of the active antenna can be calculated as [12]:

$$\mathrm{AR} = \cot\left|\frac{1}{2}\arcsin\left(\frac{2p_x p_y}{p_x^2 + p_y^2}\sin(\alpha - 90)\right)\right|, \tag{3.11}$$

where $\alpha = \alpha_y - \alpha_x$, has been introduced.

As far as the polarisation is concerned, in the following, the incident wave will be assumed to propagate in the $+z$ direction.

3.5.1. Simulated Behaviour

The behaviour of the complete active antenna topology, as shown in Figure 3.2, has been simulated for three different values of the synchronisation power P_s.

According to the analysis shown in Figure 3.5, a 360° relative phase shift range is enough to cover all the polarisation states that can be achieved with the proposed system configuration; left hand circular polarisation is obtained both with $\Delta\phi = -180°$, and with $\Delta\phi = 180°$, and the polarisation states are repeated outside this range.

Strictly speaking, since the elliptical polarisations present little practical interest, the two orthogonal linear polarisations, along with left hand and right hand circular polarisation can be achieved with a 270° phase shift range (from −180° to 90° or from 90° to 180°, as shown in Figure 3.5).

Hence, the required phase shift range can be exceedingly covered by tuning the control voltage of only one of the IL3HSOM circuits. However, as discussed in Section 3.4.2, the frequency response of the circuits exhibits wider fluctuations as the phase shift imposed at the centre frequency approaches the limits of the synchronisation range. Consequently, with regard to the overall frequency response of the system, it would be advantageous to simultaneously tune the phase shift imposed by both circuits, in such a way that they are set symmetrically around the centre of the synchronisation range ($\Delta\phi = 0°$ in Figure 3.7(b)).

Nonetheless, in order to evaluate the impact of the circuit frequency response on the overall antenna polarisation, as well as to illustrate the behaviour in a worst case scenario, in this analysis the whole range of polarisation states will be covered by tuning the control voltage of one single IL3HSOM circuit.

The control voltage of HSOM$_y$, V_{c_y}, has been swept throughout its stable range (Figure 3.7(a)), while keeping HSOM$_x$ working at the centre point. In Figure 3.9, the evolution of the axial ratio as a function of the control voltage V_{c_y}, has been represented. As the phase shift $\Delta\phi$ produced by the IL3HSOM circuits is a monotonically increasing function of the control voltage, as shown in Figure 3.7(b), the peaks and minima in this case represent the same polarisation states indicated in theoretical analysis presented in Figure 3.5. For each of the synchronisation power levels considered, the performance at six frequency points, uniformly distributed throughout the input band ($f_{in_k} = 11.11 + 0.04k$ GHz, $k = 1, \ldots, 6$), have been displayed.

Both circular polarisations are successfully obtained ($AR < 3$ dB), for all the synchronisation power levels and at all the frequency points considered. With the linear polarisations, on the other hand, due to their higher sensitivity to the phase shift (Figure 3.5), a somewhat more frequency selective response is observed. This is especially apparent for $P_s = -30$ dBm, where both linear polarisations ($AR > 30$ dB) are only achieved at some frequencies. For the two lower synchronisation power levels ($P_s = -35$ and $P_s = -40$ dBm), LP− is stable for all the considered frequency values, whereas for LP+, the axial ratio drops below the 30 dB threshold at some point. The behaviour for $P_s = -40$ dBm has been magnified in the first inset of Figure 3.9, showing peaks at two successive V_{c_y} values, which take place at different frequency points (Figure 3.10). This suggests the existence of an intermediate working point between those two, providing higher axial ratio levels, together with a better frequency performance.

The variation of the axial ratio over frequency is shown in Figure 3.10. Since the circular polarisations have been found to be stable in the input band (Figure

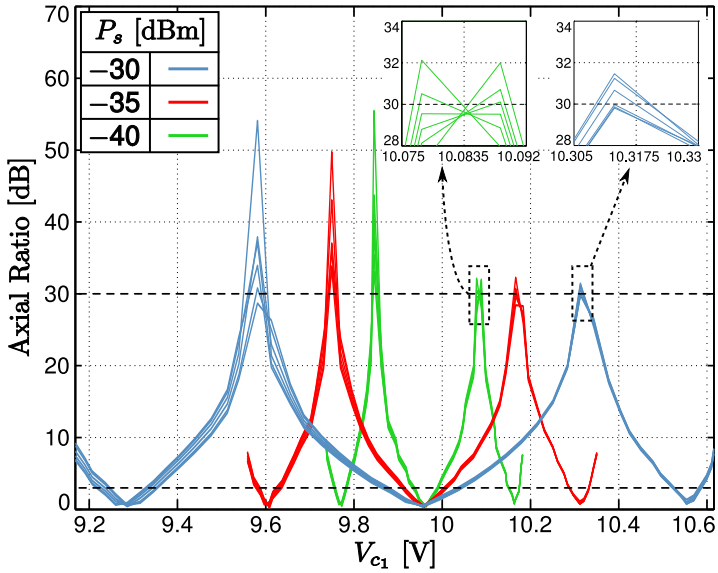

Figure 3.9: Variation of the axial ratio at the centre of the input frequency band (f_{in_c} = 11.25 GHz), as the control voltage V_{c_1} is swept, while keeping $HSOM_2$ working at the centre of its synchronisation range. For each synchronisation power level, the behaviour at six points of the input frequency band is displayed.

3.9), only the linear ones, corresponding to the working points specified in the legend, have been represented. For $P_s = -40$ dBm, the behaviour at the two successive V_{c_y} values corresponding to LP+ have been included, showing linear polarisation in two different frequency ranges. The most limited frequency performance is observed for $P_s = -30$ dBm. The polarisation LP− is maintained along the input band for the two lower synchronisation power levels, whereas for LP+, the axial ratio drops below 30 dB at some point within this band.

In conclusion, the performance of the IL3HSOM based phase shifter circuit is more stable over frequency for lower values of the synchronisation power, as discussed in Section 3.4.2, leading to potentially wider polarisation bandwidths. Nevertheless, since the phase shift can be varied within a continuous range, the working point selected also has an important impact on the frequency performance, especially for linear polarisations.

3.6. Experimental Results

For the experimental characterisation of the polarisation agile active antenna system that has been proposed, a prototype of the complete topology outlined in Figure 3.2 has been manufactured. As has been justified, due to the compati-

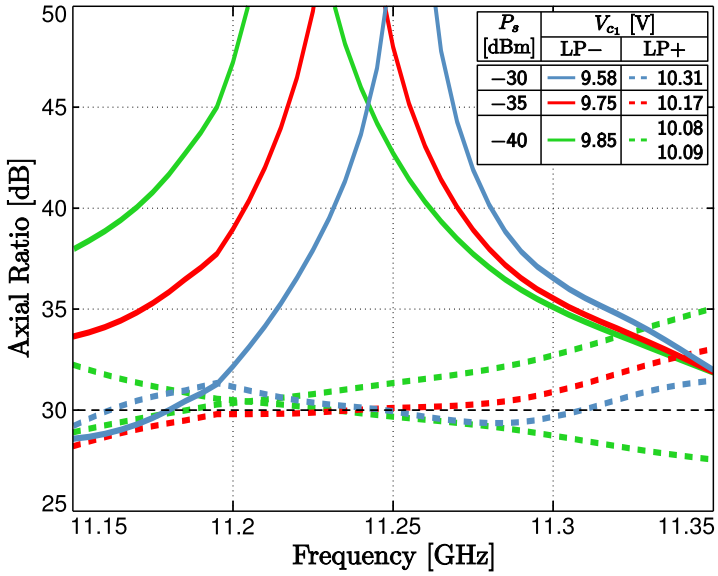

Figure 3.10: Variation of the axial ratio over frequency for the working points specified in the legend.

bility between both topologies, the auxiliary networks designed for the antenna array system addressed in Chapter 2, have been reused here. The prototype has been likewise mounted on the same wooden support structure, which enables its appropriate mechanical suspension on the anechoic chamber.

3.6.1. Measurement Set-up

In order to experimentally evaluate the polarisation behaviour of the active antenna, the prototype has been measured in an anechoic environment, using the set-up outlined schematically in Figure 3.11.

Once again, taking advantage of the similarities between this system and the active antenna array, the required equipment is analogous. The same power supplies and associated DC wiring is used, although fewer channels are needed in this case, due to the fact that only two instead of four IL3HSOM circuits are employed. Similarly, the same microwave signal generators, vector network analyser and RF cabling are used, as well as the pyramidal horn antenna, which has a highly pure linear polarisation.

The main difference in the set-up is that, since only two IL3HSOM circuits are employed in this prototype, instead of using a microwave switch, the sample signals of both outputs are simultaneously monitored using two Agilent 89600 vector network analysers (N8201A - N8221A).

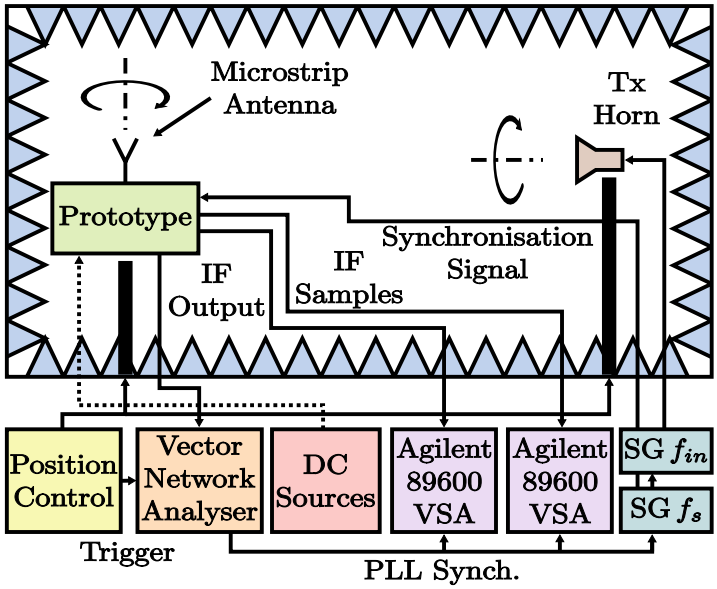

Figure 3.11: Schematic diagram of the measurement set-up in the anechoic chamber.

3.6.2. Polarisation Pattern

The polarisation of an antenna is completely characterised by the parameters of its polarisation ellipse (axial ratio and tilt angle) along with the sense of rotation.

Among the various techniques that have been proposed in the literature for the measurement of antenna polarisation, one of the simplest procedures to determine the paremeters of the polarisation ellipse is known as the *polarisation pattern method* [13]. This method entails the measurement of the power received at the output of the antenna under test, as the transmitting antenna—with linear polarisation—is rotated about the axis intersecting both antennas.

Thus, the unit polarisation vector of the transmitting antenna, as function of the rotation angle α is given by:

$$\hat{u}_t = \cos\alpha\hat{x} + \sin\alpha\hat{y}, \tag{3.12}$$

assuming that, for $\alpha = 0°$, $\hat{u}_t$ is parallel to the x axis. Similarly, for a generic polarisation vector $\vec{u}_g = \hat{x} + \rho e^{j\phi}\hat{y}$, the corresponding unit vector can be written as:

$$\hat{u}_g = \frac{\hat{x} + \rho e^{j\phi}\hat{y}}{\sqrt{1+\rho^2}}, \tag{3.13}$$

where ρ and ϕ are the parameters that define the generic polarisation.

The *polarisation loss factor*, which represents the link power loss produced by the polarisation mismatch, can be defined as the dot product between the unit vectors, as follows:

$$\mathrm{PLF} = |\hat{u}_g \cdot \hat{u}_t|^2 . \tag{3.14}$$

As per its definition, the polarisation loss factor is a real number that varies between 0, corresponding to orthogonal polarisations in transmitter and receiver, and 1, corresponding to perfectly matching polarisations.

Introducing (3.12) and (3.13) into (3.14) and simplifying, the polarisation loss factor can be particularised to the polarisation pattern measurement as:

$$\mathrm{PLF}(\alpha) = \frac{1}{\sqrt{1+\rho^2}} \left(\cos^2\alpha + \rho^2 \sin^2\alpha + 2\rho \cos\alpha \sin\alpha \cos\phi\right). \tag{3.15}$$

As the transmitting antenna is rotated the angle α, the received power varies in accordance with (3.15). The received power will be maximum when the angle α is such that the transmitted linear polarisation is aligned with the major axis of the ellipse, and minimum when it is parallel to the minor axis. Thus, by calculating the relationship between the maximum and the minimum of (3.15), the axial ratio squared is obtained:

$$\mathrm{AR}^2 = \frac{\max\{\mathrm{PLF}(\alpha)\}}{\min\{\mathrm{PLF}(\alpha)\}}. \tag{3.16}$$

Similarly, the rotation angle of the transmitting antenna for which the maximum received power takes place α_{max}, corresponds to the tilt angle of the polarisation ellipse ψ.

The unit polarisation ellipse associated with $\rho = 1$ and $\phi = \pi/4$ has been represented in Figure 3.12, together with the corresponding polarisation pattern (square root of (3.15)). The polarisation pattern intersects the polarisation ellipse at the ends of the major and minor axes.

Although this approach enables the identification of the geometrical parameters of the polarisation ellipse—axial ratio and tilt angle—no information is obtained as to the sense of rotation.

Nevertheless, since output signal is measured in both magnitude and phase, if the signal received for two perpendicular orientations of the probe are compared, the sense of rotation is determined by rotating the phase leading component towards the phase lagging component [10].

In fact, the polarisation state could be completely determined through the amplitude and phase measurement of those two components, as they define the parameters of the polarisation unit vector (3.13). On the other hand, the calculation of the polarisation state exclusively based on two individual measurements is more vulnerable to practical errors, whereas the continuous variation shown in the polarisation pattern, exposes the potential artefacts that might appear in the measurement process.

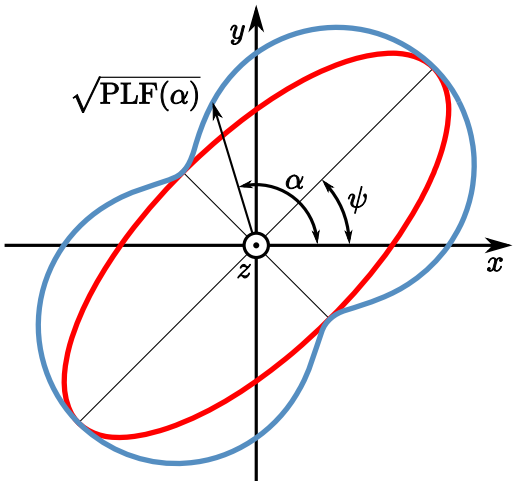

Figure 3.12: Unit polarisation ellipse for $\rho = 1$ and $\phi = \pi/4$, with the associated polarisation pattern

3.6.3. Measurements

The performance of the system prototype is evaluated using the anechoic chamber set-up that has been described, in which the receiving antenna is illuminated with the far fields of the pyramidal horn, in the input frequency band $f_{in} = 11.15 - 11.35$ GHz.

In accordance with the simulations that have been performed, the polarisation tuning capabilities of the system will be experimentally assessed by tuning the control voltage of one of the IL3HSOM circuits V_{c_1}, while keeping the other at the centre of the synchronisation range.

3.6.3.1. Polarisation Tuning

In order to measure the polarisation pattern of the receiving active antenna system, the output power at intermediate frequency is registered while the transmitting horn is rotated about the axis that intersects both antennas.

Since all the parameters that influence the link budget, modelled through the Friis transmission equation [10] are kept constant—except for the polarisation loss factor—the fluctuation of the received power must be due to this parameter, whose variation can thus be determined.

The polarisation tuning capabilities of the system have been evaluated while sweeping the control voltage V_{c_1} throughout the synchronisation range. Since, the simulations showed better performance for lower values of the synchronisation power, the measurements have been carried out for $P_s = -35$ and $P_s = -40$ dBm.

At the centre of the input frequency band ($f_{in_c} = 11.25$ GHz), the normalised output power received at intermediate frequency, for a synchronisation power level $P_s = -35$ dBm, has been represented in Figure 3.13, as a function of the control voltage V_{c_1} and the rotation angle α, of the transmitting antenna. An analogous representation for $P_s = -40$ dBm is shown in Figure 3.14. For the sake of clarity, only a representative set of the measurements carried out has been included in these figures.

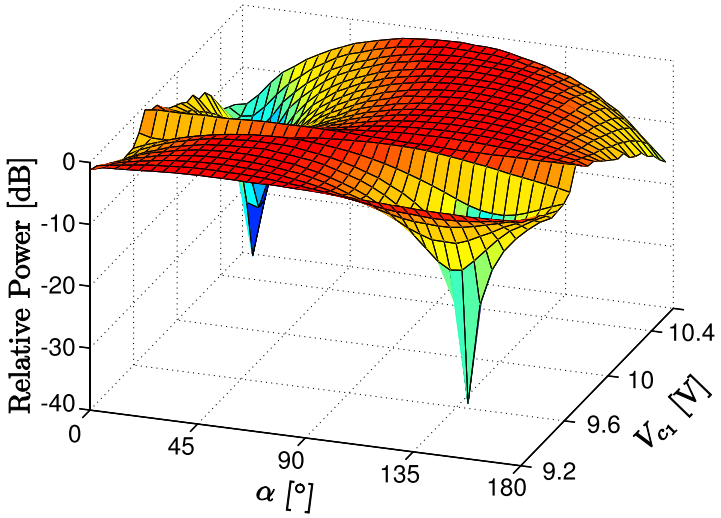

Figure 3.13: Relative IF power measured at the output of the active antenna at the centre frequency of the input band ($f_{in_c} = 11.25$ GHz), as a function of the control voltage and the rotation angle α of the transmitting antenna, for $P_s = -35$ dBm.

The axial ratio measured at the centre frequency of the input band has been displayed versus the control voltage V_{c_1} in Figure 3.15, for $P_s = -35$ and $P_s = -40$ dBm.

A small deviation on the performance of the manufactured IL3HSOM circuits has been found, producing stronger variations of the conversion gain with the control voltage, especially at the upper end of the synchronisation range. Although, as a consequence of this deviation, the second left hand circular polarisation observed in simulation (corresponding to the higher value of the control signal), is not reached in measurement, all the desired polarisations have been successfully attained. Furthermore, note that, for this experimental set-up the second HSOM circuit has been kept at a fixed working point and therefore, a double phase shift tuning range is available.

The variation of the axial ratio over frequency is represented in Figure 3.16, for the two orthogonal linear polarisations (LP+ and LP−), and for RHCP and

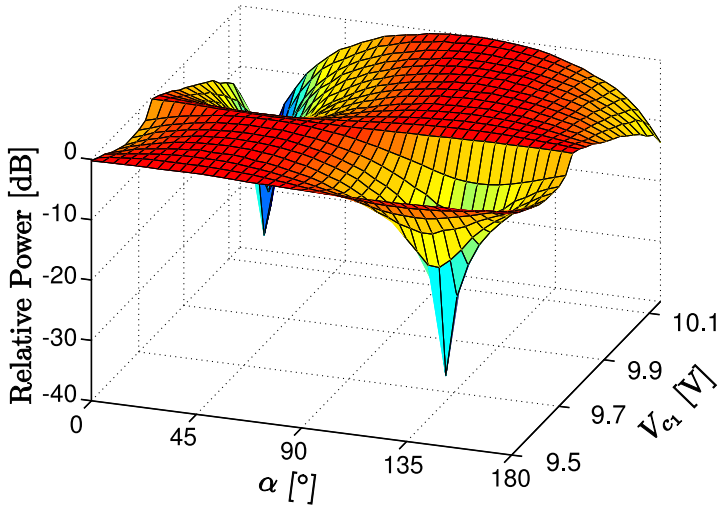

Figure 3.14: Relative IF power measured at the output of the active antenna at the centre frequency of the input band (f_{in_c} = 11.25 GHz), as a function of the control voltage and the rotation angle α of the transmitting antenna, for $P_s = -40$ dBm.

LHCP. Unlike in the simulation, the values of the control signal V_{c_1} have been carefully selected to produce the best possible frequency performance. Both linear polarisations are maintained over almost the whole input frequency band for both synchronisation values, although a slightly wider bandwidth is observed for $P_s = -40$ dBm.

The stronger variation in the conversion gain of the practical circuits mentioned earlier, has a greater impact on the circular polarisations, which consequently present a poorer frequency performance. The polarisation bandwidth is reduced with respect to the simulated results, although for $P_s = -40$ dBm, the axial ratio remains below the 3 dB threshold throughout a substantial part of the band.

3.6.4. Radiation Pattern

The radiation pattern of the active antenna at the centre frequency f_{in_c} = 11.25 GHz, has been measured by rotating the complete prototype about the azimuth axis of the anechoic chamber, while the polarisation of the transmitting horn is oriented in the $\varphi = 45°$ direction. The results are displayed in Figure 3.17 for two different synchronisation power levels and for the linear polarisation LP+, as well as for right hand circular polarisation.

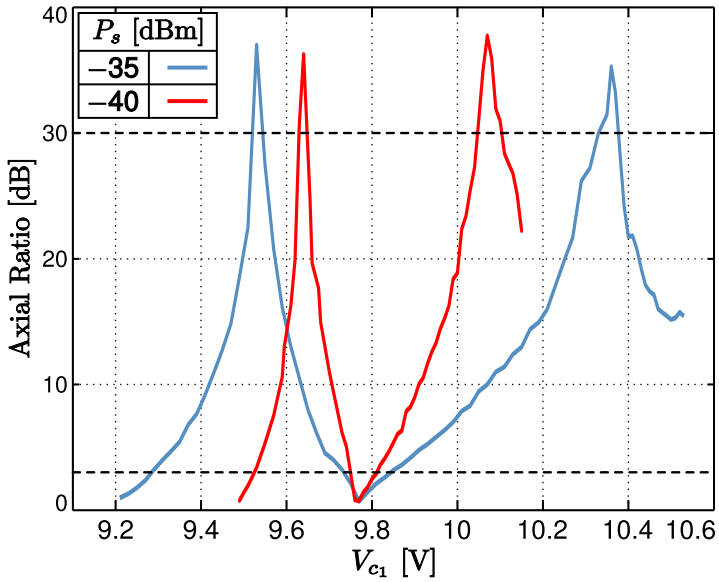

Figure 3.15: Measured axial ratio for $P_s = -35$ and $P_s = -40$ dBm as a function of the control voltage V_{c_1} at the centre of the input frequency band ($f_{in_c} = 11.25$ GHz).

3.7. Conclusions

A receiving polarisation agile antenna topology based on injection locked third harmonic self oscillating mixers has been presented in this chapter. Taking advantage of the multifunctional nature of the IL3HSOM circuit, the continuous range phase shifting—required to control the antenna polarisation—has been integrated with the frequency downconversion operation and the local oscillator signal generation, obtaining an overall positive coversion gain.

The proposed topology enables the control of the antenna polarisation state in a continuous range that comprises two orthogonal linear polarisations, along with left hand and right hand circular polarisation.

Through the constrained reoptimisation of the circuit, its frequency response has been enhanced, in order to reduce the polarisation state fluctuation throughout the input frequency band. The global frequency response of the system has been further studied, observing a more stable behaviour for lower values of the synchronisation power level.

A prototype of the complete system has been manufactured and measured in the anechoic chamber, for the experimental validation of the design process. The results that have been obtained are in good agreement with the simulations.

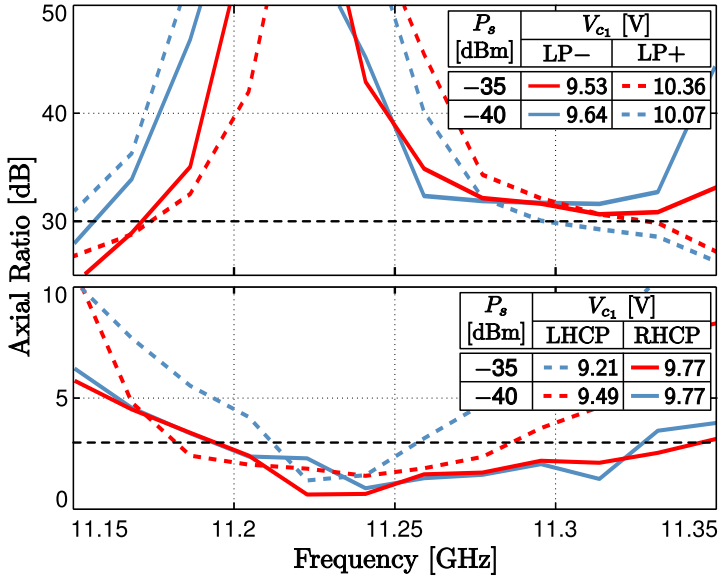

Figure 3.16: Measured axial ratio for $P_s = -35$ and $P_s = -40$ dBm as a function of frequency for LP− and LP+ (upper subfigure), and for RHCP and LHCP (lower subfigure), at the centre of the input frequency band ($f_{in_c} = 11.25$ GHz).

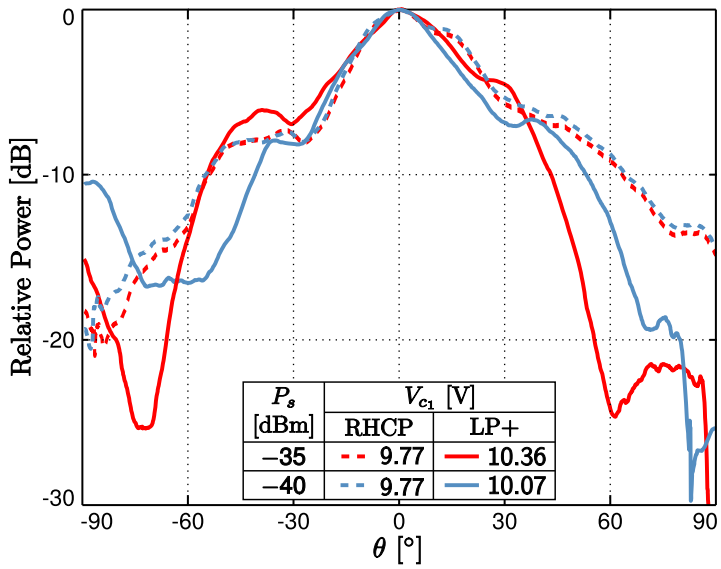

Figure 3.17: Radiation pattern of the active antenna at $f_{in_c} = 11.25$ GHz, for LP+ and RHCP and for two synchronisation power levels, measured with the polarisation of the transmitting oriented in the $\alpha = 45°$ direction.

Bibliography

[1] Rui-Hung Chen and J.-S. Row. Single-fed microstrip patch antenna with switchable polarization. *Antennas and Propagation, IEEE Transactions on*, 56(4):922–926, April 2008.

[2] Y.J. Sung, T.U. Jang, and Y.-S. Kim. A reconfigurable microstrip antenna for switchable polarization. *Microwave and Wireless Components Letters, IEEE*, 14(11):534–536, Nov. 2004.

[3] S.-H. Hsu and Kai Chang. A novel reconfigurable microstrip antenna with switchable circular polarization. *Antennas and Wireless Propagation Letters, IEEE*, 6:160–162, 2007.

[4] P.M. Haskins and J.S. Dahele. Varactor-diode loaded passive polarisation-agile patch antenna. *Electronics Letters*, 30(13):1074–1075, Jun 1994.

[5] Carlos Vázquez, Samuel Ver Hoeye, Germán León, Miguel Fernández, Luis Fernando Herrán, and Fernando Las Heras. Transmitting polarisation agile microstrip antenna based on injection locked oscillators. *Journal of Electromagnetic Waves & Applications*, 22(17/18):24, December 2008.

[6] C. Vazquez, S. Ver Hoeye, M. Fernandez, L.F. Herran, and F. Las Heras. Analysis of the performance of injection locked oscillators in a data transmitting polarisation agile antenna application. *Progress in Electromagnetics Research Letters*, 12:1 – 10, 2009.

[7] Shih-Chieh Yen and Tah-Hsiung Chu. A beam-scanning and polarization-agile antenna array using mutually coupled oscillating doublers. *Antennas and Propagation, IEEE Transactions on*, 53(12):4051–4057, Dec. 2005.

[8] G. Leon, S. Ver Hoeye, M. Fernandez, C. Vazquez, L.F. Herran, and F. Las Heras. Novel polarization agile microstrip antenna. In *Antennas and Propagation Society International Symposium, 2008. AP-S 2008. IEEE*, pages 1–4, July 2008.

[9] Jin Au Kong. *Electromagnetic Wave Theory*. EMW Publishing, 2000.

[10] Constantine A. Balanis. *Antenna Theory: Analysis and Design*. John Wiley & Sons, Inc., New York, 1982.

[11] M. Fernandez, S. Ver Hoeye, L.F. Herran, and Fernando Las Heras. Nonlinear optimization of wide-band harmonic self-oscillating mixers. *Microwave and Wireless Components Letters, IEEE*, 18(5):347–349, May 2008.

[12] Sophocles J. Orfanidis. *Electromagnetic Waves and Antennas*. Rutgers University, 1999.

[13] Ieee standard test procedures for antennas. *ANSI/IEEE Std 149-1979*, pages 0–1, 1979.

Chapter 4

Low Power Fourth Harmonic Oscillator

Contents

4.1. Introduction

A wide variety of high efficiency oscillator designs have been presented in the literature [1; 2]. Those circuits are typically optimised to generate a carrier with a high power level (of the order of 1 W), as well as to minimise the power consumption, leading to power efficiencies that may exceed 80% [2].

For low range point-to-point reconfigurable communications between mobile or portable devices, in which the required power levels are relatively low, the implementations presented in the previously referenced works are not appropriate since, in spite of the high efficiencies attained, the excessive output power levels delivered by those topologies give rise to a relatively high power consumption that is generally difficult to sustain in battery powered devices.

On the other hand, ultra low power consuming oscillator topologies for applications such as passive RFID (Radio Frequency Identification) tags or biomedical telemetry, have also been presented [3; 4], with power consumption levels even lower than 1 mW. However, since the RF output power level is not a concern in those applications, it can be as low as -32 dBm [4], which is generally insufficient—even for low range—wireless communications.

The purpose of the present chapter is to develop an oscillator circuit with an output power level of about -5 dBm at a frequency $f_o = 10$ GHz, while keeping a contained power consumption which makes it suitable for low range reconfigurable point-to-point portable or mobile communication schemes, as well as for battery powered applications in general.

A solution implemented in monolithic technology that fulfils the specified design requirements was presented in [5]. An LC tank oscillator at 2.4 GHz with

an output power level about −6 dBm was obtained, with a power consumption of 3 mW.

However, in order to enable the use the designed circuit topology to control a reconfigurable antenna array implementation, its capability to operate as a phase shifter will be of paramount importance. Therefore, in the design that will be addressed in the following, the fourth harmonic component of the oscillation will be optimised as the output signal, leading to a 720° theoretical phase shift range, which guarantees practically usable range exceeding 360°.

For the thorough experimental validation of the design, a prototype will be manufactured and measured under various operating conditions. The phase noise performance of the fourth harmonic oscillator will be evaluated, both free running and injection locked. The capability of the circuit to transmit modulated signals while preserving the phase shifting functionality will also be investigated.

4.2. Circuit Topology

The electrical diagram of the fourth harmonic oscillator design that will be developed in the present chapter is shown schematically in Figure 4.1. The external generator connected to the input port of the circuit is required for its injection locked operation, which will be considered in subsequent sections. The topology is constituted by the following fundamental parts:

- ***Transistor:*** A Hewlett-Packard ATF-36077 Pseudomorphic High Electron Mobility Transistor (pHEMT) has been chosen for this design, owing to its ultra low noise performance capabilities in its operating band, from 2 to 18 GHz.

- ***Series Feedback:*** A resonant network is connected to the source terminal of the transistor in order to synthesise the required oscillation start-up conditions at the operating frequency $f_0 = 2.5$ GHz. A varactor diode is integrated in this series feedback network, enabling the fine tuning of the oscillation frequency f_0.

- ***Varactor:*** The chosen device is a Microsemi-GC15007, which provides a capacitance range between 0.2 and 2.8 pF, for control voltages from 20 to 0 V.

- ***Multiharmonic Loads:*** In order for the accurate control and optimisation of the harmonic content present in the circuit, transmission line newtworks whose frequency response can be precisely tailored, are required. In this particular design, two such networks have been used, connected to the drain and gate terminals of the transistor. These components are implemented through arbitrarily width modulated transmission line segments,

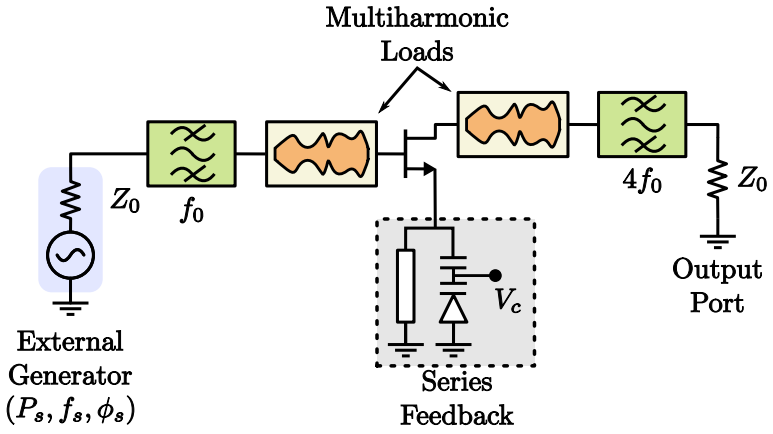

Figure 4.1: Schematic topology of the proposed fourth harmonic oscillator.

which provide high design flexibility and low complexity, as will be shown later in this section.

The complete low power fourth harmonic oscillator design is implemented in a Rogers 3003 substrate laminate, whose properties are summarised in Table 4.1.

Symbol	Parameter	Value	Unit
ε_r	Relative Permittivity	3	
$\tan(\delta)$	Loss Tangent	0.0013	
h	Thickness	0.75	mm
h_c	Cladding Thickness	17	μ m

Table 4.1: Datasheet specification of the Rogers 3003 substrate. Electrical properties measured at 10GHz.

The circuit topology that has been presented includes additional components with specific functionalities (filters, DC bias networks, etc.), which were designed separately prior to addressing the complete oscillator topology. These components are described in detail in the following dedicated subsections.

4.2.1. Multiharmonic DC Bias Network Based on Arbitrarily Width Modulated Microstrip Line

Active RF circuits generally receive their power supply though the direct connection to a DC source. However, the connection of this power source must be performed in such a way that its presence does not affect the normal RF behaviour

of the circuit. This is achieved through the design of a DC bias network, or bias tee, which presents a high input impedance at the RF connection point for the frequencies of operation of the circuit, preventing the RF power from being delivered to the DC power source.

Because basic RF active components generally operate over limited frequency ranges, it usually suffices to obtain this RF rejection behaviour in this restricted operation bandwidth. A simple and widely used bias tee topology for high frequency circuits consists of a quarter wavelength open circuited stub, plus a quarter wavelength connecting transmission line. The quarter wavelength stub shows a short circuit at its input, which is subsequently transformed into an open circuit at the input of the connecting line. Radial stubs are usually employed, since they provide a low impedance level at a well specified insertion point in a wide frequency band [6]. The rejection bandwidth can be further increased by introducing several cascaded sections.

Nonetheless, circuits with an optimised harmonic content require feeding networks that prevent the power transfer to the DC source at multiple harmonic components. Radial stub based feeding structures with several blocking bands tend to be highly sensitive to the design parameters and to present a relatively narrowband behaviour, which makes them rarely appropriate for this kind of applications. As a versatile alternative to overcome these limitations, a novel feeding network based on Arbitrarily Width Modulated Microstrip Lines (AWMML) has been designed [7].

The structure of the arbitrarily width modulated microstrip line is shown schematically in Figure 4.2. The total structure length L is uniformly divided into a large number N of microstrip tapered sections of equal length, $\Delta L = L/N$. In order to impose the continuity of the modulating function, the width of one of the two parallel sides of each particular trapezium shaped section $W_{n-1,2}$, is set to the width of the corresponding side of the adjoining section, $W_{n,1} = W_{n-1,2}$, as outlined in Figure 4.2. The width of the remaining side is left as a design parameter, giving rise to a number of degrees of freedom N, equal to the total number tapered sections. The feeding network ends with a narrow transmission line segment on the RF side and with a DC pad for the connection of the power supply at the other side.

In a first stage, the bias network for $N = 200$ is implemented using the distributed element models included in the Agilent Advanced Design System (ADS) circuit simulation libraries. The design parameters are adjusted through a nominal optimisation process, to obtain the RF blocking behaviour in the bands of interest. A minimum input impedance value $|Z_{\text{in,min}}| = 1$ kΩ is required over a 200 MHz bandwidth, centred at the first four harmonic components of the circuit oscillation frequency $f_0 = 2.5$ GHz.

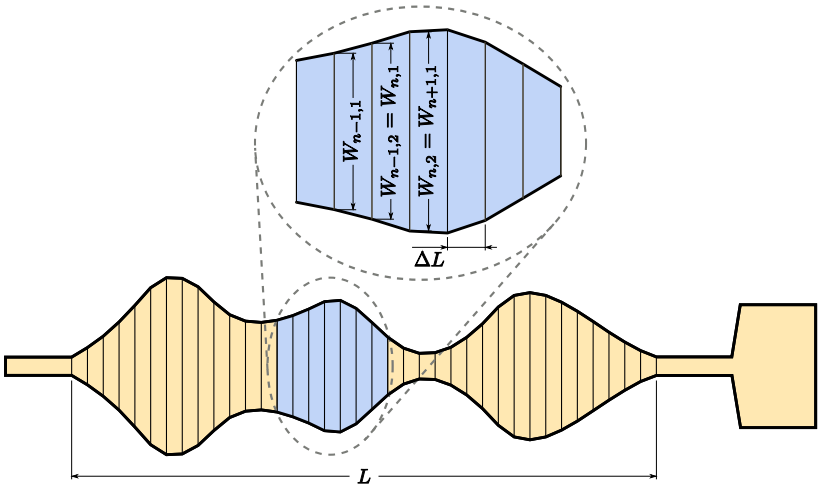

Figure 4.2: Schematic diagram of the arbitrarily width modulated feeding network.

Once the design requirements are fulfilled using library components, the performance of the structure is assessed through Method of Moments (MoM) electromagnetic simulations of the entire network. Small deviations from the design requirements can normally be corrected at this stage, through the fine tuning of certain sensitive parameters of the structure, such as the length L. The shape of the final optimised design is presented in Figure 4.3(a). The input impedance Z_{in} values calculated both using library components and through electromagnetic simulation are compared in Figure 4.4. Although the peaks obtained in the electromagnetic simulation are lower, sufficiently high impedance values are observed in all the bands of interest.

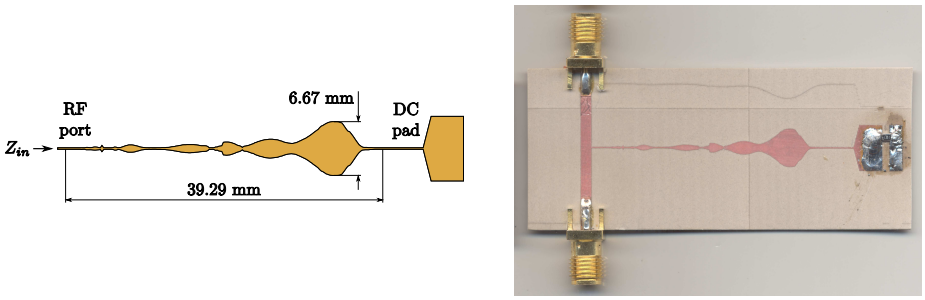

(a) (b)

Figure 4.3: (a) Shape of the final optimised design. (b) Prototype for the experimental validation of the arbitrarily width modulated feeding network.

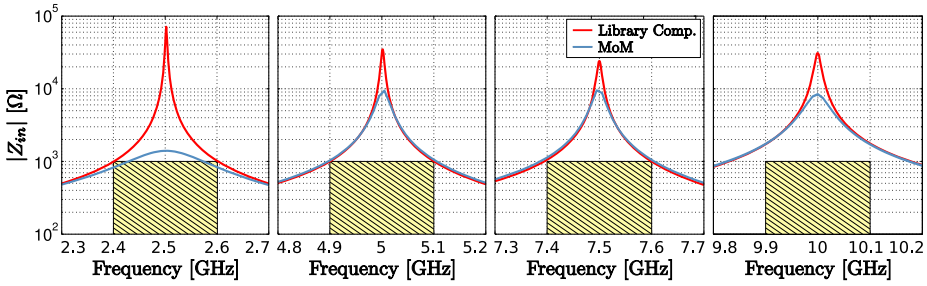

Figure 4.4: Simulated input impedance $|Z_{in}|$ in the bands of interest, both using library components and through the MoM electromagnetic simulation of the complete structure. The yellow hatched areas indicate the design requirements for the optimisation process.

For the experimental validation of the feeding structure, a simple prototype in which the DC bias network is connected to a transmission line segment of characteristic impedance 50 Ω at 2.5 GHz, has been manufactured (Figure 4.3(b)). The $|S_{21}|$ parameter of the network has been measured in the bands of interest, connecting the DC pad to ground through three different resistors of values R_{DC} =0.01 Ω, 50 Ω and 10 kΩ. As can be observed in the results presented in Figure 4.5, the bias network has a limited influence over the RF response of the transmission line in the bands of operation, without regard to the resistor value connected.

Therefore, this feeding network design is appropriate for the low power fourth harmonic oscillator circuit addressed in the present chapter, and will be used for the DC biasing of the transistor, both in its drain and gate terminals, as well as to control the operation point of the varactor diode.

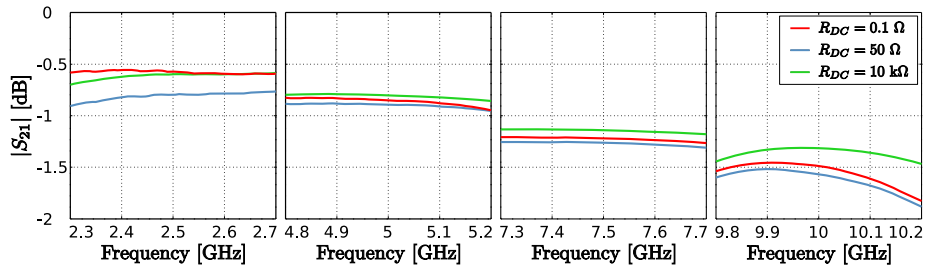

Figure 4.5: Measured $|S_{21}|$ parameter of the prototype shown in Figure 4.3(b), connecting the DC pad to ground through three different resistor values R_{DC} = 0.01 Ω, 50 Ω and 10 kΩ.

4.2.2. Input Filter

For the injection locked operation of the fourth harmonic oscillator, which enables its performance as a continuous range phase shifter, an external reference signal at the oscillation frequency $f_0 = 2.5$ GHz, needs to be introduced in the circuit. For this purpose, an input port that gives access to the gate terminal of the transistor is introduced in the topology, as depicted in Figure 4.1. However, since the performance of the oscillator can be severely damaged in the presence of certain spurious signals, a filter that restricts the input through that port to a specific passband around the fundamental frequency $f_0 = 2.5$ GHz, is required.

It is well known that signals at the harmonic components of the fundamental frequency, either produced by the normal harmonic distortion of the external generator or by any other source, are especially detrimental, as they can lead to undesired harmonic synchronisations that may bring about harsh deviations from the circuit expected performace. Thus, the attenuation levels introduced by the input filter at these harmonic components will be a critical aspect to take into consideration during its design process.

An image of the manufactured prototype of the final filter is shown in Figure 4.6(a). A three stage design has been adopted for this network; one independent parallel coupled quarter wavelength transmission line section on either side of the structure, along with an optimum open circuited stub based bandstop filter in the central part.

The parallel coupled transmission line sections are designed to present maximum coupling in the vicinity of 2.5 GHz, giving rise to a passband around this frequency. This type of structure theoretically produces transmission zeroes at the even harmonic components of the passband (in this case 5 GHz, 10 GHz, 15 GHz, and so forth), which is a useful feature to increase the attenuation of these components. However, in practice, the stopbands produced by these transmission zeroes—which are intrinsically narrowband—do not take place at the exact integer multiples of the passband, thus making it difficult to achieve high attenuation levels at 5 and 10 GHz simultaneously. In order to overcome this limitation, two slightly different coupled line sections have been used; one of them has been fine-tuned to centre the stopband at 5 GHz, while the other has been adjusted to maximise the attenuation at 10 GHz. In addition, the coupled transmission line topology is particularly advantageous for the input filter design due to its inherent DC blocking behaviour, which prevents the normal biasing of the transistor gate terminal from originating a direct current flow through the external RF generator.

The coupled transmission line sections that have been described provide high attenuation levels at the second and fourth harmonic components of the fundamental frequency—5 and 10 GHz, respectively—whereas little consideration has been given so far to the component at 7.5 GHz. In order to address this defi-

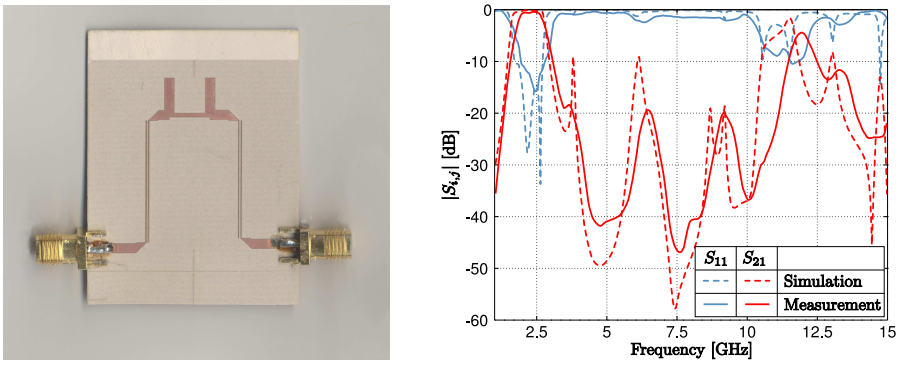

(a) (b)

Figure 4.6: (a) Manufactured input filter prototype. (b) Simulated and measured scattering parameters of the input filter design.

ciency, the topology has been complemented with a third filtering stage, aimed at improving the rejection of this harmonic component.

An optimum open circuited stub based bandstop filter has been introduced between the two coupled transmission line sections. Conventional bandstop filters with open circuited stubs are composed of shunt quarter wavelength open circuited stubs separated by unit elements, which are quarter wavelength long transmission line segments at the mid stopband frequency. Nevertheless, it has been shown [6], that the traditional design approach of this kind of filters leads to redundant unit elements, whose potential filtering properties are not fully exploited. Therefore, by taking into consideration the unit elements in the design process, relevant improvements in the attenuation characteristic can be attained for the same filter order.

An optimum open circuited stub bandstop filter has been developed according to the design equations derived in [6], for a Chebyshev response with 0.044 dB passband ripple. A second order topology with 100% fractional bandwidth $FBW = \Delta f / f_c$, centred at $f_c = 7.5$ GHz has been chosen for this filter stage.

A prototype of the complete structure has been manufactured for the experimental validation of the design (Figure 4.6(a)). The measured scattering parameters of the prototype are compared with the electromagnetic method of moments simulation of the whole structure in Figure 4.6(b). The measured behaviour is in good agreement with the simulation results: a well defined passband with low insertion loss has been obtained around the fundamental frequency $f_0 = 2.5$ GHz, while high attenuation levels are introduced at the corresponding harmonic components at 5, 7.5 and 10 GHz.

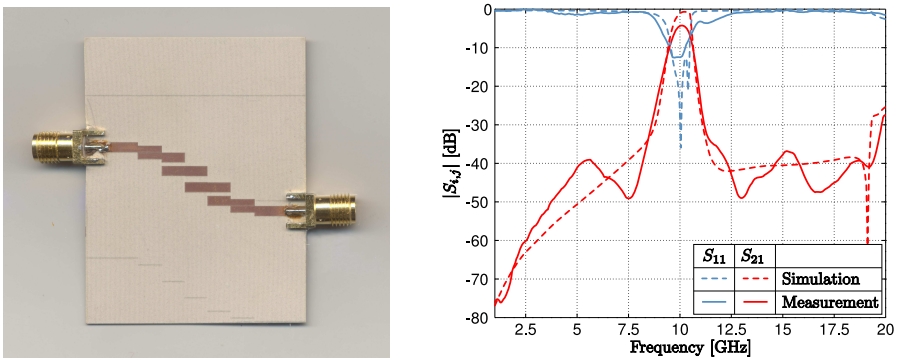

(a) (b)

Figure 4.7: (a) Manufactured output filter prototype. (b) Simulated and measured scattering parameters of the output filter design.

4.2.3. Output Filter

The low power fourth harmonic oscillator is designed to maximise the amplitude of the fourth harmonic component of the oscillation frequency, at 10 GHz, that is delivered to the external load connected to the transistor drain terminal through the multiharmonic load, as shown in Figure 4.1. Nonetheless, in order to further improve the signal purity in the output port, a passband filter that increases the attenuation of the adjacent harmonic components is integrated in the circuit topology.

A parallel coupled filter with half wavelength resonators has been realised using the design equations summarised in [8]. A fourth order Butterworth response with a fractional bandwidth $FBW = 0.1$ GHz centred at 10 GHz, has been chosen for this design. As was the case with the input filter, the DC blocking behaviour of the coupled line topology is advantageous to prevent the direct current flow through the external output load, enabling the normal DC biasing of the transistor drain terminal.

The prototype of the final filter shown in Figure 4.7(a) has been manufactured for the experimental validation of the design. The measured scattering parameters are compared with the results of the electromagnetic MoM simulation of the structure in Figure 4.7(b). The measured insertion loss in the passband is about 4 dB, slightly higher than the simulated results. As expected, high attenuation levels are introduced at the remaining harmonic componets of the fundamental frequencies.

4.3. Simulation Set-up

The auxiliary networks described in the foregoing sections have been individually developed to meet the specific a priori requirements of the fourth harmonic oscillator design. Since these subcircuits have already been optimised for their particular purpose within the circuit topology presented schematically in Figure 4.1, they will not be modified during the design process of the complete circuit structure.

In order to provide an accurate model of these networks for the subsequent simulations of the complete circuit topology, full wave electromagnetic simulations of these individual components have been performed using the Method of Moments (MoM) simulator included in Advanced Design System (ADS). Since the design process will be mainly based on non-linear analyses, the frequency plan chosen for the electromagnetic simulations is primarily focused on the harmonic components of the fundamental oscillation frequency $f_0 = 2.5$ GHz. The performance of the subcircuits is evaluated in 1 GHz wide frequency bands centred at the first ten harmonic components of the oscillation frequency (as well as between DC and 500 MHz), with a 1 MHz step, and complemented with a general sweep between DC and 25.5 GHz with a 50 MHz step.

Since a footprint of the transistor packaging must be introduced in the circuit to solder the device, this footprint has also been modelled through electromagnetic simulations with the same frequency plan.

Once the electromagnetic models in terms of scattering parameters of these individual components have been obtained, they are introduced in the oscillator topology shown in Figure 4.1, composed in the schematic simulator of ADS. The remaining transmission line networks: the multiharmonic loads, series feedback, input and output connecting lines, etc.—which are subject to changes during the design and optimisation process—are implemented with the library models of the simulator.

Although the particular details of the simulations of the circuit that will carried out in the following will be specified in each case, the set-up that has been described will be the base for all of them, unless otherwise stated.

4.4. Oscillation Start-up

The circuit topology shown schematically in Figure 4.1 intrinsically presents a trivial non-oscillatory solution, which makes it an attractive choice for the implementation of amplifier designs. However, for oscillator based applications in which a robust autonomous solution is sought, this DC solution must be made unstable, in order to allow the onset of the required oscillatory solutions.

The stability of a particular steady state solution, as has been widely explained in Section 1.2.3, is determined by its behaviour in the presence of the small perturbations that always exist in practical systems. The solution will be stable if it is capable of recovering from these perturbations. Because the stability properties of a particular steady state solution depend exclusively on the response of the system to small perturbations, the stability analysis can be performed through the linearisation of the system about this specific solution.

As described in Section 1.3.3.2, a closed loop transfer function of the circuit, associated with a linearisation about a given steady state solution can be obtained by simply perturbing the system operation regime with a small signal current generator, connected to a sensitive node of the circuit; in this case, the transistor drain terminal has been chosen. The single input single output transfer function can be directly calculated as the input impedance of the perturbed node, given by the relationship between the node voltage V_n and the perturbing current I_n at the frequency ω, as follows:

$$Z_n(\omega) = \frac{1}{Y_n(\omega)} = \left.\frac{V_n}{I_n}\right|_{\omega}. \tag{4.1}$$

Unless exact pole zero cancellations occur, all the closed loop transfer functions associated with the different circuit nodes provide the necessary stability information about the selected solution of the circuit. In particular, as discussed in Section 1.3.3.2, fulfilment of (4.2), which can be easily checked by simply observing the behaviour of the input admittance $Y_n(\omega)$, indicates the existence of a pair of complex conjugate poles with positive real part, which makes the solution unstable.

$$\begin{aligned} Y_n^r(\omega_0) &< 0 \\ Y_n^i(\omega_0) &= 0 \\ \frac{\partial Y_n^i(\omega_0)}{\partial \omega} &> 0 \end{aligned} \tag{4.2}$$

The closed loop transfer function $Z_n(\omega)$ obtained through this procedure corresponds to a linearisation of the circuit about the solution that has been perturbed in the simulation. Taking advantage of the fact that conventional harmonic balance simulations converge unaided to the DC solution of the circuit, no additional initialisation techniques are required for the simulation of this solution. Thus, the harmonic balance simulation can be performed considering one single fundamental: the frequency of the perturbation generator, which is swept throughout the desired frequency range. Due to the small amplitude of the perturbation, no harmonic components of this fundamental need to be considered.

Thus, using these simulations, the circuit networks have been tuned to synthesise a pair of complex conjugate poles with positive real part in the closed

loop transfer function associated with the DC solution, which makes this spurious equilibrium unstable. The input admittance of the tuned design $Y_n(\omega)$ is shown in Figure 4.8, where the fulfilment of (4.2) at 2.5 GHz can be verified.

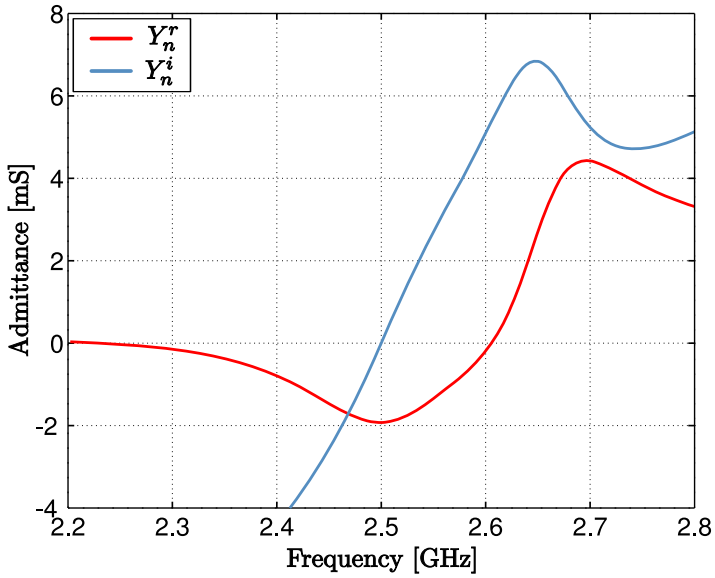

Figure 4.8: Fulfilment of (4.2), that indicate the existence of a pair of complex conjugate poles with positive real part in the closed loop transfer function $Z_n(\omega)$, linearised about the DC solution of the circuit.

The existence of a pair of complex conjugate poles with positive real part at 2.5 GHz means that the DC solution of the system is not practically observable, as the slightest perturbation of this steady state regime will start an oscillatory transient at this frequency, with—initially—exponentially growing amplitude, which will take the circuit to a stable steady state solution. Since the linearised analysis that has been performed progressively loses its accuracy as the amplitude of the perturbation grows, this final stable steady state solution cannot be predicted using this linearisation, and a complete non-linear analysis must be carried out. Nonetheless, the frequency of the unstable poles (in this case 2.5 GHz) is generally a good starting point for the non-linear optimisations, as will be shown in the next sections.

4.5. Periodic Steady State Solutions

As has been discussed in Section 1.3.2, the simulation of autonomous regimes in the frequency domain is not straightforward and it generally requires the use of complementary initialisation techniques, such as the introduction of non-

perturbing auxiliary generators, which enable the analysis of autonomous solutions as conventional forced regimes.

The non-linear analysis of this fourth harmonic oscillator design is performed using harmonic balance simulations with one single fundamental, $f_0 = 2.5$ GHz, taking into account its first ten harmonic components. The autonomous solution is initialised using a voltage auxiliary generator connected to the transistor drain terminal. In order to assure that the circuit can spontaneously sustain the solutions calculated through this approach, the auxiliary generator must fulfil the non-perturbation condition (4.3), in terms of the input admittance at the auxiliary generator connection node Y_{AG}:

$$Y_{AG} = \left.\frac{I_v}{V_{AG}}\right|_{\omega=\omega_{AG}} = 0, \tag{4.3}$$

which guarantees that the auxiliary generator does neither deliver energy to the circuit nor dissipate it. Fulfilment of (4.3) adds two additional equations to the conventional harmonic balance system, together with three degrees of freedom associated with the parameters of the auxiliary generator: voltage V_{AG}, frequency $\omega_{AG} = 2\pi f_{AG}$ and phase φ_{AG}.

For the analysis of a conventional free running oscillator, the phase of the auxiliary generator can be arbitrarily set to 0, taking advantage of the independence of the solution of the phase origin, and the frequency and amplitude of the auxiliary generator are optimised to fulfil the non-perturbation condition (4.3).

Nonetheless, the goal in this case is to synthesise an oscillatory steady state solution with the desired amplitude and frequency ($f_{AG} = 2.5$ GHz and $V_{AG} = 1.9$ V) . Thus, the frequency and amplitude of the auxiliary generator are set to these values and the geometrical parameters of the networks implemented with library components are optimised to fulfil the non-perturbation condition. This optimisation process leads to a design that possesses an autonomous steady state solution with the values of amplitude and frequency imposed by the auxiliary generator. However, no further assumption can be made as to the stability of this solution, which must be subsequently evaluated using the techniques described in Section 1.3.3.2.

The preliminary design obtained as a result of this first optimisation presents the output power levels shown in Figure 4.9. The output power P_o is the power delivered to the Z_0 impedance that represents the output port in the circuit topology shown in Figure 4.1.

The output power spectrum of the preliminary design shows a dominant fourth harmonic component at 10 GHz, with a level about -41 dBm. However, this behaviour is in fact originated by the response of the output filter (shown in Figure 4.7(b)), which attenuates the first harmonic components over 60 dB.

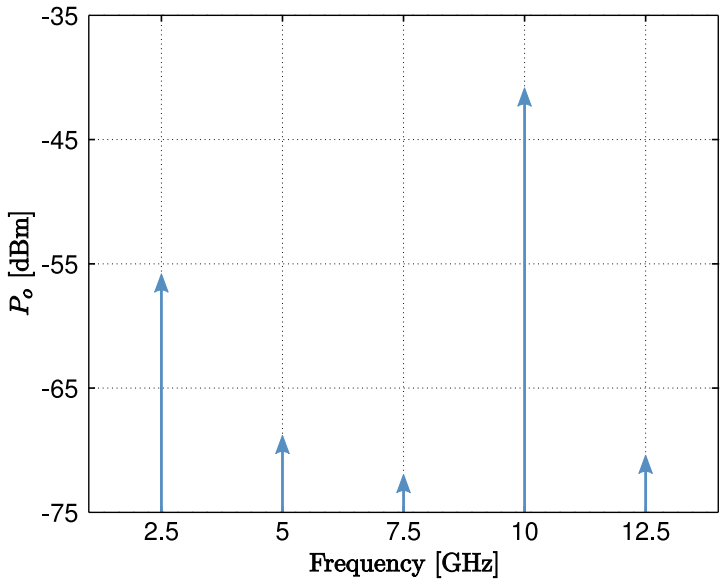

Figure 4.9: Output power spectrum of the preliminary fourth harmonic oscillator design.

Therefore, this first circuit version generates a dominant component at the oscillation frequency and a relatively weak fourth harmonic at 10 GHz, leading to the low output power level that has been observed. To increase the output power level at this harmonic component, the circuit must be optimised to enhance the fourth harmonic generation at the non-linear device, as well as to improve the transmission of this component through the output networks to the load, as will be shown in the following.

4.5.1. Harmonic Content Enhancement

The desired output signal for this circuit topology is the fourth harmonic of the fundamental oscillation, at $4f_0 = 10$ GHz, while the presence of the rest of harmonic components in the output of the circuit is detrimental and must be kept under control. The output filter has been designed to introduce relatively high attenuation levels to this undesired harmonic components, in order to assure certain degree of purity in the output signal.

In the preliminary design obtained in the previous section, the filter response severely attenuates the undesired components, giving rise to an output power spectrum dominated by the weak fourth harmonic generated by the circuit. The performance of the design could be improved by optimising the harmonic content generated in the circuit, both to increase the level of the fourth harmonic produced and to reduce the power of the other undesired components.

Nonetheless, even though the fundamental oscillation at $f_0 = 2.5$ GHz is not valuable as an output signal, its amplitude determines the operation regime of the transistor, which has a strong influence on the harmonic content generated. Since a relatively high fourth harmonic generation has been observed for an amplitude of the fundamental oscillation about 1.9 V, this value—which is directly imposed by the auxiliary generator—will be maintained constant throughout this design stage.

Thus, the geometrical parameters of the circuit multiharmonic loads, series feedback, input and output networks are optimised to improve the level of the fourth harmonic delivered to the output load, as well as to reduce—as far as possible—the power delivered at the remaining components, while keeping the amplitude of the auxiliary generator $V_{AG} = 1.9$ V. The output power spectrum of the optimised design with enhanced harmonic content is presented in Figure 4.10.

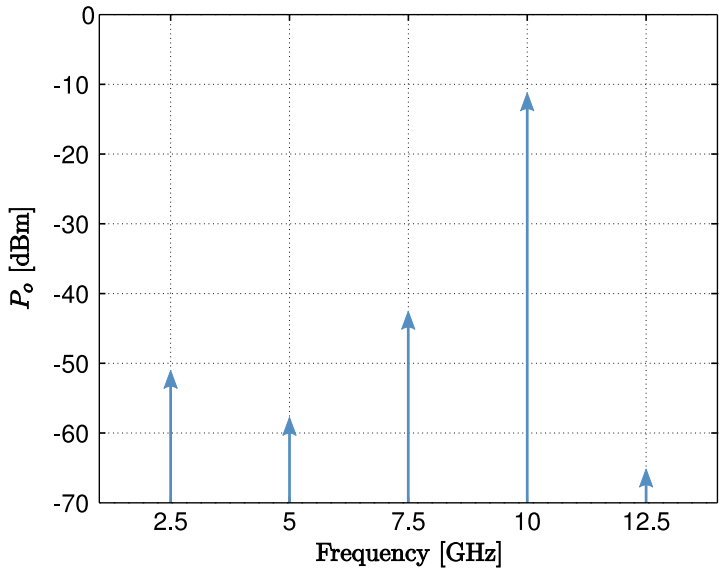

Figure 4.10: Output power spectrum of the design with enhanced harmonic content.

The power level delivered to the output load at the fourth harmonic component has increased to $P_o(4f_0) = -11.45$ dBm. Although the amplitude of the fundamental component at the drain terminal has been kept constant by the auxiliary generator, the power level delivered to the load at this frequency has slightly increased with regard to the previous preliminary design (from -55.82 to -51.24 dBm). Despite the unintended increase in the output level at the undesired frequency components, as a result of the optimisation process, these components are maintained over 31 dB below the fourth harmonic ($P_o(3f_0) = -42.76$ dBm).

$P_o(4f_0)$ [dBm]	$P_o(4f_0)$ [μW]	I_D [mA]	P_{DC} [mW]	η [%]
-11.45	71.6	15	28.5	**0.25**

Table 4.2: Summary of the power levels delivered and consumed by the design with enhanced harmonic content that has been obtained.

The transistor device is biased with a voltage $V_{DS} = 1.9$ V, using a DC power supply connected to the drain terminal through the associated bias network. The current absorbed by this design with enhanced harmonic content is $I_D = 15$ mA, corresponding to a total DC power consumption $P_{DC} = 28.5$ mW. Considering the power efficiency of the circuit η, as the ratio—in percentage terms—between the output power delivered at the fourth harmonic component of the oscillation $P_o(4f_0)$ and the DC power consumed P_{DC}, as follows:

$$\eta = \frac{P_o(4f_0)}{P_{DC}} \cdot 100, \tag{4.4}$$

and taking into account the output levels and power consumption that have been specified, the design presents a power efficiency $\eta = 0.25\%$, as summarised in Table 4.2.

The design with enhanced harmonic content that has been presented exhibits a moderately high DC power consumption, leading to a relatively low efficiency value. Moreover, this power consumption limits the potential application of this circuit in low power portable or mobile solutions, where this parameter is a critical aspect. Hence, even though the harmonic content of the circuit could be further optimised to produce higher output power levels, the following design stage will be primarily aimed at reducing the power consumption, giving rise to a suitable solution for this kind of applications.

4.5.2. Low Power Optimisation

The fourth harmonic oscillator topology addressed in the present chapter has been conceived as a multifunctional control circuit for the implementation of reconfigurable active antenna arrays applied to low power point-to-point communications between portable or mobile devices. Nevertheless, since the efficiency and—especially—the power consumption, are critical limiting factors in this type of systems, which are generally battery powered, the relatively high power consumption that has been observed in the design presented in the previous section seriously compromises its potential use for this target application.

To tackle this limitation, the purpose of this section is to produce a low power consuming design that preserves an optimised harmonic content, characterised

by the generation of a fourth harmonic component with relatively high output power level.

The non-linear device chosen for this topology is a depletion mode pseudomorphic high electron mobility transistor. When this type of device is biased with a drain to source voltage V_{DS}, the current drawn from the power supply through the drain terminal I_D, can be controlled through the gate to source bias voltage V_{GS}. In the depletion mode case, the DC power flow I_D, for a given drain to source voltage V_{DS}, is maximum for the gate to source voltage $V_{GS} = 0$ V. As the gate to source union is reversely biased ($V_{GS} < 0$ V), the drain current I_D progressively decreases until it completely vanishes for the pinch off voltage $V_{GS} = V_{\text{pinch off}}$.

The operation point chosen for the transistor in the previous designs corresponds to $V_{DS} = 1.9$ V and $V_{GS} = 0$ V. Therefore, the current drawn by the circuit from the DC supply can be limited by introducing a gate to source reverse bias voltage $V_{GS} < 0$ V, giving rise to a lower power consumption. Since the gate source union of this pHEMT device is a Shottky barrier, the current flow through the gate terminal is negligible and consequently, this biasing does not contribute to increasing the power consumption.

After a preliminary analysis of the transistor performance in different operation points, in terms of the absorbed power, harmonic content generated and other parameters, a gate to source voltage value $V_{GS} = -0.51$ V has been chosen. The drain to source voltage, on the other hand, is maintained at the previous value $V_{DS} = 1.9$ V, in which an adequate behaviour regarding harmonic generation has been observed.

The modification of the transistor operation point directly affects its electrical parameters and, in consequence, the input and output impedances it must be loaded with to operate in a specific regime. As has been commented, in order to enable the onset of the desired stable periodic steady state regime, the instability of the coexisting constant solution inherent in this circuit topology must be verified. Hence, the design parameters of the input and output networks have been readjusted for the fulfilment of (4.2) at the selected operating point.

As has been described, the large signal solutions of the circuit are studied through harmonic balance simulations initialised using a non-perturbing voltage auxiliary generator connected to the transistor drain terminal. The amplitude of the fundamental oscillation is set to a fixed value V_{AG}—imposed by the auxiliary generator—and the design parameters are optimised for the fulfilment of the non-perturbation conditions (4.3). After evaluating the influence of the amplitude of the fundamental component on the fourth harmonic generation, the same value used in the previous cases $V_{AG} = 1.9$ V, has been maintained.

A thorough optimisation of the circuit design parameters: series feedback, input and output networks, multiharmonic loads, and so forth, has been performed

to maximise the power level at the fourth harmonic component delivered to the output load. Since the other harmonic components are detrimental as output signals, the power delivered at of these components is wasted and contributes to decrease the efficiency. Thus, the level of these components is also limited as a secondary goal of the optimisation. The output power spectrum of the low power fourth harmonic oscillator design with optimised harmonic content that has been obtained is shown in Figure 4.11.

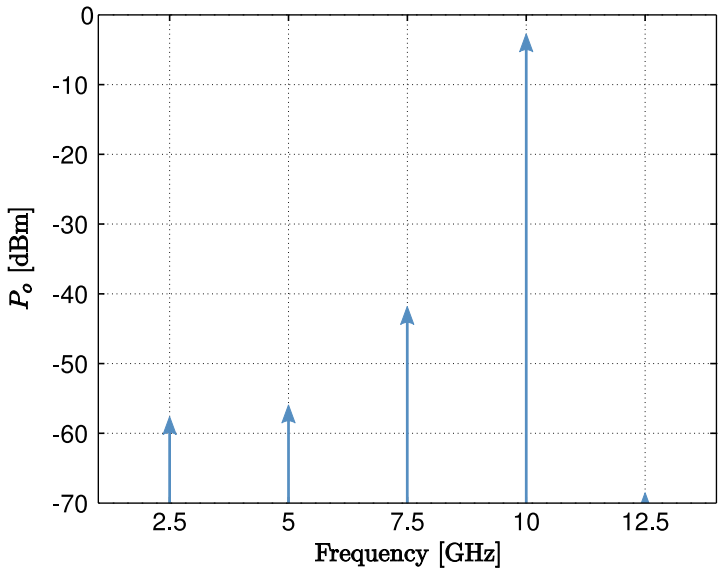

Figure 4.11: Output power spectrum of the low power fourth harmonic oscillator design with optimised harmonic content.

The low power design with optimised harmonic content that has been obtained features an output power level at the fourth harmonic $P_o(4f_0) = -2.93$ dBm, while the undesired frequency components are nearly 40 dB below the fourth harmonic ($P_o(3f_0) = -42.04$ dBm).

For the chosen transistor drain to source bias voltage $V_{DS} = 1.9$ V, the current drawn from the power supply by this optimised design is $I_D = 3.3$ mA, corresponding to a total DC power consumption $P_{DC} = 6.27$ mW. The efficiency of this low power fourth harmonic oscillator design with optimised harmonic content is $\eta = 8.12\%$, as summarised in Table 4.3.

In conclusion, the careful choice of an appropriate operating point for the transistor, together with the employment of non-linear global optimisation techniques, has enabled the control of the harmonic content in a conventional oscillator circuit topology, while maintaining a reduced power consumption, leading to a fourth harmonic oscillator design suitable for its target application in re-

$P_o(4f_0)$ [dBm]	$P_o(4f_0)$ [μW]	I_D [mA]	P_{DC} [mW]	η [%]
-2.93	509.33	3.3	6.27	**8.12**

Table 4.3: Summary of the power levels delivered and consumed by the low power fourth harmonic oscillator circuit with optimised harmonic.

configurable active antenna arrays for low power point-to-point communications between portable or mobile devices.

4.6. Injection Locked Solutions

As has been discussed in Section 1.5, when the operation of a free running oscillator with a natural frequency f_0 is perturbed by the injection of a periodic external signal of frequency f_s, under certain conditions, the interaction results in the onset of a constant phase relationship between the fundamental oscillation and the external signal, in virtue of a phenomenon known as synchronisation or injection locking.

In the particular case of fundamental synchronisation, which takes place when the frequency of the external signal f_s is close to the fundamental frequency of the oscillator f_0, the phase difference between the fundamental oscillation and the external signal $\Delta\phi = \phi - \phi_s$, is constant and therefore, the frequency of the oscillation matches that of the forcing $f_\Omega = d\phi/dt = f_s$. Moreover, this constant phase difference $\Delta\phi$, which can be varied in a theoretical range of 180°, is directly dependent on the frequency detuning $\nu_f = f_s - f_0$, given by the separation between the frequency of the forcing signal and the natural frequency of the oscillator.

The fourth harmonic oscillator topology that has been designed includes a varactor diode in the series feedback network, as shown schematically in Figure 4.1. The tuning of this device with a DC control voltage V_c, applied through the corresponding bias network, modifies the varactor capacity C_{var}, which affects the natural oscillation frequency of the circuit $f_0(V_c)$, enabling its operation as a Voltage Controlled Oscillator (VCO).

Therefore, when the fourth harmonic oscillator design is injection locked to an external signal of fixed frequency f_s, the modification of the control voltage V_c produces a variation in the frequency detuning $\nu_f = f_s - f_0(V_c)$, allowing the tuning of the phase shift between the oscillation frequency and the external reference signal $\Delta\phi$ in a theoretical continuous range of 180°, while the oscillation frequency remains constant $f_\Omega = d\phi/dt = f_s$.

Since the circuit has been optimised to produce a fourth harmonic component of the oscillation as the output signal, the theoretical stable phase shift range

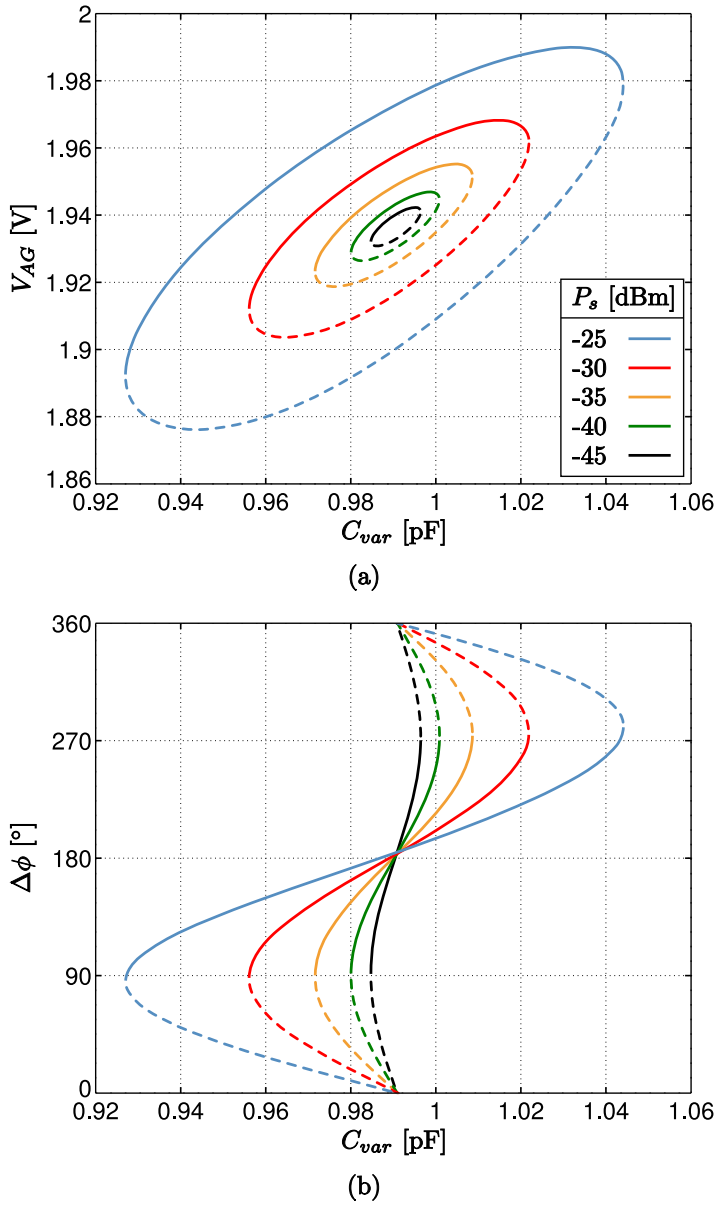

Figure 4.12: Injection locked solutions of the fourth harmonic oscillator design versus the varactor capacity C_{var}, for different values of the synchronisation power P_s. (a) Amplitude of the auxiliary generator V_{AG} (b) Phase shift at the fundamental component $\Delta\phi$. The stable ranges are indicated in solid line.

available between the fourth harmonic component ϕ_o and the synchronisation signal $\Delta\phi_o = \phi_o - \phi_s$, is four times the range at the fundamental component:

720°. Although these ranges are generally reduced in the presence of noise and other non-linear effects [9], the employment of the fourth harmonic component as the output signal guarantees a usable stable range of 360°, necessary for the control of antenna arrays.

The injection locked solutions of the circuit are calculated through the procedure explained in Section 1.5. The autonomous oscillation is conveniently initialised using a non-perturbing voltage auxiliary generator with the same frequency as the external generator $f_{AG} = f_s$. Taking advantage of the fact that the solution curves are not multivalued in phase in the interval $[0, 360°)$, the phase of the auxiliary generator ϕ_{AG} is swept throughout this interval, optimising the values of amplitude of the auxiliary generator V_{AG} and varactor capacity C_{var} that satisfy the non-perturbation conditions (4.3).

The injection locked solutions versus the varactor capacity C_{var}, obtained for power values of the external signal f_s between -45 and -25 dBm are shown in terms of amplitude of the auxiliary generator V_{AG} in Figure 4.12(a) and phase shift $\Delta\phi = \phi_{AG} - \phi_s$ in Figure 4.12(b).

As expected, the phase variation interval is the same for all the synchronisation power values considered, while the tuning range of the varactor capacity C_{var} (and, consequently, of the natural frequency of the oscillator f_0) necessary to cover it increases with the injected power P_s. The phase solution curves corresponding to the different synchronisation power levels intersect at phase values separated 180°. At these operation points, the phase shift $\Delta\phi$ is not influenced by the synchronisation power level P_s. For the sake of clarity, the phase of the external signal ϕ_s has been arbitrarily set in the simulation for the phase solution curves to intersect at $\Delta\phi = 0$.

The synchronisation loci that have been obtained are multivalued in the varactor capacity C_{var}. Because these curves have been calculated through harmonic balance simulations, no assumption can be made as to their stability properties, that must be subsequently analysed using complementary techniques. In this case, the stable parts of the solution curves—which are indicated in solid line—have been determined using envelope transient simulations.

The solution curves for the output power $P_o(4f_0)$ are shown in Figure 4.13(a), and for the phase shift of the output signal ϕ_o with regard to the external reference $\Delta\phi_o = \phi_o - \phi_s$ in Figure 4.13(b). The stable ranges calculated using envelope transient simulations are indicated in solid line. In order to clearly show the separation between the output power loci, their central region has been magnified in the inset of Figure 4.13(a).

In this case, the phase solution curves for the different synchronisation power levels intersect at phase values separated 720°. Once again, the phase of the external signal ϕ_s has been arbitrarily set in the simulation for the phase curves to intersect at $\Delta\phi_o = 0°$.

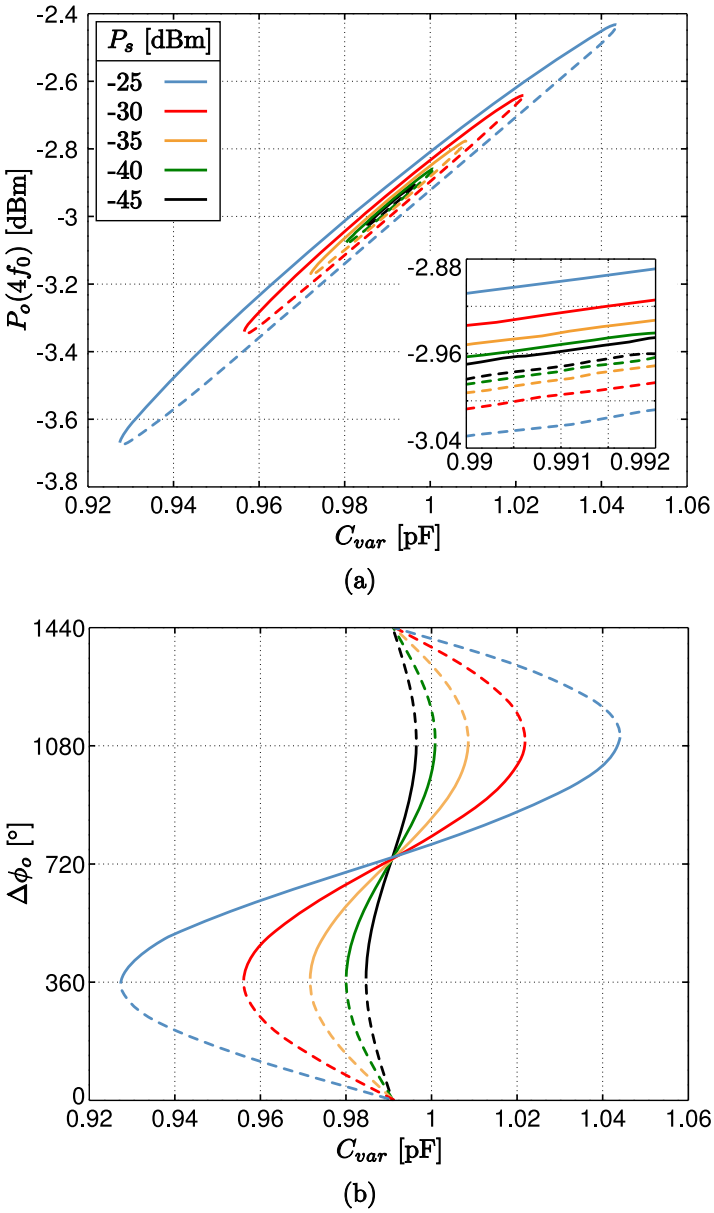

Figure 4.13: Injection locked solutions of the fourth harmonic oscillator design versus the varactor capacity C_{var}, for different values of the synchronisation power P_s. (a) Output power $P_o(4f_0)$ (b) Phase shift of the output signal $\Delta\phi_o$. The stable ranges are indicated in solid line.

The selection of the fourth harmonic component as the output signal provides a stable continuous phase shift range of about 720°, that considerably exceeds the

360° range usually required for the control of antenna arrays. Hence, the required 360° range can be entirely covered in the central part of the stable range, leading to a higher linearity of the phase shift response versus frequency. Moreover, the detrimental non-linear effects that generally appear when operating close to the limits of the synchronisation region [9] may be avoided.

4.7. Experimental Results

For the experimental validation of the fourth harmonic oscillator that has been designed in the preceding sections, the prototype shown in Figure 4.14 has been manufactured.

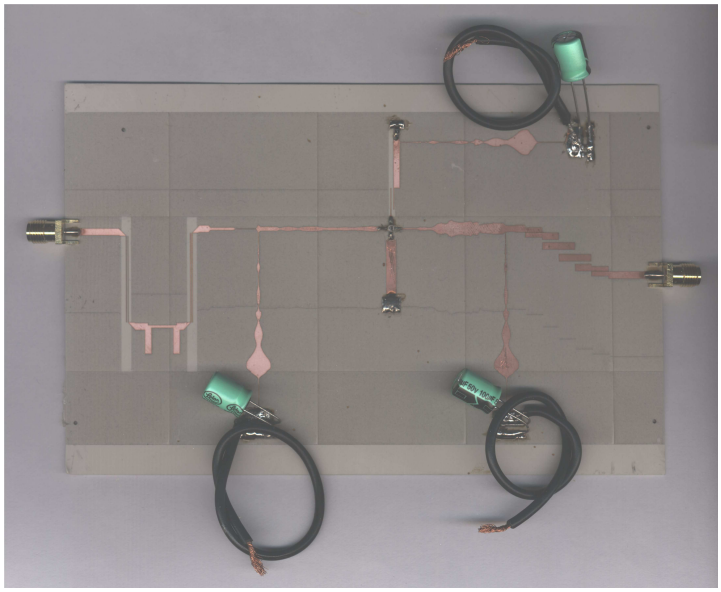

Figure 4.14: Manufactured prototype of the fourth harmonic oscillator circuit.

The potential fluctuations of the DC bias signals may have a detrimental effect on the circuit performance. Thus, in order to stabilise the bias signals, minimising these fluctuations, a 100 pF and a 100 nF chip capacitor have been connected in parallel with each of the DC pads, together with a 100 μF electrolytic capacitor.

In this section, the performance of the circuit under multiple operating conditions will be analysed though different types of measurements.

4.7.1. Output Power Spectrum

The output power spectrum of the circuit has been measured with a Rohde & Schwarz FSP 40 spectrum analyser. An image of the measurement set-up is shown in Figure 4.15.

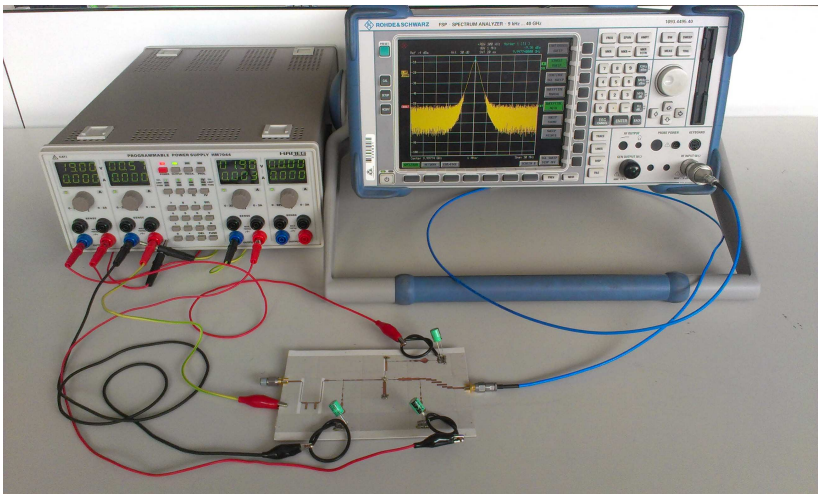

Figure 4.15: Output power spectrum measurement set-up.

Three channels of the DC source has been used to bias the circuit. From left to right in Figure 4.15, the first and second channels are used to reversely bias the varactor diode and the gate terminal of the pHEMT transistor, while the third, which is the only one delivering power to the circuit, is connected to the drain terminal.

The varactor diode is reversely biased with a voltage $V_c = 19$ V, corresponding to low value of the union capacitance. The drain terminal is biased with the design voltage $V_{DS} = 1.9$ V and, when the gate terminal is reversely biased with a voltage $V_{GS} = -0.57$ V, the circuit draws a current $I_D = 3$ mA through the drain terminal.

Since, under these conditions, the 4HOSC circuit is operating as a free running harmonic oscillator and the input port is not used, it has been terminated with a 50 Ω load.

Due to the additional losses introduced by the connecting RF cable and the output end launch connector, the power measured by the spectrum analyser will be appreciably lower than the output power generated by the circuit. Therefore, the frequency dependent losses of the connector and the RF cable have been measured separately, in order to correct the measured spectrum, referring it to the power delivered at the output microstrip line. The combined losses at 10 GHz amount to $L(10\text{ GHz}) = 4.45$ dB.

The complete corrected output power spectrum of the circuit, measured between 2 and 13 GHz, has been represented in Figure 4.16.

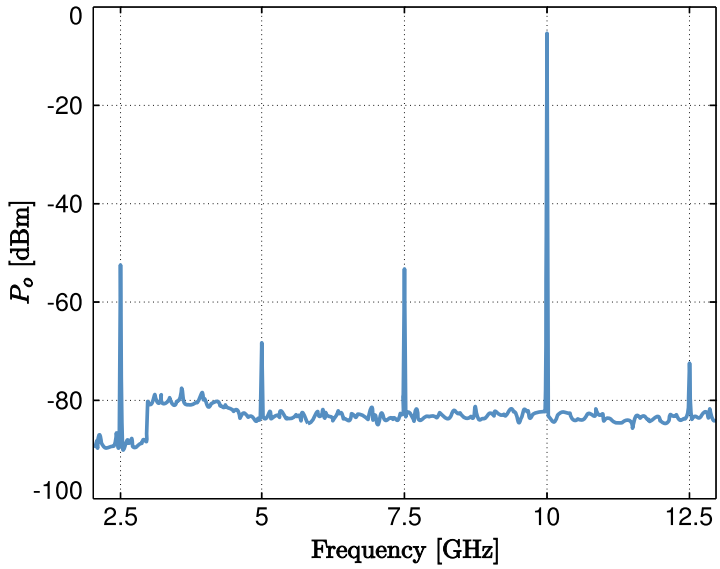

Figure 4.16: Corrected output power spectrum of the fourth harmonic oscillator circuit.

The spectrum is dominated by the fourth harmonic component of the oscillation, at a frequency $4f_0 = 9.998$ GHz, with a level $P_o(4f0) = -5.05$ dB.

This measured level is lower than the value obtained in the simulated results (-2.93 dB), shown in Figure 4.11. Similarly, other discrepancies have been observed between the simulated and measured levels of the different harmonic components.

Nonetheless, this disagreement is clearly originated by the behaviour of the output filter. As was already shown in Figure 4.7(b), the electromagnetic simulation of the filter, which has been used to perform the circuit optimisation, follows reasonably well the trend of the measured performance, although the specific values at the circuit harmonic components present some differences.

At the first and second harmonic components, where the measured filter insertion losses are lower than the simulated values, the measured output power at those components is higher than the simulated results. Conversely, at the third, fourth and fifth harmonic components, the measured filter insertion losses are higher than the simulated value, and the measured levels of those components are lower than the simulated values.

Hence, the steady state regime observed in the practical circuit matches the solution optimised in the simulations. As per its power efficiency, a value $\eta = 5.48\%$ has been attained, as summarised in Table 4.4.

$P_o(4f_0)$ [dBm]	$P_o(4f_0)$ [μW]	I_D [mA]	P_{DC} [mW]	η [%]
-5.05	31.26	3	5.7	**5.48**

Table 4.4: Summary of the power levels delivered and consumed by the manufactured fourth harmonic oscillator.

Due to the additional insertion losses observed in the passband of the output filter, with regard to the simulated result, the measured output power does not reach the simulated result, limiting the power efficiency value that can be achieved.

For the design of this first prototype, stringent requirements were imposed in terms of the attenuation of the output filter at the undesired harmonic components to prevent potential practical problems. Nevertheless, after verifying that those requirements can be relaxed, the efficiency of the circuit could be straightforwardly improved by redesigning the output filter to reduce the insertion losses in the passband.

4.7.2. Operation as a Voltage Controlled Oscillator

In the fourth harmonic oscillator circuit topology that has been described, a varactor diode was introduced in the series feedback network for tuning purposes. By changing the DC control voltage of this diode V_c, the frequency at which the autonomous oscillation occurs can be varied: $f_0 = f_0(V_c)$, giving rise to a Voltage Controlled Oscillator (VCO) implementation.

The oscillation frequency tuning capabilities of the circuit have been measured with a Rohde & Schwarz FSP 40 spectrum analyser, while sweeping the varactor bias voltage V_c, throughout the continuous range between 16.35 and 20.37 V, where the circuit exhibits a stable, free from hysteresis behaviour.

The circuit performance has been evaluated at 13 operating points, corresponding to 13 operating frequencies uniformly spaced throughout the tuning range. The associated output power spectra are shown in Figure 4.17(a), focusing on the fundamental oscillation component, while those corresponding to the fourth harmonic component, are presented in Figure 4.17(b).

The fundamental oscillation frequency f_0 can be tuned in a 12 MHz range between 2.4903 and 2.5022 GHz. The low amplitude levels observed in the fundamental component are produced by the high attenuation level introduced by the output filter at that frequency.

As expected, the fourth harmonic component presents substantially higher power levels, together with a frequency tuning range four times as wide: 48 MHz, from 9.961 to 10.009 GHz.

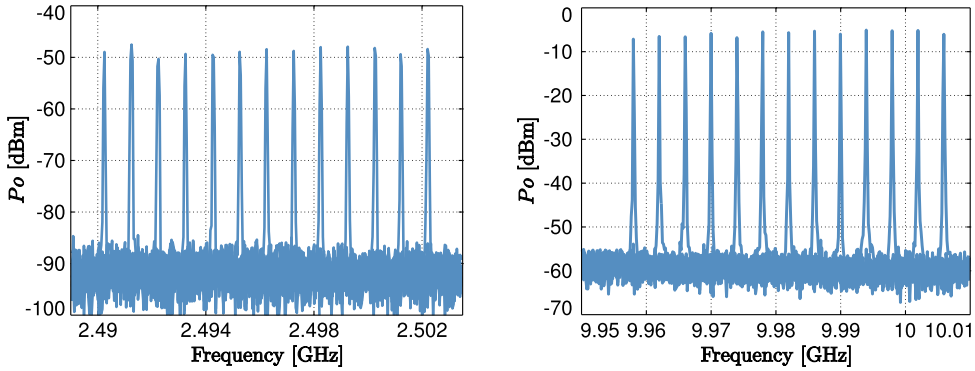

(a) (b)

Figure 4.17: Measured output spectra of the fourth harmonic oscillator: (a) About the fundamental oscillation component. (b) Focusing on the fourth harmonic component.

Since the fourth harmonic component of the oscillation is the desired output signal, in the interest of clarity, the output power level and frequency are related to the applied control voltage in Figure 4.18.

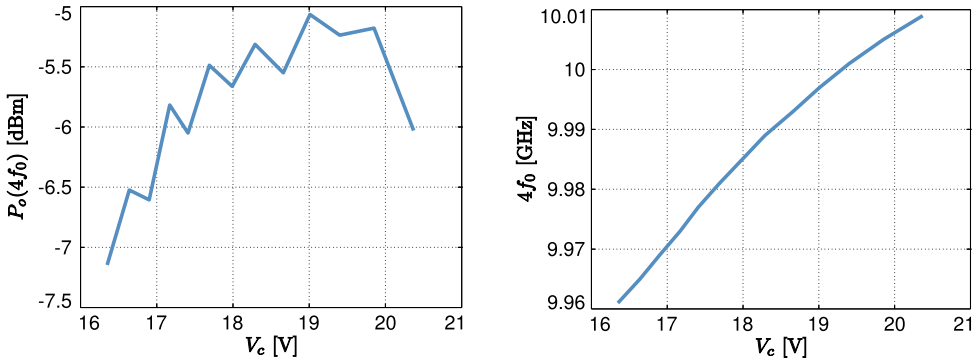

(a) (b)

Figure 4.18: (a) Output power level at the fourth harmonic component versus the applied control voltage V_c. (b) Frequency of the fourth harmonic component versus the applied control voltage V_c.

The output power level shows uneven fluctuations between adjacent points, caused by the relatively low frequency resolution of the spectrum analyser, for the frequency span selected in Figure 4.17(b). Nevertheless, the power level exhibits a very limited variation which barely exceeds 2 dB throughout the whole tuning range.

The frequency of the fourth harmonic component, as shown in Figure 4.18(b), presents a nearly linear dependence on the control voltage. At each operating point, the frequency of the fundamental oscillation can be calculated as one forth of those values.

4.7.3. Injection Locked Operation

The operation of the fourth harmonic oscillator as a continuous range phase shifter requires the injection of an external signal of power P_s, frequency f_s and phase ϕ_s. As has been commented, under specific conditions, the presence of the external perturbation leads to the onset of a constant relationship between the phase of the external signal ϕ_s and the phase of the autonomous oscillation ϕ, in virtue of a phenomenon known as injection locking.

In the particular case of fundamental injection locking, which takes place when the frequency of the external signal is close to the circuit natural frequency, $f_s \approx f_0$, the constant phase relationship can be written as $\Delta\phi = \phi - \phi_s$, causing the circuit to oscillate at the frequency of the external forcing $f_\Omega = 1/2\pi d\phi/dt = f_s$. Furthermore, the constant phase shift between the autonomous oscillation and the external signal, which is determined by the frequency detuning $\nu = f_s - f_0$: $\Delta\phi = \Delta\phi(\nu)$, can be controlled in a continuous theoretical range of 180°.

For most practical applications, where the phase tuning of a carrier with constant frequency is required, the appropriate operation regime of the fourth harmonic oscillator would be to injection lock it to an external signal of constant frequency f_s. Thus, the oscillation frequency of the circuit will remain constant $f_\Omega = f_s$, while the frequency detuning $\nu = f_s - f_0$, which, in turn, determines the phase shift of the oscillation signal, can be controlled through varying the oscillator natural frequency f_0, taking advantage of its operation as a voltage controlled oscillator that has been evaluated in the previous section.

As has been discussed in detail in Section 1.5, the range of frequency detuning values for which the circuit remains injection locked to the external signal—usually referred to as synchronisation range—generally increases with the power of the external signal, for relatively low power levels. The operation outside the synchronisation range has limited practical interest, since the circuit is no longer injection locked to the external signal and it oscillates at a different frequency $f_\Omega \neq f_s$, giving rise to a time dependent phase relationship $\Delta\phi = \Delta\phi(t)$. Nevertheless, the frequency tuning capabilities of the circuit, operating as a VCO, must be wide enough to enable the frequency detuning ν, to be swept throughout the synchronisation range as, otherwise, the associated phase shift range would be further reduced from the 180° theoretical value.

Hence, the frequency tuning range of the circuit, measured in the foregoing section, needs to be taken into account to adequately select the frequency of the external synchronisation signal, which cannot be too close to either limit of the

frequency tuning range, as this would result in a contraction of the maximum phase shift range that can be attained. Moreover, since the synchronisation range typically widens as the synchronisation power is increased (for relatively low power levels), for sufficiently high power levels, the circuit might become unable to cover the whole synchronisation range, regardless of the synchronisation frequency f_s chosen, remaining synchronised for all the values of the varactor control voltage V_c.

However, for practical applications, it is clearly advantageous in terms of system efficiency to maintain the required synchronisation power as low as possible. In this case, in order to be able to illustrate the injection locked performance of the circuit for synchronisation power levels between -40 and -20 dBm, the frequency of the reference signal has been chosen to be $f_s = 9.997$ GHz.

The injection locked operation of the circuit has been evaluated using an Agilent N5247A PNA-X Vector Network Analyser, which provides the external reference signal at a frequency $f_s = 9.997$ GHz, and measures the power and phase shift of the desired harmonic component of the oscillation through the output filter, as the varactor bias voltage V_c, is swept throughout the synchronisation range.

The measured synchronised solutions corresponding to the fundamental oscillation, for power levels P_s from -40 to -20 dBm, in steps of 5 dB, are shown in Figure 4.19(a), in terms of power, and in Figure 4.19(b), in terms of phase shift $\Delta\phi$.

Since the fundamental component is severely attenuated by the output filter, very low power levels have been measured at that component. As expected, for higher power levels of the external signal, the synchronisation range progressively widens, as does the interval of varactor bias voltages that needs to be swept to cover it.

The power level of the fundamental component increases its variation with the varactor control voltage for higher synchronisation power levels, the overall variation remains under 1.5 dB for all the measured cases.

With regard to the phase shift response, shown in Figure 4.19(b), a continuous phase shift range wider than 160° has been measured for $P_s = -25$ and $P_s = -20$ dBm. The measured phase shift ranges become increasingly smaller for lower values of the synchronisation power P_s. Although the phase shift ranges generally show a mild dependence on the applied synchronisation power, this dependence does not justify the significant contractions that have been observed, which are caused by practical limitation of the measurement set-up employed.

The varactor control voltage V_c is imposed using a Hameg HM7044 DC power supply, with a 10 mV voltage resolution. As the power of the external reference signal P_s is reduced and, consequently, the synchronisation range shrinks, the 10 mV step represents an increasingly greater fraction of the whole range.

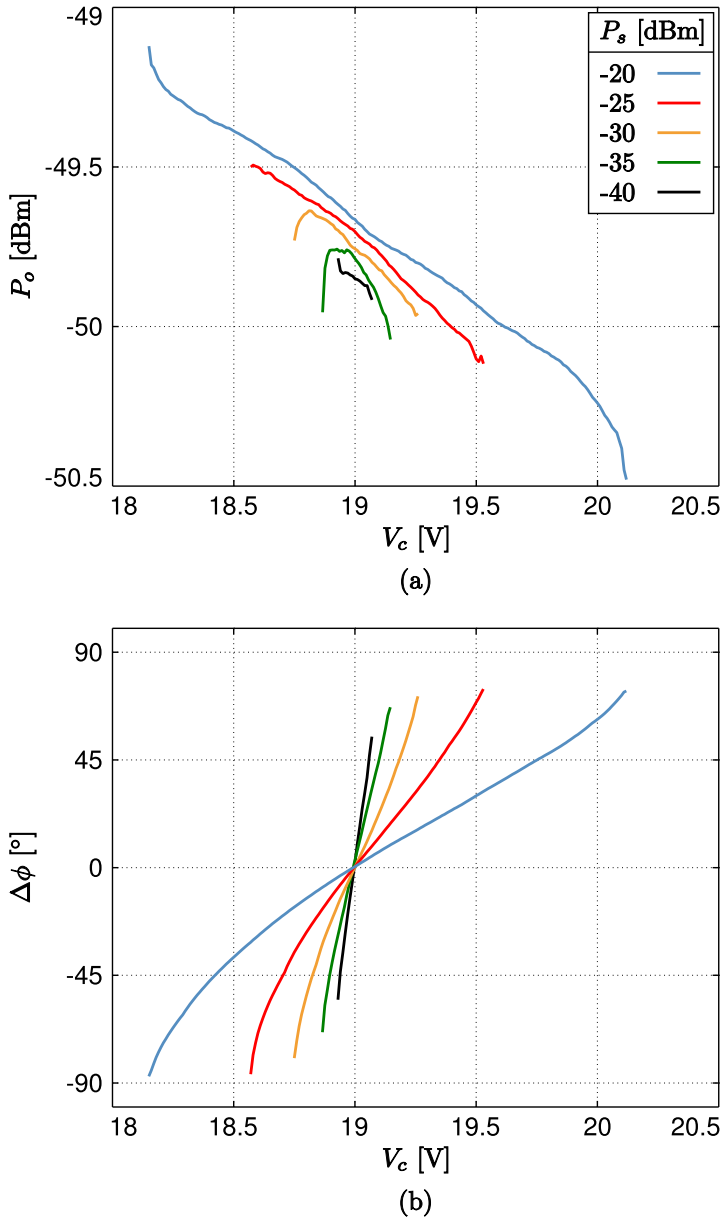

Figure 4.19: Measured synchronised solutions at the fundamental component of the fourth harmonic oscillator versus the varactor control voltage V_c. (a) Power measured through the output filter. (b) Phase shift with regard to the external reference signal.

Therefore, fewer of the practically available varactor voltage values correspond to injection locked solutions, giving rise to a relatively coarser sweep that restricts

closest proximity to the limits of the synchronisation range at which the measurement can be performed. Since the slope of the trace becomes maximum when approaching those limits, relatively small variations of the voltage at which the measurement is carried out bring about important fluctuations of the associated phase shift. Nonetheless, this limitation is not intrinsic to the circuit dynamics and could be mitigated by increasing the control voltage resolution.

The traces corresponding to all the measured synchronisation power values intersect for the operating point $V_c = 19$ V, at which the free running oscillator frequency equals that of the external reference signal: $f_0(V_c = 19\text{ V}) = f_s$. For the sake of clarity, the phase reference has been arbitrarily set for the associated phase shift to be $\Delta\phi(V_c = 19\text{ V}) = 0°$, at that operating point.

Since the desired output signal of the circuit is the fourth harmonic component of the oscillation, the injection locked solutions corresponding to that component have been analogously measured. The results are presented in Figure 4.20(a) in terms of output power and in Figure 4.20(b) in terms of phase shift with regard to the external reference $\Delta\phi_o = \phi_o - \phi_s$.

The output power exhibits a very limited variation with the control voltage V_c, which remains under 0.4 dB in all the studied cases. The power level slightly increases with the applied synchronisation power P_s.

Regarding the phase shift performance, stable ranges wider than 620° have been measured for $P_s = -25$ and $P_s = -20$ dBm. For lower synchronisation power levels, the observed ranges are narrower due to the limited resolution of the DC power supply. Once again, the phase reference has been deliberately established for the intersection between the different traces to take place at $\Delta\phi_o = 0°$.

In conclusion, the injection locked operation of the fourth harmonic oscillator provides a carrier signal with a relatively constant amplitude, whose phase can be straightforwardly controlled in a continuous range wider than 620°. Since only a 360° range is required for most practical applications, it can be covered with a restricted subinterval of the synchronisation range, which can be chosen to optimise different aspects of the circuit behaviour. For instance, according to 4.20(b), the operation of the circuit in the central region of the synchronisation range increases the linearity of its response to the control voltage V_c.

4.7.4. Phase Noise

The fundamental component of the oscillator signal has hitherto been considered a pure sinusoid of the form:

$$x_p(t) = A\cos(\omega_0 t + \phi_0), \tag{4.5}$$

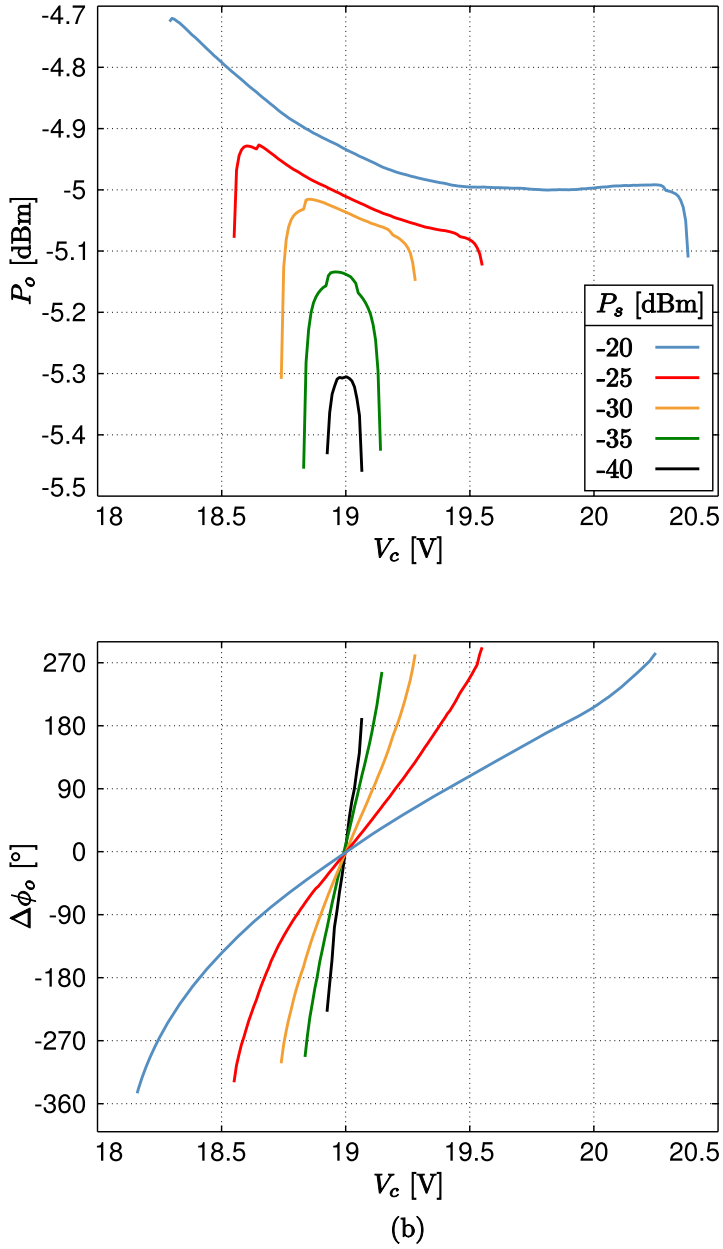

Figure 4.20: Measured synchronised solutions at the fourth harmonic component of the oscillation versus the varactor control voltage V_c. (a) Output power. (b) Phase shift with regard to the external reference signal.

where $\omega_0 = 2\pi f_0$, is the fundamental angular frequency of the oscillation. Due to the non-linearity of the circuit, a collection of discrete harmonic components are generated, whose relative levels have been optimised for different purposes.

However, in practice, the oscillator circuit operates under the influence of multiple perturbing phenomena of random nature, that affect the generated signals. Therefore, a more accurate model for the fundamental component can be written as:

$$x(t) = [A + \varepsilon(t)] \cos(\omega_0 t + \phi_0 + \phi(t)), \tag{4.6}$$

where $\varepsilon(t)$ and $\phi(t)$ are the instantaneous amplitude and phase random fluctuations, respectively. Both $\varepsilon(t)$ and $\phi(t)$, represent deviations or departures from a nominal value, and are thus defined as zero mean magnitudes, $\mathrm{E}\{\varepsilon(t)\} = \mathrm{E}\{\phi(t)\} = 0$, where $\mathrm{E}[\cdot]$ represents the expectation operator.

As has been pointed out, the non-linear steady state autonomous regime of the oscillator is self limited, in the sense that it is capable of recovering from perturbations that drive it outside the associated limit cycle, even though the dynamics of this recovery may be very slow. Conversely, due to the fact that an arbitrarily time shifted solution of an autonomous system is also a solution, the system is unable to recover from phase perturbations, that may thus accumulate indefinitely. Since this section is devoted to phase noise analysis, the amplitude fluctuations will henceforth be neglected.

Multiple works can be found in the literature, addressing the modelling simulation and prediction of the phase noise performance of different devices under various operating conditions [10; 11; 12; 13]. Nevertheless, those topics lie beyond the scope of this section, which is aimed at the measurement of the phase noise characteristics of the fourth harmonic oscillator circuit that has been designed, in several operation regimes. In order to perform these measurements, two different methodologies, which can be implemented with the existing laboratory equipment, will be described and compared.

Given the random nature of the the phase fluctuations $\phi(t)$, an adequate statistical characterisation of the process will be required in order to model the fundamental oscillation according to (4.6). Assuming $\phi(t)$ is a wide sense stationary process, it can be described through its power spectral density[1] $S_\phi(f)$, which represents the distribution of its average power over the frequency domain[2]. The phase spectrum $S_\phi(f)$, is considered a one-sided spectral density, only specified for frequencies $f \geq 0$.

The phase noise represents the single sideband spectral density of the phase fluctuations which, assuming symmetry between the sidebands, is defined as one

[1] In spite of the fact that $\phi(t)$ represents a phase, expressed in radians, and thus, its squared value cannot be considered *power*, the term *power spectral density* is commonly used in the literature notwithstanding, in analogy to the treatment given to conventional voltage signals.

[2] Note that, for notation convenience and in agreement with the existing literature in the field, the ordinary frequency f, instead of the angular frequency ω, has been chosen as the spectral domain variable in this section.

half of the phase spectrum $S_\phi(f)$, as follows [14]:

$$\mathscr{L}(f) = \frac{1}{2} S_\phi(f). \tag{4.7}$$

As the phase fluctuation $\phi(t)$ is measured in radians, the dimensions of the phase spectrum $S_\phi(f)$ are [rad^2/Hz]. The phase noise $\mathscr{L}(f)$, is typically represented in logarithmic scale in the independent variable f, and using decibels referred to 1 rad^2/Hz:

$$\mathscr{L}(f) = 10 \log \left(\frac{1}{2} S_\phi(f) \right) \quad \left[\mathrm{dB} \frac{\mathrm{rad}^2}{\mathrm{Hz}} \right]. \tag{4.8}$$

4.7.4.1. Direct Spectrum Measurement: Amplitude Approximation

Neglecting the amplitude instantaneous deviation $\varepsilon(t)$ and focusing on the phase fluctuations, the fundamental component of the oscillation can be modelled by rewriting (4.6) as:

$$x(t) = A \cos(\omega_0 t + \phi_0 + \phi(t)). \tag{4.9}$$

Using basic trigonometric identities, (4.9) can be expanded as follows:

$$x(t) = A[\cos(\omega_0 t + \phi_0) \cos(\phi(t)) - \sin(\omega_0 t + \phi_0) \sin(\phi(t))]. \tag{4.10}$$

Without a specific knowledge of the function $\phi(t)$, the characteristics of (4.10) are, in general, difficult to anticipate. Nevertheless, in case the function $\phi(t)$ is known to be bounded in absolute value by a relatively small number, compared to one radian, then the following approximations can be introduced into (4.10):

$$|\phi(t)| \ll 1 \quad \Rightarrow \quad \begin{cases} \cos(\phi(t)) & \rightarrow & 1 \\ \sin(\phi(t)) & \rightarrow & \phi(t) \end{cases} \tag{4.11}$$

and, strictly under these simplifying assumptions, the fundamental oscillation signal modelled by (4.10), can be approximated by:

$$x(t) \approx \tilde{x}(t) = A[\cos(\omega_0 t + \phi_0) - \phi(t) \sin(\omega_0 t + \phi_0)]. \tag{4.12}$$

The expected value of the approximate model of the fundamental oscillator signal can be calculated as:

$$\mathrm{E}\{\tilde{x}(t)\} = A \cos(\omega_0 t + \phi_0), \tag{4.13}$$

where the facts that $\phi(t)$ is a zero mean stochastic process $\mathrm{E}\{\phi(t)\} = 0$, and that it is uncorrelated with deterministic signals, have been taken into account.

Similarly, the autocorrelation of $\tilde{x}(t)$, can be calculated through the definition:

$$\begin{aligned} R_{\tilde{x}}(t, t+\tau) &= \mathrm{E}\{\tilde{x}^*(t)\tilde{x}(t+\tau)\} = \\ &= \mathrm{E}\{A^2[\cos(\omega_0 t + \phi_0)\cos(\omega_0(t+\tau)+\phi_0) \\ &- \phi(t+\tau)\cos(\omega_0 t + \phi_0)\sin(\omega_0(t+\tau)+\phi_0) \\ &- \phi(t)\cos(\omega_0(t+\tau)+\phi_0)\sin(\omega_0 t + \phi_0) \\ &+ \phi(t)\phi(t+\tau)\sin(\omega_0 t + \phi_0)\sin(\omega_0(t+\tau)+\phi_0)]\}. \end{aligned} \tag{4.14}$$

Once again, taking into account that $\phi(t)$ is uncorrelated with deterministic signals, together with the fact that $\mathrm{E}\{\phi(t)\} = \mathrm{E}\{\phi(t+\tau)\} = 0$, the terms in the third and fourth lines of (4.14) vanish. Moreover, since $\phi(t)$ is assumed to be a wide sense stationary process, its autocorrelation will not depend on the specific time instant t: $R_\phi(t, t+\tau) = \mathrm{E}\{\phi(t)\phi(t+\tau)\} = R_\phi(\tau)$. Therefore, after further trigonometric simplification, (4.14) can be rewritten as:

$$\begin{aligned} R_{\tilde{x}}(t, t+\tau) = \frac{A^2}{2}\big[&\cos(\omega_0(2t+\tau)+2\phi_0) + \cos(\omega_0\tau) \\ &+ R_\phi(\tau)[\cos(\omega_0\tau) - \cos(\omega_0(2t+\tau)+2\phi_0)]\big]. \end{aligned} \tag{4.15}$$

In accordance with the *Wiener-Kinchine theorem* [15], for a wide sense stationary process, its power spectral density can be calculated as the Fourier transform of its autocorrelation. Even though the process $\phi(t)$ has been assumed to be wide sense stationary, it is straightforward to verify that $\tilde{x}(t)$ is not wide sense stationary. From (4.13) and (4.15), it is obvious that the expected value and the autocorrelation of $\tilde{x}(t)$ are dependent on the specific time instant t, at which they are calculated.

Nonetheless, since the autocorrelation of $\tilde{x}(t)$, given by (4.15), is clearly periodic in t, with period π/ω_0, the process $\tilde{x}(t)$ can be considered *almost cyclostationary in the wide sense*[3][16]. A generalisation of the Wiener-Kinchine theorem can be obtained for such processes [16], whereby their power spectral density can be calculated as the Fourier transform of the time averaged autocorrelation.

The time averaged autocorrelation of $\tilde{x}(t)$ can be calculated from (4.15) as:

$$R_{\tilde{x}}(\tau) = < R_{\tilde{x}}(t, t+\tau) > = \frac{A^2}{2}[\cos(\omega_0\tau) + R_\phi(\tau)\cos(\omega_0\tau)], \tag{4.16}$$

where $< \cdot >$, represents time averaging. The power spectral density of $\tilde{x}(t)$ can be finally obtained as the Fourier transform of (4.16). The one-sided power spectral density of $\tilde{x}(t)$, $S_{\tilde{x}}(t)$, is therefore given by:

$$S_{\tilde{x}}(f) = \frac{A^2}{2}[\delta(f_0) + S_\phi(f - f_0)]. \tag{4.17}$$

[3]In order to be cyclostationary in the wide sense, the mean of the process should also be periodic in t, with the same period as the autocorrelation [16] which, according to (4.13), is not fulfilled in the case of $\tilde{x}(t)$.

When the frequency content of a signal is studied with a spectrum analyser, the result obtained in the output display represents, for each frequency point in the considered sweep, the power integrated after passing the input signal through a bandpass resolution filter centred at that point. The function obtained by the spectrum analyser for an input signal $\tilde{x}(t)$, with power spectral density $S_{\tilde{x}}(f)$, can be expressed as:

$$P_{\mathrm{SA}}(f) = \int_{-\infty}^{\infty} S_{\tilde{x}}(\gamma)|\Pi_{RBW}(\gamma - f)|^2 \,\mathrm{d}\gamma, \tag{4.18}$$

where $\Pi_{RBW}(f)$ represents the transfer function of the bandpass resolution filter employed, centred at the origin.

Note that, since the process $\phi(t)$ has been defined with zero mean: $\mathrm{E}\{\phi(t)\} = 0$, its power spectral density also vanishes for $f = 0$: $S_\phi(0) = 0$. Therefore, providing the resolution filter is sufficiently narrow, the power level displayed in the spectrum analyser at f_0, for the input signal $\tilde{x}(t)$, would be $P_{\mathrm{SA}}(f_0) \approx A^2/2$. On the other hand, for offset frequencies $f_m = f - f_0 \neq 0$, by normalising the measurement for a 1 Hz resolution bandwidth [17], the following result is obtained:

$$P_{\mathrm{SA}}(f_m)|_{1\ \mathrm{Hz}} \approx \frac{A^2}{2} S_\phi(f_m) \quad f_m \neq 0. \tag{4.19}$$

Hence, providing $|\phi(t)| \ll 1$, an approximation of the single sideband phase noise spectral density can be calculated as

$$\mathscr{L}(f) \approx \frac{1}{2} \frac{P_{\mathrm{SA}}(f_m)|_{1\ \mathrm{Hz}}}{P_{\mathrm{SA}}(f_0)}. \tag{4.20}$$

The approximate measurement of $\mathscr{L}(f)$ from the spectrum analyser display, is outlined schematically in Figure 4.21. Based on that measurement approach, the phase noise $\mathscr{L}(f)$ is sometimes expressed in dBc/Hz, although in this work, only the standard unit dBrad^2/Hz will be used. The phase noise measurement applications based on spectrum analysers that are commercially available [17], rely on this simple procedure. In particular, the R&S FS-K4 software embedded in a Rohde & Schwarz FSP40 spectrum analyser, that will be used for some of the phase noise measurements of this section, uses the same principles.

Nevertheless, it must be noted that the phase noise measurement obtained from a spectrum analyser is only valid under the assumption that the approximation (4.12) can be performed, which strictly requires that $|\phi(t)| \ll 1$ radian.

4.7.4.2. Proposed Measurement Method: Phase Demodulation

In practical oscillators, the fundamental frequency cannot be considered constant, as it generally exhibits certain degree of drift and/or fluctuation about a

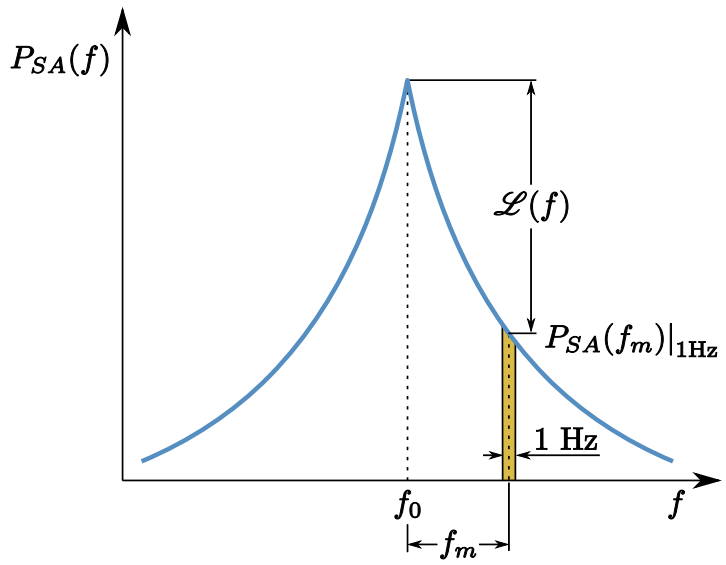

Figure 4.21: Phase noise approximate measurement using a spectrum analyser.

nominal value, over time. Since the model of the fundamental oscillation, given by (4.6), was defined with a constant angular frequency $\omega_0 = 2\pi f_0$, any departure of the instantaneous frequency from that nominal value must be reflected by $\phi(t)$, giving rise to the appearance of an additive linear term in the form $\phi_{\Delta f}(t) = 2\pi\Delta f t$. At microwave frequencies, even relatively small frequency fluctuations Δf (of the order of one kilohertz or hundreds of hertz), maintained over a short period of time, may bring about large variations of $\phi(t)$.

Consequently, except for the particular case of frequency synthesisers or phase locked loops, which usually present an extraordinarily high frequency stability, the approximations for $|\phi(t)| \ll 1$ radian cannot typically be assumed in practical free running oscillators. Therefore, the direct spectrum measurement method described in the foregoing section, is not valid, in general, for this type of circuits.

As an alternative to assess the phase noise performance of free running oscillators, a method based on the demodulation of the oscillator signal has been developed.

Since the free running oscillator frequency is not constant, its fundamental component will be demodulated using a local oscillator with frequency $\omega_{OL} \approx \omega_0$, which, for the time being, will be considered constant. The limitations that the frequency instability of the local oscillator introduces in the measurement will be commented later in this section.

By quadrature demodulating the fundamental oscillator signal, given by (4.6), the following low-pass components are obtained [15]:

$$x_I(t) = \frac{A+\varepsilon(t)}{2}\cos((\omega_0-\omega_{OL})t+\phi_0+\phi(t)) \tag{4.21}$$

$$x_Q(t) = \frac{A+\varepsilon(t)}{2}\sin((\omega_0-\omega_{OL})t+\phi_0+\phi(t)) \tag{4.22}$$

where unity amplitude local oscillator and unity gain ideal low-pass filtering have been considered. From these quadrature components, the demodulated phase $\phi_d(t)$ can be directly calculated as:

$$\phi_d(t) = \arctan\left(\frac{x_Q(t)}{x_I(t)}\right) = (\omega_0-\omega_{OL})t+\phi_0+\phi(t). \tag{4.23}$$

The phase noise is defined as the single sideband spectral density of the phase fluctuation $\phi(t)$. However, in the demodulated phase $\phi_d(t)$, the phase fluctuation appears together with a constant ϕ_0, and an additional term linearly dependent on time, originated by the difference between the nominal frequency ω_0, and the local oscillator frequency ω_{OL}. By calculating the linear least squares fitting of the demodulated phase $\phi_d(t)$: $L_{\phi_d}(t)$, the phase fluctuations can be extracted from the demodulated phase $\phi_d(t)$, as follows:

$$\tilde{\phi}(t) = \phi_d(t) - L_{\phi_d}(t). \tag{4.24}$$

By definition, the recovered phase fluctuation $\tilde{\phi}(t)$, has zero average and it does not contain any additive component linearly dependent on time. Therefore, $\tilde{\phi}(t)$ represents the phase fluctuations about the average frequency of the oscillator signal $x(t)$, over the observed time interval.

The recovered phase $\tilde{\phi}(t)$ is sampled at a frequency $F_s = 1/T_s$, over an interval of length T_M, obtaining the sequence $\tilde{\phi}[n] = \tilde{\phi}(nT_s)$, $n = 0, 1, \ldots, N-1$, where $N = T_M/T_s$. Assuming the sample frequency fulfils the sampling theorem $F_s > 2B$, where B represents the maximum frequency component contained in $\tilde{\phi}(t)$, the power spectral density of the recovered phase fluctuations can be estimated using classical spectral analysis techniques of digital signal processing.

The average power of the continuous signal $\tilde{\phi}(t)$, over the interval $(0, T_M)$, can be approximated through the sampled sequence $\tilde{\phi}[n]$, providing the sampling period T_s is sufficiently small, as follows:

$$P_{\tilde{\phi}} = \frac{1}{T_M}\int_0^{T_M} \tilde{\phi}^2(t)\,\mathrm{d}t \approx \frac{1}{N}\sum_{n=0}^{N-1} \tilde{\phi}^2[n]. \tag{4.25}$$

From the sampled sequence $\tilde{\phi}[n]$, samples of the Fourier transform of the continuous function $\tilde{\phi}(t)$, truncated in the interval $(0, T_M)$, can be calculated

through the Discrete Fourier Transform (DFT) [18]:

$$\tilde{\Phi}(f = k\frac{F_s}{N}) = \frac{1}{N}\sum_{n=0}^{N-1} \tilde{\phi}[n]e^{-j2\pi k\frac{n}{M}}, \qquad k = 0, 1, \ldots, N-1. \tag{4.26}$$

Applying Parseval's Relation [18], the average power of the continuous signal $\tilde{\phi}(t)$ given by (4.25), can be related to the samples of its spectrum, calculated in (4.26), as follows:

$$P_{\tilde{\phi}} \approx \frac{1}{N}\sum_{n=0}^{N-1} \tilde{\phi}^2[n] = \sum_{k=0}^{N-1} \left|\tilde{\Phi}(k\frac{F_s}{N})\right|^2. \tag{4.27}$$

The average power of the continuous signal $\tilde{\phi}(t)$, can also be obtained through the integration of its power spectral density, $S_{\tilde{\phi}}(f)$, in the frequency domain. Assuming that the sampling frequency has been correctly chosen, the integration can be restricted to the interval $(-F_s/2, F_s/2)$. Moreover, using samples of the power spectral density, the integral can be approximated by:

$$P_{\tilde{\phi}} = \int_{-\infty}^{\infty} S_{\tilde{\phi}}(f)\,\mathrm{d}f = \int_{-\frac{F_s}{2}}^{\frac{F_s}{2}} S_{\tilde{\phi}}(f)\,\mathrm{d}f \approx \frac{F_s}{N}\sum_{k=0}^{N-1} S_{\tilde{\phi}}(k\frac{F_s}{N}). \tag{4.28}$$

By equating (4.27) and (4.28), an estimate of the power spectral density of $\tilde{\phi}(t)$: $\tilde{S}_{\tilde{\phi}}(f)$, sampled at frequencies kF_s/N, can be obtained:

$$\tilde{S}_{\tilde{\phi}}(k\frac{F_s}{N}) = \frac{N}{F_s}\left|\tilde{\Phi}(k\frac{F_s}{N})\right|^2 \qquad k = 0, 1, \ldots, N-1. \tag{4.29}$$

The estimate of the power spectral density given in (4.29) is usually referred to in the literature as *periodogram*. It can be shown [19], that the periodogram constitutes an asymptotically unbiased estimator of the power spectral density, i.e. the expected value of the periodogram converges to the actual power spectral density of the process when the observation time (or, equivalently, the number of samples N), tends to infinity.

Nonetheless, in general, the variance of the periodogram estimate of the power spectral density does not decay to zero, even if the number of samples tends to infinity. In fact, the variance of the estimate may be relatively high (for certain type of processes, it is of the order of the actual power spectral density squared, at each frequency point [19]).

Therefore, even though its expected value tends asymptotically to the actual power spectral density, the periodogram is an inconsistent spectral estimator, which continues to fluctuate around the actual power spectral density of the

process, with a non-zero variance, even if the number of samples N, is increased unboundedly.

Multiple periodogram based methods have been proposed in the literature to reduce the variance of the estimate obtained. In particular, a simple approach would be to acquire a number L of non overlapping successive (although not necessarily consecutive) sequences of N samples $A_i = \{\tilde{\phi}_i[n]\}_{n=0}^{N-1}$, $i = 0, 1, \ldots, L-1$. From each sequence A_i, an independent periodogram $\tilde{S}_{\tilde{\phi}}^i$, is calculated according to (4.29), and the estimate of the power spectral density $\tilde{S}_{L,\tilde{\phi}}$, is finally obtained by averaging the L periodograms, as follows:

$$\tilde{S}_{L,\tilde{\phi}} = \frac{1}{L} \sum_{i=0}^{L-1} \tilde{S}_{\tilde{\phi}}^i. \tag{4.30}$$

The *averaged periodogram*, given by (4.30), is equivalent to Bartlett's method, when the sequences A_i are acquired consecutively. Under these conditions, it can be shown [19] that the variance of the averaged periodogram is divided by the number of averaged sequences L, with regard to the case in which one single periodogram is considered. This result can be assumed to extrapolate to a scenario where the sequences A_i are not consecutively acquired, providing they correspond to independent realisations of the process.

The phase noise single sideband spectral density can be calculated from the averaged periodogram as

$$\mathscr{L}(f) \approx \tilde{S}_{L,\tilde{\phi}}, \qquad f \geq 0, \tag{4.31}$$

without imposing any restriction on the behaviour of $\phi(t)$, as was the case with the direct spectrum approach, described in the previous section.

Experimental Set-up and Practical Limitations

In the phase noise measurement procedure that has been described, the oscillator output signal is demodulated using a local oscillator signal of frequency ω_{OL}, which has been assumed to be constant and close to the nominal oscillator frequency. The subsequent signal processing performed has been designed to eliminate the potential offset of the local oscillator signal, referring the computed phase fluctuations to the average oscillator frequency in the observed interval.

Nonetheless, in practical implementations, the local oscillator frequency will not remain constant, as it will possess its own phase noise characteristics. As is the case with the direct spectrum technique [17], the phase noise of the local oscillator will limit the sensitivity of the measurement set-up, in such a way that only higher phase noise levels than those of the local oscillator employed can be reliably measured.

In this case, the phase noise measurement technique that has been described, will be practically implemented with an Agilent N5247A PNA-X Vector Network Analyser. In continuous wave analysis mode, the input signal is quadrature demodulated at the selected carrier frequency and sampled in the time domain, which matches the requirements of the specified measurement procedure. However, since this piece of equipment was not conceived for the desired purpose, it imposes several practical limitations that must be taken into account, as they condition the measurement capabilities. Some of these limitations are detailed next:

- ***Sample Buffer:*** The maximum number of consecutive samples that can be acquired is limited to $N = 32001$. After a data processing and display delay, a new sequence of data can be sampled.
- ***IF Bandwidth:*** The maximum bandwidth that can be managed at intermediate frequency is $BW_{IF} \leq 15$ MHz. The IF bandwidth can be reduced from that limit through digital filtering. However, the reduction of the IF bandwidth brings about an increased acquisition time.
- ***Acquisition Time:*** The minimum acquisition time for the maximum number of samples $N = 32001$, which takes place for the maximum IF bandwidth $BW_{IF} = 15$ MHz, is $T_{acq} = 1.60005$ ms.
- ***Sampling Frequency:*** From the previous specifications, for a sequence of $N = 32001$ samples, the minimum acquisition time, corresponding to an IF bandwidth of 15 MHz, is $T_{acq} = 1.60005$ ms. Thus, the maximum acquisition frequency will be $F_s = N/T_{acq} = 20$ MHz.

The phase noise is normally displayed in logarithmic scale for offset frequencies from as close to the carrier as possible, to a maximum of the order of a few megahertz, at which the levels are typically very low. For this purpose, the IF bandwidth of 15 MHz would generally suffice. However, note that the minimum sampling frequency required to represent such bandwidth without distortion is 30 MHz, and the maximum sampling frequency that can be practically achieved is $F_s = 20$ MHz.

Furthermore, no improvement can be obtained through the reduction of the IF bandwidth, as the additional delay introduced by the digital filter would give rise to an increase of the acquisition time, leading to a proportionally lower sampling frequency.

Hence, the best configuration is attained with the maximum IF bandwidth $BW_{IF} = 15$ MHz, which corresponds to an acquisition time $T_M = T_{acq} = 1.60005$ ms and a sampling frequency $F_s = 20$ MHz. Although aliasing may take place between 5 and 15 MHz, the spectrum is, in principle, free from distortion up to that frequency.

On the other hand, the maximum number of consecutive samples determines the frequency resolution and the minimum positive frequency at which the phase noise will be evaluated: $f_{min} = F_s/N = 625$ Hz. Consequently, the phase noise will be reliably measured from $f_{min} = 625$ Hz to approximately 5 MHz. Nonetheless, note that these limitations are not intrinsic to the phase demodulation method, but they are imposed by the available measurement equipment.

Finally, in order to reduce the variance of the spectral estimate obtained, the averaged periodogram corresponding to a number L of successively acquired sequences will be calculated. Results for different numbers of averaged periodograms L, will be compared.

4.7.4.3. Measurement Method Experimental Comparison

In order to validate the implementation of the measurement procedures that have been described, the results they produce when measuring a common RF source will be analysed and compared.

Since the direct spectrum method can only be applied to sources with a limited phase fluctuation, it cannot be used to measure a free running oscillator, as it has already been commented. Thus, a PLL based frequency synthesised source with a relatively high frequency stability will be measured instead.

As has been explained in Section 4.7.3, the injection locked performance of the 4HOSC circuit is assessed by using the PNA-X internal generator to produce the reference signal at a frequency $f_s \approx 2.5$ GHz. Inasmuch as the same set-up will be used later in this section to evaluate the phase noise levels of the 4HOSC circuit, under different injection locked operating conditions, the phase noise characteristics of the reference generator need to be determined.

Therefore, the phase noise of the PNA-X internal generator, configured to produce an output signal of frequency $f_s = 2.5$ GHz, has been characterised using the measurement procedures that have been described.

Firstly, the R&S FS-K4 software, embedded in a Rohde & Schwarz FSP40 spectrum analyser has been used. The results, for offset frequencies from 10 Hz to 100 MHz, are shown in Figure 4.22, labelled as *FSP Measurement*.

The phase noise performance of the same source has been evaluated using the phase demodulation technique, implemented with the PNA-X. The variance of the spectral estimation performed has been reduced by averaging a number $L = 10.000$, of independent periodograms. The results, for offset frequencies from 625 Hz to 10 MHz, have been labelled as *PNA-X Measurement* in Figure 4.22.

The measurements obtained through both procedures are in good agreement. As has been pointed out, the PNA-X measurement suffers aliasing in the higher region of the band, approximately over 5 MHz, which distorts the results. The 5 MHz value was obtained by considering the 3 dB bandwidth of the resolution

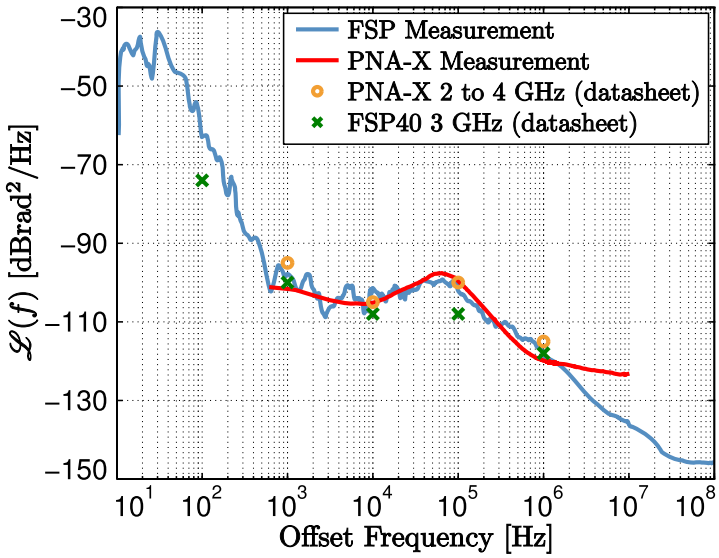

Figure 4.22: Phase noise measurements of a 2.5 GHz tone, generated by the PNA-X internal source. Measurements performed with the direct spectrum technique (FSP), and through phase demodulation (PNA-X). The datasheet phase noise specification of both local oscillators have been superimposed.

filter. However, in practice, the aliasing effect seems to be appreciable at slightly lower frequencies.

As a reference, the manufacturer datasheet specification of the phase noise characteristics of the local oscillators employed in both systems, have also been superimposed in Figure 4.22. Note that, in the case of the PNA-X measurement, the local oscillator employed is identical to the source under test.

Due to the fact that the phase noise levels of the source under test are comparable to those of the local oscillators employed, neither measurement can be considered quantitatively rigorous. Nevertheless, the agreement, both between the measurements, and with the PNA-X source datasheet specification, can be regarded as an experimental validation of the methods, for the lowest phase noise levels that will be analysed in the following.

Comparatively, the direct spectrum method provides relatively accurate results over a wider offset frequency range, which are acquired in a straightforward manner, without requiring any further data processing. However, the restrictive small phase fluctuation condition ($|\phi(t)| \ll 1$ rad), invalidates it for the evaluation of most practical oscillators, for which the phase demodulation technique still offers accurate results.

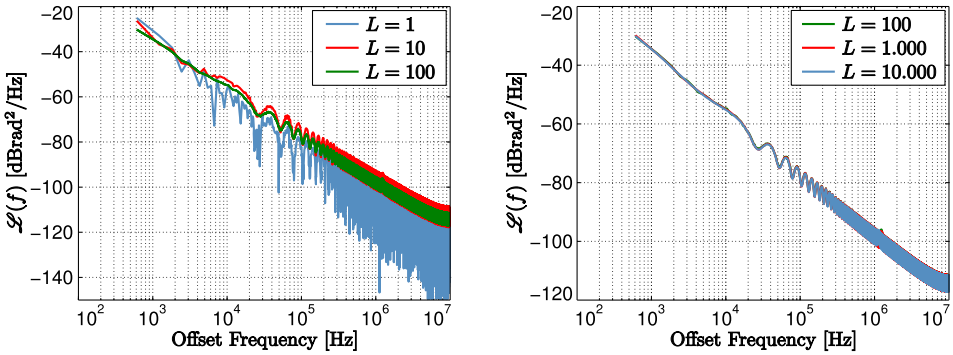

(a) (b)

Figure 4.23: Phase noise measurements of the fundamental component of the 4HOSC circuit at $f_{0_c} = 2.496$ GHz, for different numbers of averaged periodograms L. (a) $L = 1$, 10 and 100. (b) $L = 100$, 1.000 and 10.000.

4.7.4.4. Free Running 4HOSC: Number of Averaged Periodograms

The phase noise performance of the fundamental component of the free running 4HOSC circuit has been measured through phase demodulation. As has been justified, the number of averaged periodograms is an important parameter that directly affects the variance of the spectral estimate obtained. In order to illustrate the influence of that parameter, results for different values will be calculated and compared.

The 4HOSC circuit is operated at the centre of its frequency tuning band, $f_{0_c} = 2.496$ GHz, and the fundamental component is measured through the input port, to avoid the high attenuation level introduced by the output filter. The phase noise results for three different numbers of averaged periodograms $L = 1$, 10 and 100, are represented in Figure 4.23(a).

When considering one single periodogram to estimate the spectral density ($L = 1$), the results exhibit very wide fluctuations, especially at high frequencies. Nevertheless, if the data is smoothed through a moving average filter, the output will approximate to the results obtained with higher numbers of averaged periodograms (note that, due to the logarithmic dB representation, the moving average will be relatively close to the upper side of the fluctuations).

The amplitude of the fluctuations in the results clearly reduces for $L = 10$, and slightly more for $L = 100$, as the variance of the spectral estimate should divide by the number of averaged periodograms.

The results for higher numbers of averaged periodograms $L = 100$ and 1.000, are presented in Figure 4.23(b), where the trace for $L = 100$, has been repeated for ease of comparison. As can be observed, the amplitude of the fluctuations

barely reduces when increasing the number of averaged periodograms over $L = 100$.

Hence, in following measurements, a number of averaged periodograms $L = 100$, will be generally used, except when the maximum precision in the spectral estimation is strictly necessary, in which case it will be explicitly stated.

4.7.4.5. Operation as a Voltage Controlled Oscillator

The natural oscillation frequency f_0, of the 4HOSC circuit can be modified by tuning the varactor control voltage V_c. The phase noise levels of the circuit operating at 5 different oscillation frequencies, uniformly distributed throughout its frequency tuning range, are compared in Figure 4.24. Once again, the fundamental component has been measured through the input port.

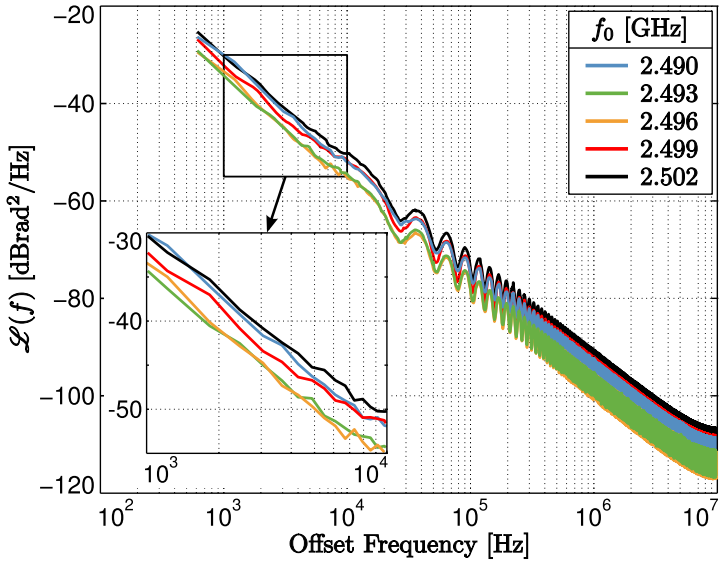

Figure 4.24: Phase noise levels of the fundamental component of the 4HOSC circuit, for 5 different oscillation frequencies.

Higher phase noise levels have been measured close to the ends of the frequency tuning range, whereas lower levels have been obtained towards the centre. Anyway, the variation observed is not very significant and barely reaches 5 dB.

4.7.4.6. Fourth Harmonic Component

The 4HOSC circuit has been optimised to produce the fourth harmonic component of the oscillation as its output signal. Therefore, the phase noise behaviour of that harmonic component needs to be characterised.

In general, harmonic content of order $N \in \mathbb{Z}$, $N > 1$, is generated in non-linear devices due to the appearance of powers of the same order in the constitutive relationships that model their physical behaviour. If the fundamental oscillator signal, as modelled by (4.9), is raised to the N^{th} power

$$\begin{aligned} x^N(t) &= A^N \cos^N(\omega_0 t + \phi_0 + \phi(t)) \\ &= B\cos(N\omega_0 t + N\phi_0 + N\phi(t)) + z(t), \end{aligned} \tag{4.32}$$

the trigonometric expression can be expanded as a term in which the argument is multiplied by N—corresponding to the N^{th} harmonic component, with frequency Nf_0—plus some additional lower order terms, gathered in $z(t)$.

According to (4.32), the phase fluctuation at the N^{th} harmonic component is equal to the fluctuation at the fundamental oscillation, $\phi(t)$, multiplied by N. Thus, the power spectral density of the phase fluctuations at the N^{th} harmonic component $S_{\phi,N}(f)$, can be related to that of the fundamental component $S_\phi(f)$, as

$$S_{\phi,N}(f) = N^2 S_\phi(f). \tag{4.33}$$

From (4.33), the phase noise level at the N^{th} harmonic component $\mathscr{L}_N(f)$, can be analogously related to that at the fundamental component, in dB, as follows:

$$10\log\frac{\mathscr{L}_N(f)}{\mathscr{L}(f)} = 20\log(N). \tag{4.34}$$

Thus, the phase noise level increases with the order of the harmonic component employed. In particular, for the fourth harmonic component used in the 4HOSC circuit, the increment in the phase noise level with regard to the fundamental component will be:

$$10\log\frac{\mathscr{L}_4(f)}{\mathscr{L}(f)} = 20\log(4) \approx 12.04 \text{ dB}. \tag{4.35}$$

The phase noise level of the 4HOSC circuit at the centre of the frequency tuning range has been measured, both at the fundamental, and at the fourth harmonic component. In order to enable an accurate comparison between both measurements, the number of averaged periodograms has been increased, in this case, to $L = 10.000$.

The results have been represented in Figure 4.25. As has been indicated in the figure, the offset between the traces is approximately 12 dB, in accordance with (4.35).

4.7.4.7. Fourth Harmonic Component: Operation as a VCO

The phase noise performance of the fundamental component has been assessed for different oscillation frequencies. Nonetheless, since the output signal of the

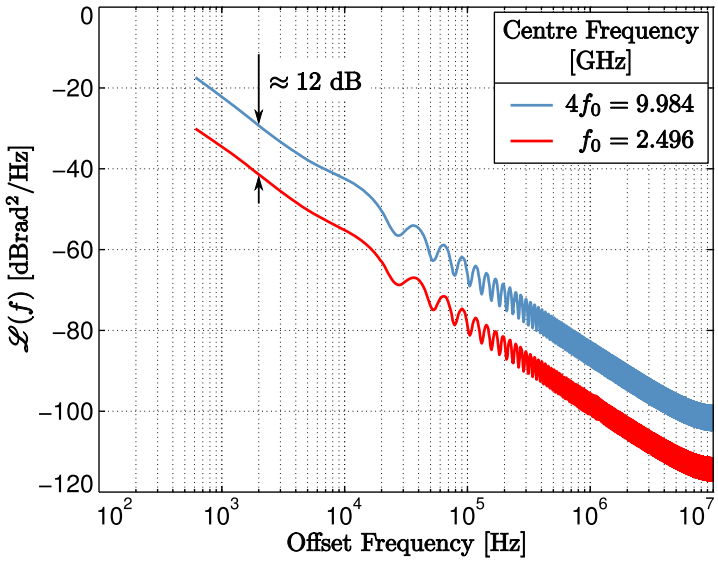

Figure 4.25: Phase noise level of the 4HOSC circuit, both at the fundamental and at the fourth harmonic component.

circuit is the fourth harmonic component, its phase noise characteristics have been measured for seven oscillation frequencies, uniformly spaced throughout the frequency tuning range.

The measurement results are presented in Figure 4.26. As was the case at the fundamental component, higher phase noise levels are obtained at the ends of the frequency tuning band. In this case, with a higher number of measurement frequencies, it can be clearly observed that the lowest phase noise levels are obtained at $4f_0 = 9.969$, 9.977 and even at 9.985, whereas the levels increase for higher frequency values. Hence, the minimum phase noise levels take place closer to the lower end of the frequency tuning range, rather than exactly at the centre.

As was the case with the fundamental component, the variation is not very significant, and barely reaches 5 dB. Note, however, that the absolute levels in this case are about 12 dB higher, as has been properly justified.

4.7.4.8. Injection Locked Behaviour: Synchronisation Power

In order for the 4HOSC circuit to operate as a phase shifter, it must be injection locked to an external reference signal. The main parameters that condition the synchronise operation regime of the circuit are the synchronisation power P_s and frequency f_s, together with the natural oscillation frequency of the circuit f_0.

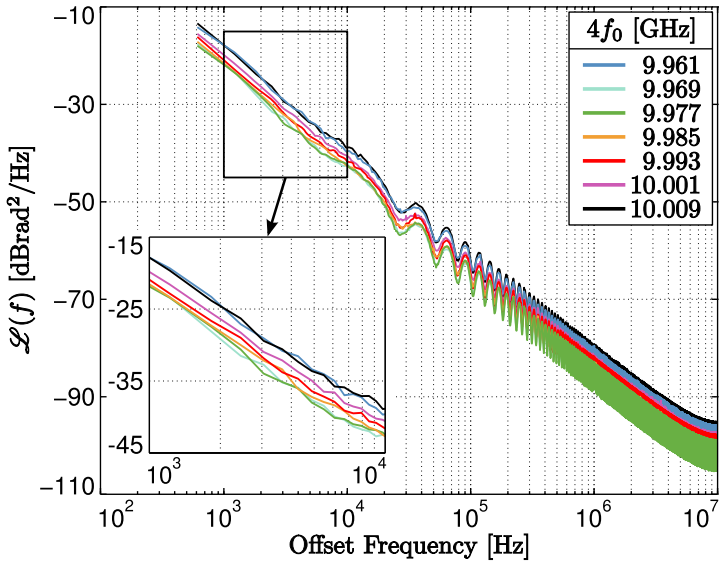

Figure 4.26: Phase noise levels of the fourth harmonic component of the 4HOSC circuit, for seven different oscillation frequencies.

In this section, the phase noise performance of the injection locked circuit has been analysed versus the synchronisation power level P_s. To guarantee that the circuit remains injection locked for all the synchronisation power levels imposed, the measurement is carried out at the centre of the frequency tuning range $f_s = 2.496$ GHz, tuning the varactor control voltage so that $f_s = f_0$.

Since the circuit input port is used to inject the external reference signal, the fundamental component cannot be measured through that port. On the other hand, the high attenuation introduced by the output filter at the fundamental component would bring about a very noisy acquisition. Thus, under injection locked operation conditions, only the fourth harmonic component will be measured.

The results are represented in Figure 4.27, for the synchronisation power values $P_s = -45$, -42.5, -40, -37.5, -35, -30, -25, -20, -15, -10, -5 and 0 dBm. Additionally, the phase noise performance of the fourth harmonic component of the free running 4HOSC circuit, as well as that of the PNA-X, which is used as synchronisation generator, have been included for comparison.

As has been graphically indicated in the figure, the phase noise levels continually decrease as the synchronisation power is increased. Even for a very low synchronisation power, such as $P_s = -45$ dBm, the phase noise level is significantly reduced (a minimum of 15 dB), with regard to the free running operation. The levels progressively decrease and adopt the shape of the trace corresponding to the reference signal, until—for relatively high values of the synchronisation

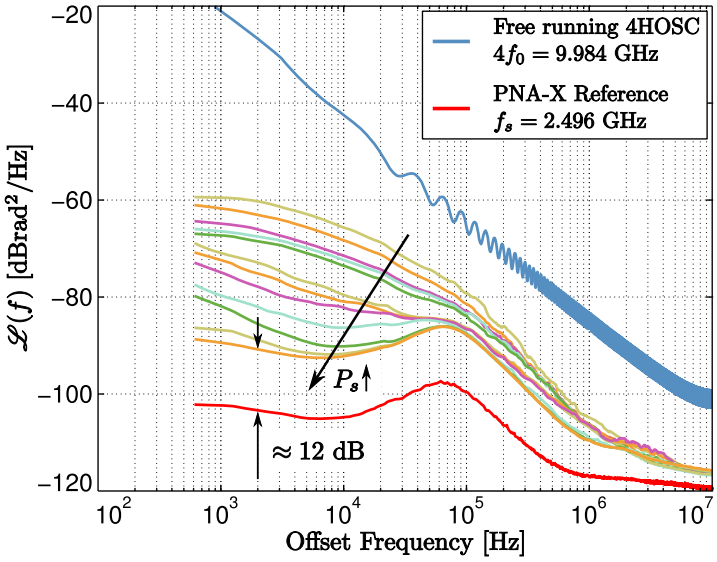

Figure 4.27: Phase noise levels of the fourth harmonic component of the injection locked 4HOSC circuit, for different synchronisation power levels. The free running performance and that of the reference signal have been superimposed for comparison.

power—the phase noise level saturates to approximately the characteristic for $P_s = 0$ dBm.

Note that the trace for $P_s = 0$ dBm approximately matches the characteristic of the PNA-X reference signal, offset upward about 12 dB. The fact that the represented trace corresponds to the fourth harmonic component of the 4HOSC circuit oscillation means that, according to (4.35), the fundamental oscillation approximately matches the phase noise characteristic of the reference signal. Thus, for relatively high synchronisation power levels, the phase noise performance at the fundamental component of the injection locked oscillator tends to match that of the external reference.

Injection locking has traditionally been employed as a means of improving the frequency stability of oscillators [20; 21]. As has been verified, even with a very low synchronisation power level, the phase noise performace of the circuit can be substantially improved.

4.7.4.9. Injection Locked Behaviour: Phase Shift Tuning

The phase noise characteristic of the injection locked 4HOSC circuit have been studied for different synchronisation power levels P_s. However, to take advantage of the phase shift tuning capabilities of the circuit, the difference between the

frequency of the external signal f_s, and the natural oscillator frequency f_0— the frequency detuning—must be varied.

The phase noise performance of the injection locked circuit has been analysed for different values of the frequency detuning, controlled through the varactor bias voltage V_c.

The results for a synchronisation signal with power $P_s = -35$ dBm and frequency $f_s = 2.496$ GHz, are shown in Figure 4.28. The trace colours correspond to different phase shift values $\Delta\phi_o$, uniformly spaced throughout the associated synchronisation locus, as indicated in the upper inset.

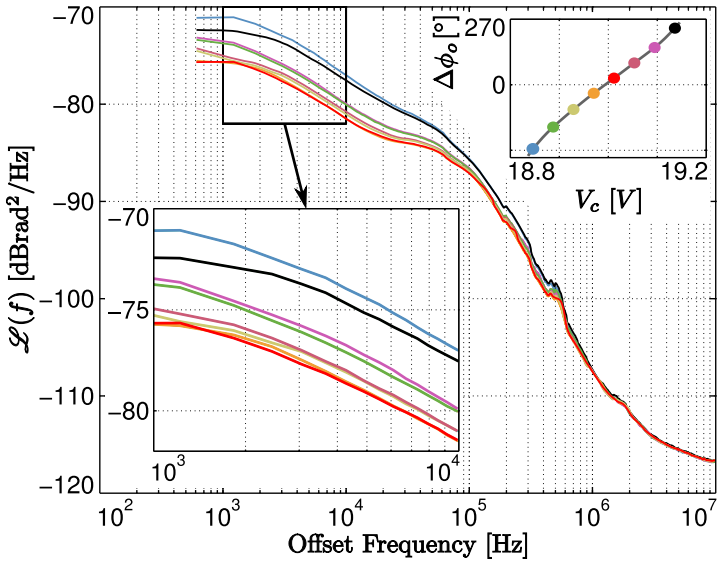

Figure 4.28: Phase noise levels of the 4HOSC circuit, injection locked to an external signal of power $P_s = -35$ dBm and frequency $f_s = 2.496$ GHz, for different phase shift values, as indicated in the inset.

Higher phase noise levels have been observed at both end points of the interval of phase shift values considered. Very similar and appreciably lower levels are obtained at the penultimate point at either end of the interval. The phase noise levels continue to reduce towards the centre of the locus, although a limited variation is further observed.

It is important to emphasise the fact that an interval of phase shift values of nearly 540° has been considered while, for practical applications, a range wider than 360° is rarely necessary. A 360° range can be effectively covered without considering the two end values of the interval depicted in the inset of Figure 4.28, in which case the variation of the phase noise level with the phase shift value imposed is lower than 2.5 dB.

The phase shift performace of the circuit has been analogously analysed for a synchronisation power level $P_s = -40$ dBm. A slightly greater than 360° phase shift interval has been considered in this case, as shown in Figure 4.29.

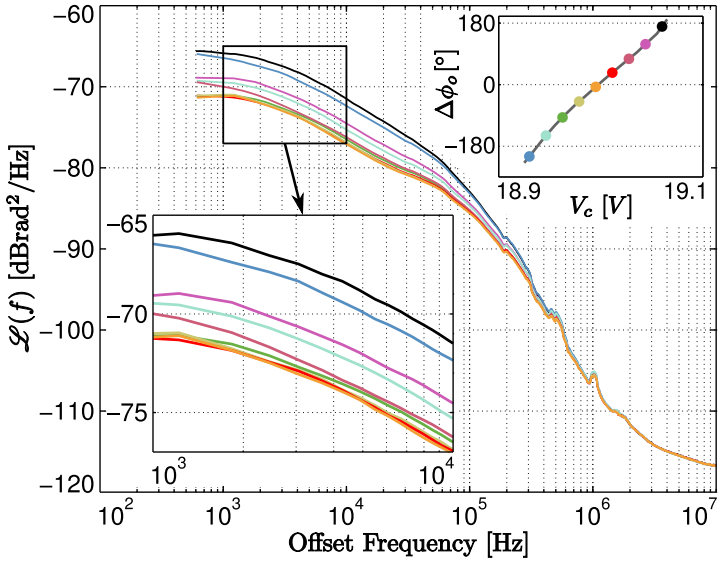

Figure 4.29: Phase noise levels of the 4HOSC circuit, injection locked to an external signal of power $P_s = -40$ dBm and frequency $f_s = 2.496$ GHz, for different phase shift values, as indicated in the inset.

In accordance with the analysis presented in the previous section, the absolute phase noise levels for $P_s = -40$ dBm have increased with regard to the case with $P_s = -35$ dBm.

The phase noise spectral density is still higher at the end points of the phase shift interval, and progressively decreases towards the centre of the locus. However, in this case, the whole considered interval is required to cover a 360° phase shift range, giving rise to a variation of the phase noise level slightly higher than 5 dB.

Thus, as a result of reducing the synchronisation power P_s, the absolute phase noise levels observed have increased, as has the variation of those levels with the imposed phase shift $\Delta\phi_o$, within a 360° range.

Nonetheless, despite the variation with the phase shift value imposed, it is important to notice the substantial reduction of the phase noise levels that has been attained, even with a very low synchronisation power level, such as $P_s = -40$ dBm, with regard to the free running oscillator performance.

4.7.5. Transmission of Phase Modulated Signals

The fourth harmonic oscillator circuit that has been designed, optimised and experimentally evaluated, presents a number of interesting features, such as an optimised harmonic content, which leads to a reduced power consumption, and a wide continuous phase shift range, very attractive for the control of antenna arrays. Nonetheless, in the foregoing analyses, the circuit operation regime has been restricted to the transmission of simple carrier signals, which significantly constrains the range of prospective applications. In order to enable the use of the 4HOSC circuit as a stand-alone transmitter in general purpose communication systems, it must be capable of generating—or, at least, dealing with—modulated signals.

Different approaches to the use of oscillator based circuits in communication systems can be found in the literature [22; 23; 24; 25]. In analogy to the classical superheterodyne transmitter topology, the modulated signal can be introduced in an oscillator circuit, duly optimised to extract the appropriate intermodulation product, leading to a self oscillating mixer implementation [26]. By optimising the generated harmonic content to perform the mixing operation with a harmonic component of the oscillation signal, a harmonic self oscillating mixer topology, like the one used in Chapters 2 and 3, can be obtained. As has been pointed out, that topology integrates the signal downconversion and continuous range phase shifting operations, together with the local oscillator generation, providing an overall positive conversion gain. The conversion gain of the circuit can be further optimised for wideband operation by deliberately forcing the operation of the circuit in the vicinity of several instabilities, through bifurcation control techniques [27].

Harmonic self oscillation mixer design is generally performed using a small signal approach, i.e. under the assumption that the oscillatory solution behaves linearly with respect to the input signal. This condition is usually fulfilled in receiving topologies, in which the input signal has commonly been highly attenuated by the propagation, having a relatively low level.

Conversely, for transmitting topologies, in which a high output signal level is generally required, the power of the input IF signal needs to be increased and, consequently, the small signal approach can no longer be employed. Therefore, the presence of an additional signal with relatively high power in the circuit will give rise to the generation of harmonic components, as well as intermodulation products with the oscillatory solution, which must be taken into account in the harmonic balance frequency basis, increasing the computational complexity of the simulations accordingly. Furthermore, the presence of an arbitrary external signal with relatively high power will in general perturb the oscillatory solution, to the extent that it may even affect its stability properties. Thus, the design of

a transmitting harmonic self mixer topology with a relatively high output power constitutes a daunting task that has rarely been practically addressed.

As an alternative to the self oscillating mixer approach for transmitting topologies, several techniques based on the direct modulation of the oscillator signal have been proposed. The main advantage of directly modulating the oscillatory solution is that the output modulated signal level can in principle be as high as the output power of the selected oscillator. On the other hand, the circuit dynamics will condition the range of modulation formats that can be introduced in the oscillatory solution.

The self limited nature of the non-linear oscillatory regime limits the capability of the circuit to modify the amplitude of its steady state solution. Therefore, a major restriction in the range of modulation schemes that can be applied to the oscillatory solution is that they must have constant amplitude.

As has been shown, the fourth harmonic oscillator circuit can be used as a VCO, changing its oscillation frequency as a function of the oscillator bias voltage. However, when the circuit is injection locked to an external signal, the oscillation frequency is imposed by that external reference. Variations of the synchronisation signal frequency result in changes in the frequency detuning which, in turn, bring about changes in the applied phase shift. Therefore, frequency modulations schemes are also not appropriate, as they cannot coexist with the phase shifting functionality.

With regard to phase modulations, the fourth harmonic oscillator circuit has experimentally proved to operate as an effective continuous range phase shifter. Taking advantage of that known property, several approaches to the use of oscillator based circuits for the transmission of phase modulated signals have been presented in the literature [28; 29; 30; 31; 32; 33; 34]. However, the focus of those works has been centred in the modulation of the oscillator signal, while overlooking the capability of simultaneously using the circuit as a variable phase shifter.

In this section, different techniques for the modulation of the oscillator signal will be discussed and evaluated for the particular case of the fourth harmonic oscillator design that has been presented, while focusing on preserving the variable phase shifting capability. The addition of the capacity to deal with phase modulated signals to the 4HOSC circuit would lead to a multifunctional circuit topology that can be used as a stand-alone front end for the control of transmitting antenna array elements.

4.7.5.1. Modulation of the Varactor Bias Voltage

As has been demonstrated, under injection locked operation conditions, the phase shift of the 4HOSC circuit output signal can be controlled through the

varactor bias voltage V_c. Thus, by adequately changing the amplitude of the varactor bias voltage, the 4HOSC output signal can be phase modulated.

This modulation technique was proposed in the literature [28; 29], to generate BPSK (Binary Phase Shift Keying) signals, using fundamentally injection locked oscillators. Since those circuits are known to provide a theoretical phase shift range of about 180°, the whole range needs to be used to produce the two symbols of the BPSK constellation, which are separated 180°. However, as has been experimentally observed, the theoretical ranges tend to reduce in practice due to the appearance of non-linear effects as the circuit approaches the instabilities at the limits of the synchronisation range, where the phase noise performance also becomes poorer.

In [30], a discrete 180° phase shifter based on a PIN diode switch, is combined with an injection locked oscillator providing an additional 90° phase shift range by tuning its drain to source bias voltage. That topology enables the generation of both BPSK and QPSK (Quadrature Phase Shift Keying) signals.

A more recent version of this approach was presented in [31], using a push-push oscillator topology, whose output signal is the second harmonic component, doubling the theoretical phase shift range available. Therefore, the 360° range can be used to generate BPSK and even QPSK signals, while leaving a *stability margin* at either side of the range—that does not need to be used—in order to prevent degradations in the performance of the circuit.

Due to the relatively narrow phase shift ranges available in the aforementioned works, the modulation of the oscillator signal is performed at the expense of the phase shifting functionality. Nevertheless, one of the main advantages of the 4HOSC circuit topology is the extended phase shift range, which has been experimentally verified to be wider than 620°. Taking advantage of that extended range, a BPSK modulation comprising the symbols with phase shift $< \Delta\phi_o > -90°$ and $< \Delta\phi_o > +90°$ can be generated, in which the centre phase shift $< \Delta\phi_o >$, can still be varied in a 360° range. Note that $360° + 180° = 540° < 620°$.

The non-linear response of the phase shift introduced by the 4HOSC circuit, with regard to the varactor bias voltage V_c, that has been shown in Figure 4.13, will determine the characteristics of the time varying control voltage $V_c(t)$, that is necessary to obtain the desired modulation of the output signal.

For a given centre phase shift $< \Delta\phi_o >$, the phase shift corresponding to the symbol "1" will be $< \Delta\phi_o > +90°$, whereas, for the symbol "0", the corresponding phase shift will be $< \Delta\phi_o > -90°$, as shown in the inset of Figure 4.30(a). Therefore, the required varactor bias voltage corresponding to either symbol of the constellation, versus the required centre phase shift $< \Delta\phi_o >$, can be obtained by simply introducing a 90° and a −90° offset, respectively, in the experimental synchronisation locus depicted in Figure 4.13.

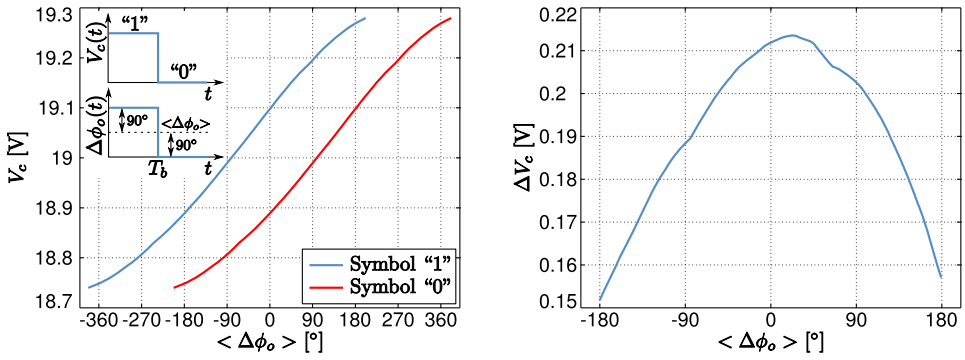

Figure 4.30: (a) Varactor bias voltages corresponding to the symbols of the BPSK modulation, versus the centre phase shift $< \Delta\phi_o >$, for $P_s = -30$ dBm. (b) Amplitude of the required varactor bias voltage waveform versus the centre phase shift $< \Delta\phi_o >$.

The varactor control voltage levels corresponding to the symbols of the BPSK constellation are illustrated in Figure 4.30(a), as a function of the desired centre phase shift $< \Delta\phi_o >$, for the particular case of $P_s = -30$ dBm.

For the range of centre phase shift values $< \Delta\phi_o > \in [-180°, 180°]$, the voltage levels corresponding to both symbols of the constellation have been specified. After a relatively narrow interval at either side of that range, the trace associated with one of the symbols is no longer defined. As has been discussed, the DC sources employed in the experimental set-up limited the measurement close to the ends of the synchronisation range, which is in fact slightly wider than the represented trace. Nonetheless, since a $360° + 180° = 540°$ phase shift range is required for this application, the performance of the circuit will necessarily start to degrade within that range.

Furthermore, note that the difference between the varactor bias voltage required for the symbols of the constellation is not constant, and varies with the desired centre phase shift $< \Delta\phi_o >$. Thus, the required varactor bias voltage waveform $V_c(t)$, will have a centre value $< V_c >$, and an amplitude ΔV_c, both dependent on the centre phase shift $< \Delta\phi_o >$.

The amplitude of the required varactor bias voltage waveform ΔV_c, has been represented as a function of the centre phase shift in Figure 4.30(b). A non-linear variation in the required amplitude greater than 30% is observed, which substantially complicates the control circuitry.

If that required amplitude variation were neglected, applying a constant amplitude and changing only the centre value $< V_c >$, the symbols of the BPSK modulation would not be separated 180° for all the values of the centre phase

shift $< \Delta\phi_o >$, which has a negative impact on the probability of error of the modulation. More importantly, if the amplitude of the varactor control voltage waveform is not decreased when approaching the limits of the centre phase shift range (-180 and $180°$), the response of one of the circuits becomes increasingly sensitive to the control voltage, to the point that it might be pushed out of synchronisation.

Hence, in a scenario where multiple 4HOSC circuits are used to control the elements of an antenna array transmitting phase modulated signals, control waveforms with different amplitudes and centre values need to be generated for the different elements, which significantly complicates the associated control circuitry. In addition, the wide phase shift range required with this approach forces the operation of the circuit far from the centre of the synchronisation range, giving rise to degradations in the performance.

Consequently, the practical limitations that have been mentioned discourage the modulation of the varactor bias voltage as a means for the 4HOSC circuit to transmit BPSK signals, while preserving the phase shifting functionality. A more advantageous modulation technique will be commented and analysed in the the following section.

4.7.5.2. Phase Modulated Reference Signal

Under injection locked operating conditions, the phase shift introduced by the 4HOSC circuit can be controlled through the varactor bias voltage V_c, and that phase shift is referred to the external reference signal. Therefore, if the phase of that external reference changed, the phase of the circuit output signal would follow that variation after a transient regime.

Taking advantage of that phenomenon, an array of oscillator based active antennas, injection locked to a phase modulated signal was presented in [32]. The modulated signal is directly injected to the centre element of the array, while the remaining elements become injection locked through electromagnetic coupling.

The same concept was applied in [33; 34] to a fifth order subharmonically injection locked oscillator. Due to the subharmonic synchronisation, the phase shifts introduced in the reference signal are multiplied by five in the oscillator output. Thus, the amplitude of the phase modulation introduced in the reference signal must be divided by five. A GMSK (Gaussian Minimum Shift Keying) modulation was successfully obtained.

Although that possibility was not considered in the previously referenced works, the approach that has been described enables the modulation of the oscillator output signal without taking advantage of its phase shifting capabilities, which remain completely available for simultaneous exploitation.

The modulation of the oscillator signal while using its phase shifting functionality, was explored by the author of this Thesis in [35], in a polarisation agile antenna based on fundamentally injection locked oscillators. The phase shift range provided by those circuits is sufficient to control the polarisation state of an antenna, as demonstrated in [36], although it is not enough to drive a general purpose antenna array.

In this section, the performance of the fourth harmonic oscillator circuit, injection locked to digitally phase modulated signals, will be experimentally evaluated under different operating conditions, while focusing on preserving its phase shifting functionality.

Modulation of the Reference Signal

The 4HOSC circuit synchronisation signal, with frequency $f_s \approx 2.5$ GHz and power P_s, must be phase modulated. Although any type of phase modulation could, in principle, be employed, only digital Phase Shift Keying (PSK) signals will be considered in this work.

In the simplest case, the Binary Phase Shift Keying (BPSK) modulation scheme, features a constellation comprising two symbols separated 180°: for instance 0° and 180°. Due to the harmonic nature of the 4HOSC circuit, in order to produce a BPSK simulation in the circuit output, the symbols in the reference signal must be placed 45° apart (180/4=45°).

Taking advantage of the fact that the synchronisation signal is a single tone at a constant frequency $f_s \approx 2.5$ GHz, its phase modulation is relatively easy to perform. Multiple passive phase shifter based PSK modulator topologies can be found in the literature, which can be employed for the reference signal phase modulation. The required modulation could even be obtained by using two consecutive symbols of a commercially available 8PSK modulator. Note that, since a relatively low power level is generally required for the synchronisation, the losses introduced by the modulator will have a limited impact on the system overall efficiency.

In this particular case, the modulation has been generated using the Rohde & Schwarz IQ Modulation Generator AMIC, together with the Rohde & Schwarz SMV03 Vector Signal Generator. This equipment is capable of producing a broad range of fully configurable complex modulations, which exceedingly covers the requirements of this measurement set-up.

To illustrate the quality of the modulations obtained, the modulated signals generated for different output power levels have been measured with an Agilent N5247A PNA-X Vector Network Analyser, operating in continuous wave as a quadrature demodulator. The measurements for different output power levels P_s, are shown in Figure 4.31.

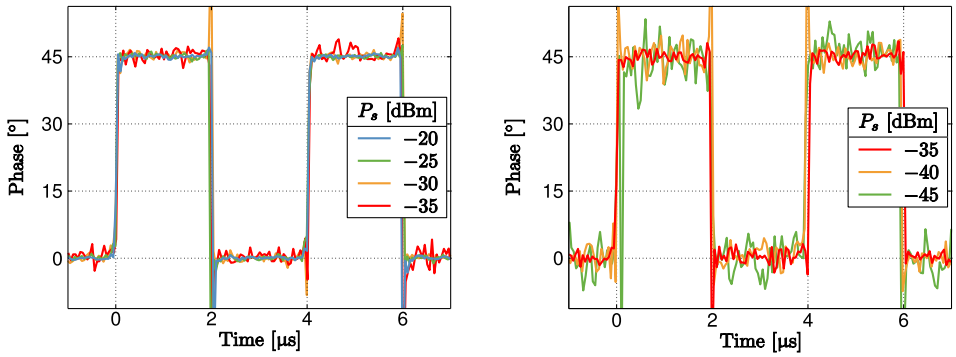

(a) (b)

Figure 4.31: AMIC phase modulated signals for different output power levels. (a) $P_s = -35$, -30, -25 and -20 dBm. (b) $P_s = -45$, -40 and -35 dBm.

Given the sampling frequency limitations of the PNA-X that have been commented in the previous section, the signals have been sampled at the maximum available frequency, $F_s = 20$ MHz.

The modulated signals become increasingly noisy as the carrier power is reduced. Moreover, regardless of the output power selected, very sharp spikes are produced both at the beginning and at the end of the edges of the signal. The fact that those spikes are not observed in every edge may be due to the relatively low sampling frequency that has been employed.

Circuit Dynamical Response: Synchronisation Power

The injection locked solutions of the 4HOSC circuit are generally greatly influenced by the synchronisation power P_s applied. Therefore, the dynamical response of the circuit to a 45° step in the reference signal phase—which brings about a 180° step in the circuit output—has been analysed for different synchronisation power levels P_s. The results are shown in Figure 4.32(a).

The circuit response is increasingly fast for higher synchronisation power levels. For relatively high synchronisation power levels, the circuit may seem to exhibit overshoot. Nonetheless, note that the phase also features a sharp decrease from the low level, just before the positive edge of the signal, which cannot be explained by that phenomenon.

Consequently, as the synchronisation power level is increased and the circuit dynamics become increasingly fast, the response follows more closely the behaviour of the reference, and the spikes of the latter can be appreciated in the former. Conversely, as the synchronisation power level is reduced, the circuit dynamics become slower, giving rise to a monotonic transient response.

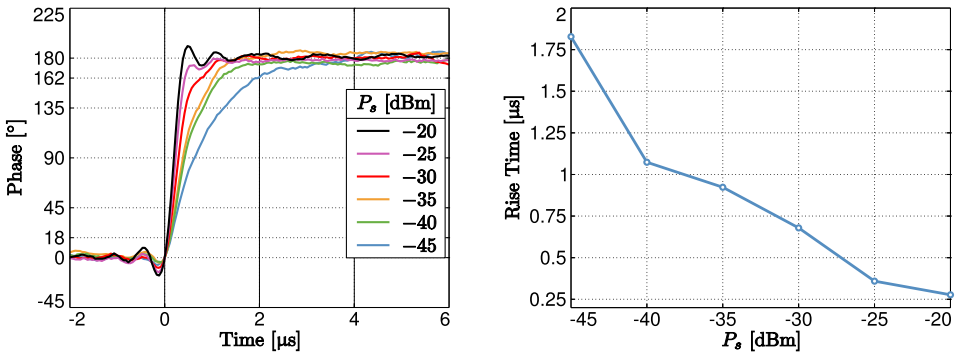

(a) (b)

Figure 4.32: (a) Dynamical response of the circuit to a 45° step in the reference signal phase. (b) Rise time versus synchronisation power level P_s.

For a step response, the rise time is usually defined as the time taken for the signal to change between a 10 and a 90% of the amplitude of the step. In this case, for the 180^circ step, it would be the time taken by the signal to change between 18 and 162^circ, as indicated in Figure 4.32(a).

The rise time versus the synchronisation power level have been represented in Figure 4.32(b). As expected, the rise time progressively decreases as the synchronisation power is increased.

Circuit Dynamical Response: Phase Shift Tuning

As has been discussed, the fourth harmonic oscillator circuit can be used to transmit phase modulated signals while preserving its continuous range phase shifting capabilities. In this section, the dynamics of the circuit are evaluated at different working points within its synchronisation locus, corresponding to different phase shift values imposed.

The reference signal is modulated so that the 4HOSC circuit output is a BPSK signal of frequency $f_b = 0.5$ MHz. For a synchronisation power level $P_s = -30$ dBm, the response of the circuit at 8 operating points, uniformly spaced throughout the associated synchronisation locus, are presented in Figure 4.33.

The noisy fluctuations of the reference signal that have been observed in Figure 4.31(a) for $P_s = -30$ dBm, limit the conclusions that can be drawn from the comparison of the different traces, which are reasonably similar. It seems clear, nevertheless, that the response becomes slower towards the very ends of the synchronisation locus. However, those two end points lie outside the 360°

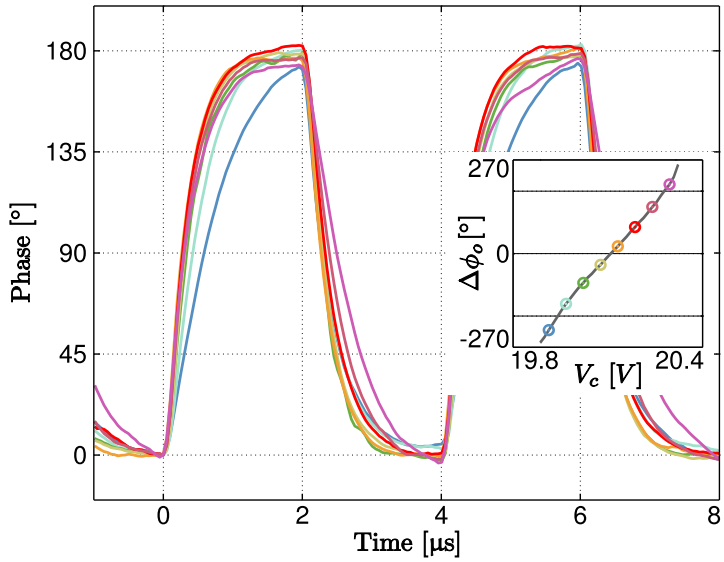

Figure 4.33: BPSK modulated signal with frequency $f_b = 0.5$ MHz, measured at eight different working points, uniformly spaced throughout the associated synchronisation locus, as shown in the inset. The synchronisation power is $P_s = -30$ dBm.

phase shift range that is usually required in practical applications, and therefore, the circuit would very rarely need to operate in those regimes.

For a synchronisation power level $P_s = -40$ dBm, the circuit response has been analogously measured at nine working points uniformly spaced throughout the corresponding injection locked solution locus. The results are presented in Figure 4.34.

As expected, the dynamics of the circuit have become faster for a higher synchronisation power level. Once again, the outer points considered in the synchronisation locus correspond to slightly slower dynamics, although those points are outside the usually required 360° phase shift range.

As a conclusion, the fourth harmonic oscillator has experimentally proved to be capable of transmitting phase modulated signals, while preserving its phase shifting functionality. The circuit dynamics do not exhibit a strong dependence on the phase shift value imposed, although the response tends to become appreciable slower when approaching the limits of the synchronisation range. However, due to the wide phase shift range provided by the 4HOSC circuit, a 360° phase shift range can be effectively provided in the central region of the locus, where the dynamics remain reasonably fast.

On the other hand, the synchronisation power level directly affects the dynamical response of the circuit, which becomes faster when increasing the reference

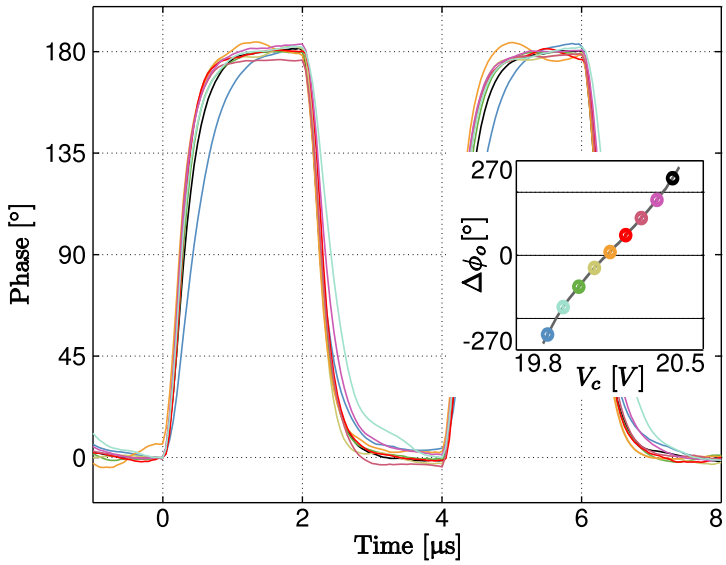

Figure 4.34: BPSK modulated signal with frequency $f_b = 0.5$ MHz, measured at nine different working points, uniformly spaced throughout the associated synchronisation locus, as shown in the inset. The synchronisation power is $P_s = -25$ dBm.

signal power level. Thus, the 4HOSC topology will be especially indicated for applications with moderate throughput requirements, in which case the circuit can be injection locked with a relatively low synchronisation power level, like those studied above. For instance, for a synchronisation power $P_s = -30$ dBm, and taking into account the fact that the output signal power is $P_o \approx -5$ dBm, the 4HOSC circuit can be considered a continuous range phase shifter with a power gain $G \approx 25$ dB.

Increasing Data Rate

Multiple techniques have been presented in the field of signal theory to increase the data rate of modulations. A common approach is usually to increase the number of symbols in the associated constellation, which brings about a higher data rate at the expense of reducing the bit error rate.

Since the nature of the 4HOSC circuit imposed that all the symbols must have the same amplitude, only the phase can change between different symbols, leading to a generalised N-PSK modulation, which comprises N uniformly spaced symbols in a circumference.

In order to illustrate this technique, a 4-PSK, usually referred to as a Quadrature Phase Shift Keying (QPSK) modulation has been generated. The symbols

in the reference signal must be separated 22.5°, between 0° and 67.5°. The QPSK modulated signal measured at the output of the 4HOSC is shown in Figure 4.35, for $P_s = -25$ and -30 dBm.

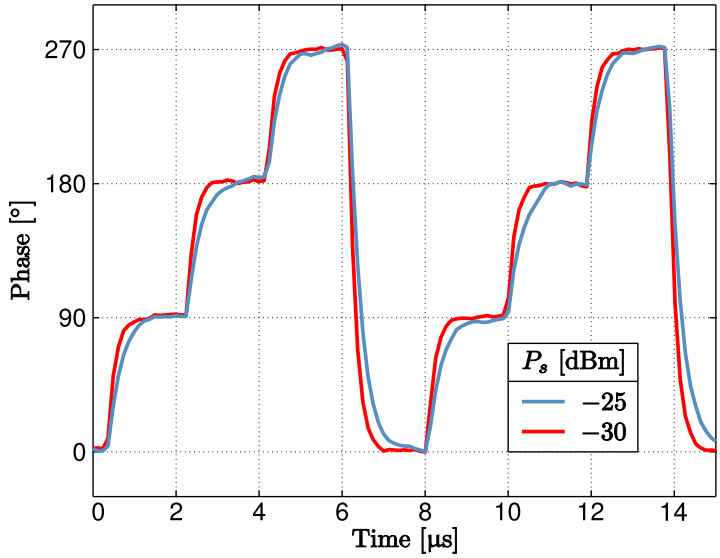

Figure 4.35: QPSK modulated signal measured at the output of the 4HOSC circuit.

4.8. Conclusions

A fourth harmonic oscillator circuit has been designed. The optimisation of the fourth harmonic component of the oscillation, at 10 GHz, as the output signal gives rise to a theoretical phase shift range of 720°. A practically usable phase shift range wider than 620° has been measured in the manufactured prototype.

The harmonic content generated has been optimised through non-linear optimisation techniques to maximise the output power at the fourth harmonic component, as well as to minimise the DC power consumption. A measured output power $P_o \approx -5$ dBm was attained, with a power consumption $P_{DC} = 5.7$ mW, corresponding to a power efficiency $\eta \approx 5.48\%$.

The phase noise performance of the fourth harmonic oscillator was evaluated both free running and injection locked to an external generator. In the latter case, the phase noise level observed decreases as the power of the external reference signal is increased, and it progressively converges (at the fundamental component) to the phase noise characteristic of the reference generator. Moreover, when used as a phase shifter, the phase noise performance of the circuit is

better close to the centre of the associated synchronisation loci, and it worsens towards the ends.

The capability of the circuit to transmit modulated signals has been assessed. When the circuit is injection locked to a phase modulated external signal, the output signal will follow the same phase modulation, with an amplitude multiplied by four. The circuit can be simultaneously used as a variable phase shifter, by tuning the varactor bias voltage. The dynamics of the circuit become increasingly faster for higher synchronisation power levels, as well as close to the centre of the synchronisation locus.

Hence, the fourth harmonic oscillator that has been presented is a multifunctional topology that can be used as a stand-alone front end for the control of antenna array structures transmitting phase modulated signals. Furthermore, the low power consumption that has been attained enable the use of that topology in portable or mobile applications.

Bibliography

[1] E.W. Bryerton, W.A. Shiroma, and Z.B. Popovic. A 5-ghz high-efficiency class-e oscillator. *Microwave and Guided Wave Letters, IEEE*, 6(12):441–443, 1996.

[2] Seunghyun Lee, Sanggeun Jeon, and Jinho Jeong. Harmonic-tuned high efficiency rf oscillator using gan hemts. *Microwave and Wireless Components Letters, IEEE*, 22(6):318–320, 2012.

[3] M. Azarmehr, R. Rashidzadeh, and M. Ahmadi. Low-power oscillator for passive radio frequency identification transponders. *Circuits, Devices Systems, IET*, 6(2):79–84, 2012.

[4] M.R. Haider, A.B. Islam, and S.K. Islam. Reduction of supply voltage and power consumption of an injection-locked oscillator for biomedical telemetry. In *Radio and Wireless Symposium (RWS), 2010 IEEE*, pages 408–411, 2010.

[5] Chieh-Lun Chiang, Chin-Lung Yang, and Shao-Ping Yu. Low-power oscillator with memory reduction tail transistors for 2.4 ghz ism band applications. In *Microwave Integrated Circuits Conference (EuMIC), 2012 7th European*, pages 532–535, 2012.

[6] Jia-Sheng Hong and M. J. Lancaster. *Microstrip Filters for RF/Microwave Applications*. John Wiley & Sons, Inc., 2001.

[7] S. Ver Hoeye, C. Vázquez Antuña, M. González Corredoiras, M. Fernández García, L. F. Herrán Ontañón, and F. Las Heras Andrés. Multi-harmonic dc-bias network based on arbitrarily width modulated microstrip line. *Progress In Electromagnetics Research Letters*, 11:119 – 128, 2009.

[8] L. Young G. Mattaei and E. M. T. Jones. *Microwave Filters, Impedance-Matching Networks, and Coupling Structures*. Artech House, Norwood, MA, 1980.

[9] Samuel Ver Hoeye, Almudena Suárez, and Sergio Sancho. Analysis of noise effects on the nonlinear dynamics of synchronized oscillators. *Microwave and Wireless Components Letters, IEEE*, 11(9):376–378, Sep 2001.

[10] V. Rizzoli, F. Mastri, and Diego Masotti. A general-purpose harmonic-balance approach to the computation of near-carrier noise in free-running microwave oscillators. In *Microwave Symposium Digest, 1993., IEEE MTT-S International*, pages 309–312 vol.1, 1993.

[11] V. Rizzoli, F. Mastri, and Diego Masotti. General noise analysis of nonlinear microwave circuits by the piecewise harmonic-balance technique. *Microwave Theory and Techniques, IEEE Transactions on*, 42(5):807–819, 1994.

[12] A. Suarez, S. Sancho, S.V. Hoeye, and J. Portilla. Analytical comparison between time- and frequency-domain techniques for phase-noise analysis. *Microwave Theory and Techniques, IEEE Transactions on*, 50(10):2353–2361, 2002.

[13] F. Ramirez, M. Ponton, S. Sancho, and A. Suarez. Phase-noise analysis of injection-locked oscillators and analog frequency dividers. *Microwave Theory and Techniques, IEEE Transactions on*, 56(2):393–407, 2008.

[14] Ieee standard definitions of physical quantities for fundamental frequency and time metrology - random instabilities. *IEEE Std 1139-1999*, 1999.

[15] A. Bruce Carlson, Paul B. Crilly, and Janet C. Rutledge. *Communications Systems*. McGraw-Hill, 2002.

[16] W.A. Gardner. *Introduction to Random Processes with Applications to Signals and Systems*. McGraw-Hill, 1990.

[17] In *Hewlett Packard RF and Microwave Phase Noise Measurement Seminar*, June 1985.

[18] A. S. Willsky A. V. Oppenheim and W. T. Young. *Signals and Systems*. Prentice-Hall, Englewood Cliffs, NJ, 1983.

[19] Petre Stoica and Randolph Moses. *Spectral Analysis of Signals*. Prentice Hall, 2005.

[20] J.R. Ashley and F.M. Palka. Measured fm noise reduction by injection phase locking. *Proceedings of the IEEE*, 58(1):155–157, 1970.

[21] T. Sugiura and S. Sugimoto. Fm noise reduction of gunn-effect oscillators by injection locking. *Proceedings of the IEEE*, 57(1):77–78, 1969.

[22] K.D. Stephan. Inter-injection-locked oscillators for power combining and phased arrays. *Microwave Theory and Techniques, IEEE Transactions on*, 34(10):1017–1025, 1986.

[23] Jenshan Lin, Siou Teck Chew, and Tatsuo Itoh. A unilateral injection-locking type active phased array for beam scanning. In *Microwave Symposium Digest, 1994., IEEE MTT-S International*, pages 1231–1234 vol.2, 1994.

[24] Xiangdong Zhang and A.S. Daryoush. Full 360 degrees phase shifting of injection-locked oscillators. *Microwave and Guided Wave Letters, IEEE*, 3(1):14–16, 1993.

[25] I.L. Morrow, P.S. Hall, and J.R. James. Measurement and modeling of a microwave active-patch phased array for wide-angle scanning. *Antennas and Propagation, IEEE Transactions on*, 45(2):297–304, 1997.

[26] Guan-Wu Wang, Terng-Jie Lin, Wen-Chung Liu, and Shu-Yuan Yang. A low cost dbs low noise block downconverter with a dr stabilized mesfet self-oscillating mixer. In *Microwave Symposium Digest, 1994., IEEE MTT-S International*, pages 1447–1450 vol.3, 1994.

[27] M. Fernandez, S. Ver Hoeye, L.F. Herran, and Fernando Las Heras. Nonlinear optimization of wide-band harmonic self-oscillating mixers. *Microwave and Wireless Components Letters, IEEE*, 18(5):347–349, May 2008.

[28] S. Drew and V.F. Fusco. Phase modulated active antenna. *Electronics Letters*, 29(10):835–836, 1993.

[29] Guangjun Wen, Fuzhen Xie, Peng Ge, Jiayin Li, and Jian Zhang. An injection locked oscillator for direction-conversion bpsk modulation applications. In *Microwave and Millimeter Wave Technology, 2004. ICMMT 4th International Conference on, Proceedings*, pages 570–573, 2004.

[30] L. Dussopt, J.-M. Laheurte, A.H. Lettington, P. Papakosta, and D. Dunn. Bpsk and qpsk modulations of an oscillating antenna for transponding applications. *Microwaves, Antennas and Propagation, IEE Proceedings*, 147(5):335–338, 2000.

[31] E. Fernandez, M. Ponton, F. Ramirez, S. Sancho, and A. Suarez. Analysis of direct phase modulation with an injection-locked oscillator. In *Microwave Conference (EuMC), 2010 European*, pages 616–619, 2010.

[32] C. Kykkotis, P.S. Hall, and H. Ghafouri-Shiraz. Active antenna oscillator arrays in communication systems. In *Microwave Symposium Digest, 1997., IEEE MTT-S International*, volume 2, pages 591–594 vol.2, 1997.

[33] T. Finateu, J. Begueret, Y. Deval, and F. Badets. Gmsk modulation of subharmonic injection locked oscillators. In *Solid-State Circuits Conference, 2005. ESSCIRC 2005. Proceedings of the 31st European*, pages 101–104, 2005.

[34] T. Finateu, J-B Begueret, Y. Deval, and F. Badets. Injection locked oscillator based rf transmitters. In *Design and Test of Integrated Systems in Nanoscale Technology, 2006. DTIS 2006. International Conference on*, pages 6–9, 2006.

[35] C. Vazquez, S. Ver Hoeye, M. Fernandez, L.F. Herran, and F. Las Heras. Analysis of the performance of injection locked oscillators in a data transmitting polarisation agile antenna application. *Progress in Electromagnetics Research Letters*, 12:1 – 10, 2009.

[36] Carlos Vázquez, Samuel Ver Hoeye, Germán León, Miguel Fernández, Luis Fernando Herrán, and Fernando Las Heras. Transmitting polarisation agile microstrip antenna based on injection locked oscillators. *Journal of Electromagnetic Waves & Applications*, 22(17/18):24, December 2008.

Chapter 5

Transmitting Active Antenna Array based on Fourth Harmonic Oscillators

Contents

5.1. Introduction

The well known properties of antenna arrays in the context of communication systems have already been mentioned in previous chapters. In particular, a receiving topology based on injection locked third harmonic self oscillating mixers was reported in Chapter 2.

This versatile circuit topology implements several functional blocks required in common communication systems, such as continuous range phase shifting and signal downconversion, together with the local oscillator signal generation, providing an overall positive conversion gain.

Nevertheless, the interesting features of this circuit architecture are generally difficult to translate into transmitting topologies, owing to the higher output power requirements normally imposed to this type of implementations.

In receiving topologies, the limited power levels of both the input RF and the output IF signals, enable their analysis as a small signal regime about the oscillatory solution. On the other hand, the increase of the required RF output power, and possibly of the IF input level, will result in the generation of non-negligible harmonic components and intermodulation products by these signals, which must be taken into account, ultimately increasing the computational cost of the simulations substantially. Furthermore, the presence of arbitrary signals with relatively high power levels in the circuit may dramatically perturb the oscillatory regime, to the point of completely extinguishing the solution via a Neimark–Sacker bifurcation.

Given the intrinsic difficulties of adapting the self oscillating mixer topologies to transmitting implementations, other options have been alternatively considered. The fourth harmonic oscillator design that has been presented in Chapter 4, exhibits interesting features such as very wide continuous phase shift range and a contained power consumption for a relatively low output power, which makes it appropriate for short-range point-to-point portable or mobile reconfigurable communications.

Thus, the purpose of this chapter is to employ the fourth harmonic oscillator circuit for the implementation of a two-dimensional active antenna array. The antenna array, as well as the required auxiliary networks, will be separately designed, analysed in detail and individually tested. Finally, a prototype of the complete active antenna system will be manufactured and experimentally characterised.

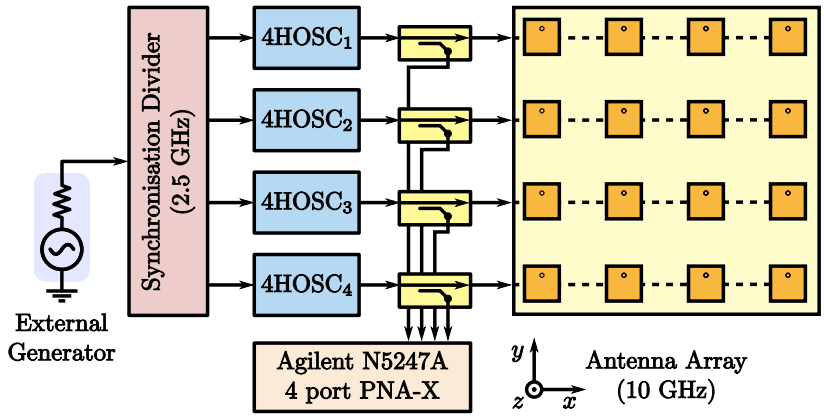

Figure 5.1: Block diagram of the transmitting active antenna array based on fourth harmonic oscillators.

5.2. System Overview

A schematic diagram of the transmitting active antenna array based on fourth harmonic oscillators is outlined in Figure 5.1. Each row of the 4×4 two-dimensional antenna array is fed with a uniform amplitude and phase distribution through a power divider network, subsequently connected to a 4^{th} Harmonic OSCillator circuit (4HOSC).

As has been analysed in detail in Chapter 4, when the fourth harmonic oscillator circuit is injection locked to an external signal at the fundamental oscillation component $f_0 = 2.5$ GHz, by tuning the varactor bias voltage V_c, the phase of its fourth harmonic component at $4f_0 = 10$ GHz—which has been optimised as the output signal—can be controlled in a continuous range exceeding 360°.

Therefore, by tuning the control signals of the four independently injection locked circuits, the pencil beam of the antenna array can be vertically steered (in the YZ plane, according to Figure 5.1).

For system monitoring purposes, a low power sample of the output signal of each of the 4HOSC circuits is extracted by means of directional couplers. These samples are simultaneously measured using a four port Agilent N5247A PNA-X vector network analyser.

5.3. Microstrip Antenna Array

Reconfigurable antenna arrays rely on separately controlling the feeding signals of the different individual elements, and thus, those signals need to be routed from each of the tuning circuits to the corresponding radiating elements.

The interconnection may not represent a challenge in linear arrays, such as the design developed in Chapter 2, where each individual signal can be accessed through a connector installed at the edge of the circuit board. However, this approach is not directly scalable to two-dimensional topologies and, although it can still be applied, it may lead to unwieldy implementations as the number of elements increases.

This limitation is overcome in [1], using a topology based on quasi Yagi antennas, in which the required tuning circuits for each row of the array are placed in a perpendicular plane.

In this work, the same arrangement of the tuning circuitry will be used. Nonetheless, in order to limit the interference of the spurious radiation produced by the circuits with the antenna radiation pattern, a two-dimensional microstrip antenna array, conveniently shielded by a common ground plane, will be designed in this section.

5.3.1. Individual Radiating Element

Due to the fact that the tuning circuits will be located under the ground plane of the antenna array, the radiating elements need to be fed from underneath. Thus, probe feeding is an appropriate technique for this purpose, since connectors associated with each of the individual elements can be installed on the ground plane, were the necessary circuitry is connected.

The impedance bandwidth of microstrip patch antennas is known to increase for higher values of the substrate thickness and for lower permittivities. However, thick substrates generally give rise to higher coupling levels, which make them inappropriate for array designs. Moreover, in simple probe fed topologies, the required length of the probe increases with the substrate thickness, leading to high inductance values that need to be subsequently compensated.

Hence, the solution that has been developed in this work relies on two stacked patches, as schematised in Figure 5.2. The first substrate layer, through which the probe is connected to the first patch, is maintained relatively thin, while the layer between the first and the second patch can be moderately thickened to improve the bandwidth.

The coaxial connector is soldered to the ground plane of the structure, while the probe is connected to the specified point on the first patch, etched on top of a 0.762 mm thick ARLON 25N substrate layer. The second patch is placed on top of a double layer of the same ARLON 25N laminate (1.524 mm).

According to the coordinate reference indicated in Figure 5.2, the design presents linear polarisation in the direction of the y axis. Therefore, the resonance frequency of either patch is primarily determined by its length in this direction. By appropriately tuning these lengths, together with the remaining dimensions, the resonances associated with the patches can be arranged close

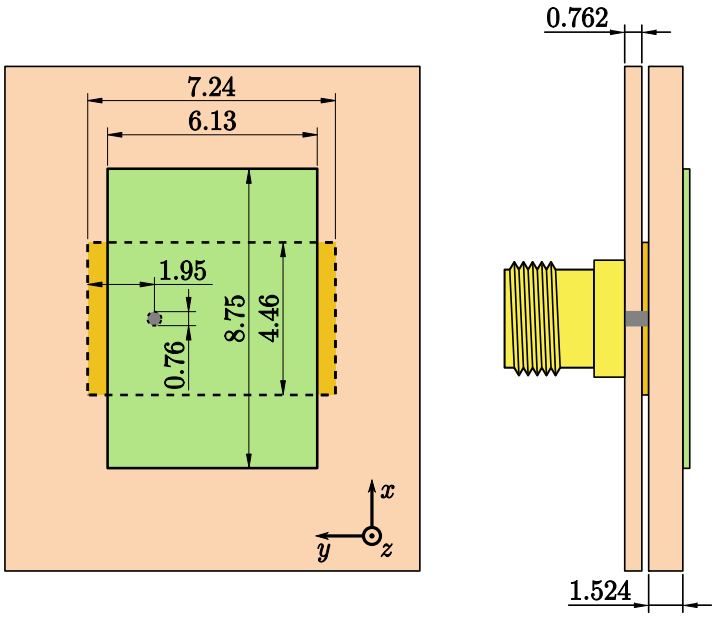

Figure 5.2: Proposed microstrip antenna design. Dimensions in millimetres.

together in the vicinity of the desired operating frequency, resulting in a bandwidth enhancement. In this case, the first patch is slightly longer than the second, giving rise to a lower resonance frequency.

The optimised design outlined in Figure 5.2 was developed by George Roberto Hotopan, M.Sc. as part of his Master's thesis [2], carried out under the supervision of the author of this doctoral work.

The design was developed relying on method of moments simulations performed with Advanced Design System 2009 (ADS). According to these simulations, an impedance bandwidth of over 1 GHz, centred at 10 GHz was obtained, as shown in Figure 5.3.

In order to experimentally validate the antenna design obtained using the simplified approach that has been described, the prototype shown in Figure 5.4, was manufactured and measured. The measured reflection coefficient of the prototype has been superimposed in Figure 5.3.

A significantly wider band of more than 1.5 GHz is observed in the prototype measurement. Two separate resonances can be clearly identified: the first one, at about 9.7 GHz, corresponds to the active patch, whereas the second, at about 10.6 GHz, is associated with the coupled (upper) patch.

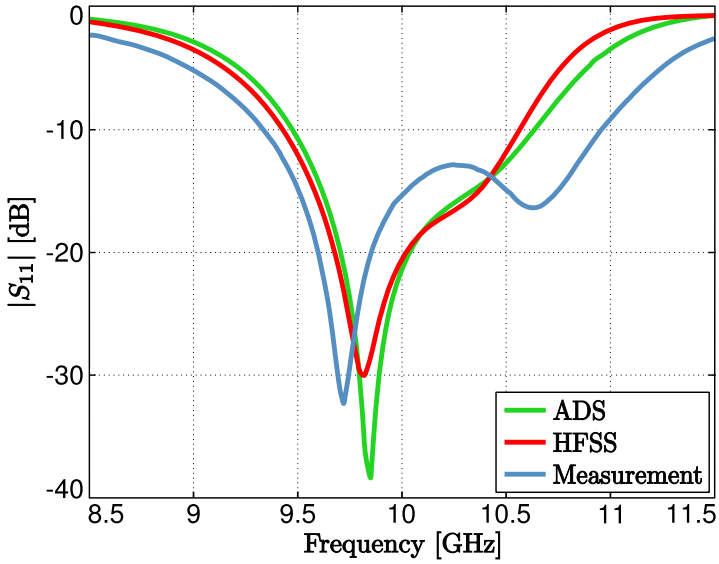

Figure 5.3: Simulation of the reflection coefficient of the antenna design, compared to measurement of the manufactured prototype.

5.3.1.1. Modelling and Simulation

The antenna design that has been described was obtained using the method of moments simulator of Advanced Design System 2009 (Momentum).

This analysis tool is usually classified as a 2.5D electromagnetic simulator, based on the fact that it only allows the existence of current components in two geometrical dimensions (2D), providing extended support for vertical currents in specific structures, such as via holes, albeit with stringent limitations [3].

Therefore, the modelling of the feeding probe is not straightforward in this simulation package. In addition to the limitations imposed on the via holes, the coaxial mode excitation is not specifically supported. By introducing certain geometric modifications in the design, the structure can still be excited using the available ports, but these artificial techniques generally lead to unreliable results.

As an alternative, the structure can be simulated by placing an internal port [3], directly onto the feeding point of the active patch, assuming an infinite and continuous ground plane. Nonetheless, the effect of the feeding probe is completely overlooked with this simplified approach.

The simulation results corresponding to the latter simulation set-up, implemented in Advanced Design System 2009 (ADS), have been presented in Figure 5.3.

As has been commented, the prototype exhibits an enhanced bandwidth with regard to the simulation result, which exceedingly fulfils the design requirements.

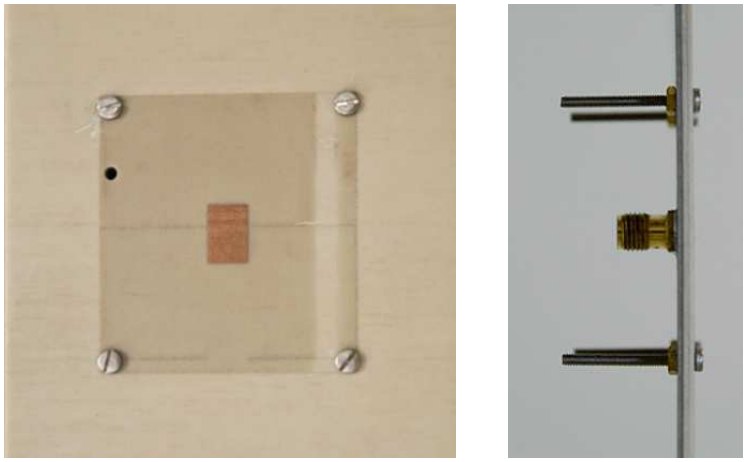

(a) (b)

Figure 5.4: Manufactured prototype of the microstrip antenna design: (a) Top view. (b) Side view.

However, in order to be able to effectively optimise the performance of the antenna element in the design process, it would be necessary to develop an accurate and reliable electromagnetic model of the structure.

The divergence between simulation and measurement can in principle be attributed to the simplified simulation set-up that has been employed, which completely neglects the effects of the feeding probe.

In order to verify the validity of this hypothesis, a full three-dimensional (3D) model of the design has been created in the Ansys HFSS Finite Element Method (FEM) simulator. The geometry of the antenna element has been accurately modelled, including the feeding probe and the connector soldered to the ground plane of the structure, which is directly excited with a coaxial mode.

The reflection coefficient obtained with the HFSS simulation, which is also represented in Figure 5.3, is surprisingly similar to the result calculated in the ADS simulation. In conclusion, the feeding probe seems to have a minor effect on the return loss performance, which certainly does not account for the deviation that has been observed in the manufactured prototype.

5.3.1.2. Radiation Pattern

The radiation features of the individual antenna design have been evaluated using the two simulation set-ups that have been described. The radiation patterns at the centre frequency, 10 GHz, have been calculated within both the E plane (YZ as indicated in Figure 5.2), and the H plane (XZ according to Figure

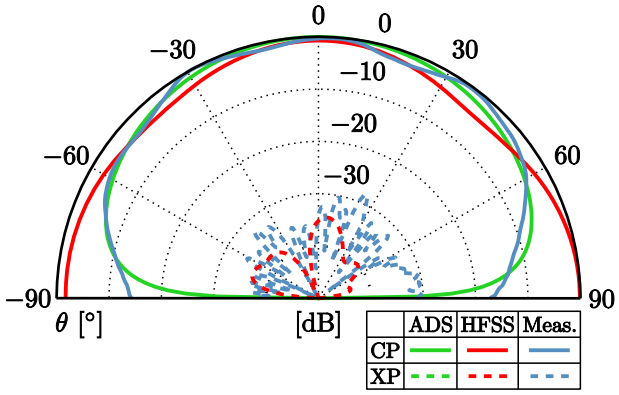

(a)

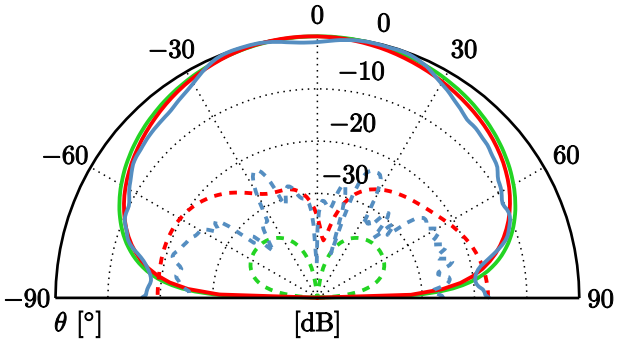

(b)

Figure 5.5: Simulated radiation patterns compared to measurements of the manufactured prototype at 10 GHz: (a) E plane (YZ plane in Figure 5.2). (b) H plane (XZ plane according to Figure 5.2).

5.2). The normalised results for the co-polar (CP) and cross-polar (XP) components are represented in Figure 5.5, versus the spherical coordinate θ. Predicted gain values of 5.17 and 6.5 dBi have been obtained using the ADS and HFSS simulations respectively.

The corresponding radiation patterns of the manufactured prototype have been measured in the anechoic chamber. The results have been superimposed in Figure 5.5, for comparison.

The co-polar components of the radiation patters that have been obtained with both simulation techniques are similar, showing a general agreement with the measurements. On the E plane, the ADS simulation produces more accurate results, especially for $|\theta| > 60°$, whereas, on the H plane, both analyses yield analogous results.

The measured radiation intensity for angles close to the dielectric surface ($|\theta| \rightarrow 90^{\circ}$), is higher than the levels predicted by the ADS simulation in both planes. This deviation may be caused by the fact that an infinite ground plane is assumed in this simulation set-up. Nevertheless, the full 3D HFSS simulation does not offer better results for those angles, especially on the E plane.

With regard to the cross-polar components, clearly dissimilar results are yielded by both simulation techniques. Noticeably lower levels are predicted by the ADS simulations (note that, on the E plane, they cannot even be appreciated in the scale of Figure 5.5). Although the shape of the radiation patterns are not precisely determined, the HFSS simulation provides a better prediction of the the approximate cross-polar levels.

The prototype exhibits a pure linear polarisation (parallel to the y axis) throughout an important part of the E plane. On the H plane, linear polarisation is observed in the vicinity of the bore sight direction, and it deteriorates as $|\theta|$ increases.

5.3.2. Two-dimensional Array Design

The microstrip antenna array that has been presented will be employed as the individual radiating element in a two-dimensional antenna array. The elements are arranged in a 4×4 rectangular grid, as shown in Figure 5.1.

The geometrical disposition of the elements, together with their individual radiation characteristics, determine the overall array radiation pattern. In general, for a constant element spacing d, if a progressive phase shift distribution is applied, the radiation pattern will exhibit a main beam which will be narrower for higher values of the element spacing. However, for $d > 0.5\lambda$, where λ is the free space wavelength at the frequency of operation, copies of the main lobe—known as *grating lobes*—will appear in the diagram, for certain steering angles of the main beam. These grating lobes will be present for any steering angle when $d > \lambda$.

In this work, as has been illustrated in Figure 5.1, each row of the array will be fed with a uniform amplitude and phase distribution through a power divider network, which will be connected to a fourth harmonic oscillator circuit. Therefore, the array synthesises a pencil beam that can be steered in the YZ plane by tuning the control voltages of the 4HOSC circuits.

As a design requirement, a Side Lobe Level (SLL) lower than -10 dB has been specified for steering angles $|\theta| < 25^{\circ}$. For a vertical element spacing $d_y = 0.7\lambda$, where $\lambda = 30$ mm is the free space wavelength at 10 GHz, a grating lobe higher than -10 dB appears in the radiation pattern for a steering angle $\theta = 25^{\circ}$. Thus, a vertical spacing $d_y = 0.6\lambda$ has been chosen instead, at the expense of slightly widening the main beam.

Conversely, since no steering is applied to the elements of each row, which are fed with a uniform amplitude and phase distribution, a horizontal element separation $d_x = 0.7\lambda$ can be established, fulfilling the SLL design requirement.

5.3.3. Mutual Coupling

The mutual coupling between individual elements is a key parameter that must be kept under control in antenna arrays, as it may lead to severe degradations of the overall performance.

In order to evaluate the mutual coupling levels between the elements of the antenna array with the spacings d_x and d_y that have been specified, simulations of the complete 4×4 antenna array have been performed using both the ADS and the HFSS set-ups that have been described.

The analysis of the simulated results indicates that the coupling levels observed between adjacent elements vary noticeably depending on their type of alignment, i.e. on whether they are relatively located in such a way that they share a common E or H plane. These types of arrangements will be referred to as E and H plane alignment respectively.

However, similar coupling levels were observed between adjacent elements with the same type of alignment, regardless of the particular pair of elements chosen.

Therefore, for the sake of clarity, only the coupling levels for one representative pair of neighbouring elements with either alignment have been represented in Figure 5.6.

Higher coupling levels are predicted with both simulation schemes between elements aligned along their E plane, which are separated $d_y = 0.6\lambda$, than between those aligned along their H plane, which are separated $d_x = 0.7\lambda$. Similar values have been obtained with both simulation methods for either case.

For the validation of these results, measurements of the manufactured prototype have also been superimposed in Figure 5.6. As opposed to the simulated results, the measured coupling levels are very much alike for both types of alignments and lie approximately in the middle between the simulations for either case.

5.3.4. Defected Ground Structure for Coupling Reduction

The coupling levels that have been observed between elements of the antenna array (about -21 dB in the worst case), are generally considered sufficient to ensure the proper operation of the antenna array without significant performance degradation.

Beyond its potential direct impact on the antenna array performance, mutual coupling between elements is especially detrimental when using oscillator based

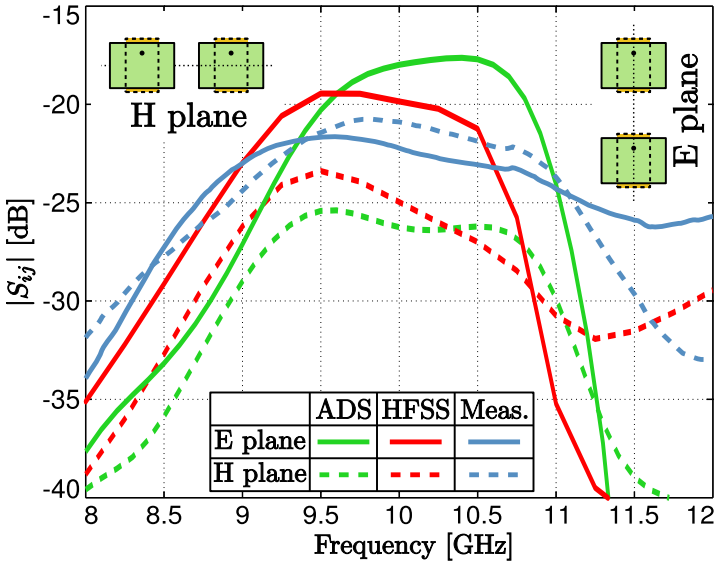

Figure 5.6: Mutual coupling (S_{ij} parameter) between adjacent elements aligned along either their E or their H plane.

phase shifters. As has been extensively discussed, the mutual coupling between injection locked oscillators generally gives rise to contractions of the phase shift ranges, with regard to the isolated behaviour. Moreover, excessive coupling levels between elements might lead to undesired synchronisations, ultimately causing dysfunctional operation.

According to the system topology outlined in Figure 5.1, each row of the array will be controlled—through a power divider network—by an independent injection locked fourth harmonic oscillator. Therefore, the elements of each row will be connected to a single 4HOSC circuit and, although the mutual coupling between these elements may affect the radiation pattern, it does not increase the coupling levels between oscillator circuits.

On the other hand, since adjacent elements within the same column are connected to different 4HOSC circuits, the mutual coupling between them constitutes a coupling path between the associated oscillators that must be taken into consideration. Consequently, in order to prevent the appearance of potential detrimental effects, the mutual coupling levels between elements of the same column, which are aligned along their E plane, need to be reduced.

Different methods for the reduction of mutual coupling between antenna array elements have been proposed in the literature. An array of shorting pins between the patch and the ground plane is introduced in [4], leading to substantially decreased coupling levels. Other works focus on suppressing the surface wave generation by optimising the antenna dimensions [5], using silicon micromachined

substrate structures [6], or introducing superstrates [7]. Different approaches have been presented, based on Electromagnetic Band Gap (EBG) structures using either shorted [8] or floating [9] elements.

Defected Ground Structures (DGS) are implemented by etching slots of different shapes in the ground planes. They have been employed to improve the performance in multiple applications such as filters, couplers or dividers, as well as to reduce the mutual coupling between elements of antenna arrays [10].

In this section, a defected ground structure for mutual coupling reduction between the antenna elements aligned collinearly along their E plane will be proposed and optimised.

5.3.4.1. Mutual Coupling

Two different simulation set-ups have been used for the design and analysis of the proposed probe fed microstrip antenna. However, neither approach has stood out as a clearly superior model in terms of accuracy when compared with experimental results.

The ADS simulation set-up is considerably simpler than the full 3D HFSS scheme, leading to far shorter simulation times. Hence, since no appreciable improvement has been observed in the performance, the ADS simulation set-up will be used in the following, in order to take advantage of the lower computational cost.

The interaction between two antenna elements aligned collinearly along their E plane, has been studied as a function of frequency, for different values of the spacing, from $\lambda/2$ to λ, in steps of $\lambda/30$ ($\lambda = 30$ mm is the free space wavelength at 10 GHz). The results are shown in terms of reflection coefficient in Figure 5.7(a), and in terms of mutual coupling in Figure 5.7(b).

The reflection coefficient is not significantly affected by the presence of the second element and an impedance bandwidth greater than 1.12 GHz is observed for all the studied values of the separation. Since the S_{22} parameter exhibits a completely analogous behaviour, it has not been represented.

Except for the first three studied values, $d = 15$, 16 and 17 mm, which have been represented in dotted line, as they show a slightly different variation pattern, the mutual coupling decreases monotonically as the element separation is increased.

5.3.4.2. Proposed DGS Design

The defected ground structure proposed in this work is composed of rectangular slots, as shown schematically in Figure 5.8, where the design parameters are the lengths l_i and widths w_i, $i = 1, \ldots, 5$, and the separation between them

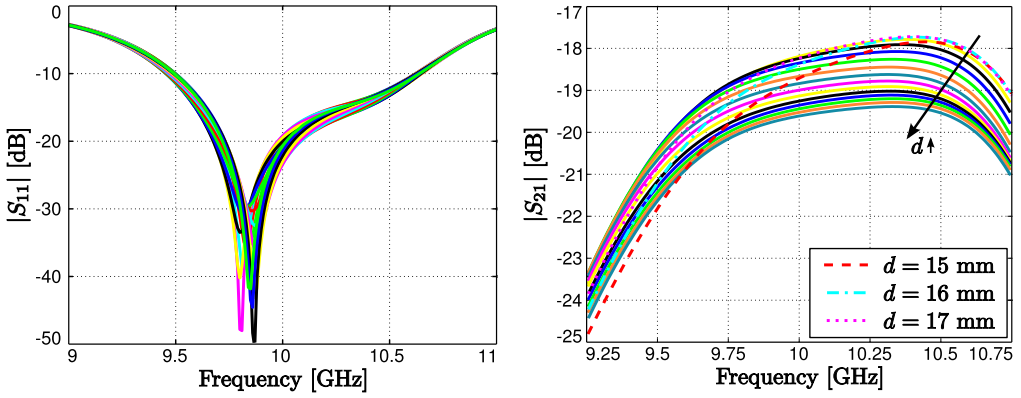

(a) (b)

Figure 5.7: Simulated scattering parameters for different values of the separation between elements d (from $\lambda/2 = 15$ mm to $\lambda = 30$ mm in steps of $\lambda/30 = 1$mm). (a) $|S_{11}|$. (b) $|S_{21}|$.

$d_{i-1,i}$, $i = 2, \ldots, 5$. Two different structures with 3 and 5 slots will be optimised. In both cases, the structure is placed in such a way that the middle slot is centred—both vertically and horizontally—with respect to the two antenna elements, which are separated $d = 0.6\lambda$. The remaining slots are vertically centred.

The design was developed through a nominal gradient descent optimisation process, based on ADS Momentum electromagnetic simulations. The goal of the defected ground structure was to reduce the mutual coupling between the antenna elements throughout its band of operation, and especially at 10 GHz, which is the fourth harmonic component of the fundamental oscillation of the 4HOSC circuit.

Since, as has been shown in Figure 5.3, the centre of the measured impedance bandwidth slightly shifted towards higher frequency, with regard to the simulation results, the optimisation target is set up to minimise the mutual coupling at 9.8 GHz.

In spite of the limited efficiency of the ADS optimisation process based on electromagnetic simulations, an effective reduction of the mutual coupling has been attained using a structure with narrow, closely spaced slots. The optimised dimensions of both the three and five slot designs are specified in Table 5.1.

The simulated performance of the final optimised DGS designs is presented in Figure 5.9, compared to the behaviour without DGS. The mutual coupling has been reduced throughout an important fraction of the antenna operating bandwidth. A greater reduction has been attained with the five slot design (around 11 dB with regard to the results without DGS), although a slightly

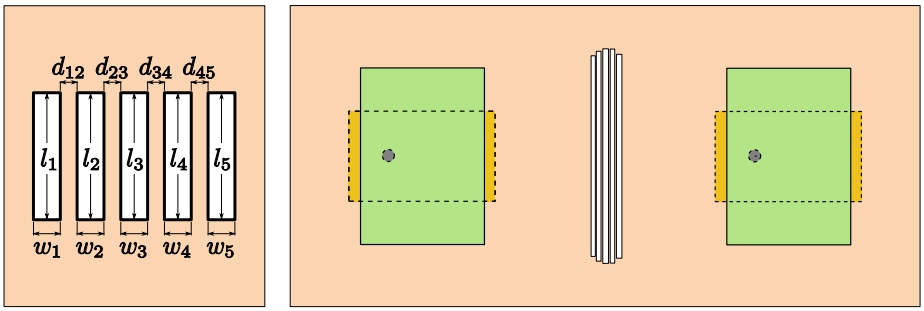

(a) (b)

Figure 5.8: (a) Outline (not to scale) of the proposed defected ground structure, indicating its design parameters. Two element antenna array with the optimised five slot DGS design.

narrower bandwidth is observed. The three slot design presents a smoother frequency variation, with a maximum mutual coupling reduction of around 9 dB.

5.3.4.3. Experimental Results

For the experimental validation of the simulated results, prototypes of the two element antenna array with both optimised DGS designs have been manufactured. An image of the top layer, which is common for both manufactured prototypes, is shown in Figure 5.10(a). The bottom substrate layer of the prototypes with the three and five slot design are presented in Figures 5.10(b) and (c), respectively.

Microscope photographs of the manufactured three slot DGS design are shown in Figure 5.11(a), and of the five element design in Figure 5.11(b). The designs have been manufactured through laser prototyping equipment, which provides a cutting accuracy of ± 2 μm, with a focused beamwidth of 25 μm.

Among the multiple technologies used in the fabrication processes of the commercially available substrate laminates for RF applications, in the particular case of the ARLON 25N substrate used for this antenna design, the 18 μm thick copper sheet is glued on top of the dielectric material.

During the laser prototyping process, very high temperatures are reached in the vicinity of the structured edges. This effect becomes especially critical when thin metal strips need to be implemented in the design, in which case the adhesive material under the metal layer may deteriorate, causing the structured strip to come unstuck.

Therefore, although the dimensions of the optimised DGS structures, summarised in Table 5.1, are far from the accuracy limits of the fabrication equipment, the tendency of the metal layer to peel off has appreciably complicated the

(μm)	l_1	w_1	$d_{1,2}$	l_2	w_2	$d_{2,3}$	l_3
3 slots	–	–	–	10 348	223	91	10 613
5 slots	10 075	233	87	10 398	234	79	10 619

(μm)	w_3	$d_{3,4}$	l_4	w_4	$d_{4,5}$	l_5	w_5
3 slots	201	112	10 380	222	–	–	–
5 slots	226	114	10 329	222	74	9 939	268

Table 5.1: Dimensions of the optimised defected ground structure, in micrometres.

process. Nonetheless, well defined edges and sharp corners have been obtained in both designs, as shown in Figure 5.11.

The measurements, compared to the performance of the array without DGS are presented in Figure 5.12. According to the design goal, the minimum of the mutual coupling with both DGS designs takes place at about 10 GHz, matching the fourth harmonic component of the 4HSOM circuit. Minima of about −28 and −30 dB have been achieved with the three and five slot designs respectively.

Furthermore, the mutual coupling is reduced throughout a wider bandwidth with the five slot design. Therefore, inasmuch as the manufacturing complexity of both designs is analogous, the five element version will be chosen for the final two-dimensional antenna array prototype.

5.3.5. Feeding Network

As has been commented, each fourth harmonic oscillator circuit controls one row of the two-dimensional antenna array, whose elements are fed with a uniform amplitude and phase distribution through a power divider network.

For the implementation of the required one-to-four equal split power dividers, the two stage topology based on Wilkinson dividers that has been repeatedly used in previous chapters, presents interesting features such as relatively broadband response, high isolation levels, lossless operation when driving matched loads, among others.

Four identical power dividers are needed for the feeding network of the 4×4 antenna array—one for each row—which will be realised using the same Wilkin-

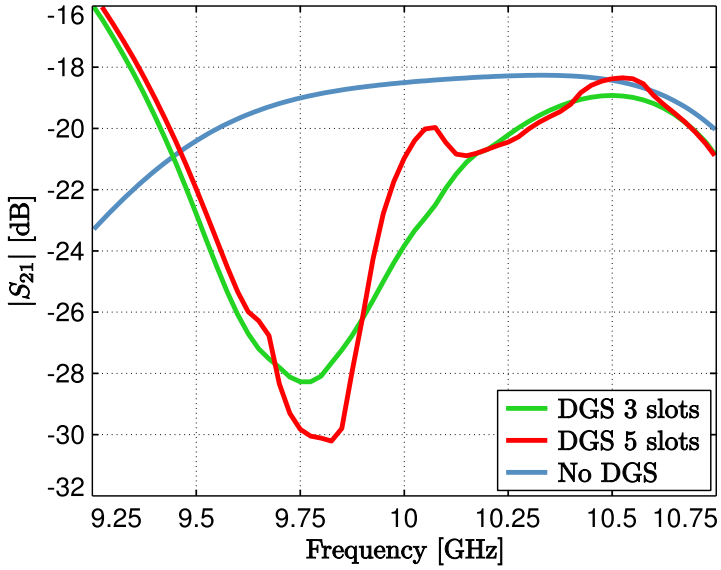

Figure 5.9: Simulated S_{21} parameter in the two element antenna array with the optimised DGS designs, compared to the results without DGS.

son based topology. The symmetry maintained in the transmission line layout results in a uniform phase distribution in the four outputs of the network.

Additionally, an analogous power divider has been designed to feed the four row dividers with a uniform amplitude and phase distribution, enabling the evaluation of the antenna array radiation pattern separately.

An image of the manufactured power dividers is presented in Figure 5.13. The four row dividers are shown on the right hand side, while the transversal auxiliary divider is on the left side. Note the difference in the output port spacing, which is $0.6\lambda = 18$ mm for the row dividers, and $0.7\lambda = 21$ mm for the transversal divider.

In spite of the fact that the dividers were designed to show identical amplitudes and phases at their outputs, 10 GHz is a sufficiently high frequency for the slightest manufacture errors to bring about observable deviations in the practical performance. Therefore, the measured transmission coefficients of the power dividers are shown in Figure 5.14(a), in terms of normalised amplitude and in Figure 5.14(b), in terms of relative phase.

Each of the traces represents the transmission coefficient S_{i5}, from the input port (port 5) of one of the manufactured dividers, to each of its output ports $i \in \{1, \ldots, 4\}$, at 10 GHz. All the traces are normalised with respect to the same value.

A maximum amplitude deviation smaller than 2.5 dB has been observed. With regard to the output phase distribution, the maximum deviation is lower

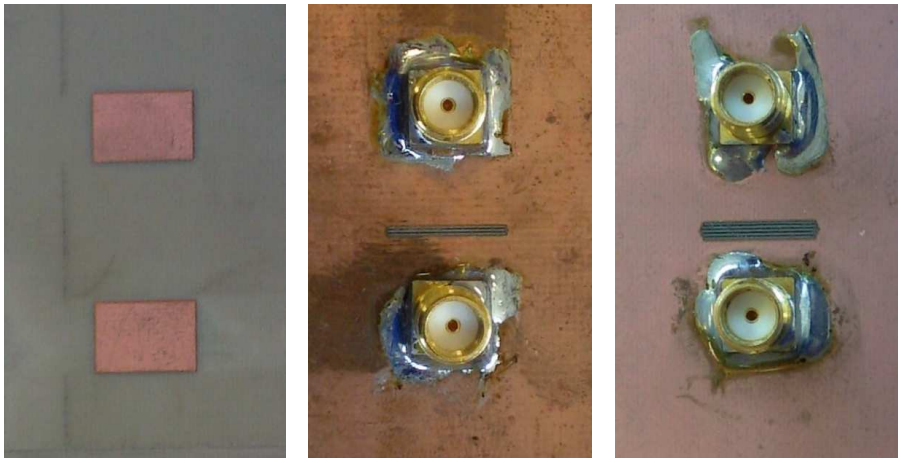

(a) (b) (c)

Figure 5.10: Images of the manufactured two element antenna array prototypes with the DGS designs (a) Top view, upper radiating patches. (b) Bottom view, three slot DGS design. (c) Bottom view, five slot design.

than 14°, which is acceptable for the separate evaluation of the antenna array radiation pattern.

On the other hand, when the array is controlled by the fourth harmonic oscillators, as schematised in Figure 5.1, the transversal power divider is not needed, and the phase of the input signals of the row dividers can be arbitrarily varied. Thus, through an adequate tuning of the control signals, the average phase deviation between the different row dividers can be subsequently compensated. Although the phase errors between the outputs of a specific divider cannot be corrected, not very significant deviations are observed in Figure 5.14(b), with a maximum under 8°.

5.3.6. Final 4×4 Antenna Array Prototype

Using the individual antenna element that has been described, a prototype of the 4×4 antenna array has been manufactured. The optimised five slot defected ground structure has been introduced to reduce the mutual coupling between the antenna elements aligned along their E plane, which are separated 0.6λ.

An image of the manufactured prototype is shown in Figure 5.15(a). The multilayer structure is aligned and held together through 2 mm nylon screws.

As has been commented, the elements on each row of the array will be fed with a uniform amplitude and phase distribution through the power divider networks that have been presented, which will be connected to a fourth harmonic oscillator.

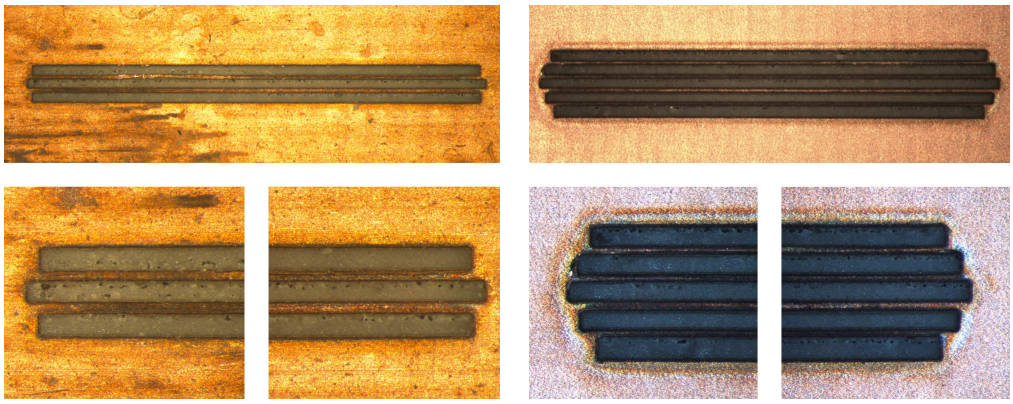

(a) (b)

Figure 5.11: Microscope photographs of the manufactured DGS designs. (a) Three slot design. (b) Five slot design.

In order to evaluate the performance of the antenna array prototype separately, the 4HSOM circuits have been replaced by an additional power divider, designed to feed the four divider inputs with equal amplitude and phase. An image of the complete prototype is shown in Figure 5.15(b).

The three-dimensional radiation pattern of the antenna array prototype, with the fixed uniform feeding network, has been measured in the anechoic chamber at 10 GHz. The prototype has been mounted on the rotary platform according to the coordinate reference established in Figure 5.2, which will be preserved for the radiation pattern.

Different formats can be employed for the representation of the radiation intensity in the different directions in the three-dimensional space. In the UV space, the unit vector in any given direction—specified by its spherical coordinates θ and ϕ—is represented by its projection onto the XY plane, in such a way that the x and y components are referred to as u and v, respectively, as follows:

$$\begin{aligned} u &= \sin\theta\cos\phi \\ v &= \sin\theta\sin\phi \end{aligned} \tag{5.1}$$

Note that, in order for the relation (5.1) to be unambiguous, the representation must be restricted to one semispace: either $z > 0$ or $z < 0$.

The measured radiation pattern for $z > 0$ has been represented in the three-dimensional UV space in Figure 5.16. The height above the UV plane represents the magnitude of the radiation pattern, in dB. Similarly, a 2D UV representation, in which the magnitude is indicated by the colour scale, is shown in Figure 5.17. Finally, the conventional 3D radiation pattern, in which the magnitude in a given

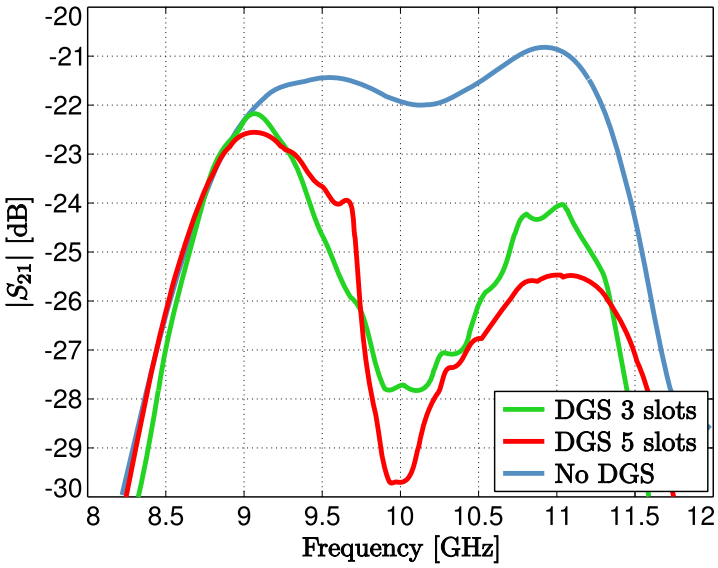

Figure 5.12: Measured S_{21} parameter of the two element antenna array with the optimised DGS designs, compared to the results without DGS.

direction is indicated by the distance to the origin in that direction, is shown in Figure 5.18.

The array shows a pencil beam pointed at the bore sight direction $z > 0$, with a side lobe level lower than -10 dB. As expected, beamwidth in the XZ plane is narrower than in the YZ plane, due to the difference in the element spacings that has been mentioned ($d_x = 0.7\lambda$ and $d_x = 0.7\lambda$).

5.4. Auxiliary Networks

In addition to the functional blocks that have hitherto been described, certain interconnection networks are required, in order to complete the system block diagram presented in Figure 5.1.

The required microwave networks have been developed in microstrip technology and implemented in 0.75 mm thick Rogers 3003 substrate laminate, whose datasheet specification was summarised in Table 4.1.

5.4.1. Synchronisation Power Divider

The external synchronisation signal, at $f_s = 2.5$ GHz must be delivered to each of the 4HOSC circuits independently, with equal power level and phase.

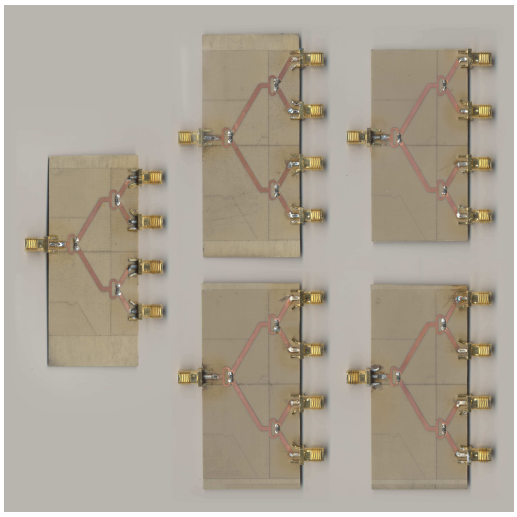

Figure 5.13: Manufactured power dividers: row dividers on the right side and transversal divider on the left side.

The same topology presented in Section 5.3.5 for the antenna array feeding network has been used for the synchronisation power divider. The two stage Wilkinson based network is shown in Figure 5.19(a).

Since the operating frequency of the synchronisation divider, is significantly lower than that of the antenna array feeding network, the fabrication errors in this case lead to negligible deviations. The measured output amplitude deviation is lower than 0.1 dB and the phase variation remains under 1°.

Isolation levels higher than 25 dB have been measured between the output ports. Due to the low synchronisation power level required by the 4HOSC circuits, the isolation could be further improved—if necessary—at the expense of increasing the network losses, without significantly degrading the overall system efficiency.

A straightforward method to increase the isolation is to connect an attenuator to each of the output ports of the power divider. Thus, while the power required from the synchronisation generator is risen by the attenuator value, the isolation between ports increases twice as much, with regard to the separate performance of the power divider.

Although the isolation could be alternatively improved through the careful design of the power dividers, four 10 dB π-type resistor attenuators have been manufactured to reduce the circuit interaction in the prototype. Since the synchronisation power levels required by the circuits are very low, the absolute power loss due to the attenuators is not very significant.

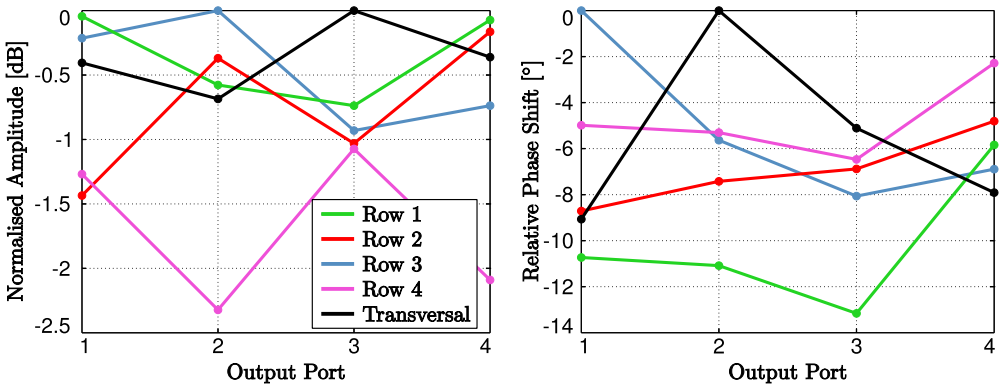

(a) (b)

Figure 5.14: Measured transmission coefficients of the power dividers at 10 GHz. (a) Normalised amplitude (b) Relative phase.

5.4.2. Output Sampling Directional Couplers

For system monitoring purposes, low power samples need to be extracted separately from the output signal of each of the 4HOSC circuits.

The sampling networks will be implemented through microstrip coupled line directional couplers, like those employed in Section 2.5.2 for an analogous application.

The directional couplers, shown in Figure 5.19(b), were designed for a tap loss of 16 dB at 10 GHz, although the measured values are slightly higher. The variation of the magnitudes or phases of the samples extracted by the different couplers is not a critical parameter, as it can be subsequently compensated for through calibration.

Nonetheless, the main design requirement for the directional couplers is that they exhibit similar insertion loss values, as they would otherwise result in an amplitude tapering of the antenna array feeding signals. The insertion losses observed on the prototypes are about 2 dB, with a variation of less than 0.5 dB.

5.5. Experimental Results

The individual parts that compose the active antenna array based on fourth harmonic oscillators have been separately designed and experimentally validated in the foregoing sections.

The purpose of this section is to set about the development of a prototype of the complete system and to evaluate its practical performance through measurements.

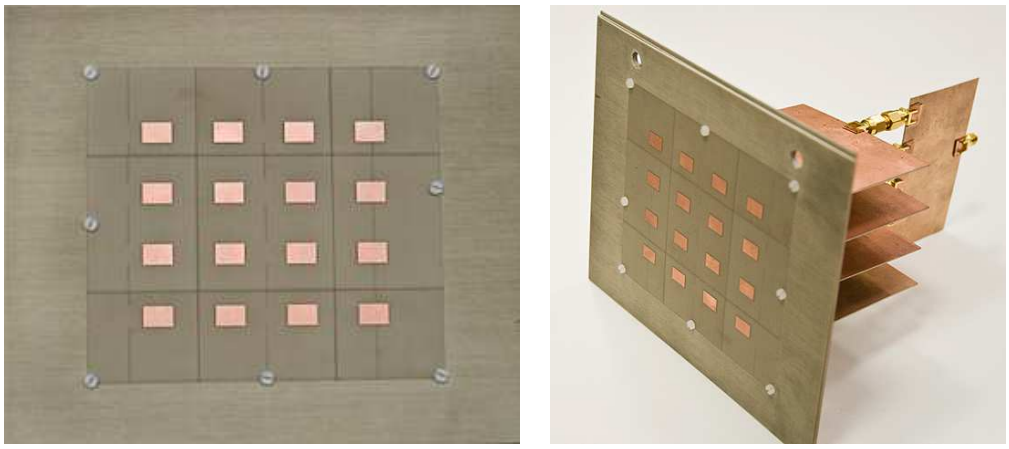

(a) (b)

Figure 5.15: Images of the manufactured prototype. (a) Top view of the two-dimensional antenna array. (b) Antenna array with feeding network.

5.5.1. Prototype Assembly

The different composing parts of the active antenna array based on fourth harmonic oscillators, according to the schematic diagram shown in Figure 5.1, have been manufactured in separate circuit boards, provided with SMA end launchers, for network interconnection. The prototype has therefore been assembled using SMA plug-plug straight adaptors.

In order to limit the mechanical stress undergone by the RF connectors and to enable its suspension in the anechoic chamber, the prototype has been mounted on an adapted wooden support structure, as shown in Figure 5.20(a).

A close-up of the prototype is presented in Figure 5.20(b). The power divider located on the left hand side of the image, delivers the synchronisation signal to the four independent 4HOSC circuits. The output of these circuits, is sampled through directional couplers and finally delivered to the antenna array. The sample signals are collected through the blue RF cables routed underneath the prototype.

In order to prevent the spurious radiation produced by the circuitry from interfering with the antenna array radiation pattern, the prototype has been surrounded with absorbing material. In the final design, the circuitry must be provided with an appropriate shielding enclosure to block these emissions.

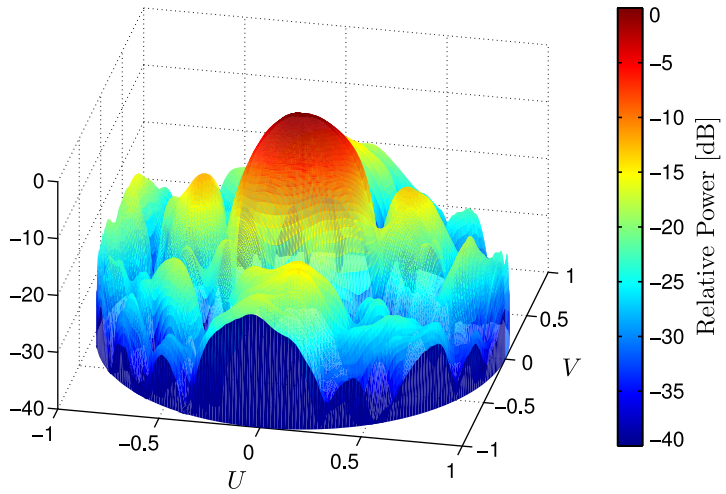

Figure 5.16: Measured radiation pattern of the 4×4 microstrip antenna array with fixed feeding network, represented in three-dimensional UV space.

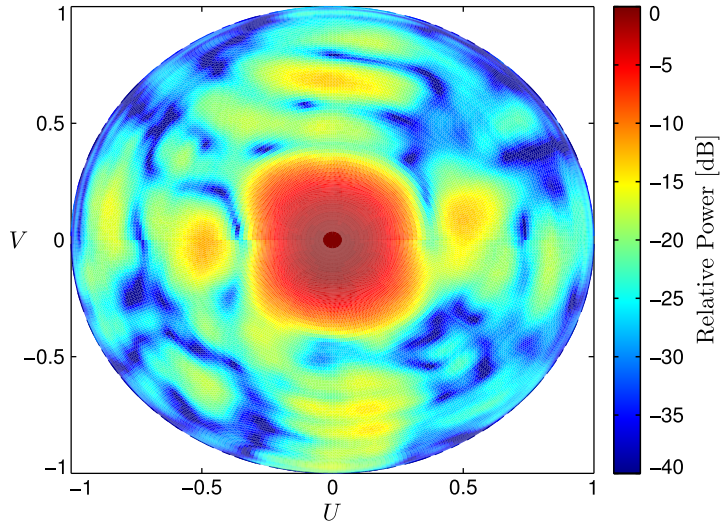

Figure 5.17: Planar UV space representation of the measured radiation pattern of the 4×4 microstrip antenna array with fixed feeding network.

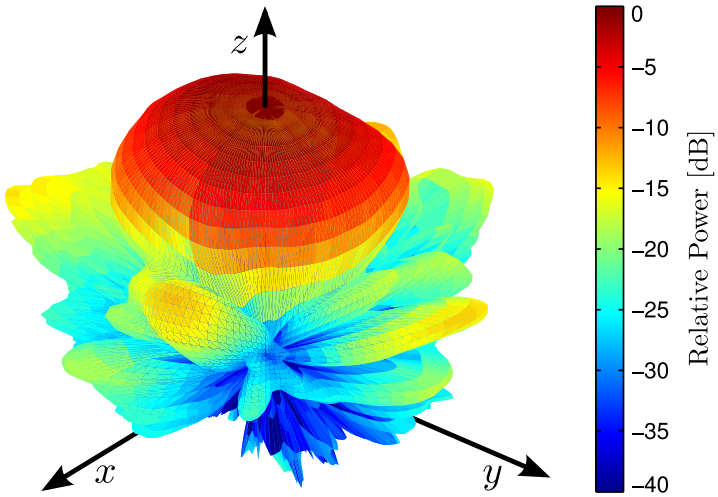

Figure 5.18: Measured three-dimensional radiation pattern of the 4×4 microstrip antenna array with fixed feeding network.

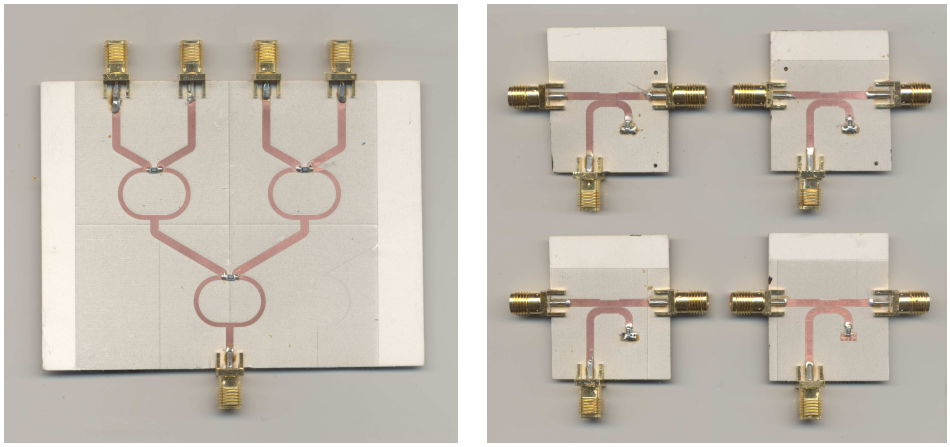

(a) (b)

Figure 5.19: (a) Synchronisation power divider. (b) Coupled line directional couplers.

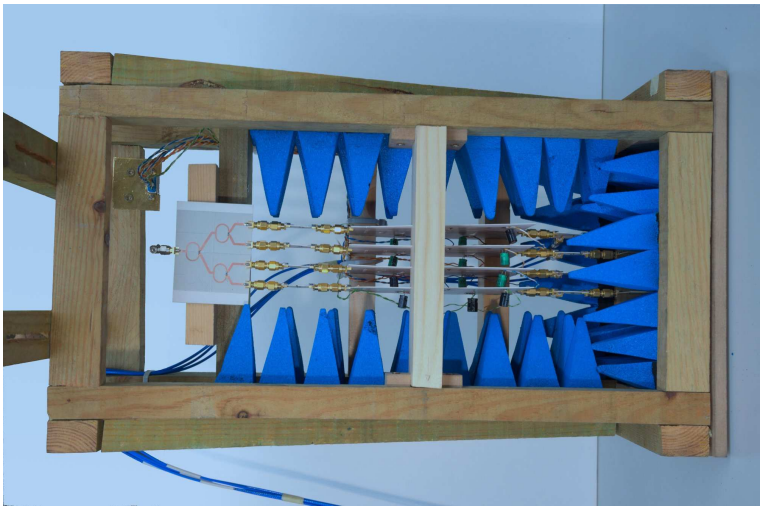

(a)

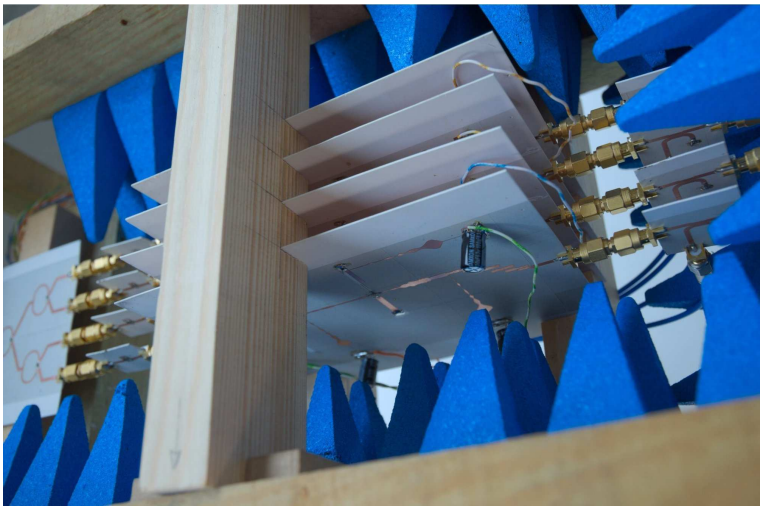

(b)

Figure 5.20: (a) Active antenna array prototype mounted on wooden frame. (b) Close-up of the prototype.

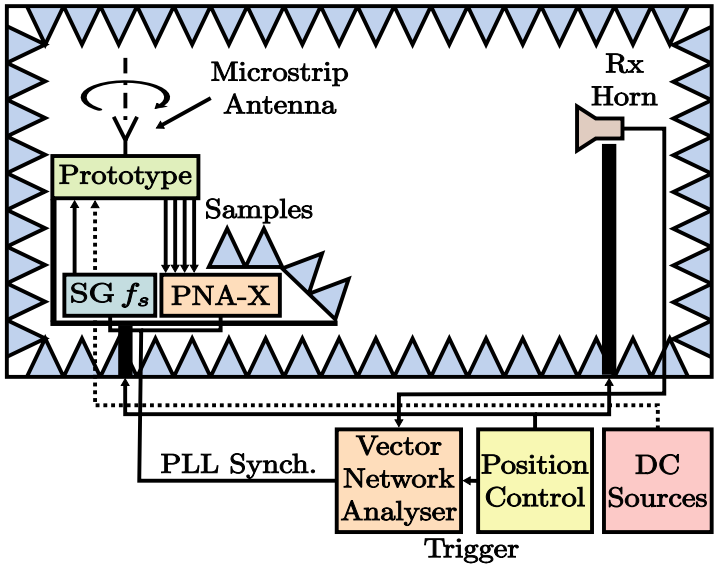

Figure 5.21: Schematic diagram of the measurement set-up.

5.5.2. Measurement Set-up

The experimental characterisation of the active antenna array based on fourth harmonic oscillators has been evaluated using the measurement set-up outlined schematically in Figure 5.21.

The fundamental equipment and accessories that compose this set-up are briefly described in the following:

- ***DC Power Supplies Hameg HM7044 and HM7042-5:*** In order to control the three DC bias signals of each of the 4HOSC circuits independently, 12 separate power supply channels are required. The ammeters of the power sources enable the real time monitoring of the power consumption of the circuits, which is closely related to their operating points.

- ***Agilent N5247A PNA-X 4 Port Vector Network Analyser:*** Using this piece of equipment, the low power samples extracted from the output signals of the 4HSOM circuit are simultaneously monitored. In order to enable an accurate measurement of the 10 GHz output signal—especially in phase—any movement of the cables must be suppressed. Therefore, a support structure has been built to sustain the vector network analyser on the rotary platform. The measured data was remotely accessed through a wired network connection.

- ***Microwave Signal Generator Rohde & Schwarz SMR40:***: This generator produces the synchronisation signal for the circuits at $f_s = 2.5$ GHz.

This generator, also located on the rotary platform, is controlled by the vector network analyser through a GPIB interface. The phase locked loops of all the generation and measurement equipment share a 10 MHz reference signal which sets a common phase reference.

- ***Pyramidal Horn Antenna:*** Used as a probe antenna to receive the signal radiated by the system.
- ***Spherical Range in Anechoic Chamber:*** In order to minimise the impact of reflections and spurious signals in general, the complete measurement process has been carried out in an anechoic environment.
- ***Vector Network Analyser Rohde & Schwarz ZVK 10 MHz–40 GHz:*** This analyser is part of the equipment of the anechoic chamber and, as such, it is triggered by the control system of the different rotary platforms.
- ***DC wiring:*** For the independent power supply and control of the 4HOSC circuits, multiple DC circuits are required. A purpose-built VGA cable was used to route these circuits and a VGA jack was installed on the support structure to simplify the connection and disconnection.
- ***Ethernet cabling:*** Required in order for the equipment located inside the anechoic chamber to be controlled from the outside through a network connection.

An image of the prototype suspended on the azimuthal positioner of the anechoic chamber is shown in Figure 5.22(a). The prototype has been wrapped in absorbing material to prevent the spurious radiation produced by the control circuitry from interfering with the antenna radiation pattern.

The measurement equipment—also covered with absorbing material—has been placed on the base on the rotary platform, as shown in Figure 5.22(b). The RF cables have been clamped to the post of the rotary platform to minimise their movement during the measurement process, as can be observed in the close-up of the front part presented in Figure 5.22(c).

5.5.2.1. Set-up Calibration

The measurement set-up has been designed to evaluate the radiation pattern of the active antenna array system, while the output signals of the four active circuits are simultaneously monitored. For this purpose, directional couplers have been inserted in the output port of each of the circuits, to extract low power samples.

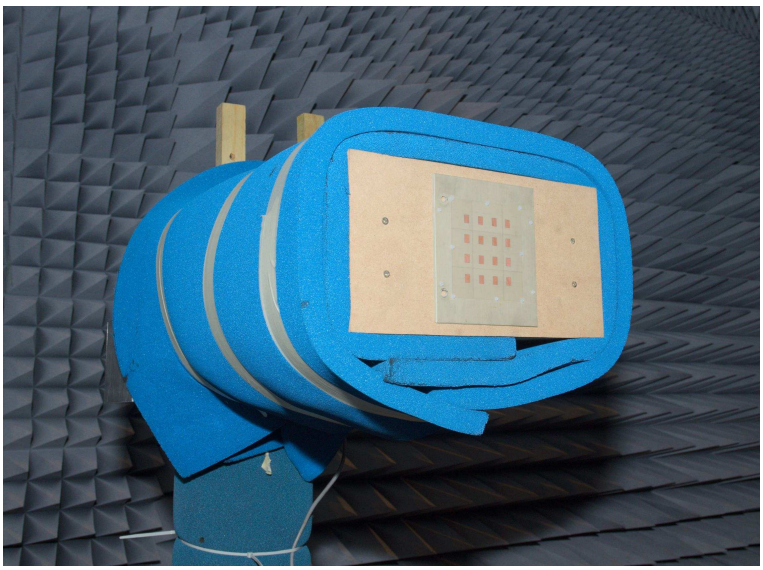

(a)

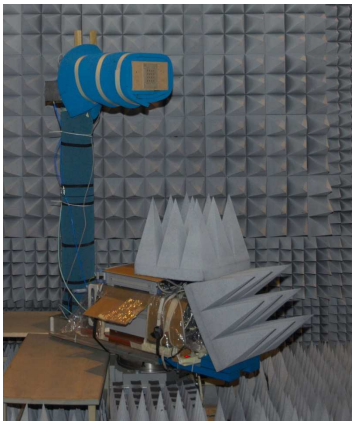

(b)

(c)

Figure 5.22: (a) Prototype suspended on the anechoic chamber. (b) Overview of the rotary platform. (c) Close-up of the equipment located on the base of the rotary platform.

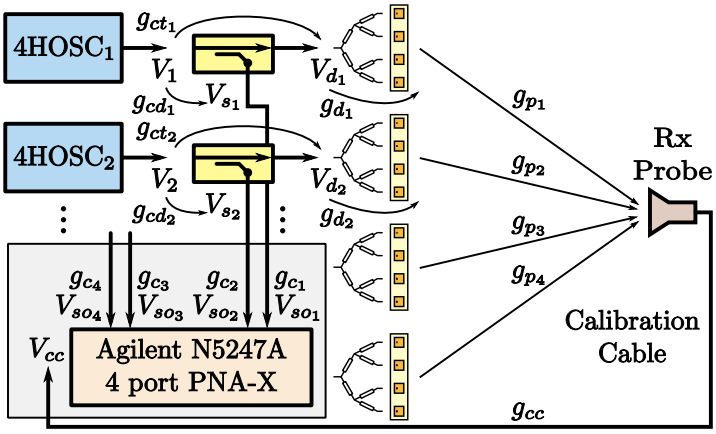

Figure 5.23: Schematic diagram of the measurement set-up calibration procedure.

However, due to the relatively high operating frequency—about 10 GHz—the slightest fabrication error may lead to appreciable changes in the performance, especially in terms of phase. Note the differences in the behaviour of the power dividers that feed the antenna array, that have been observed in Figure 5.14. Furthermore, since the RF cables that deliver the sample signals to the 4 port PNA-X vector network analyser are not identical, they also contribute to perturb the measurement.

Hence, a calibration process needs to be carried out to derive a relationship between the signals radiated by the antenna elements controlled by each of the 4HOSC circuits, and its corresponding sample signal, as it is delivered to the 4 port PNA-X.

Since each of the active circuits controls four antenna array elements through a power divider, the radiated signal cannot be directly accessed. The signal delivered to each power divider could be considered instead, neglecting the effect of each particular power divider and assuming they are identical. However, in addition to the differences in the behaviour of the dividers that have been commented, this technique would require the disconnection of the antenna array, together with its feeding network, to perform the calibration. The subsequent reconnection of this part might result in mechanical alterations of the prototype that would invalidate the calibration.

In order to be able to perform the calibration without partially disassembling the prototype, the procedure shown schematically in Figure 5.23, has been employed.

It is important to notice that the two-dimensional antenna array is positioned on the azimuthal positioner of the anechoic chamber in such a way that the rows driven be each 4HOSC circuit are vertically oriented, as is the rotation axis. Thus,

each of these uniformly fed linear arrays exhibit a main lobe pointed at the bore sight direction in the vertical plane and, when they are simultaneously excited by the 4HOSC circuits, a pencil beam that can be scanned in the horizontal plane is synthesised. Since the probe is placed at the same height as the antenna array, it receives the maximum of the radiation pattern in the vertical plane.

In the diagram shown in Figure 5.23, the signals at different parts of the system have been represented with voltage phasors, labelled with the letter V. Similarly, the relationship between some of these phasors—indicated with an arrow and referred to with the letter g—have been calculated as complex voltage transfer functions, as follows:

$$g_{ct_1} = \frac{V_{d_1}}{V_1}, \tag{5.2}$$

assuming the linearity and invariance of the microwave networks involved. The subindex 1 indicates that these magnitudes correspond to the first row of the array, connected to 4HOSC_1.

The purpose of the calibration is to obtain a relationship between the sample signals delivered to the ports of the PNA-X, V_{so_i}, $i \in \{1, \ldots, 4\}$, and the signal radiated by the corresponding array elements, which cannot be directly accessed. Nonetheless, after the propagation to the receiving probe, accounted for by the propagation gain terms g_{p_i}, these signals are available at the output port of the pyramidal horn.

The calibration technique shown schematically in Figure 5.23, relies on the dedicated RF cable that connects the Rx probe with the PNA-X, labelled as *calibration cable*. The transfer function g_i that relates the sample signal available at the PNA-X port, V_{so_i}, to the output of the calibration cable V_{cc}, when only 4HOSC_i is operating, can be written as:

$$g_i = \frac{V_{cc}}{V_{so_i}} = \frac{g_{d_i} g_{ct_i}}{g_{c_i} g_{cd_i}} g_{p_i} g_{cc}. \tag{5.3}$$

The terms g_{cc} and g_{p_i} represent the transfer function of the calibration cable and the propagation effects to the output of the probe antenna, respectively. While the former term is constant, regardless of the particular 4HOSC circuit that is operating, the latter varies in each case—especially in phase—due to the differences in the propagation distance. This variation is minimum when the probe lies in the perpendicular drawn from the centre of the two-dimensional antenna array and therefore, the calibration process is performed in this position.

Under these conditions, the variation of the g_{p_i} parameters is primarily determined by the distance between the probe and the antenna array. As long as the measurement is carried out within the far field region of the antenna array,

which starts at a distance of about[1] 0.6 m, the maximum phase variation of the g_{p_i} parameters is, by definition, lower than $\pi/8$ rad.

Since, in this case, the probe is separated from the antenna array about 5 m, the range of variation of the g_{p_i} parameters will be much smaller (of the order of 2.7°), and will therefore be neglected, considering the parameters identical $g_{p_i} = g_{p_j}$, $\forall i, j \in \{1, \ldots, 4\}$. In any case, the error introduced by this approximation is the same assumed by measuring the radiation pattern with this experimental set-up.

Consequently, considering that the output of the calibration cable is related to the radiated signal by the terms $g_{p_i} g_{cc}$ of (5.3), and assuming these are constant regardless of the particular 4HOSC circuit operated, the ratio between the measured sample signal V_{so_i} and the corresponding radiated signal can be calculated from the measured transfer function g_i, as $g_i / g_{p_i} g_{cc}$.

Nonetheless, as far as the the radiation pattern is concerned, it is sufficient to determine the relative amplitude and phase radiated by the elements of the antenna array, rather than their absolute value. The relationships g_i, between the output of the calibration cable, V_{cc}, and the measured sample signal V_{so_i} are measured by sequentially operating one of the 4HOSC circuits at a time.

Thus, taking one of the transfer functions as a reference, e.g. g_1, the ratio g_i/g_1, $i \in \{2, \ldots, 4\}$, will represent the relationship between the signal radiated by the subarrays i and 1, when the corresponding measured samples, V_{so_i} and V_{so_1}, are equal. By correcting the measured sample relationships V_{so_i}/V_{so_1}, $i \in \{2, \ldots, 4\}$ with the inverse factor g_1/g_i, the corrected sample ratios will be equal to 1 when the signals radiated by the subarrays i and 1 are identical in both amplitude and phase.

An additional limitation lies in the fact that only four ports are available in the vector network analyser, making it impossible to measure the four transfer functions g_i simultaneously. However, this is overcome by substituting the calibration cable for the sample cable associated with the fourth circuit and measuring the transfer functions g_1^4, g_2^4 and g_3^4, in a first stage, and then substituting it for the sample cable three and measuring g_1^3, g_2^3 and g_4^3, in a second stage.

The superindices indicate the sample port to which the calibration cable has been connected in either case. The connection of the calibration cable to a different port changes its position and may affect the associated response g_{cc}, resulting in differences in the transfer functions measured with both configurations, i.e. $g_1^4 \neq g_1^3$ and $g_2^4 \neq g_2^3$. However, when considering the ratio g_i/g_1, the differences cancel out and it is in fact verified that $g_2^4/g_1^4 = g_2^3/g_1^3$.

[1] The Fraunhofer region is considered when the following conditions are fulfilled:
$d >> \lambda = 30$ mm
$d \geq \frac{2D^2}{\lambda} \approx 601$ mm
$D = 95$ mm is the maximum dimension of the antenna array.

As opposed to the calibration cable, which is a provisional, very long and loosely laid cable, the sample cables are securely fastened to the rotary platform and have restricted movements. Therefore, the successive connection and disconnection of the sample cables 3 and 4 to carry out the calibration process should not significantly affect their response, and this potential change has been overlooked. After the calibration process, the calibration cable is no longer needed and is thus removed from the experimental set-up.

5.5.3. Radiation Pattern Measurements

Using the experimental set-up that has been described, the radiation patterns of the active antenna array based on 4HOSC circuits have been measured for different progressive phase shift distributions.

When the circuits are at the selected operating regime and injection locked to an external signal of power $P_s = -40$ dBm, the control voltages of the circuits are tuned until the desired phase shift distribution—-measured in real time by the PNA-X vector network analyser—is obtained. The radiation pattern is subsequently measured by rotating the prototype, by means of the azimuth rotary platform, as the relative power received by the pyramidal horn, located in the far field region of the antenna array, is registered.

The measured normalised radiation patterns at 10 GHz, for several steering angles of the main beam θ_m: 0°, ±5°, ±10°, ±15°, ±20°, ±25°, ±30° and ±35°, are shown in Figure 5.24.

The main lobe can be successfully scanned in the range $-25° \leq \theta_m \leq 30°$ with a side lobe level lower than −10 dB. For $\theta_m = -30°$, the side lobe level is slightly over the −10 dB threshold and, as expected according to the simulations, this level is exceeded for higher steering angles $|\theta_m| > 30°$.

Finally, the prototype has been rotated 90° about the perpendicular drawn from the centre of the antenna array in order to evaluate the H plane radiation pattern. The measured radiation pattern in the H planes is compared to that of the E plane, when the elements are fed in phase, in Figure 5.25.

In accordance with the design criteria, the pencil beam is narrower in the H plane, with a 3 dB beamwidth $\mathrm{BW_{3dB}} = 18°$, owing to the greater element spacing $d_y = 0.7\lambda$ in that plane, with regard to the beamwidth in the E plane, which is about $\mathrm{BW_{3dB}} = 21°$, due to the smaller separation $d_x = 0.6\lambda$ in that direction.

5.6. Conclusions

A transmitting two-dimensional active antenna array based on fourth harmonic oscillators has been presented. Each row of the array is fed with progres-

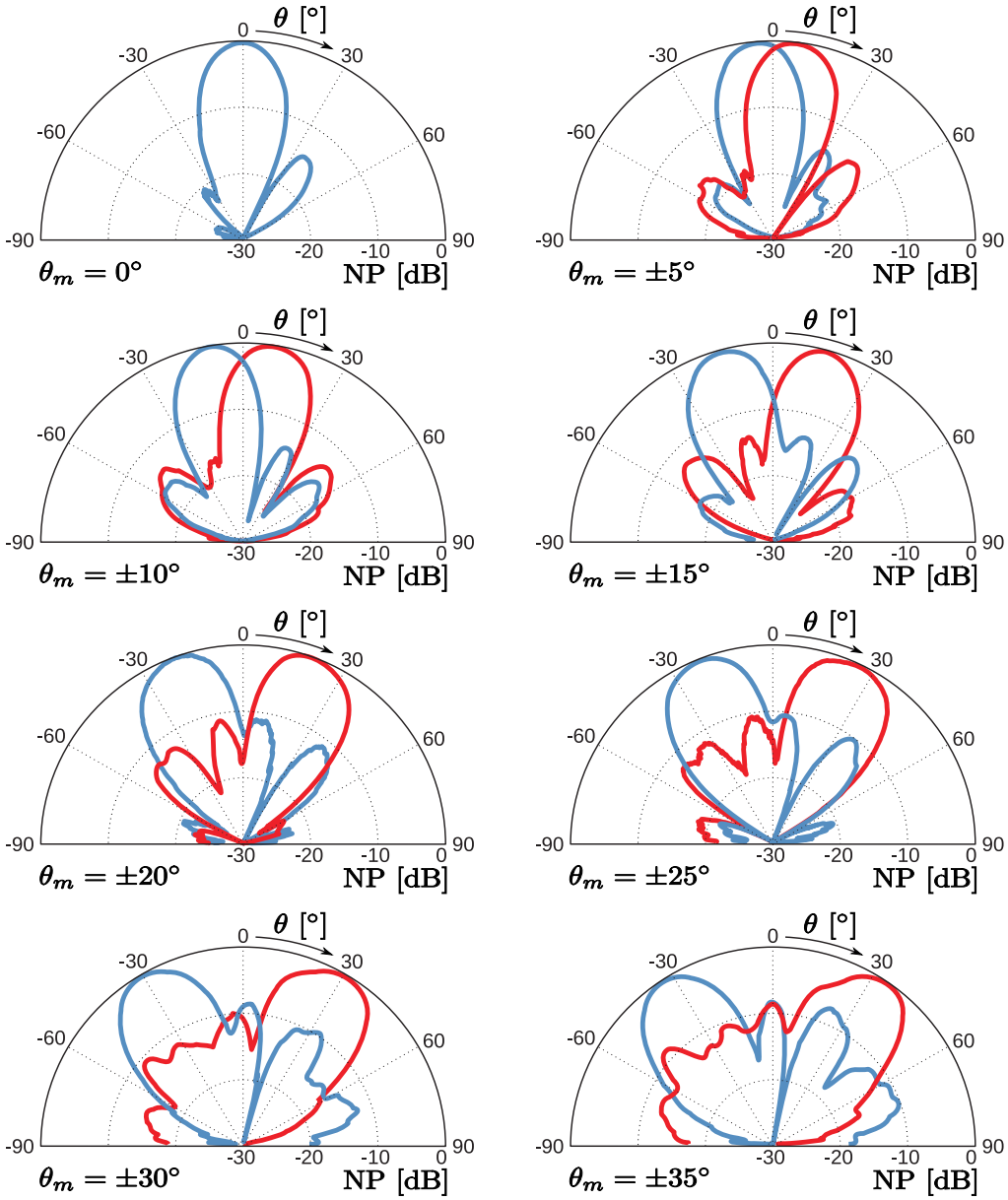

Figure 5.24: Normalised E plane radiation Patterns (NP), in dB, measured at 10 GHz, for different steering angles of the main lobe θ_m: 0°, ±5°, ±10°, ±15°, ±20°, ±25°, ±30° and ±35°.

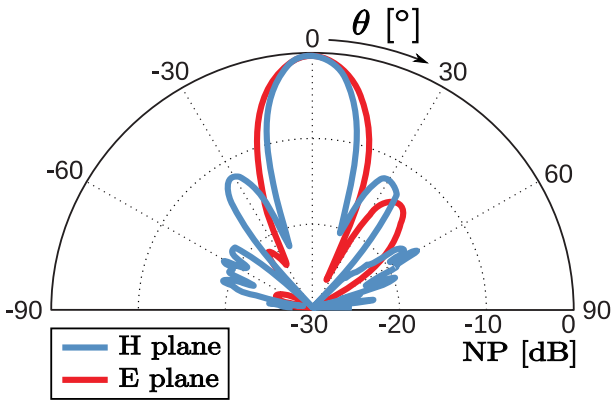

Figure 5.25: E and H plane Normalised radiation Patterns (NP), measured at 10 GHz, corresponding to a steering angle $\theta_m = 0°$.

sive amplitude and phase distributions through a power divider network, which is subsequently controlled by an injection locked fourth harmonic oscillator.

A 4×4 antenna array composed of probe fed individual elements has been designed. The individual element is a microstrip design with two stacked patches exhibiting over 1.5 GHz bandwidth centred about 10 GHz.

In order to prevent the potential appearance of undesired synchronisations between circuits, that might perturb their operation in the practical prototype, a defected ground structure for mutual coupling reduction between antenna elements has been optimised, attaining a coupling reduction of about 8 dB.

The radiation pattern of the complete prototype has been assessed through anechoic chamber measurements. The pencil beam can be effectively steered in the E plane in the range $-25° \leq \theta_m \leq 30°$, with a side lobe level lower than -10 dB.

Bibliography

[1] W.R. Deal, N. Kaneda, J. Sor, Y. Qian, and T. Itoh. A new quasi-yagi antenna for planar active antenna arrays. *Microwave Theory and Techniques, IEEE Transactions on*, 48(6):910–918, Jun 2000.

[2] George Roberto Hotopan. Analysis of Modified Probe Feeding Techniques for Bandwidth Enhancement in Two-Dimensional Antenna Arrays with Individually Fed Radiating Elements. Master's thesis, University of Oviedo, Gijón, Spain, 2009.

[3] Agilent Technologies. *Advanced Design System 2009 Documentation*. 2009.

[4] M.M. Nikolic, A.R. Djordjevic, and A. Nehorai. Microstrip antennas with suppressed radiation in horizontal directions and reduced coupling. *Antennas and Propagation, IEEE Transactions on*, 53(11):3469–3476, Nov. 2005.

[5] A.K. Bhattacharyya, D.R. Jackson, J.T. Williams, and R. Smith. Microstrip patch designs which do not excite surface waves. In *Antennas and Propagation Society International Symposium, 1991. AP-S. Digest*, pages 68–71 vol.1, Jun 1991.

[6] Jong-Gwan Yook and L.P.B. Katehi. Micromachined microstrip patch antenna with controlled mutual coupling and surface waves. *Antennas and Propagation, IEEE Transactions on*, 49(9):1282–1289, Sep 2001.

[7] N. Alexopoulos and D. Jackson. Fundamental superstrate (cover) effects on printed circuit antennas. *Antennas and Propagation, IEEE Transactions on*, 32(8):807–816, Aug 1984.

[8] Y. Q.1 Fu, Q. R.1 Zheng, Q.1 Gao, and G. H.1 Zhang. Mutual coupling reduction between large antenna arrays using electromagnetic bandgap (ebg) structures. *Journal of Electromagnetic Waves & Applications*, 20(6):819–825, 2006.

[9] E. Rajo-Iglesias, O. Quevedo-Teruel, and L. Inclan-Sanchez. Mutual coupling reduction in patch antenna arrays by using a planar ebg structure and

a multilayer dielectric substrate. *Antennas and Propagation, IEEE Transactions on*, 56(6):1648–1655, June 2008.

[10] F. Y. Zulkifli, E. T. Rahardjo, , and D. Hartanto. Mutual coupling reduction using dumbbell defected ground structure for multiband microstrip antenna array. *Progress In Electromagnetics Research Letters*, 13:29–40, 2010.

Chapter 6

Full Duplex Self Oscillating Mixer

Contents

6.1. Introduction

Multiple oscillator based circuits, together with their practical application in active antenna systems, have been presented in the previous sections.

Harmonic self oscillating mixers offer a complete set of functionalities which makes them a very attractive solution for receiving topologies [1], even providing

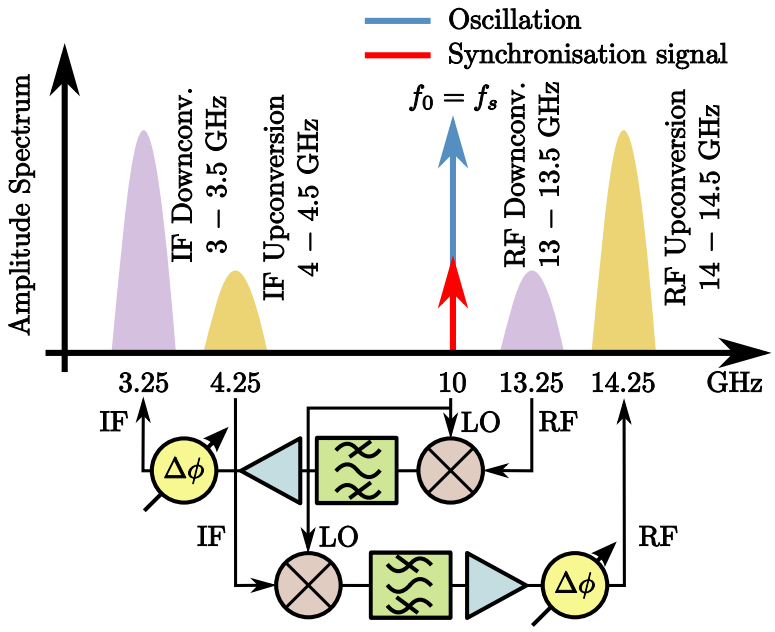

Figure 6.1: Frequency bands involved in the operation of the FDSOM circuit.

positive conversion gain over relatively wide bandwidths [2] . On the other hand, the low power fourth harmonic oscillator that has been described in Chapter 4, has experimentally proved to constitute a an efficient stand-alone front end for the control of antenna array elements transmitting phase modulated signals.

The purpose of this chapter is to introduce a design that can manage both the transmission and the reception simultaneously, enabling the control of full duplex communication systems.

The proposed topology is based on a self oscillating mixer that downconverts the reception channel and upconverts the transmission channel, using as local oscillator the fundamental oscillatory solution of the circuit, which will be injection locked to an external reference signal to improve, its stability and phase noise properties.

The operation of the Full Duplex Self Oscillating Mixer (FDSOM) is shown schematically in Figure 6.1. The circuit is designed to oscillate at $f_0 = 10$ GHz and injection locked to an external signal at the same frequency. An RF channel is defined for the reception, between 13 and 13.5 GHz, which will be downconverted to the corresponding IF band, between 3 and 3.5 GHz. The signal for the transmission will be delivered to the circuit at the IF band between 4 and 4.5 GHz, which will be upconverted to the associated RF band, between 14 and 14.5 GHz.

Note that, since the circuit is injection locked at the fundamental oscillation component, the maximum phase shift range that will be theoretically available is limited to 180°, which is not sufficient for the complete control of an antenna array. Therefore, the FDSOM circuit has been conceived to be injection locked to the output of a low power fourth harmonic oscillator, in a two stage topology.

The fourth harmonic oscillator circuit provides an output at 10 GHz, whose phase shift can be easily tuned in a very wide phase shift range, with a low power consumption. Furthermore, since the power required for the synchronisation of a second stage ought not to be very high, the power consumption of the 4HOSC circuit could probably be further reduced using the techniques applied in Chapter 4.

As has been discussed, the presence of signals with relatively high power level in an oscillator based circuit complicates the design process extraordinarily. Thus, since a limited power level will be obtained for the transmission, the use of this topology will be restricted to short range low power communications.

6.2. Circuit Topology

The electrical diagram of the proposed full duplex self oscillating mixer design that will be addressed in the present chapter is shown schematically in Figure 6.2. Given the multiple signals that need to be managed by the circuit, moderately complex input and output networks will be required to combine and separate those signals. The topology of the circuit is otherwise analogous to other designs described in the previous sections, and it comprises following fundamental parts:

- ***Transistor:*** A Hewlett-Packard ATF-36077 Pseudomorphic High Electron Mobility Transistor (pHEMT) has been chosen for this design, owing to its ultra low noise performance capabilities in its operating band, from 2 to 18 GHz.
- ***Series Feedback:*** A resonant network is connected to the source terminal of the transistor in order to synthesise the required oscillation start-up conditions at the operating frequency $f_0 = 10$ GHz. A varactor diode is integrated in this series feedback network, enabling the fine tuning of the oscillation frequency f_0.
- ***Varactor:*** The chosen device is a Microsemi-GC15007, which provides a capacitance range between 0.2 and 2.8 pF, for control voltages from 20 to 0 V.
- ***Multiharmonic Loads:*** In order for the accurate control and optimisation of the harmonic content present in the circuit, transmission line newtworks whose frequency response can be precisely tailored, are required.

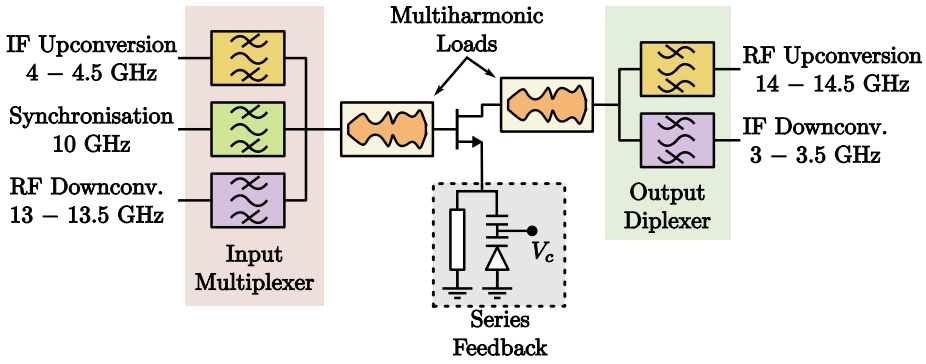

Figure 6.2: Schematic topology of the proposed full duplex self oscillating mixer.

Two of these components, implemented through arbitrarily width modulated transmission line segments, will be connected to transistor gate and drain terminals.

The full duplex self oscillating mixer design will be implemented in a Rogers 3003 substrate laminate, whose properties were summarised in Table 4.1.

The circuit topology, as shown schematically in Figure 6.2, includes additional networks, such as the input multiplexer and the output diplexer, which could be considered auxiliary and overlooked in the design process. Nevertheless, since oscillator based circuits tend to be extremely sensitive on the loads that are connected to them, those networks have been modelled through electromagnetic MoM simulations and taken into account in the whole design process. Those components, together with the required bias structures are described in detail in the following dedicated subsections.

6.2.1. Multiharmonic DC Bias Network Based on Arbitrarily Width Modulated Microstrip Line

The full duplex self oscillating mixer is an active circuit and, as such, it requires an external power supply to operate, which is generally provided through the connection of a DC source. However, since the connection of that source may disturb the normal operation of the circuit, it must thus be performed through a bias network.

The bias network must be designed to present high input impedance values at the frequencies of operation of the circuit, preventing the RF power from being delivered to the DC source. As has been described, multiple bands are involved in the operation of the FDSOM circuit: the IF bands from 3 to 3.5 GHz and from 4 to 4.5 GHz, the self oscillation component at 10 GHz, along with the RF bands between 13 and 13.5 GHz and between 14 and 14.5 GHz. Three such networks will be required to bias each of the transistor terminals: gate, drain and source.

The implementation of the DC bias network has been addressed using Arbitrarily Width Modulated Microstrip Line (AWMML) structure, analogous to the design that has been described in Section 4.2.1, for the fourth harmonic oscillator circuit.

In fact, the design procedure that has been followed in this case is equivalent: a set of $N = 200$ trapezium shaped microstrip sections is employed and the continuity of the modulating function is imposed, leading to the same number N, of degrees of freedom. Also, the structure is completed with a narrow transmission line segment on the RF side, and with a DC pad for the connection of the power supply at the opposite end.

The structure is initially simulated using the distributed element models included in the ADS circuit simulation libraries, and the design parameters are adjusted through a nominal optimisation process, to produced the desired blocking behaviour throughout the bands of operation of the circuit.

Nonetheless, the various frequency bands that must be covered by the bias network constitute a stringent set of requirements that must be imposed on its performance, significantly complicating the design process, with regard to the case of the 4HOSC circuit.

Therefore, the requirements in terms of minimum input impedance have had be relaxed to $|Z_{\text{in,min}}| < 400\ \Omega$, evaluated from the RF side of the network, with the DC terminal connected to ground.

The convergence of the optimisation process has been found to be easier to achieve by merging the two IF and the two RF sub-bands, and imposing the design requirements on three bands: between 3 and 4.5 GHz, between 9.5 and 10.5 GHz for the fundamental oscillation, and from 13 up to 14.5 GHz.

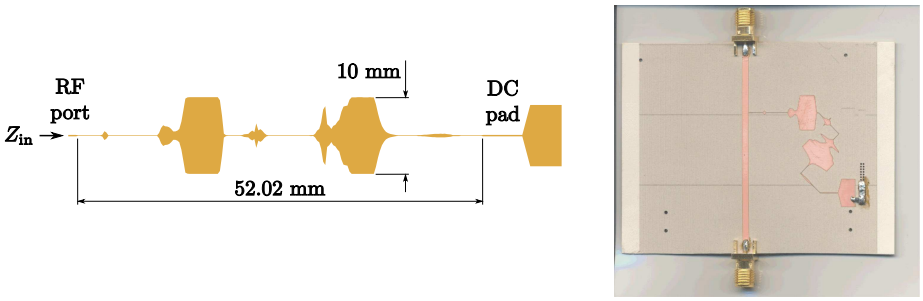

(a) (b)

Figure 6.3: (a) Shape of the final optimised design. (b) Prototype for the experimental validation of the arbitrarily width modulated feeding network.

Once the optimisation process converges and the design requirements are fulfilled, the performance of the entire network is evaluated through Method of Moments (MoM) electromagnetic simulations. Minor deviations from the expected

behaviour can generally be corrected by fine tuning certain parameters of the network. The shape of the final optimised design is shown in Figure 6.3(a). The input impedance values, calculated both using library components and through electromagnetic simulations are compared in Figure 6.4.

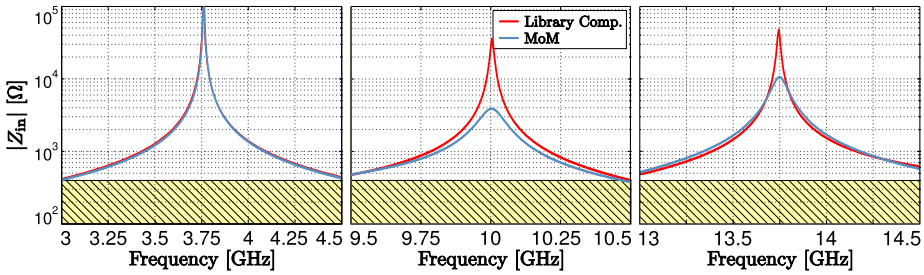

Figure 6.4: Simulated input impedance $|Z_{\text{in}}|$ in the bands of interest, both using library components and through the MoM electromagnetic simulation of the complete structure. The yellow hatched areas indicate the design requirements for the optimisation process.

Although higher peak values are obtained in the simulations using library transmission line models, the results of the MoM simulations meet the design requirements throughout the specified frequency bands.

According to the diagram shown in Figure 6.3(a), the optimised bias network that has been obtained, presents a relatively high aspect ratio, which might make it difficult to accommodate it in the circuit layout. Therefore, the design has been folded up, giving rise to a nearly square footprint.

For the experimental validation of the folded optimised design, the prototype shown in Figure 6.3(b) has been manufactured, in which the structure is connected to a transmission line segment terminated with a port at either end.

The insertion loss introduced by that topology has been assessed both experimentally and through MoM electromagnetic simulations. The results that have been obtained in the bands of interest when connecting the DC pad to ground, both directly and through a 10 kΩ resistor, are compared in Figure 6.5.

The insertion loss values that have been obtained through both approaches are very low and, more importantly, nearly independent on the load connected to the DC pad. Consequently, the bias network exhibits the desired behaviour: the RF power in the bands of interest delivered through the structure is negligible due to the high input impedance, regardless of the load connected to the DC pad.

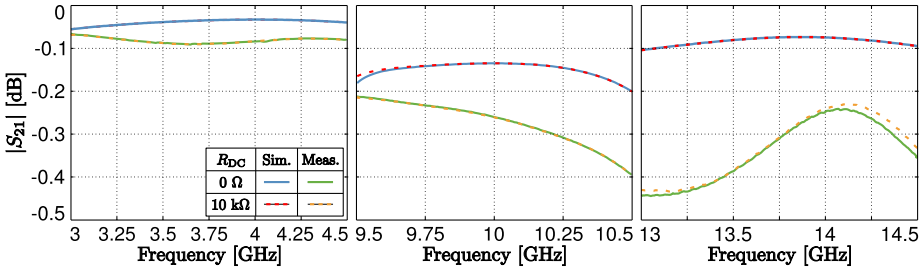

Figure 6.5: Measured $|S_{21}|$ parameter of the prototype shown in Figure 6.3(b), connecting the DC pad to ground through two different resistor values $R_{\mathrm{DC}} = 0\ \Omega$ and $10\ \mathrm{k}\Omega$.

6.2.2. Input Multiplexer

The full duplex self oscillating mixer topology receives three input signals: the external reference for injection locking, the IF input for the upconversion operation and the RF input for the downconversion operation. Since those three input signals need to be delivered to the circuit branch directly connected to the transistor gate terminal, a multiplexer has been designed.

Taking advantage of the fact that the input signals are located at three separate frequency bands, bandpass filters can be used to select the appropriate band at each of the input ports, while rejecting the others. The layout of the final multiplexer design, in which the port corresponding to each of the input signals has been indicated, is shown schematically in Figure 6.6.

Firstly, each of the filters must be individually designed to meet the required design criteria. For this first prototype of the full duplex self oscillating mixer design, particularly strong requirements in terms of rejection of the undesired signals have been imposed, in order to minimise the presence of undesired signals that might disturb the normal operation of the circuit. The main characteristics of the individual filters that have been designed are described next.

Synchronisation Input

As has been described, the FDSOM circuit must be designed to be injection locked at the fundamental oscillation frequency $f_0 = 10$ GHz. In order to ensure the purity of the reference signal, the output filter designed for the fourth harmonic oscillator topology that has been addressed in Chapter 4 will be reused for this design, taking advantage of its high selectivity properties.

Downconversion RF Input

The input RF band, between 13 and 13.5 GHz, will be selected through a parallel coupled bandpass filter with half wavelength resonators, that has been realised

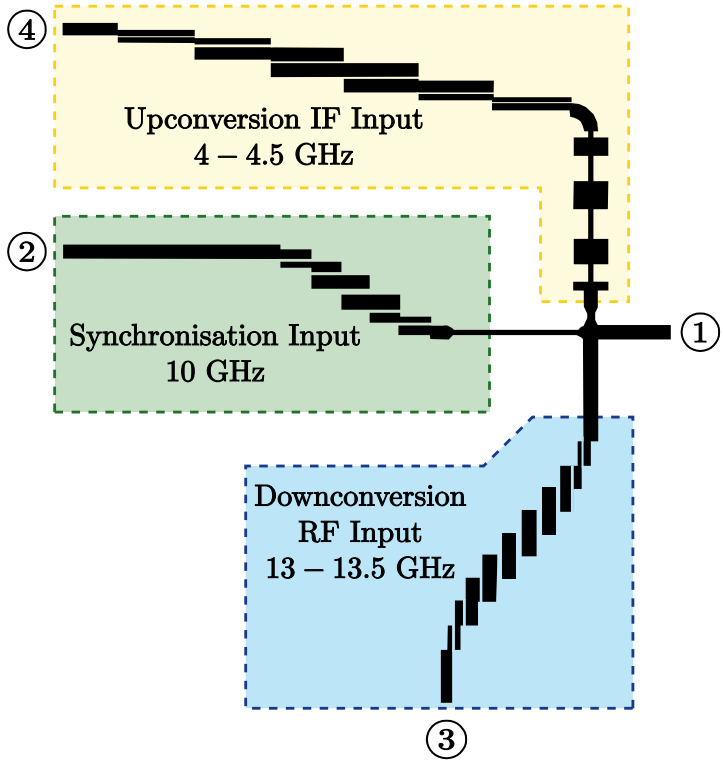

Figure 6.6: Layout of the final input multiplexer design. The port labelled as 1 corresponds to the output of the multiplexer, that will be connected to the input port of the circuit.

using the design equations summarised in [3]. To obtain a sharp roll-off characteristic on the upper end of the passband, giving rise to high attenuation levels on the neighbouring upconversion RF band, starting at 14 GHz, an eight order implementation has been adopted for this design. The method of moments simulation of the filter is shown in Figure 6.7(a). The filter introduces attenuation levels higher than 45 dB in between 14 and 15 GHz, and higher than 35 dB at 10 GHz.

Upconversion IF Input

The corresponding input IF band, between 4 and 4.5 GHz, must be selected while introducing high attenuation levels at the adjacent downconverted IF output, from 3 to 3.5 GHz, as well as at the oscillation frequency $f_0 = 10$ GHz and at the RF bands. In order to properly reject the downconverted IF output, a five order maximally flat parallel coupled bandpass filter with half wavelength resonators [3] has been designed. The MoM simulation of the filter, presented

in Figure 6.7(b), shows that attenuation is higher than 35 dB between 3 and 3.5 GHz. Nevertheless, since the quarter wavelength coupled line sections that have been employed show similar performance at frequencies corresponding to $3\lambda/4$, $5\lambda/4$, etc., additional passbands will appear approximately at odd harmonic components of the main passband. In this case, as shown in Figure 6.7(b), a spurious passband is observed close to the downconversion RF input, at 13 GHz.

In order to remove that additional passband, a stepped impedance low-pass filter has been designed, according to [4]. An eight section topology with a maximally flat response and a cut-off frequency of 6 GHz, has been adopted. The simulated performance (Figure 6.7(b)) exhibits very low insertion losses at the desired passband, while introducing attenuation levels of nearly 40 dB at 13 GHz. The respose of the final filter, obtained by cascading both sections, is also represented in Figure 6.7(b).

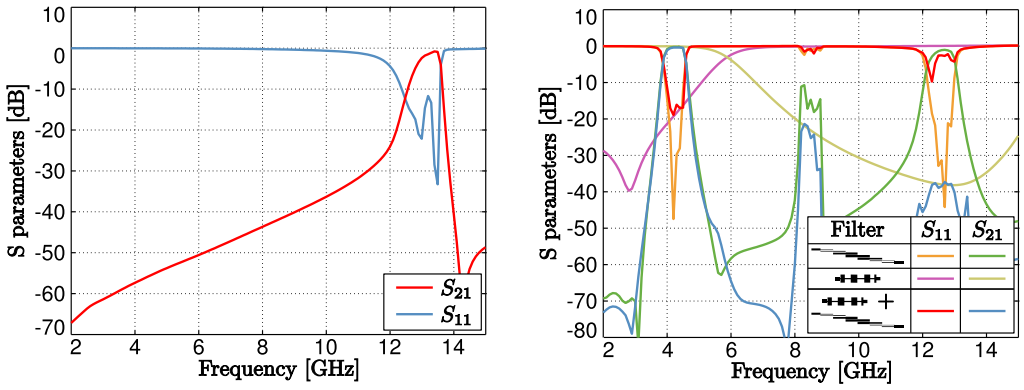

(a) (b)

Figure 6.7: Method of moments simulations of the filter designs used in the input multiplexer (a) Downconversion RF input. (b) Upconversion IF input. The stepped impedance low-pass filter and the coupled line bandpass filter are simulated separately, as well as together in the final design.

The performance that has been obtained in the simulations of the individual filter designs corresponds to a 50 Ω port impedance. Nonetheless, when the output ports are connected together in the multiplexer topology, the load impedance seen by the filters may not be the same, giving rise to potential variations in their behaviour.

In order to minimise the variations in the performance of the filters, each of them has been connected to the common point through a matching line, whose width and length have been subsequently optimised. The multiplexer has been designed for a load impedance of 50 Ω at the output (port 1 in Figure 6.6).

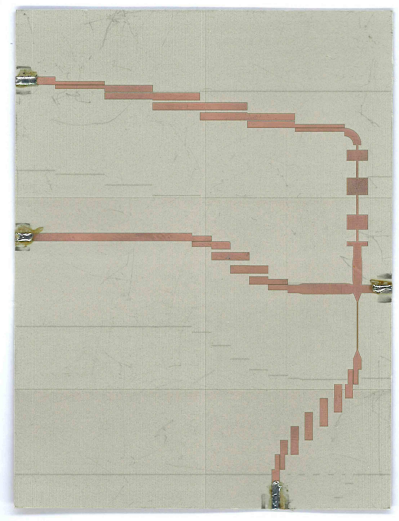

Figure 6.8: Image of the manufactured input multiplexer.

For the experimental validation of the final input multiplexer, the prototype of the optimised design shown in Figure 6.8 has been manufactured and measured. The measurements of the manufactured prototype are compared with the corresponding MoM electromagnetic simulation results in Figure 6.9(a) for the reflection coefficients, and in Figure 6.9(b) for the transmission coefficients. The port numbering has been assigned according to Figure 6.6.

A return loss greater than 10 dB has been obtained at both the IF upconversion and the synchronisation inputs, whereas, for the RF downconversion input port, the measured impedance matching is poorer than in simulation.

With regard to the transmission coefficients, a separate band is clearly selected at each of the three input ports, while introducing high attenuation levels at the remaining bands. The insertion losses have slightly increased with regard to the simulation results, especially a the synchronisation and RF downconversion inputs. Nevertheless, very sharp roll-off characteristics have been attained at the upconversion IF and downconversion RF inputs, introducing attenuation levels higher than 30 dB at the neighbouring downconversion IF and upconversion RF outputs.

6.2.3. Output Diplexer

According to the operation principles that have been described, two output signals are extracted from the FDSOM circuit: the downconverted IF (between 3 and 3.5 GHz) and the upconverted RF (from 14 to 14.5 GHz) outputs. Since those two signals are located far apart in frequency, they could be easily separated

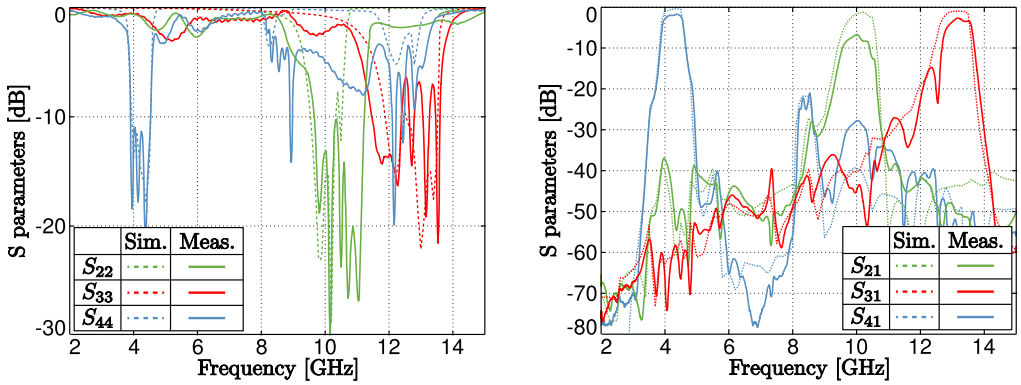

(a) (b)

Figure 6.9: Comparison between MoM simulations and measurements of the manufactured prototype of the final input multiplexer design. (a) Reflection coefficients. (b) Transmission coefficients.

using low order filters. However, as was the case with the input multiplexer, the output diplexer must also reject the signals at the adjacent upconversion IF (4 to 4.5 GHz) and downconversion RF (13 to 13.5 GHz) bands, which are also present in the circuit.

Therefore, the filters must exhibit sharp cut-off characteristics, which significantly strengthens their design requirements. Once again, the filters are separately designed to meet the specifications, prior to connecting them in the diplexer topology shown schematically in Figure 6.10. The main features of the filters that have been obtained are commented next:

Upconverted RF Output

The main design challenge of this filter is that it must select the band between 14 and 14.5 GHz, while properly rejecting the neighbouring downconversion RF band, from 13 to 13.5 GHz. Those requirements are seemingly analogous to those imposed on the input RF filter, which was effectively implemented in the previous section using a parallel coupled bandpass filter with half wavelength resonator. However, as can be verified in Figure 6.7(a), this type of structure—even with high order realisations—generally produces a far sharper roll-off characteristic on the upper end of the passband, than it does on lower end. That behaviour was acceptable for the downconversion RF input, where the closest band to reject was higher in frequency. Conversely, in this case, the passband spans between 14 and 14.5 GHz, while the undesired downconversion RF band extends from 13 up to 13.5 GHz.

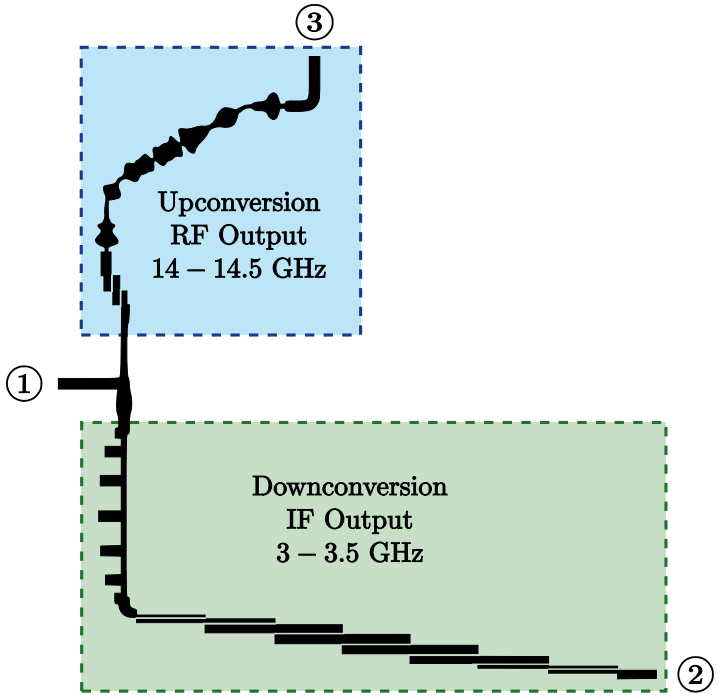

Figure 6.10: Layout of the final output diplexer design. The port labelled as 1 corresponds to the input of the network, that will be connected to the output port of the circuit.

In order to increase the attenuation of the adjacent downconversion RF band, a filter design based on an arbitrarily width modulated microstrip line has been designed. The 200 section structure has been optimised to reduce the insertion loss in the passband, while maximising the attenuation levels between 13 and 13.5 GHz.

The output diplexer will be connected to the transistor drain terminal, whose DC bias constitutes the fundamental power supply of the circuit. Therefore, due to the DC electrical continuity of the AWMML filter, the transistor bias current might be sunk through that structure and dissipated in the load connected to the upconversion RF output port. This potential problem is dealt with by cascading a first order coupled line filter with the AWMML structure, as shown schematically in Figure 6.10, thus breaking the electrical continuity of the network.

The MoM simulation of the complete filter structure is shown in Figure 6.11(a). The insertion loss in the passband has slightly increased to about 4 dB. On the other hand, a sharp roll-off characteristic has been attained at the lower end of the passband, reaching attenuation levels greater than 30 dB in the band between 13 and 13.5 GHz, as well as at 10 GHz and from 3 to 4.5 GHz.

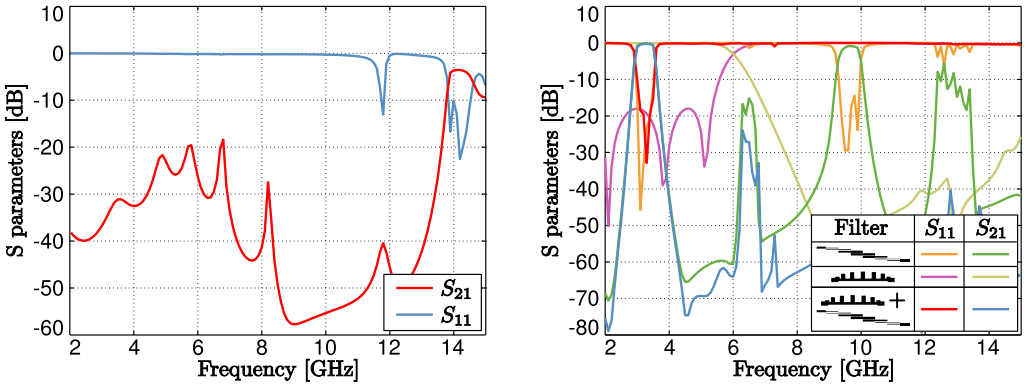

(a) (b)

Figure 6.11: Method of moments simulations of the filter designs used in the output diplexer (a) Upconverted RF output. (b) Downconverted IF output. The stepped impedance low-pass filter and the coupled line bandpass filter are simulated separately, as well as together in the final design.

Downconverted IF Output

An interesting solution to select the downconverted IF band is to use a parallel coupled bandpass filter with half wavelength resonators. A sixth order topology with a maximally flat response has been designed for this purpose. The simulated response has been represented in Figure 6.11(b).

As was the case with the input multiplexer design, this type of filter structure based on quarter wavelength coupled line sections brings about additional passbands at odd multiples of the main passband frequency. In this particular design, low attenuation levels are obtained at 10 GHz—corresponding to the self oscillation frequency—as well as at the downconversion RF band, at 13 GHz.

In order to improve the rejection of those important bands, the filter that has been described will be complemented with a low-pass design. As opposed to the case upconversion IF input of the input multiplexer, the coupled line filter designed here shows very poor attenuation levels (about 10 dB) at 10 GHz. Hence, since the FDSOM can be expected to exhibit a relatively high power level at the fundamental oscillation component in the output port, a more selective low-pass filter will be required for this design.

Using a low-pass topology based on open circuited stubs, a compact implementation for a thirteen pole response has been obtained, whose simulated behaviour is shown in Figure 6.11(b). A cut-off frequency of 6 GHz has been selected to avoid the introduction of additional insertion losses in the passband. The attenuation level is higher than 45 dB at 10 GHz and higher than 30 dB between 14 and 14.5 GHz.

The final filter design is obtained by cascading both stages. Its simulated response, represented in Figure 6.11(b), shows a well defined passband with insertion losses lower than 1 dB between 3 and 3.5 GHz, while attenuation levels higher than 40 dB are attained at the other frequency bands coexisting in the system.

The final diplexer, shown schematically in Figure 6.10, is obtained by connecting the input port of the filters to a common port. In order to minimise the impact the interconnection of the filters has in their individual performance, either filter is connected through a matching line, whose width and length are subsequently optimised.

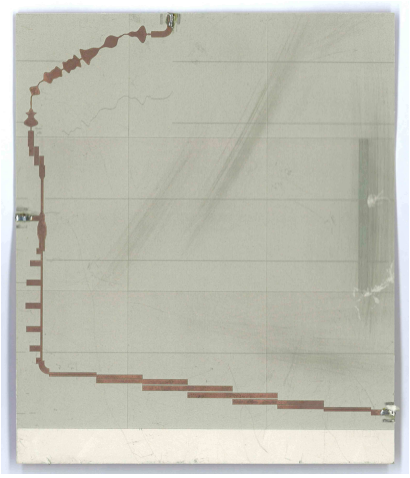

Figure 6.12: Image of the manufactured output diplexer.

The prototype of the final diplexer shown in Figure 6.12 has been manufactured and measured for the experimental validation of the design. The measured scattering parameters are compared with the results of the MoM simulations in Figure 6.13(a), for the reflection parameters, and in Figure 6.13(b), for the transmission parameters. The port numbering has been assigned according to Figure 6.10.

The input port (port 1) is matched to 50 Ω with a return loss higher than 10 dB in the band from 3 to 3.5 GHz, and in most of the band between 14 and 14.5 GHz. The output ports are also matched at their corresponding bands.

With regard to the transmission coefficients, apart from a slight increase in the insertion loss in their respective passbands, the measurements are in agreement with the simulation results. Although the introduction of the AWMML based filter for the upconverted RF output has increased the insertion loss to about 5 dB, it has also enabled the obtention of a sharp roll-off characteristic on the

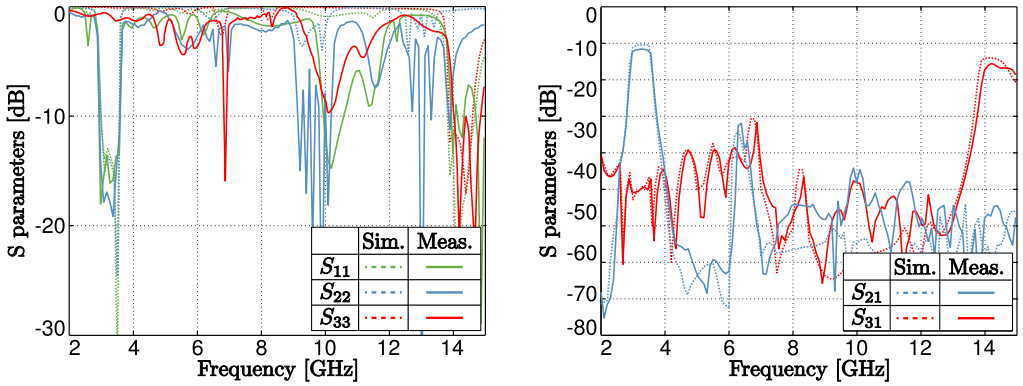

(a) (b)

Figure 6.13: Comparison between the MoM simulation of the output diplexer and the measurements of the manufactured prototype. (a) Reflection coefficients. (b)Transmission coefficients.

lower frequency end of the passband, giving rise to attenuation levels higher than 30 dB between 13 and 13.5 GHz.

6.3. Oscillator Design

The FDSOM circuit topology relies on an autonomous oscillatory solution, that will be used as the local oscillator for the full duplex mixing operations. Therefore, the first step in the design process is to obtain a stable periodic steady state solution at the desired frequency, in this case $f_0 = 10$ GHz.

The individual networks that have been described in the foregoing sections have already been optimised for their particular purpose and will not be modified during design process of the complete circuit.

Therefore, in order to obtain an accurate model of those networks, that will be used in the subsequent simulations of the circuit, full wave method of moments electromagnetic simulations of those individual components have been performed. The frequency plan used for those simulations covers the IF and RF bands, from 0 to 1 GHz and 1 GHz bandwidth around the first 4 harmonic components of the fundamental oscillation, all with a 1 MHz step. Additionally, the range between 0 and 40 GHz is covered with a 250 MHz step.

The models for the individual components as well as for the transistor device, that have been obtained through these simulations will be the base for all the analyses that will be conducted in the following sections.

6.3.1. Oscillation Start-up

The circuit topology shown in Figure 6.2 intrinsically presents a trivial non-oscillatory solution, which must be unstable to enable the onset of a stable periodic steady state solution.

The stability of the trivial solution is evaluated by perturbing the drain terminal of the transistor with a small amplitude current source, and calculating a single input single output transfer function that relates the node voltage V_n, with the perturbing current I_n, at a given frequency ω, as follows:

$$Z_n(\omega) = \frac{1}{Y_n(\omega)} = \left.\frac{V_n}{I_n}\right|_{\omega}. \tag{6.1}$$

The fulfilment of the oscillation start-up conditions, which can be straightforwardly checked by observing the behaviour of the input admittance associated with (6.1), generally indicates the existence of a pair of complex conjugate poles with positive real part that makes the trivial solution unstable.

The design parameters of the series feedback network of the circuit has been adjusted to fulfil of the oscillation star-up conditions at $f_0 = 10\ GHz$. Consequently, the trivial non-oscillatory solution of the circuit will not be practically observable, as any perturbation would trigger a transient with growing amplitude, that will take the circuit to a stable steady state, although that steady state cannot be determined with this analysis.

6.3.2. Periodic Steady State Solution

Once the trivial solution has been destabilised, the circuit parameters must be adjusted to synthesise a periodic steady state autonomous solution at the desired frequency. The non-linear analysis of such regime will be performed through harmonic balance simulations, duly initialised through a non-perturbing voltage auxiliary generator, connected to the transistor drain terminal. A frequency basis including the first four harmonic components of fundamental oscillation frequency will be used for those simulations.

For the simulation of free running oscillators, the phase of the auxiliary generator can be arbitrarily set to 0. The frequency is set to $f_{\mathrm{AG}} = 10$ GHz and the amplitude to $V_{\mathrm{AG}} = 1.5$ V, although the transistor is biased with DC voltage $V_{\mathrm{DS}} = 1.9$ V. A nominal optimisation varying the parameters of the circuit modelled with library components is performed to fulfil the non-perturbation conditions of the auxiliary generator. When that optimisation converges, the circuit will possess a periodic steady state solution with the desired amplitude and frequency, although no information is obtained regarding the stability of that solution.

The power spectrum of the circuit, simulated as output power level delivered through the synchronisation port P_s, has been represented in Figure 6.14. A dominant fundamental component with amplitude $P_s = -0.56$ dBm has been obtained at 10 GHz, while the other three harmonic components exhibit significantly lower levels.

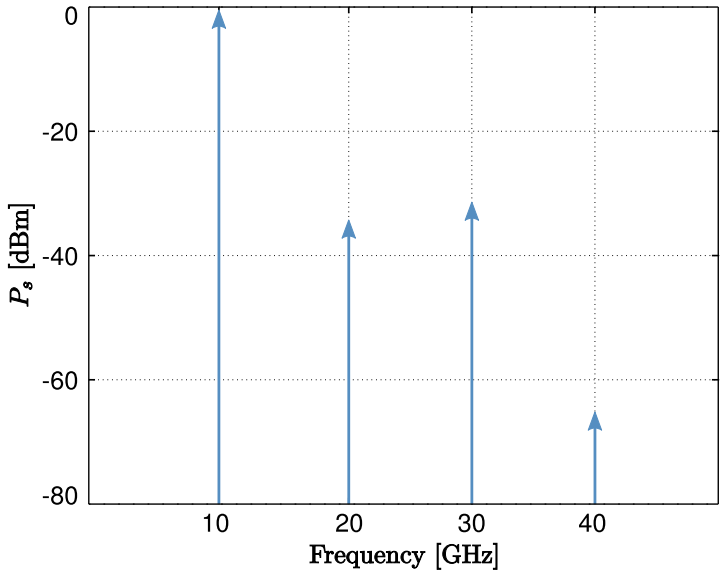

Figure 6.14: Power spectrum delivered through the synchronisation port.

6.4. Mixing Operations

The final FDSOM design must be optimised to efficiently perform the mixing operations of the two input channels with the self oscillating solution that has been synthesised in the previous section.

For the simulation of the mixing operations, additional components must be introduced in the harmonic balance frequency basis, corresponding to the new input signals, along with the intermodulation products they generate. As has been pointed out, the mixing operation will be optimised under the assumption that the input signals have low power levels and thus, the circuit exhibits a linear behaviour with regard to them, not generating harmonic components.

Initially, the optimisation of the upconversion and downconversion operations can be tackled separately. The power level at the intermodulation product associated with either channel that is delivered to the corresponding output port is maximised, while preserving the properties of the oscillatory solution. Therefore, the harmonic balance simulations can be performed with a reduced frequency

basis, consisting of the first four harmonic components of the fundamental oscillation, together with one single additional fundamental at the considered input frequency—which is subsequently swept throughout the associated channel—and the intermodulation products of order 2.

Nonetheless, after certain point in the described process, the separate optimisation of either channel starts to disturb the performance of the other and consequently, this simplified approach can no longer be employed. After that point, the global performance of the circuit needs to be taken into account in the simulations, which substantially increases their computational complexity.

The frequency basis required is composed of the first four harmonic components of the fundamental oscillation at $f_0 = 10$ GHz, along with the two components associated with the input signals, in the IF upconversion and the RF downconversion bands. Although those inputs are considered to operate in a small signal regime and their harmonic components are hence neglected, the intermodulation products of order two also need to be included in the basis.

The extension of the frequency basis brings about an increase in the computation time for every simulation and, taking into account the fact that the input frequencies must be swept throughout the corresponding bands, giving rise to multiple simulations for each frequency sweep. Moreover, the optimisation algorithm will require several sweeps for every iteration, leading to a very heavy process, from a computational viewpoint.

For the optimisation, both input signals are swept together, from 4 to 4.5 GHz and from 13 to 13.5 GHz, considering five simulation points, uniformly distributed throughout those ranges. The input power levels that have been chosen are -30 dBm for the IF upconversion input, and -40 dBm for the RF downconversion signal. Although the optimisation has been performed for those specific values, the input power levels could in principle be varied in practice, as long as they do not disturb the oscillatory solution.

After the optimisation process the conversion gain values, calculated as the ratio of output to input power in either band is represented in Figure 6.15. In order to simplify the comparison between upconversion and downconversion performance, both characteristics have been represented versus the offset from the centre frequency of the associated input band f_c, which are 4.25 and 13.25 GHz, respectively.

Through the appropriate selection of the optimisation goals, a higher peak conversion gain is obtained in the upconversion direction, exceeding 6 dB. A slightly lower peak value is obtained in the downconversion channel, although the response is less frequency selective. A positive conversion gain, throughout a bandwidth wider than 250 MHz, has been attained in both channels.

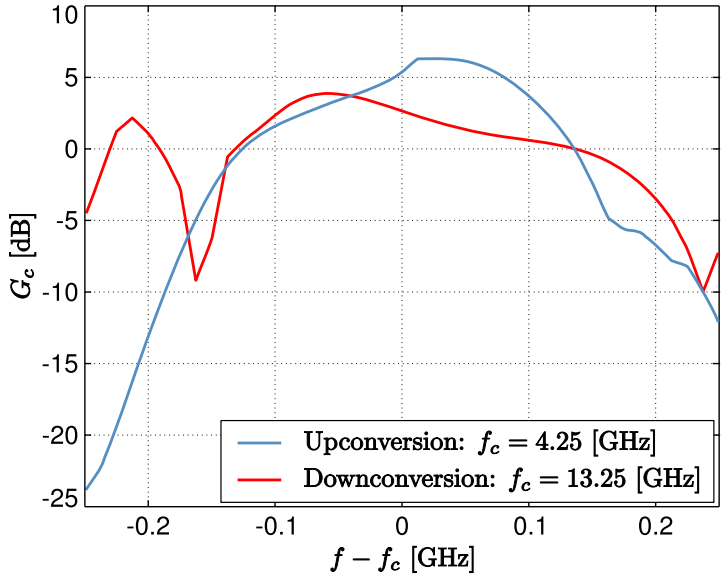

Figure 6.15: Simulated conversion gain of the optimised FDSOM circuit, as a function of the frequency offset from the centre of the corresponding input band f_c.

6.5. Experimental Results

For the experimental validation of the optimised design, the prototype of the FDSOM circuit shown in Figure 6.16, has been manufactured.

The potential fluctuation of the DC bias signals might have a detrimental effect on the circuit performance. Therefore, those signals have been stabilised by connecting a 100 pF and a 100 nF chip capacitors in parallel with each of the DC pads, along with a 100 µF electrolytic capacitor. The performance of the circuit will be assessed in the following through different types of measurements.

6.5.1. Operation as a Voltage Controlled Oscillator

A varactor diode has been embedded in the FDSOM circuit topology shown in Figure 6.2, in order to provide certain degree of frequency tuning, which can be controlled through the varactor bias voltage V_c.

The frequency tuning capabilities of the circuit have been evaluated using a Rohde & Schwarz FSP 40 spectrum analyser, while sweeping the varactor bias voltage V_c, in the continuous range between 5.5 and 16.2 V.

The power spectrum of the oscillator has been measured through the synchronisation filter at 18 operating point corresponding to oscillation frequencies uniformly spaced throughout the frequency tuning range. The measured spectra

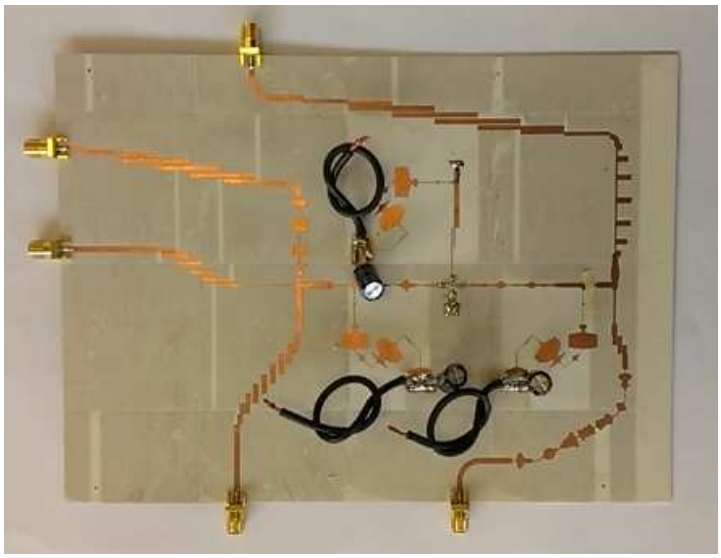

Figure 6.16: Image of the manufactured full duplex self oscillation mixer.

are shown in Figure 6.17(a), and the oscillation frequency is represented as a function of the varactor control voltage V_c, in Figure 6.17(b).

The oscillation frequency can be varied approximately between 10.28 and 10.2886 GHz, while the amplitude barely changes over that range.

However, the whole tuning range has shifted in frequency more than 280 MHz, in such a way that the design operation frequency $f_0 = 10$ GHz is not included in that range. Moreover, the power level of the fundamental component has significantly decreased from the simulated value—approximately -0.5 dBm—to about -12 dBm.

Since the circuit was conceived to oscillate at $f_0 = 10$ GHz, with a given amplitude, the design parameters of the topology were adjusted for the circuit to deliver the power level required to sustain the oscillation at that frequency. Although the practical realisation of the design presents a stable periodic steady state solution at a higher frequency, the circuit cannot readily deliver the required power level at that new frequency, leading to a lower oscillation amplitude.

6.5.2. Mixing Operations

The performance of the circuit as a mixer will be evaluated using an Agilent N5247A PNA-X Vector Network Analyser. The input signals, with a power level $P_{\text{in}} = -12$ dBm, will be varied in a 2 GHz range, rather than strictly at the designated bands, in order to obtain a better characterisation of the behaviour.

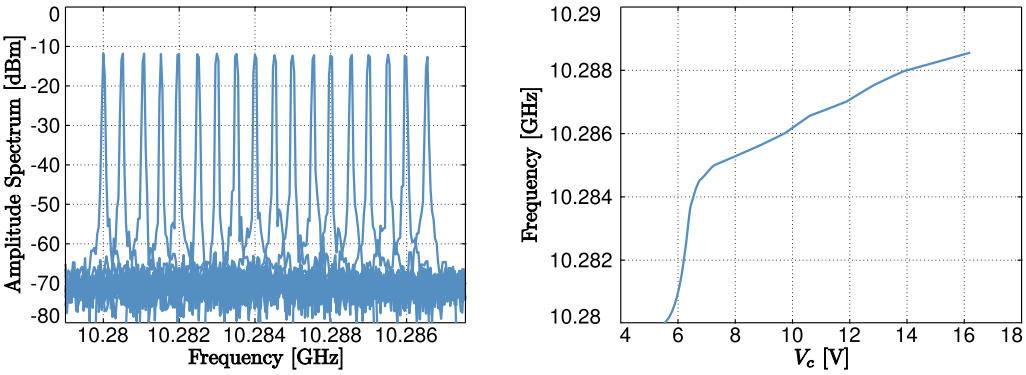

(a) (b)

Figure 6.17: (a) Power spectrum measured through the synchronisation port for different varactor bias voltages V_c. (b) Oscillation frequency versus control voltage.

For the upconversion operation, the input IF signal has been swept between 3 and 5 GHz, while the power delivered to the RF output port at the corresponding harmonic component. The measured results are shown in Figure 6.18(a). Note that, due to the shift that has been observed in the oscillation frequency, the upconversion operation will be equally shifted.

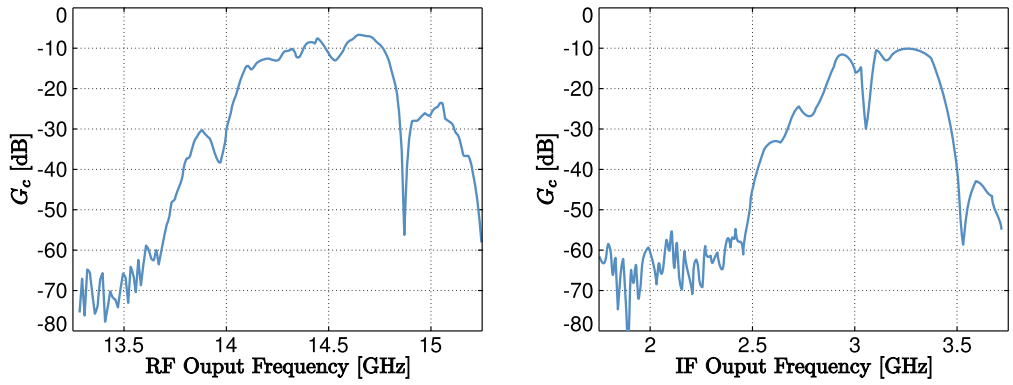

(a) (b)

Figure 6.18: Measured conversion gain. (a) Upconversion. (b) Downconversion

The signal introduced through the input IF filter between 4 and 4.5 GHz will be upconverted to a range approximately between 14.28 and 14.78 GHz. Since upconversion RF filter does not feature a particularly sharp roll-off characteristic on the upper side of the passband, the portion outside the designated band is not excessively attenuated.

Nonetheless, the peak conversion gain level that has been obtained is approximately −6 dB, nearly 13 dB under the simulated result. This disagreement may be explained by the reduction in the level of the oscillatory solution (about 12 dB) since, under linear operating conditions, that reduction in the local oscillator level would bring about a tantamount decrease in the associated intermodulation product.

With regard to the downconversion operation, an input RF signal in the band between 12 and 14 GHz has been introduced, while measuring the power delivered to the IF output port at the corresponding downconverted frequency. The results are shown in Figure 6.18(b).

Due to the shifted oscillation frequency, the RF signal introduced in the assigned band, between 13 and 13.5 GHz, would be downconverted to the band between approximately 2.72 and 3.22 GHz. The sharp cut-off characteristic of the downconversion RF filter on the upper side of the passband can be recognised in the downconverted signal, between 3.25 and 3.5 GHz.

Once again, the peak conversion gain value that has been measured—about −10 dB—has decreased around 12 dB with regard to simulated results. This behaviour is consistent with the explanation that has been given for the upconversion, whereby this degradation has been caused by the observed reduction in the level of the autonomous self oscillation.

6.5.3. Input-Output Characteristic

The linearity of amplifiers and mixers is generally described through the representation of the output power level of the device as a function of the input power, which is commonly referred to as input-output characteristic.

The input-output characteristic has been measured at the centre of the designated output frequency bands: 14.25 GHz for the upconversion and 3.25 GHz for the downconversion. The results that have been obtained are represented in Figure 6.19.

The input power in the corresponding frequency band has been swept between −30 and 0 dBm, obtaining a linear behaviour in both channels. For the upconversion operation, when the input power is increased over the −8 dB threshold, the oscillation signal is abruptly perturbed. Similarly, for the downconversion operation the input power level must not exceed 0 dBm.

Therefore, the mixing operation is performed in a linear regime, that is limited by the perturbation of the oscillatory solution for high input power values, rather than by the appearance of saturation effects.

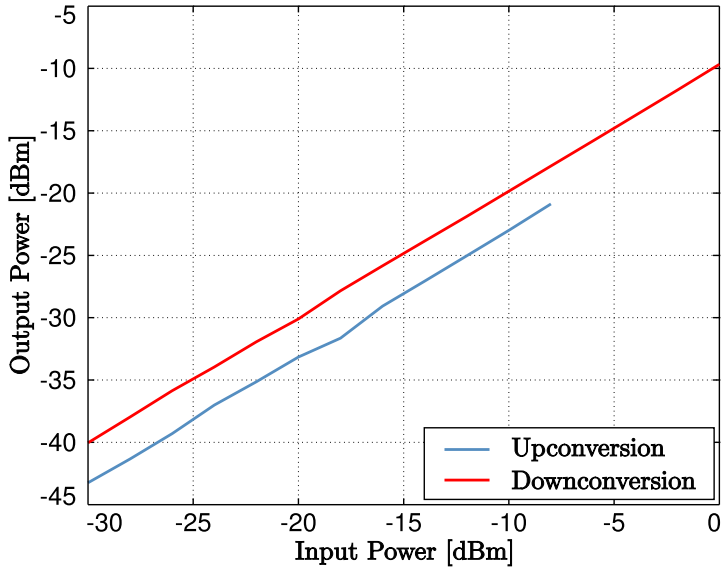

Figure 6.19: Input-output characteristic of the FDSOM circuit, calculated at the centre of the designated output frequency band, for either channel.

6.6. Conclusions

A full duplex self oscillating mixer topology has been proposed. Since the circuit is injection locked at the fundamental component of the oscillation, which is used for the mixing operations, it cannot be effectively used as a phase shifter. Therefore, the topology is intended to be injection locked to a low power fourth harmonic oscillator, which provides the phase shifting operation.

The circuit has been designed using non-linear optimisation techniques, to efficiently carry out both mixing operations. Positive conversion gain values in both channels have been obtained in simulation, over a 250 MHz bandwidth.

A preliminary prototype of the optimised design has been manufactured and measured. The oscillation frequency has shifted upwards in frequency about 280 MHz and, the amplitude of the oscillation has decreased about 12 dB.

A similar reduction has been observed in the conversion gain in both channels, which might be originated by the variation in the level of the oscillation. Peak conversion gain levels of -6 dB have been measured in the upconversion, and of about -10 dB, in the downconversion.

The mixing operation behaves linearly with regard to both input signals, although input levels higher than -8 dBm for the upconversion, and 0 dBm for the downconversion cannot be introduced as they seriously perturb the autonomous solution.

Bibliography

[1] Samuel Ver Hoeye, Luis Fernando Herrán, Miguel Fernández, and Fernando Las Heras. Design and analysis of a microwave large-range variable phase-shifter based on an injection-locked harmonic self-oscillating mixer. *IEEE Microwave Wireless Compon. Lett.*, 16(6):342–344, June 2006.

[2] M. Fernandez, S. Ver Hoeye, L.F. Herran, and Fernando Las Heras. Nonlinear optimization of wide-band harmonic self-oscillating mixers. *Microwave and Wireless Components Letters, IEEE*, 18(5):347–349, May 2008.

[3] L. Young G. Mattaei and E. M. T. Jones. *Microwave Filters, Impedance-Matching Networks, and Coupling Structures*. Artech House, Norwood, MA, 1980.

[4] Jia-Sheng Hong and M. J. Lancaster. *Microstrip Filters for RF/Microwave Applications*. John Wiley & Sons, Inc., 2001.

General Conclusions

In this work the application of several multifunctional oscillator based circuit topologies to the control of general purpose active antenna systems has been studied, and experimentally evaluated.

Firstly, Injection Locked Third Harmonic Self Oscillating Mixers (IL3HSOM) circuits are employed to control a four element receiving phased antenna array, performing several functions, such as the generation of the local oscillator signal, harmonic mixing with gain, and phase shifting in a continuous range that exceeds the generally required 360°. The design is validated by experimental results obtained through the fabrication and measurement of a prototype, in which a continuous beam scanning range between -23.5 and 23.5°, has been achieved.

The same circuit topology has been employed for the implementation of a receiving polarisation agile active antenna, in which two IL3HSOM circuits are used to control of the two orthogonal linearly polarised radiating modes of a microstrip antenna. The manufactured prototype enables the sectiong of the antenna polarisation state in a continuous range comprising both right and left hand circular polarisation, along with two orthogonal linear polarisation states.

A novel fourth harmonic oscillator has been developed for transmitting topologies, and optimised to reduce its power consumption. A prototype of the optimised design has been manufactured, exhibiting a 6 mW power consumption. Its phase noise performance has been analysed under different operating conditions, as well as the dynamics of the circuit when employed for the transmission of phase modulated signals through two different approaches.

The fourth harmonic oscillator design is applied to the control of a transmitting 4×4 active antenna array. The usability of this type of multifunctional oscillator based circuits is demonstrated through the realisation and experimental characterisation of a prototype of a transmitting active antenna array system.

Finally, a novel multifunctional circuit topology is proposed for active antennas operating as both transmitter and receiver, for low power short range communications. The full duplex self oscillating mixer solution is intended to be used in a two stage implementation, together with the low power fourth harmonic oscillator, providing several functionalities for the full duplex system. The steady

state solutions of the circuit as well, as the desired mixing operations have been optimised, obtaining positive conversion gain values. However, a disgreement has been found between the amplitude and frequency of the oscillatory solution observed in the preliminary manufactured prototype and the simulated results.

List of Publications

Publications Directly Originated by the Thesis

International Journal Papers

[1] C. Vazquez, S.V. Hoeye, M. Fernandez, G. Leon, L.F. Herran, and F. Las Heras. Receiving polarization agile active antenna based on injection locked harmonic self oscillating mixers. *Antennas and Propagation, IEEE Transactions on*, 58(3):683–689, 2010.

[2] S.V. Hoeye, C. Vazquez, M. Fernandez, L.F. Herran, and F. Las-Heras. Receiving phased antenna array based on injection-locked harmonic self-oscillating mixers. *Antennas and Propagation, IEEE Transactions on*, 57(3):645–651, March 2009.

[3] Carlos Vázquez, George Hotopan, Samuel Ver Hoeye, Miguel Fernández, Luis Fernando Herrán, and Fernando Las Heras. Microstrip antenna design based on stacked patches for reconfigurable two dimensional planar array topologies. *Progress In Electromagnetics Research*, 97:95–104, 2009.

[4] C. Vazquez, S. Ver Hoeye, M. Fernandez, L.F. Herran, and F. Las Heras. Analysis of the performance of injection locked oscillators in a data transmitting polarisation agile antenna application. *Progress in Electromagnetics Research Letters*, 12:1 – 10, 2009.

[5] C. Vazquez, S. Ver Hoeye, Gonzalez M., M. Fernandez, L.F. Herran, and F. Las Heras. Multi-harmonic dc-bias network based on arbitrarily width modulated microstrip line. *Progress in Electromagnetics Research Letters*, 11:119 – 128, 2009.

[6] Carlos Vázquez, Samuel Ver Hoeye, Germán León, Miguel Fernández, Luis Fernando Herrán, and Fernando Las Heras. Transmitting polarisation agile microstrip antenna based on injection locked oscillators. *Journal of Electromagnetic Waves & Applications*, 22(17/18):24, December 2008.

International Conference Papers

[1] C. Vazquez, G. Hotopan, S. Ver Hoeye, R. Camblor, M. Fernandez, and F. Las Heras. Transmitting active antenna array based on fourth harmonic oscillators for low power point-to-point reconfigurable communications. In *Wireless Information Technology and Systems (ICWITS), 2012 IEEE International Conference on*, pages 1–4, 2012.

[2] Carlos Vázquez, George Hotopan, Samuel Ver Hoeye, Miguel Fernández, Luis Fernando Herrán, and Fernando Las Heras. Defected ground structure for coupling reduction between probe fed microstrip antenna elements. In *Progress in Electromagnetics Research Symposium*, July 2010.

[3] Samuel Ver Hoeye, Carlos Vázquez, Miguel Fernández, Luis Fernando Herrán, and Fernando Las Heras. Use of variable phase-shifters based on injection locked harmonic self-oscillating mixers in active antenna arrays. In *IEEE International Symposium on Antennas and Propagation and USNC/URSI National Radio Science Meeting*, June 2009.

[4] Carlos Vázquez, Samuel Ver Hoeye, Miguel Fernández, Luis Fernando Herrán, and Fernando Las Heras. Transmitting polarisation agile antenna based on synchronised oscillators. In *IEEE International Symposium on Antennas and Propagation and USNC/URSI National Radio Science Meeting*, June 2009.

[5] G. Leon, S. Ver Hoeye, M. Fernandez, C. Vazquez, L.F. Herran, and F. Las Heras. Novel polarization agile microstrip antenna. In *Antennas and Propagation Society International Symposium, 2008. AP-S 2008. IEEE*, pages 1–4, July 2008.

National Conference Papers

[1] C. Vazquez, G. Hotopan, S. Ver Hoeye, M. Fernandez, R. Camblor, and F. Las Heras. Reducción del acoplo electromagnético entre antenas impresas mediante el recorte de ranuras en el plano de masa. In *XXV Simposium del Comité Español de la URSI 2010*, pages 1–4, September 2010.

[2] C. Vazquez, G. Hotopan, S. Ver Hoeye, M. Fernandez, R. Camblor, and F. Las Heras. Estudio de la influencia mutua entre osciladores individualmente sincronizados en una antena de polarización variable. In *XXV Simposium del Comité Español de la URSI 2010*, pages 1–4, September 2010.

[3] S. Ver Hoeye, C. Vazquez, M. Fernandez, Herran L. F., and F. Las Heras. Uso de desfasadores variables basados en mezcladores autooscilantes armónicos en

antenas tipo array activos. In *XXV Simposium del Comité Español de la URSI 2009*, pages 1–4, September 2009.

[4] C. Vazquez, S. Ver Hoeye, M. Fernandez, Herran L. F., and F. Las Heras. Diseño de una antena transmisora con polarización variable basada en osciladores individualmente sincronizados. In *XXV Simposium del Comité Español de la URSI 2009*, pages 1–4, September 2009.

Other Publications

International Journal Papers

[1] C. Vazquez, C. Garcia, Y. Alvarez, S. Ver-Hoeye, and F. Las-Heras. Near field characterization of an imaging system based on a frequency scanning antenna array. *Antennas and Propagation, IEEE Transactions on*, 61(5):2874–2879, 2013.

[2] Y. Alvarez, C. Garcia Gonzalez, C. Vazquez Antuna, S. Ver-Hoeye, and F. Las-Heras. Frequency scanning based radar system. *Progress In Electromagnetics Research*, 132:275–296, 2012.

[3] Rene Camblor, Samuel Ver Hoeye, Carlos Vázquez, George Hotopan, Miguel Fernández, and Fernando Las Heras. Frequency scanning array composed of antipodal linearly tapered slot antennas. *Journal of Electromagnetic Waves & Applications*, 26:468–479, 2012.

[4] M. Fernandez, S. Ver Hoeye, C. Vazquez, Hotopan G., Camblor R., and F. Las Heras. New non-linear approach for the evaluation of the linearity of high gain harmonic self-oscillating mixers. *Progress in Electromagnetics Research*, 126:149 – 168, 2012.

[5] M. Fernandez, S. Ver Hoeye, C. Vazquez, Hotopan G., Camblor R., and F. Las Heras. Non linear optimization technique for the reduction of the frequency scanning effect in a phased array based on broadband injection-locked third harmonic self-oscillating mixers. *Progress in Electromagnetics Research*, 127:479 – 499, 2012.

[6] M. Fernandez Garcia, S.V. Hoeye, C. Vazquez, G.R. Hotopan, R. Camblor, and F. Las Heras. Analysis of the locking range of rationally synchronized oscillators with high reference signal power. *Microwave Theory and Techniques, IEEE Transactions on*, 60(8):2494–2504, 2012.

[7] Y. Alvarez, C. Garcia Gonzalez, C. Vazquez Antuna, S. Ver-Hoeye, and F. Las-Heras. Measurement setup for imaging applications using frequency scanning illumination. *Instrumentation and Measurement, IEEE Transactions on*, 61(11):3014–3023, 2012.

[8] Laviada J., Y. Alvarez, C. Garcia Gonzalez, C. Vazquez Antuna, S. Ver-Hoeye, Fernandez M., Hotopan G., Camblor R., and F. Las-Heras. A novel phaseless frequency scanning based on indirect holography. *Journal of Electromagnetic Waves and Applications*, pages 1–9, 2012.

[9] Rene Camblor, Samuel Ver Hoeye, Carlos Vázquez, George Hotopan, Miguel Fernández, and Fernando Las Heras. Sub-millimeter wave frequency scanning 8 x 1 antenna array. *Progress in Electromagnetics Research*, 132:215–232, 2012.

[10] M. Fernandez, S. Ver Hoeye, C. Vazquez, Hotopan G., Camblor R., and F. Las Heras. Design and analysis of a multi-carrier tx-rx system based on rationally synchronized oscillators for localization applications. *Progress in Electromagnetics Research*, 120:1 – 16, 2011.

[11] M. Fernandez, S. Ver Hoeye, C. Vazquez, Hotopan G., Camblor R., and F. Las Heras. Optimization of the synchronization bandwidth of rationally synchronized oscillators based on bifurcation control. *Progress in Electromagnetics Research*, 119:299 – 313, 2011.

[12] Hotopan G., S. Ver Hoeye, C. Vazquez, Camblor R., M. Fernandez, and F. Las Heras. Millimeter wave microstrip mixer based on graphene. *Progress in Electromagnetics Research*, 118:57 – 69, 2011.

[13] Rene Camblor, Samuel Ver Hoeye, Carlos Vázquez, George Hotopan, Miguel Fernández, and Fernando Las Heras. Microwave frequency tripler based on a microstrip gap with graphene. *Journal of Electromagnetic Waves & Applications*, 25:1921–1929, 2011.

[14] S.V. Hoeye, M.G. Corredoiras, M. Fernandez Garcia, C. Vazquez Antuna, L. Ontanon, and F. Las-Heras Andres. Harmonic optimization of rationally synchronized oscillators. *Microwave and Wireless Components Letters, IEEE*, 19(5):317–319, 2009.

[15] L.F. Herran, S.V. Hoeye, M. Fernandez, C. Vazquez, and F. Las Heras. Analysis of phase distribution errors in mutually coupled harmonic self-oscillating mixers. *Microwave Theory and Techniques, IEEE Transactions on*, 57(12):2853–2861, 2009.

[16] L.F. Herran, S.V. Hoeye, M. Fernandez, C. Vazquez, and F.L. Heras. Nonlinear analysis of mutually coupled harmonic self-oscillating mixers. *Microwave and Wireless Components Letters, IEEE*, 18(9):614–616, 2008.

International Conference Papers

[1] S. Ver Hoeye, R. Camblor, C. Vazquez, M. Fernandez, G. Hotopan, and F. Las Heras. Terahertz frequency scanning 8x1 antenna array for imaging applications. In *Wireless Information Technology and Systems (ICWITS), 2012 IEEE International Conference on*, pages 1–4, 2012.

[2] M. Fernandez, S. Ver Hoeye, C. Vazquez, G.R. Hotopan, R. Camblor, and F. Las Heras. Experimental characterization of a coherent multi-carrier tx-rx system based on rationally synchronized oscillators. In *Wireless Information Technology and Systems (ICWITS), 2012 IEEE International Conference on*, pages 1–4, 2012.

[3] Ortiz C., Suarez M., S.and de Cos E. Ver Hoeye, M. Fernandez, Vazquez C., R. Camblor, G. Hotopan, Hadarig R., F. Las Heras, and Menendez J.L. Synthesis of flexible polymer-ceramic composites for rfid tagging of people. In *European Polymer Congress (EPC2011)*, 2011.

[4] Suarez M., Ortiz C., S.and de Cos E. Ver Hoeye, M. Fernandez, Vazquez C., R. Camblor, G. Hotopan, Hadarig R., F. Las Heras, and Menendez J.L. New materials for rfid tagging of people and metallic objects. In *MATCOMP 2011*, 2011.

[5] C. Vazquez, S. Ver Hoeye, R. Camblor, M. Hotopan, G.and Fernandez, and F. Las Heras. Millimetre wave frequency scanning probe for imaging applications. In *6th ESA Workshop on Millimetre-Wave Technology and Applications and 4th Global Symposium on Millimeter Waves*, pages 1–4, 2011.

[6] Ver Hoeye S., Rodríguez-Reinoso F., Menéndez F., Alvarez P., R. Hotopan, G.and Camblor, C. Vazquez, M. Fernandez, and F. Las Heras. Evaluation of the microwave frequency multiplication effects in microstrip gaps with graphene layers exfoliated from graphites with a different angular spread of the crystalite c-axes. In *Graphene International Conference*, pages 1–4, 2011.

[7] R. Camblor, S. Ver Hoeye, G. Hotopan, C. Vazquez, M. Fernandez, and F. Las Heras. Easily-manufacturable waveguide to microstrip submm-wave transition. In *The 35th International Conference on Infrared, Millimeter and THz Waves (IRMMW-THz 2010)*, pages 1–4, 2010.

[8] R. Camblor, S. Ver Hoeye, G. Hotopan, C. Vazquez, M. Fernandez, and F. Las Heras. Design of a submillimeter microstrip array for beam-scanning applications. In *The 35th International Conference on Infrared, Millimeter and THz Waves (IRMMW-THz 2010)*, pages 1–4, 2010.

[9] G. Hotopan, S. Ver Hoeye, C. Vazquez, R. Camblor, M. Fernandez, and F. Las Heras. Multi-harmonic submillimeter-wave dc-bias network based on an arbitrarily width-modulated microstrip line. In *40th European Microwave Conference 2010*, pages 1–4, 2010.

[10] C. Vazquez, S. Ver Hoeye, M. Fernandez, Herran L., and F. Las Heras. Frequency scanning probe for microwave imaging. In *IEEE International Symposium on Antennas and Propagation*, pages 1–4, July 2010.

[11] Herran L., C. Ver Hoeye, S.and Vazquez, M. Fernandez, and F. Las Heras. A receiving phased array antenna topology based on mutually coupled harmonic self-oscillating mixers. In *IEEE International Symposium on Antennas and Propagation*, pages 1–4, June 2009.

[12] C. Vazquez, M. Ver Hoeye, S.and Fernandez, Herran L., and F. Las Heras. Design of a three port triple band aperture coupled microstrip antenna. In *IEEE International Symposium on Antennas and Propagation*, pages 1–4, June 2009.

[13] M. Fernandez, S.and Herran L. Ver Hoeye, C. Vazquez, and F. Las Heras. Design of high-gain wide-band harmonic self oscillating mixers. In *Integrated Nonlinear Microwave and Millimetre-Wave Circuits, 2008. INMMIC 2008. Workshop on*, pages 1–4, November 2008.

National Conference Papers

[1] M. Fernandez, S. Ver Hoeye, C. Vazquez, G. Hotopan, R. Camblor, and F. Las Heras. Optimización de osciladores racionalmente sincronizados mediante técnicas de control de bifurcaciones. In *Simposium del Comité Español de la URSI 2010*, pages 1–4, September 2012.

[2] M. Fernandez, S. Ver Hoeye, C. Vazquez, G. Hotopan, R. Camblor, and F. Las Heras. Diseño y análisis de un sistema tx/rx multiportadora basado en osciladores racionalmente sincronizados. In *Simposium del Comité Español de la URSI 2010*, pages 1–4, September 2012.

[3] M. Fernandez, S. Ver Hoeye, C. Vazquez, G. Hotopan, R. Camblor, and F. Las Heras. Análisis de la linealidad de mezcladores auto-oscilantes

armónicos con elevada ganancia de conversión. In *Simposium del Comité Español de la URSI 2010*, pages 1–4, September 2012.

[4] Garcia D., R. Camblor, S. Ver Hoeye, G. Hotopan, M. Vazquez, C.and Fernandez, and F. Las Heras. Analysis and optimization of a multiplier in millimeter-wave band based on schottky diode. In *Simposium del Comité Español de la URSI 2010*, pages 1–4, September 2012.

[5] R. Camblor, S. Ver Hoeye, G. Hotopan, M. Vazquez, C.and Fernandez, and F. Las Heras. Array of linearly tapered slot antennas capable of beam scanning by frequency sweep. In *Simposium del Comité Español de la URSI 2010*, pages 1–4, September 2012.

[6] G. Hotopan, S. Ver Hoeye, C. Vazquez, R. Camblor, M. Fernandez, and F. Las Heras. Red de polarización multiarmónica, en banda submilimétrica, basada en línea microstrip modulada arbitrariamente. In *Simposium del Comité Español de la URSI 2010*, pages 1–4, September 2010.

[7] R. Camblor, S. Ver Hoeye, G. Hotopan, M. Vazquez, C.and Fernandez, and F. Las Heras. Submillimeter wave microstrip antenna array with adapted microstrip to waveguide transition. In *Simposium del Comité Español de la URSI 2010*, pages 1–4, September 2010.

[8] M. Fernandez, S. Ver Hoeye, Herran L., C. Vazquez, and F. Las Heras. Optimización no lineal de mezcladores autooscilantes de banda ancha. In *Simposium del Comité Español de la URSI 2009*, pages 1–4, September 2009.

[9] Herran L., S. Ver Hoeye, M. Fernandez, C. Vazquez, and F. Las Heras. Antena receptora basada en mezcladores autooscilantes armónicos acoplados. In *Simposium del Comité Español de la URSI 2009*, pages 1–4, September 2009.

[10] C. Vazquez, S. Ver Hoeye, M. Fernandez, Herran L., and F. Las Heras. Diseño de una antena con tres bandas de trabajo alimentadas por tres puertos independientes mediante acoplo electromagnético a través de ranura. In *Simposium del Comité Español de la URSI 2009*, pages 1–4, September 2009.